Solution Phase Behavior of Stimuli-Responsive Block Polymers in Ionic Liquid

A DISSERTATION
SUBMITTED TO THE FACULTY OF THE GRADUATE SCHOOL
OF THE UNIVERSITY OF MINNESOTA
BY

Cecilia Chloe Hall

IN PARTIAL FULFILLMENT OF THE REQUIREMENTS
FOR THE DEGREE OF
Doctor of Philosophy

Timothy P. Lodge

September 2018

Acknowledgments

I entered graduate school hoping to become a fully independent scientist. I would like to thank my advisor, Tim Lodge, for giving me just the right amount of guidance, and a very large amount of freedom. This allowed me to explore what I found interesting, as well as learn how to make and recover from mistakes. I am very grateful for the opportunity to start my own project in the group, and am very proud that I have brought it to the point where I can pass it along to a new student, Claire Seitzinger.

My research group has been an endless source of help and friendship throughout my five years in graduate school. Prof. Jenny Laaser and Peter Schmidt helped me design instruments, as well as giving me lots of thoughtful advice on my project. I was happy to have the opportunity to mentor an undergraduate, and Cecelia Rivera worked closely with me on significant portions of this work. She helped me synthesize many of the polymers and generally made my work in lab more efficient. I also was able to collaborate with a visiting researcher, Michika Onoda, who was able to put together a publication based largely on his two month visit to Minnesota. I'd like to thank Matt Irwin, Aaron Lindsay, David Giles, Sung-Soo Kim, Gray Jackson, Ron Lewis, Kyungtae Kim, Sveta Morozova, Sujay Chopade, Seyoung Jung, Julia Early, Dan Zhao, and Lucas McIntosh for helpful research discussions and conversations over many topics.

I'd like to thank my closest friends, all of whom I have met during graduate school. Annabelle Watts and I met at a visit weekend to another school, and both ended up choosing Minnesota. We helped each other through classes, our qualifying exams, and even started a student organization together. Our advice sessions over coffee both helped keep me awake and on track, Endless thanks to Annabelle for always introducing me to new friends from collaborators to her group. Without her, I would not have made strong friendships with Kali Johnson and Helena Quilter, who helped me through some of my tougher times in graduate school. Finally, Sam has loved and supported me through the ups and downs of my last year in graduate school, keeping me smiling (and well fed) the whole time.

Dedication

For Sam, for everything

Abstract

Stimuli-responsive polymer solutions have found applications from drug delivery to electrochemical devices. Fundamentally, these responsive properties arise from the interactions between the polymer and the solvent, and understanding these interactions allows for control over the response. This work has two focuses: the development of a light- and temperature-responsive block polymer/ionic liquid solution to enable light triggered ordering and disordering, and the combination of an ABC triblock terpolymer with ionic liquid to produce networks with fewer defects.

Copolymerization of a temperature-responsive monomer, benzyl methacrylate (BzMA), with a light-responsive monomer, 4-phenylazophenyl methacrylate (AzoMA), afforded a polymer with a mixture of these properties. The isomerization of azobenzene from the nonpolar *trans* state to the polar *cis* state under UV light increases the solubility of the polymer in the ionic liquid EMI TFSI. We studied the effect of varying the ratios of the two monomers and the overall polymer molecular weight, and found that AzoMA has a significant absorbance in the UV region, leading to a sample thickness dependence on the phase separation behavior. We were able to obtain copolymers with light-dependent phase separation upon heating, with phase separation temperatures up to 30 ºC. Using this statistical copolymer as a block in a block polymer generated light-responsive block polymer solutions, where samples at concentrations of 40 wt% and below generated spherical ordering upon heating, and disordered upon cooling. The ordering and disordering could also be triggered using light, showing excellent reversibility.

An ABC triblock terpolymer consisting of an insoluble A block, a soluble B block, and a temperature-responsive C block was combined with the ionic liquid EMI TFSI to generate an ion gel. When mixed at temperatures above the phase separation temperature of the C block, the polymer exists in solution as micelles with an A core. Cooling below the phase separation temperature of the C block causes aggregation, where A and C domains are crosslinked by the midblock. Due to the mutual insolubility of the two endblocks, there are no observed looping network defects. This enables higher mechanical integrity and lower necessary concentration of polymer as compared to the analogous ABA triblock.

Contents

Acknowledgments **i**

Dedication **ii**

Abstract **iii**

List of Tables **viii**

List of Figures **ix**

1 Background **1**

1.1 Introduction 1

1.2 Solution phase behavior of polymers 5

LCST and UCST solution phase behavior of homopolymers 5

Block polymers in solution 8

Light-responsive polymers 12

1.3 Thesis overview 14

2 Synthesis and characterization of thermo- and photoresponsive statistical copolymers **16**

2.1 Introduction 17

2.2 Experimental 24

Materials 24

Ionic liquid synthesis 24

Monomer synthesis 25

Chain transfer agent synthesis 28
Reversible addition-fragmentation chain transfer polymerization 30
Atom transfer radical polymerization 30
Free radical polymerization 31
Polymer characterization and molecular weight determination 32
Abbé Refractometry 32
UV-vis spectroscopy 33
2.3 Results 34
NIPAm-based polymers 34
Benzyl methacrylate-based polymers 37
UV light induced *trans* to *cis* isomerization of azobenzene 41
Kinetics of azobenzene isomerization 43
Spiropyran as a photoresponsive monomer 45
2.4 Discussion 46
Thermal stability of *cis* azobenzene 46
2.5 Conclusions 49
2.6 Acknowledgments 50

3 LCST phase behavior of a thermo- and photoresponsive statistical copolymer in an ionic liquid 51

3.1 Preface 52
3.2 Introduction 53
3.3 Experimental 59
Materials 59
Sample preparation 60
Transmittance cloud point measurement 60
Reflection cloud point measurement 61
UV–vis spectroscopy 63
3.4 Results 63
Transmittance cloud point 63

Manually controlled reflection cloud point 66
Automated reflection cloud point measurements 68
3.5 Discussion 72
Absorption of UV light by azobenzene 72
Dependence of the cloud point on molecular weight and copolymer composition 74
3.6 Conclusions 76
3.7 Acknowledgments 78

4 Controlling the morphology of a photoresponsive block polymer in an ionic liquid with light 79

4.1 Introduction 80
4.2 Experimental 82
Materials 82
Block polymer synthesis 83
Polymer characterization 84
Sample preparation 84
Small amplitude oscillatory shear rheology 85
Small angle X-ray scattering 86
Grazing incidence small angle X-ray scattering 87
Optical anisotropy measurements 87
4.3 Results 88
Characterization of block polymers 88
Morphologies of block polymers by SAXS 92
Small amplitude oscillatory shear rheology of M(B*s*A) solutions 94
Grazing incidence SAXS for detection of light-triggered LCOTs 103
Optical anisotropy measurements for detection of OOTs 104
4.4 Discussion 105
Copolymer composition and concentration dependence of block polymer morphology 105

Gap and UV power dependence of LCOTs . . . 109
4.5 Conclusions . . . 111
4.6 Acknowledgments . . . 112

5 Formation of multicompartment ion gels by stepwise self-assembly of a thermoresponsive ABC triblock terpolymer in an ionic liquid 113
5.1 Preface . . . 114
5.2 Introduction . . . 114
5.3 Experimental . . . 116
Materials . . . 116
Block polymer synthesis . . . 117
Sample preparation . . . 118
Cloud point measurements . . . 118
Rheology . . . 118
Dynamic light scattering . . . 119
Small angle X-ray scattering . . . 120
5.4 Results . . . 120
Gelation of PON triblocks in EMI TFSI . . . 121
PEP-core micelles . . . 124
Gelation of NON triblocks in EMI TFSI . . . 125
5.5 Discussion . . . 127
Efficiency of gel network formation . . . 127
Mechanism of PNIPAm phase separation in EMI TFSI compared to water . 133
5.6 Conclusions . . . 136
5.7 Acknowledgments . . . 137

6 Summary and future work 138
6.1 Introduction . . . 138
6.2 Summary and future work . . . 139

References 147

Appendix **164**

List of Tables

2.2 Kinetics of the thermal relaxation of azobenzene in B*s*A 48

4.1 Molecular characteristics of M(B*s*A) photoresponsive block polymers . . . 88

5.1 Molecular characteristics of ABC and ABA triblock polymers 117

5.2 Characteristics of ion gels in EMI TFSI 130

5.3 Characteristics of PON(3-25-11) micelles in ionic liquid and PON (3-25-10) micelles in water 136

List of Figures

1.1 Morphologies predicted for an AB diblock copolymer 2
1.2 Theoretical and experimental phase diagrams for bulk AB diblock copolymers 3
1.3 Chemical structure of various a) anions and b) cations for ionic liquids . . . 4
1.4 Cartoon illustration of an LCST phase diagram showing the spinodal and binodal 6
1.5 Solution phase portrait of a block polymer as a function of χN, f, and ϕ . . 8
1.6 Illustration of the addition of solvent to a block polymer 9
1.7 The effect of a selective solvent on a polymer with a fixed f at a range of temperatures and concentrations 10
1.8 UCST phase separation of P(AzoMA-*r*-NIPAM) in EMI TFSI 12

2.1 Poly(benzyl methacrylate) and poly(N-isopropylacrylamide) 18
2.2 Azobenzene isomerization 18
2.3 Spiropyran isomerization 20
2.4 Cartoon illustration of copolymers produced with composition drift or random incorporation 22
2.5 Synthesis of AzoMA 25
2.6 Reaction scheme for the synthesis of spiropyran acrylate 26
2.7 Synthesis of 2-(dodecylthiocarbonothioylthio)-2-methylpropionic acid . . . 29
2.8 ^{1}H NMR spectra showing conversion of BzMA monomer to polymer 31
2.9 dn/dc of PAzoMA as measured by Abbé refractometry 33
2.10 Chemical structure of chain transfer agents 34

2.11 SEC traces of P(NIPAm-*stat*-AzoMA) copolymers 35
2.12 SEC traces of PNIPAm and PAzoMA polymerized by RAFT 36
2.13 Polymerization kinetics of the ATRP of BzMA and AzoMA 37
2.14 Composition of AzoMA copolymerized with BzMA 39
2.15 SEC traces of various B*s*A copolymers with varying molecular weights and copolymer compositions 40
2.16 Isomerization of B*s*A (17-6) under UV light 41
2.17 *cis* to *trans* isomerization of AzoMA using visible light 42
2.18 Thermal reversion of B*s*A (17-6) at room temperature 43
2.19 Thermal reversion of *cis* to *trans* azobenzene at elevated temperatures . . . 44
2.20 Isomerization of SPA with visible and UV light 45
2.21 First order rate constant plots for determination of thermal azobenzene relaxation kinetics 47
2.22 Arrhenius plots of B*s*A solutions to give the activation energy 49

3.1 Light-dependent LCST phase boundaries 55
3.2 Penetration depth of light through a polymer solution 59
3.3 Transmittance cloud point diagram 61
3.4 Reflection cloud point setup 62
3.5 Transmittance cloud point of 10 wt% B*s*A (17-6) 63
3.6 UV vis spectra testing the automated transmittance cloud point apparatus . 64
3.7 Manually controlled transmittance cloud point of 1 wt% B*s*A (17-6) in EMI TFSI 65
3.8 Dewetting in reflection cloud point measurement 67
3.10 Effect of molecular weight on the cloud point of B*s*A 70
3.12 UV vis spectra of *cis* and *trans* isomerized B*s*A (28-17) 73
3.13 Cloud point temperature windows as a function of molecular weight 75

4.1 Thermogravimetric analysis of M(B*s*A) (18-31(11)) 89
4.2 SEC traces of PMMA-CTA homopolymers and M(B*s*A) block polymers . . 90

4.3 Differential scanning calorimetry of M(B*s*A) (18-31(11)) neat and in BMI TFSI 91
4.4 SAXS patterns of M(B*s*A) (24-20(10)) in EMI TFSI 93
4.5 Phase diagrams of M(B*s*A) block polymers in EMI TFSI 95
4.6 Temperature sweeps of M(B*s*A) (22-24(5)) in EMI TFSI under UV and visible light 97
4.7 Temperature sweeps of M(B*s*A) (13-46(5)) in EMI TFSI under UV and visible light 98
4.8 Temperature sweeps of M(B*s*A) (18-31(11)) in EMI TFSI under UV and visible light 99
4.9 Light-triggered LCOT of M(B*s*A) (22-24(5)) in EMI TFSI 100
4.10 Light-triggered LCOT of M(B*s*A) (13-46(5)) in EMI TFSI 101
4.11 Triggering of 35 wt% M(B*s*A) (22-24(5)) in EMI TFSI using UV light and thermal reversion of azobenzene 103
4.12 FCC and HCP peak indices on 20 wt% M(B*s*A) (22-24(5)) in EMI TFSI SAXS patterns 106
4.13 Scattering pattern of 35 wt% M(B*s*A) (22-24(5)) in EMI TFSI 107
4.14 Frequency sweep of 35 wt% M(B*s*A) (22-24(5)) in EMI TFSI at 150 ºC. . . 107
4.15 Scattering patterns of 25 and 30 wt% M(B*s*A) (22-24(5)) in repeated heating and cooling cycles 109
4.16 Rheology of 35 wt% M(B*s*A) (13-46(5)) at a larger gap and lower UV power 110

5.1 Cartoon of ABA and ABC physically associated ion gels 116
5.2 Critical strain of 10 wt% PON in EMI TFSI 119
5.3 Cloud point of PNIPAm in EMI TFSI 120
5.4 Cartoon illustration of PON gelation 121
5.5 Dynamic frequency sweep of 5 wt% PON in EMI TFSI. 122
5.6 Temperature sweeps of PON in EMI TFSI 123
5.7 Temperature sweeps of 5 wt% PON in EMI TFSI at various heating rates . 124
5.8 Impact of heating rate on gel melting 125

5.9 SAXS pattern of PEP-core micelles at elevated temperature 126
5.10 Dynamic light scattering of PON in EMI TFSI 127
5.11 Rheological measurements of NON in EMI TFSI 128
5.12 Concentration dependence of modulus for PON in EMI TFSI 129
5.13 Comparison of temperature sweeps of PON and NON ion gels 132
5.14 Comparison of the gelation of PON in water and ionic liquid 133

6.1 Cartoon illustration of an LCST phase diagram with two boundaries depending on light 139
6.2 Phase diagram of M(B*s*A) (22-24(5)) 142

6.3 ^{1}H and ^{19}F NMR spectra of EMI TFSI 164
6.4 ^{1}H and ^{19}F NMR spectra of BMI TFSI 164
6.5 ^{1}H NMR spectrum of AzoMA 165
6.6 ^{1}H NMR spectrum of **A** 166
6.7 ^{1}H NMR spectrum of **B** 167
6.8 ^{1}H NMR spectrum of **SP** 168
6.9 ^{1}H NMR spectrum of **SPA** 169
6.10 ^{1}H NMR spectrum of a CTA 169
6.11 ^{1}H NMR spectrum of PMMA-CTA 170
6.12 ^{1}H NMR spectrum of M(B*s*A)-CTA (18-31(11)) 171
6.13 ^{1}H NMR spectrum of M(B*s*A) (18-31(11)) 172

Chapter 1

Background

1.1 Introduction

The ability to control the nanoscale structure of materials has driven technological innovations, such as fuel cells,[1,2] battery technology,[3–6] and water filtration.[7–10] The structures of these materials dictate their properties, thus the ability to tune the properties arises from control of the structure. In certain applications, it is necessary to trigger changes in the structure of the material, which can be achieved through external stimuli such as light, magnetic or electric fields, or changes in temperature or pH. In the medical field, this often involves the release of a drug therapy at a specific target, requiring controlled triggering of the release.[11–15] For data storage, this involves writing a specific pattern, reading the pattern back, then eventually erasing the information.[16–19] Microfluidic devices can have valves that time the release of certain components, or simply only allow flow at specific time intervals.[20–23] The design of materials for these applications requires a fundamental understanding of how and why they react to a stimulus that allows for a change in structure.

Self-assembly of block polymers

Block polymers afford the ability to generate well-ordered structures on the 10-100 nanometer length scales. Block polymers are composed of two or more chemically distinct polymers that are covalently linked together. When the two blocks are incompatible and do

not want to mix, there is a thermodynamic drive to phase separate. The covalent linkage prevents macroscopic phase separation into two phases, as is seen in oil and water. This results in microphase separation that affords nanoscale structures that depend on the degree of polymerization, *N*, the interaction parameter, χ, and the volume fraction of each of the blocks, f.[24–30] Figure 1.1 shows the range of morphologies predicted for AB diblocks, from low to high f_{blue}, volume fraction of the blue block.

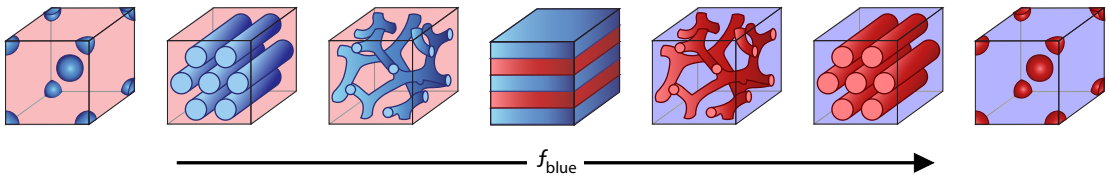

Figure 1.1: Cartoon of the morphologies predicted for an AB diblock copolymer with increasing volume fraction of the blue block. Starting from the left, the morphologies are identified as body-centered cubic spheres, BCC, hexagonally packed cylinders, HEX, gyroid, GYR, and lamellar, LAM. This trend reverses on the other side of LAM.

Block polymers form these ordered microstructures in a way that minimizes their free energy. This requires a balance of the entropy resulting from elongation of the chains and the enthalpic contribution of the interfacial tension. Depending on the volume fractions of the blocks, the interface between the two will have varying degrees of curvature.[27] For a polymer where both blocks have equal volume fractions, the interface will be flat, and the lamellar morphology will be observed. For polymers with a high degree of asymmetry in the volume fractions, the interface will be highly curved, giving body-centered cubic spheres.

The combination of the interaction parameter and the degree of polymerization, χN, is used to describe whether or not microphase separation will occur. Polymers with high χ will microphase separate even when the degree of polymerization, *N*, of both blocks is small. However, if the χ is small, phase separation can still be achieved even with low χ. Flory-Huggins theory describes how χ of a diblock can be predicted using solubility parameters, δ:

$$\chi = \frac{V_{ref}}{RT}\left(\delta_A - \delta_B\right)^2 \tag{1.1}$$

where V_{ref} is the reference volume, R is the gas constant, T is temperature, and the sub-

scripts on δ correspond to the components of the system, in this case the two blocks A and B.[31] The larger the difference in the solubility parameters, the larger χ will be. The solubility parameters are typically estimated for polymers by observing their solubility in solvents with a known solubility parameter,[32] or by simulation studies.[33] Equation 1.1 shows that χ has a temperature dependence, that increasing the temperature of the system decreases the χ, thus making mixing more likely.

Mean field theory predicts that a symmetric AB diblock, $f_A = f_B$ will have an order disorder phase transition (ODT) at $\chi N = 10.5$.[29] As the volume fractions of each block become unequal, the ODT gains a dependence on f as a result of the changing microstructure.[27] Self-consistent mean field theoretical predictions of a phase diagram for block polymer map the expected phases at a given χN and f_A, and as shown in Figure 1.2, these predictions match very well with experimental data. The ability to predict the

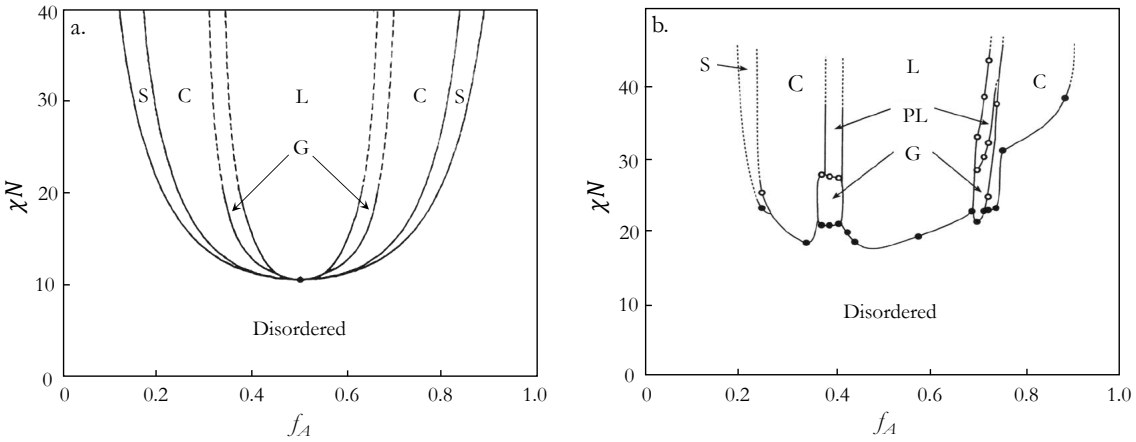

Figure 1.2: a) Theoretical predictions of morphologies expected for AB diblock copolymer in comparison with b) experimental data. The experimental data was collected on a styrene-isoprene diblock copolymer. S: body-centered cubic spheres, C: hexagonally packed cylinders, G: gyroid, L: lamellae, PL: perforated layers. Figures adapted with permission from Ref. 34 (Copyright 1994 American Physical Society) and 35 (Copyright 1995 American Chemical Society) respectively.

morphology of a given diblock is essential in designing materials for applications. While theory does not always provide an accurate phase portrait, these estimates give a starting point for identifying the block polymer architecture necessary to get the desired morphology at a temperature. In the case of more complex systems, mapping the phase diagram first allows for easier design of materials for applications.

These morphologies can be exploited for a varity of applications, such as the patterning of silicon wafers using the inherent shape and domain spacing of HEX and LAM.[36–40] While bulk block polymers have found a range of applications, the exploitation of order-order phase transitions have not received a significant amount of attention. As seen in Figure 1.2, only small composition windows show order-order phase transitions, and reaching them often requires high temperature conditions, beyond what would be usable in applications. Making these order-order phase transitions more prevalent is possible with the addition of solvent to block polymers,[41–44] which will be discussed later.

Ionic liquids

Ionic liquids are a relatively new class of solvents composed of salts that are liquid at room temperature. This is achieved by the use of large, bulky anions and cations that cannot achieve regular packing on a lattice at room temperature in the same manner as typical salts such as NaCl.[45] Various structures of anions and cations for ionic liquids are shown in Figure 1.3. Many ionic liquid cations are based on quaternized amines, appended with various alkyl chains. Increasing the length of the alkyl chain typically decreases the melting point of the ionic liquid by increasing the packing frustration of the ions. The anions are typically bulky inorganic compounds, containing fluorine to increase the hydrophobicity.[45–47] Despite the lack of a regular lattice, the intermolecular forces between the components are

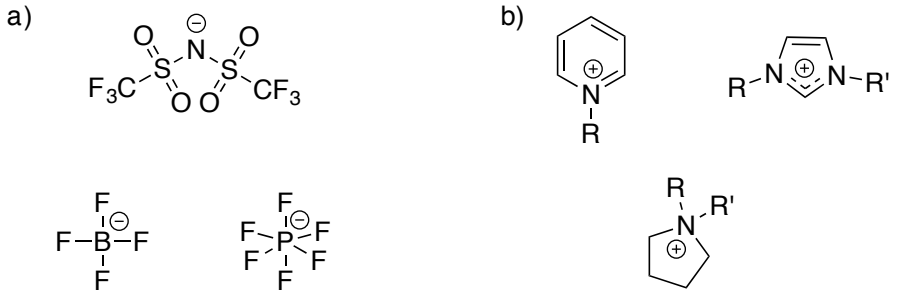

Figure 1.3: Chemical structure of various anions and cations for ionic liquids.

still extremely strong, imparting a negligible vapor pressure. This is a significant benefit in many applications where changes in temperature will not result in evaporation, and samples can be held under vacuum. A solution of ionic liquid mixed at a given concentration will

remain at that concentration, as long as it does not absorb water from ambient humidity. This water uptake can be mitigated through the use of hydrophobic ionic liquids, such as 1-ethyl-3-methyl imidazolium bis(trifluoromethanesulfonylimide) (EMI TFSI). Ionic liquids exhibit significantly wider operating temperature ranges than traditional organic solvents, often forming a solid at or below room temperature, and maintaining stability up to 400 ºC.[48] In addition to thermal stability, they have high ionic conductivities and wide electrochemical windows, making ionic liquids ideal for use in electrochemical devices. With all of these positive characteristics, the main point lacking in ionic liquids is mechanical integrity. Thus they are often combined with polymers to form stand-alone devices. The combination of ionic liquids with polymers often improves the properties of the ionic liquid. For example, one study found that a polymer gel consisting of crosslinked poly(methyl methacrylate) swollen with EMI TFSI had an increase in the number of ion carriers as compared to neat ionic liquid.[49] This was hypothesized to result from association of the non-conductive species in the ionic liquid with the polymer. Ionic liquids can also enhance the stability of polymers, showing an increase in thermal stability relative to bulk polymer. This is contrary to what is seen with traditional plasticizers, which typically decrease the degradation temperature of polymers.

1.2 Solution phase behavior of polymers

LCST and UCST solution phase behavior of homopolymers

The degree to which a polymer and solvent mix depends upon the free energy of mixing. Flory-Huggins theory can be used to describe the free energy of mixing, ΔG_m of a polymer and solvent:

$$\frac{\Delta G_m}{kT} = \phi_s ln(\phi_s) + \frac{\phi_p}{N_p} ln(\phi_p) + \phi_s \phi_p \chi \tag{1.2}$$

where ϕ_s is the volume fraction of solvent, ϕ_p is the volume fraction of polymer, and N_p is the degree of polymerization of the polymer.[50,51] The $\phi_s ln(\phi_s) + \frac{\phi_p}{N_p} ln(\phi_p)$ terms comprise the entropic contribution, and the $\phi_s \phi_p \chi$ is the enthalpic component. This equation assumes mean field behavior, that the local composition is the same as the composition of the entire

system. The enthalpic term contains χ, which imparts a temperature-dependence to the free energy of mixing.

The mixing of polymer and solvent can be mapped to a phase diagram as a function of polymer concentration and temperature, shown for lower critical solution temperature (LCST) phase behavior in Figure 1.4, which has two distinct boundaries. The dashed line

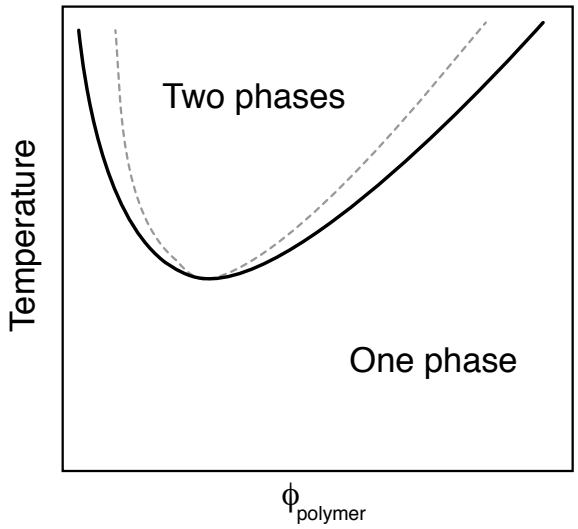

Figure 1.4: Cartoon illustration of a polymer/solvent mixture phase diagram showing the spinodal, dashed grey line, and binodal, solid black line.

represents the spinodal, or the stability limit. The solid line is the equilibrium curve, or the binodal. If a polymer at a given concentration is taken to a temperature between the spinodal and the binodal, the solution will phase separate into a polymer-rich phase, ϕ', and polymer-poor phase, ϕ'' after undergoing nucleation and growth. If it is taken past the spinodal, the phase separation event will be spontaneous. Both the stability limit and the equilibrium condition can be defined using the free energy of mixing. Phase separation is spontaneous when phase separation into two phases with compositions ϕ' and ϕ'' decreases the free energy of mixing. If splitting into two phases increases the free energy of mixing, the solution is stable. These events occur when $\Delta G_m/RT$ is concave down and concave up, respectively. Thus the region of stability occurs when the second derivative of $\Delta G_m/RT$ with respect to ϕ is positive. The equilibrium curve is defined as the points where the chemical potential of the polymer, $\Delta\mu_{polymer}$, is equal in both phases ϕ' and ϕ''. The same condition also must be true of the solvent. In practical terms, the spinodal can be obtained

through small angle neutron scattering measurements, and the binodal can be approximated by cloud point measurements.[52]

A polymer solution can undergo phase separation upon heating, called lower critical solution temperature (LCST) phase behavior, or upon cooling, called upper critical solution temperature (UCST) phase behavior. Figure 1.4 is an illustration of an LCST phase diagram. LCST phase behavior has been observed with a variety of polymers in ionic liquids, including poly(ethylene oxide) (PEO) in EMI/BMI BF_4[53,54] and EMI/BMI Cl,[55] poly(*n*-butyl methacrylate) (P*n*BMA) in EMI/BMI TFSI,[52,56] and poly(benzyl methacrylate) (PBzMA) in EMI TFSI.[57–60] This LCST phase behavior arises due to strong interactions between the ionic liquid and polymer, such as hydrogen bonding between PEO and imidazolium-based ionic liquids. In the case of PBzMA, the imidazolium cation of the ionic liquid and the pendant phenyl rings of the polymer form cation-π interactions which show a liquid clathrate structure.[59] In both examples, the formation of a structure upon solvation could allow for a loss of entropy upon mixing, which in turn may favor LCST phase behavior. The sign of ΔG_m does not determine spontaneity of mixing, as discussed in the previous paragraph, so a negative entropy is not necessarily the direct cause for the observed phase behavior, although it does help rationalize it. The exact temperature of the LCST phase boundary can be tuned by varying the alkyl chain length of the imidazolium cation, increasing over 40 ºC from EMI TFSI to BMI TFSI in the case of PEO.[53]

UCST phase behavior has also been observed in ionic liquids, in the combination of PNIPAm and EMI TFSI.[61,62] This is in contrast to solvation of PNIPAm in water, where LCST phase separation is observed.[63] The LCST phase separation in water has been explained as resulting from hydrogen bonding allowing for solvation at low temperatures, then driving phase separation upon heating due to the negative entropy of these interactions. This explanation also factors in the solvation of the non-polar isopropyl group, further driving the system to phase separate.[64] The LCST phase separation has little dependence on molecular weight or concentration, and shows a very sharp phase transition temperature. The UCST phase separation in water varies with molecular weight and concentration, indicating that the interactions that cause the phase separation in the two solvent systems are distinct.[61,62] The dominant interactions between EMI TFSI and PNIPAm seem to be van der

Waals forces, which are significantly weaker than the hydrogen bonding seen with water. The UCST phase separation from ionic liquid has been explained as PNIPAm having inter- and intramolecular hydrogen bonding between PNIPAm chains at low temperatures in the phase separated state, and that mixing leads to an increase in entropy that would contribute to the UCST phase behavior.[64]

Block polymers in solution

The addition of solvent to block polymers greatly enhances the phase portrait, adding a third dimension of polymer concentration, ϕ, to the χN and f dependent phase diagram of a bulk block polymer.[43] Figure 1.5 illustrates this, showing the three possible views of the phase diagram. The morphologies can be observed at a constant temperature, giving the xz-plane. In applications where temperature must be constant, this view of the phase diagram would be useful to determine the block polymer architecture and concentration in solvent needed to achieve a specific morphology. At a constant volume fraction, the yz-plane

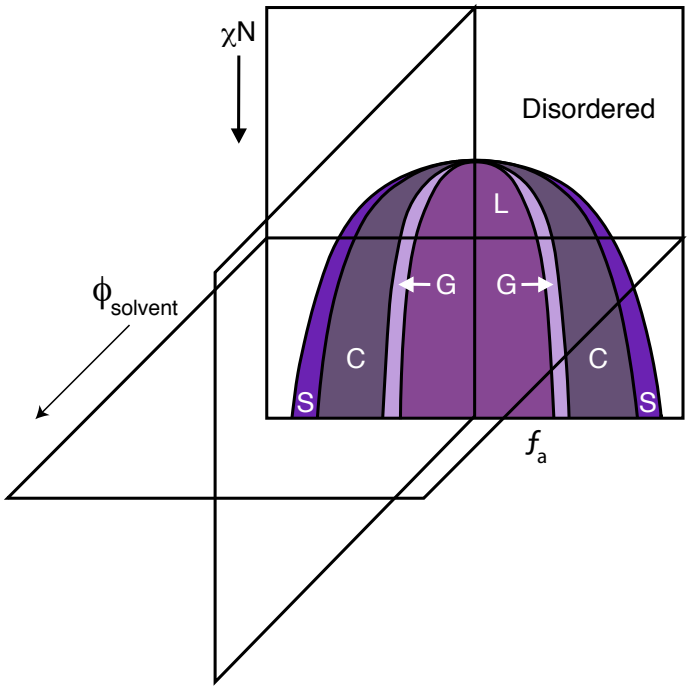

Figure 1.5: Solution phase portrait of a block polymer as a function of χN in the y-direction, f in the x-direction, and ϕ in the z-direction. Figure adapted from Ref. 43. Copyright 2002 American Chemical Society.

shows the morphologies available to a single block polymer as a function of temperature and solvent concentration. Finally at a constant concentration of polymer, the xy-plane shows the range of morphologies possible as a function of temperature and f. Construction of this phase portrait requires synthesis of a range of block polymers with varying volume fractions, followed by characterization of each polymer across a range of concentrations and temperatures.

The morphologies observed for a block polymer with a fixed f along the yz-plane depend upon how the solvent interacts with the two blocks. Previous work in the Lodge group focused on the solvation of styrene-isoprene (SI) diblock copolymers in various dialkyl phthalates. In the case of a neutral solvent, where both blocks are solvated, the polymer is simply diluted and follows similar phase behavior to the bulk.[41] As the solvent selectivity increases, it self-segregates into a single block. As more solvent is added, the solvent-laden block swells, increasing the effective volume fraction. Figure 1.6 shows how the addition of a selective solvent can alter the interfacial curvature between the two blocks, leading to a change in morphology with increasing solvent concentration.

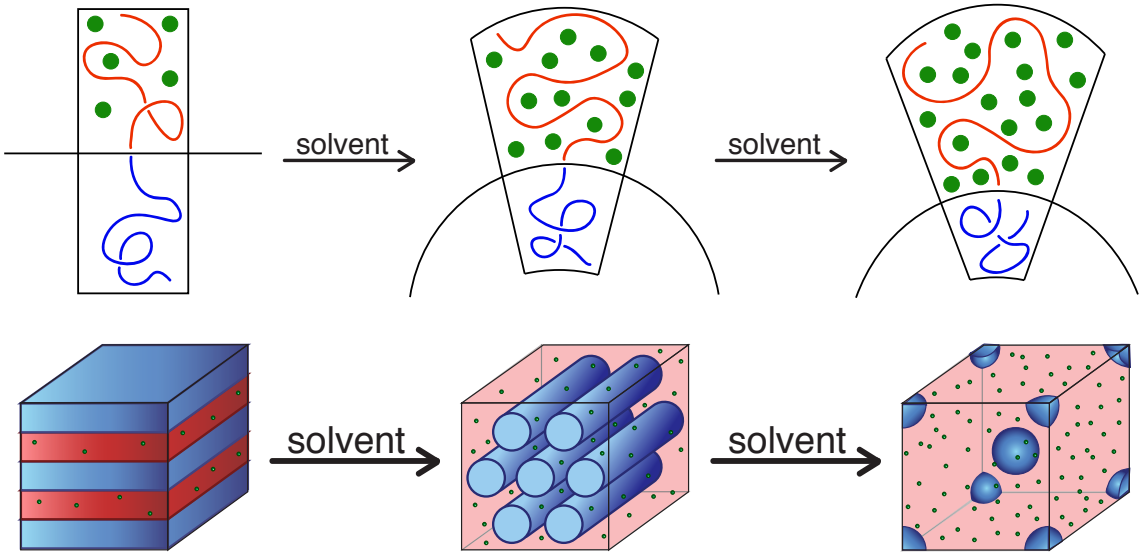

Figure 1.6: The addition of solvent (green circles) that is selective for the red block of a block polymer, inducing interfacial curvature that corresponds to a change in the morphology.

The addition of selective solvents was found to increase the number of available mor-

phologies for SI block polymers at fixed f, an example of which is shown in Figure 1.7.[65] Not only does the solvent cause the increase in interfacial curvature, it also allows for a change in solvent selectivity based on temperature. The cartoon in Figure 1.7 illustrates a solvent becoming more neutral upon cooling, causing a decrease in the interfacial curvature. This view of the phase diagram can be directly compared to Figure 1.2b, the bulk phase diagram for SI diblocks. While some compositions of neat SI afford OOTs, a single polymer composition gives rise to the entire phase diagram of morphologies in Figure 1.7.

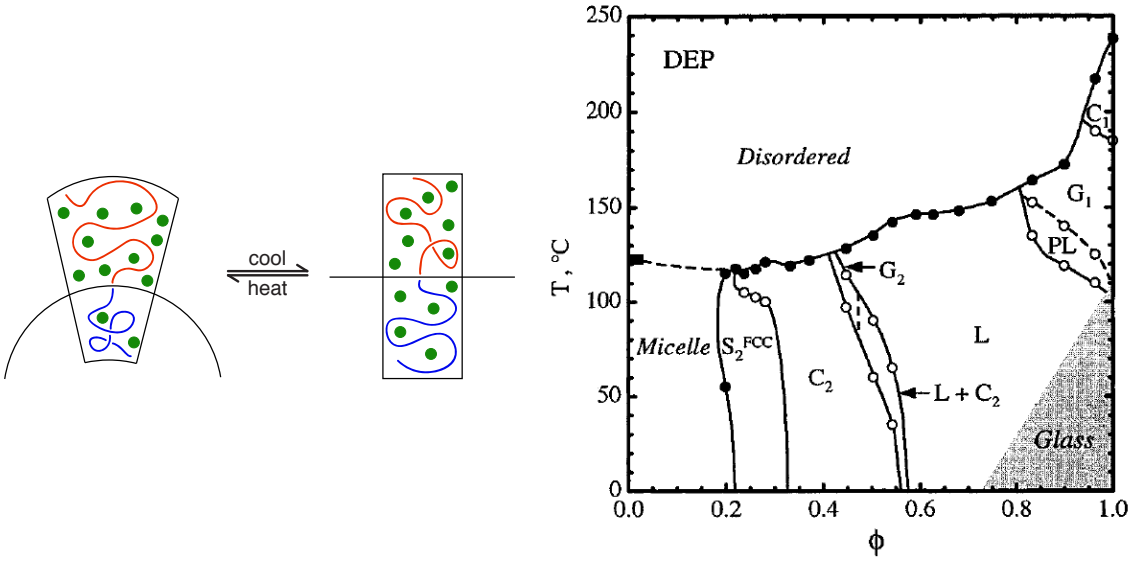

Figure 1.7: Illustration of changing solvent selectivity with temperature, and data of SI(11-21) in diethyl phthalate at a range of concentrations and temperatures. Open symbols correspond to OOTs, closed symbols correspond to ODTs. High concentrations of polymers result in a glassy polymer. Figure of SI(11-21) in diethyl phthalate reproduced with permission from Ref. 65. Copyright 2000 American Chemical Society.

The phase boundaries in these diagrams were primarily identified using static birefringence and small amplitude oscillatory shear rheology. Static birefringence allows for the differentiation between isotropic and anisotropic morphologies.[66–68] A sample is placed between two crossed polarizers, and a laser is passed through. An anisotropic sample, such as lamellae, will depolarize the light, allowing for transmittance through the second polarizer. An isotropic sample, such as body-centered cubic spheres, will not change the polarization, and no light will pass through the second polarizer. By measuring the transmittance of light as a function of temperature, OOTs between isotropic and anisotropic states and ODTs of

anisotropic states can be detected.

A significant drawback to static birefringence is that it cannot detect changes between two isotropic states, such as the ODT of spheres. Small amplitude oscillatory shear (SAOS) rheology can be used as a complimentary technique to study the mechanical properties of the material.[26,42,44] Measurements in the linear viscoelastic regime of the dynamic storage, G', and loss modulus, G'', can reveal OOTs/ODTs and give rudimentary information about the morphology present at a given temperature.[69] The morphology of a block polymer at a given temperature can be verified using small angle X-ray scattering (SAXS), where differences in electron density in the two blocks cause elastic scattering of a collimated beam of X-rays. The scattering wave vector, q, is defined by the wavelength of the X-rays, λ, and the angle of scattering, θ:

$$q = \frac{4\pi}{\lambda} sin\left(\frac{\theta}{2}\right) \tag{1.3}$$

Scattering data are plotted as intensity vs. q, and the observed peaks can be used to characterize the morphology. The reflections of the principal scattering peak, q^*, are peaks at specific multiples of q^* that are specific to a given morphology. The combination of SAXS, static birefringence, and SAOS rheology can be used together to produce the phase diagrams, as shown by the work on SI diblocks in various phthalates.[42–44,65,70]

Another significant area of study in the solution phase behavior of block polymers has been on a group of PEO/poly(propylene oxide) (PPO) block polymers known by the trade name of Pluronics.[71–83] These polymers have been widely studied due to their use as surfactants in applications from cosmetics to pharmaceuticals. Studies of PEO-PPO-PEO triblocks with varying block lengths showed that increasing the molecular weight of the PEO blocks increased the number of possible morphologies.[71,74] The addition of a non-polar organic solvent was found to selectively swell the PPO block, inducing changes in the interfacial curvature as expected with the introduction of a selective solvent.[74,76] Early studies focused on determining the impact of molecular weight and concentration on the observed morphologies.[73,82] This work was extended to generate concentration vs. temperature phase diagrams with studying the impact of adding additional solvents or compounds

that are present in the end applications.[72,76–78,80,81]

Light-responsive polymers

Up through this point, we have discussed thermally-induced changes in polymer solutions. While temperature is an effective way to achieve phase separation, OOTs, and ODTs in block polymer solutions, many applications require a constant temperature. In this case a contactless mode of triggering such as light would allow for isothermal changes in phase behavior. Ueki and coworkers have explored the copolymerization of azobenzene-based monomers, a light-responsive molecule, with NIPAm and BzMA to generate polymers with light-responsive phase separation behavior in EMI TFSI.[84–86] The *trans* ground state of azobenzene is relatively nonpolar, and can be driven to a polar *cis* excited state upon irradiation with UV light. This *cis* isomer will thermally revert back to the *trans* state, or can be driven back using visible light. Incorporation of the azobenzene-based methacrylate monomer, 4-phenylazophenyl methacrylate (AzoMA), into a copolymer with a monomer that has UCST or LCST phase behavior will modulate the solubility of the polymer in the solvent. This has the effect of changing the phase separation temperature, as is shown in Figure 1.8.[85] The polar *cis* isomer increases the solubility of the polymer chain in the

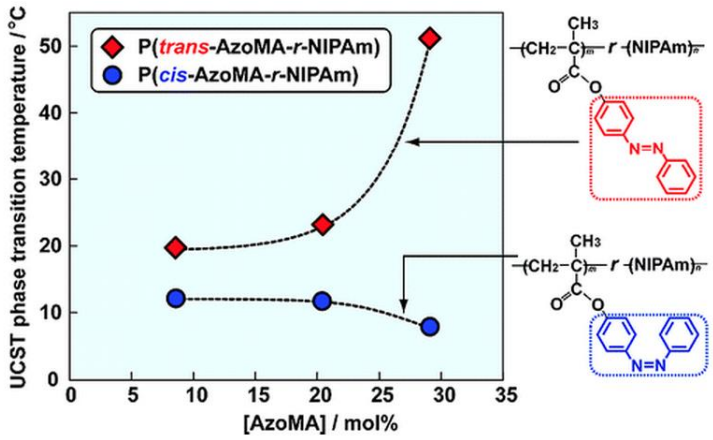

Figure 1.8: UCST phase separation of 3 wt% P(AzoMA-*r*-NIPAM) in EMI TFSI in the *cis* (blue) and *trans* (red) states. Figure reproduced with permission from Ref. 85. Copyright 2011 American Chemical Society.

ionic liquid, decreasing the UCST. The nonpolar *trans* isomer has the effect of increasing

the UCST, as the PAzoMA homopolymer is completely insoluble in EMI TFSI. The window between the *trans* and *cis* phase separation temperatures is a bistable region, where phase separation and dissolution can be triggered by light at a constant temperature. By increasing the amount of AzoMA, the polymer is affected to a greater degree by the light, generating a wider bistable window. In general, the widest bistable window possible is desirable, as it allows for minor thermal fluctuations to occur and not push the system out of the bistable region. In the PNIPAm/AzoMA copolymers, using the highest AzoMA incorporation of *ca.* 30 mol% gives a wide bistable window of ∼40 ºC, but it also broadens the temperature range over which the phase separation occurs. The gradual phase transition makes this bistable window artificially wide, as the temperatures close to the edges will begin to undergo phase separation as well. The compromise of a narrower bistable window from a smaller amount of AzoMA affords a sharp phase transition, eliminating this issue. A similar bistable window was observed in AzoMA/BzMA copolymers, where the *cis* azobenzene molecules increased the solubility of the copolymer in EMI TFSI, increasing the LCST.[84] In this case, the phase transitions remained sharp with bistable windows of 22 ºC with only 4 mol% incorporation of AzoMA. While these materials seemed to have superior light-responsive polymers, Ueki and coworkers continued to focus on NIPAm/AzoMA copolymers, expanding the system to various block polymers.

They explored the light-responsive micellization behavior of PEO-*b*-P(AzoMA-*r*-NIPAm) in BMI PF_6, where the *r* denotes a random copolymer between AzoMA and NIPAm, and the *b* stands for block.[87] They were able to achieve micellization upon cooling both under UV and visible light, at 73 and 77 ºC, respectively. The micelles were held at 75 ºC under UV light to produce dissolved polymer chains, then irradiated with visible light. The visible light triggered micellization, as detected by an increase in the hydrodynamic radius by dynamic light scattering. These micelles can subsequently be redissolved by UV light. Ueki and coworkers extended this concept to ABA triblock copolymer gels in BMI PF_6, where the A endblocks are P(AzoMA-*r*-NIPAm) and the midblock is PEO.[88,89] The mechanical properties of the materials were monitored as a function of temperature, with in-situ light exposure. They observed gelation in the *trans* form at 56 ºC, and at 48 ºC for the *cis* form. This afforded a wide bistable window between the two gelation temperatures

where gelation could be controlled using light. At the intermediate temperature of 53 ºC, triggering of sol-gel and gel-sol transitions were achieved with no significant change in the modulus of the material over the course of 6 cycles.[88] The gels were also shown to have self-healing properties.[89] Damage caused to a gel by a razor blade could be erased using UV light to induce flow of the material, followed by visible light to allow the gel to re-form.

Light-controlled ordering of block polymers has also been explored, both in liquid crystal-containing block polymers,[90–93] and in Langmuir-Blodgett monolayers of polymer thin films.[94,95] The liquid crystal-containing block polymers show the ability to align block polymer domains, based on the use of an azobenzene-based mesogen. Other studies have shown the ability to trigger order-disorder transitions, based on liquid crystalline ordered phases such as nematic.[96–98] While azobenzene has been widely employed in studies of liquid crystalline polymers, "coil-coil" diblocks have received less attention. Work looking at Langmuir-Blodget monolayers was able to obtain order-order phase transitions of block polymer thin films, however these transitions were not reversible and required high levels of humidity.[94,95]

1.3 Thesis overview

This thesis explores the combination of the solution phase behavior of block polymers with light- and temperature-responsive blocks. This work sought to bring together ideas from a range of projects, which required a considerable amount of work to understand how to generate materials that reliably responded to stimuli. From there, the individual components that impact the stimuli-responsive behavior could be explored, to generate a greater fundamental understanding of these materials. The chapters are arranged to logically follow the development of the light-responsive polymer project, then concludes with work on temperature responsive ABC triblock terpolymer gels. Chapter 2 describes the methods required to reproducibly generate light- and temperature-responsive copolymers with a controlled molecular weight distribution, and the kinetic properties of their light-responsive behavior. Chapter 3 focuses on the phase separation behavior of the copolymers in the ionic liquid EMI TFSI under UV and visible light conditions, exploring how sample thickness, molec-

ular weight, and copolymer composition play a role. Chapter 4 uses the copolymers as a block in a block polymer, and maps out phase diagrams for certain volume fractions and azobenzene incorporations as a function of temperature and concentration in EMI TFSI. Certain compositions were triggered between order and disorder using light as a stimulus. Finally, Chapter 5 discusses how the use of an ABC triblock terpolymer can generate gels in EMI TFSI with fewer network defects than the corresponding ABA triblocks, as well as draws a comparison to the gelation of the same ABC triblock in water.

Chapter 2

Synthesis and characterization of thermo- and photoresponsive statistical copolymers [i]

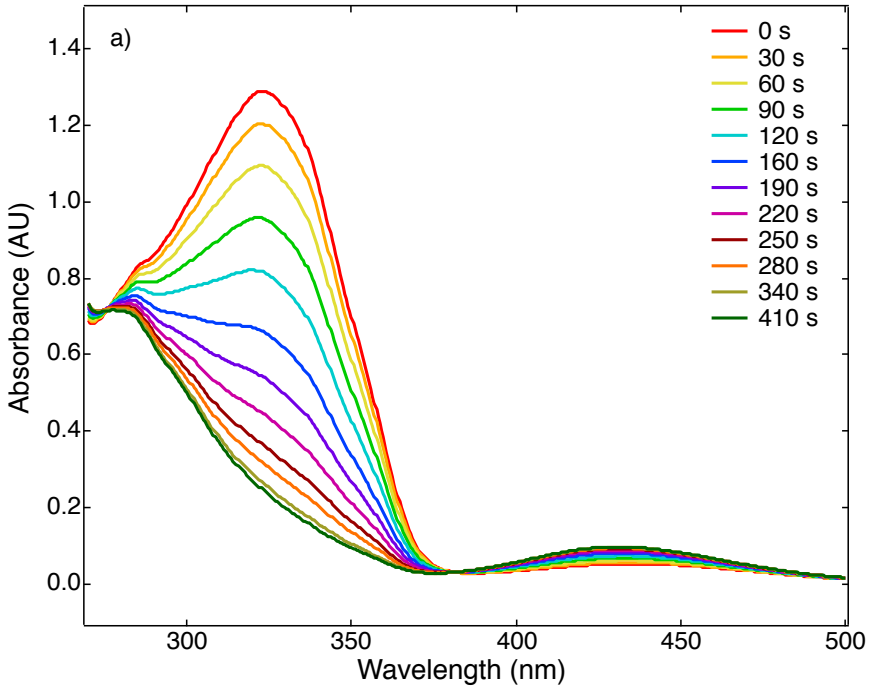

[i]This work was done in collaboration with Cecelia Rivera.

2.1 Introduction

Whether a polymer is well-mixed or phase separated in solution depends upon the interactions between the polymer chains and the solvent. For different polymers and solvents, these interactions can change significantly, from hydrogen bonding, Coloumbic interactions, to simple van der Waals forces. Whether or not the two are miscible is dictated by the free energy of mixing, as described in Chapter 1. The interactions between polymer and solvent can also be altered by chemical or physical changes to the system.[64,99] Chemical stimuli include pH[69,100–106] and ionic strength,[107–109] both of which are simple to achieve and often do not require synthetically complex polymers. However, the addition of acid, base, or salt permanently alters the composition of the solutions. As a result, it is not possible to achieve the same response with repeated cycling. These stimuli are well-suited for biomedical applications such as drug delivery, which typically require a one-time release. Physical stimuli such as magnetic fields,[110–113] electric fields,[12,114–117] temperature,[53,63,118–120] and light[14,21,121–143] are all able to induce changes in polymer solutions without chemically altering the system. This opens up the possibility of use in devices with repeated cycling, such as electronic devices. To realize the use of these responsive polymers in applications, it is important that the synthetic procedure is relatively robust and simple. Thus finding the right combination of monomers and reaction conditions is necessary to allow for further work on employing these polymers in various applications.

The choice of solvent will dictate which polymers display stimuli-responsive properties. Ionic liquids have recently received a significant amount of attention as replacements for traditional organic solvents. Their negligible volatility, high thermal stability, high conductivity, and wide electrochemical activity make them desirable for uses in many applications.[46] In these applications, it can be desirable to have stimuli responsive behavior. The thermoresponsive polymer poly(*N*-isopropyl acrylamide) (PNIPAm) has been extensively explored as a thermoresponsive polymer in water, as is displays lower critical solution temperature (LCST) phase behavior around body temperature,[63,144] making it highly desirable for biological applications. In LCST phase behavior, the polymer is soluble at temperatures below the LCST, and iphase separates above it. This phase behavior changes in ionic

liquid, showing instead upper critical solution temperature (UCST) phase behavior, where now the polymer is soluble at elevated temperatures and insoluble below the UCST.[61] The mechanism of phase separation changes as a result of the changing interactions between the polymer and solvent, which changes the free energy of mixing. Another thermoresponsive polymer is poly(benzyl methacrylate), PBzMA, which displays LCST phase behavior in ionic liquids.[57,59,145] The structure of the two polymers are shown below in Figure 2.1, and the mechanisms of the phase separation behavior for these polymers will be discussed in detail in Chapter 3.

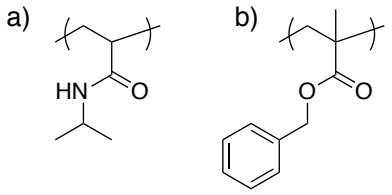

Figure 2.1: The chemical structures of a) poly(N-isopropyl acrylamide) and b) poly(benzyl methacrylate), two polymers which display thermoresponsive behavior in ionic liquid

Copolymerization of these thermoresponsive monomers with monomers that change polarity under different wavelengths of light can lead to light-dependent phase separation behavior. Figure 2.2 shows an example of a photoresponsive molecule, azobenzene, which undergoes isomerization to a *cis* excited state under UV light, and thermally reverts to the *trans* ground state, or can be triggered back to *trans* under visible light.[146] In the ground

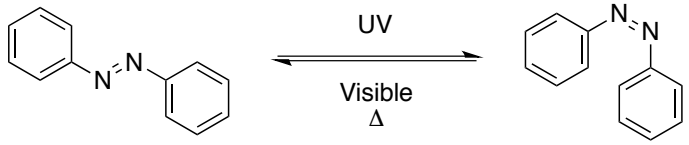

Figure 2.2: *cis/trans* isomerization of azobenzene as a function of light and temperature

trans state, azobenzene is relatively nonpolar as the two dipole moments from the lone pairs on nitrogen and the phenyl rings are equal and opposite, effectively canceling, giving a dipole moment of $\sim$0 Debye.[146] Ionic liquids are inherently polar, therefore the nonpolar *trans* azobenzene is relatively insoluble. A significant dipole moment of 3 Debye is induced when azobenzene is isomerized to the excited *cis* state as a result of having the phenyl rings

and the lone pairs *cis* across the azo bond.[146] This increase in polarity increases the potential for solubility in ionic liquids. The mechanism for azobenzene isomerization has been suggested to follow two possible pathways, rotation around the N-N bond and inversion, where it is generally believed that the inversion pathway leads to the *cis/trans* isomerization.[147] Regardless of how isomerization proceeds, there is no significant mechanism for degradation during isomerization. Photocyclization requires that the azobenzene must first be protonated in order for cyclization to occur.[148] Additionally, the quantum yield for this process is only 0.015.[149] The use of aprotic solvents, such as ionic liquids, can remove this pathway altogether. As such, azobenzenes are often chosen for applications where repeated cycling of photoresponsive behavior is needed.

The relative ability to isomerize and the stability of the resulting isomers depends on the substitution of the azobenzene ring. Depending on the chemical structure, azobenzene molecules can be classified as azobenzene-type, aminoazobenzene, and pseudo-stilbenes.[147] Azobenzene-type chromophores are the closest to unsubstituted azobenzene, showing a large peak in the UV region corresponding to the $\pi - \pi^*$ transition, and a small peak in the visible region corresponding to the $n - \pi^*$ transition. Aminoazobenzenes have electron-donating groups, commonly amines, in positions ortho or para to the azo group. This brings the $\pi - \pi^*$ and $n - \pi^*$ transitions closer together and shifts both into the visible light region. Pseudo-stilbenes have an electron donating group para to the azo group on one phenyl ring, and an electron withdrawing group para to the azo on the other. This push-pull substitution pattern causes the $\pi - \pi^*$ and $n - \pi^*$ peaks to overlap, and irradiation at that wavelength will cause cycling between the two isomerization states. For the use in triggering changes in polarity of polymers, the azobenzene-type chromophore offers the most attractive qualities – the *cis* isomer has the longest lifetime, the larger gap between the two absorption bands makes it easier to trigger isomerization in a certain direction without overlap into the other band, and the lack of substitution makes the molecule easier to synthesize as a monomer.

Another photoresponsive molecule that can easily be incorporated as a monomer is spiropyran. Figure 2.3 shows the isomerization of the ground state, spiropyran, to the excited ring-opened merocyanine form. Merocyanine exists as a zwitterion, and the dramatic change in polarity from an uncharged compound to the zwitterion produces a correspond-

ing significant shift in solubility. While spiropyran is more polar than *trans* azobenzene at ∼4-6 Debye, the shift to merocyanine increases the polarity to ∼14-18 Debye, ∼3 times greater than the change in polarity to *cis* azobenzene.[150–152] The mechanism for spiropyran

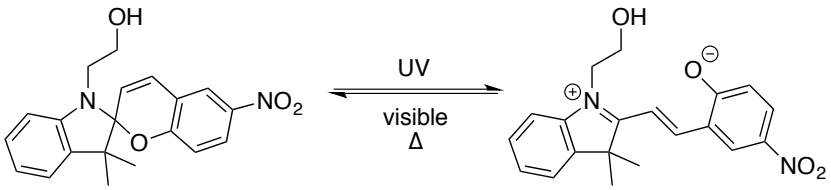

Figure 2.3: Ring-opening isomerization of spiropyran to merocyanine under UV light, and reversion with visible light or heat.

isomerization to merocyanine begins with C-O bond cleavage, followed by rotation around the C-C bond to generate the *trans* conformation of merocyanine.[153] This isomerization is easily detectable by UV-vis spectroscopy, however the exact position of the peaks is strongly dependent upon the identity of the solvent.[154] Small molecule spiropyrans have been studied in ionic liquid, showing slower thermal reversion in ionic liquids as compared to organic solvents with similar polarities, with imidazolium-based cations showing slower thermal reversion than pyridinium or phosphonium cations.[155] This is because the ionic liquid stabilizes the zwitterionic merocyanine form, enabling a longer lifetime. At temperatures up to 40 ºC, reversible switching between spiropyran and merocyanine was achieved. As the lifetime of the merocyanine isomer is so strongly dependent upon solvent, it is simpler to choose a different ionic liquid rather than synthesizing different spiropyrans to produce a more stable merocyanine isomer.

In the case of both chromophores, the isomerization state is influenced by temperature as well as light. Merocyanine and *cis* azobenzene are both excited states, and have the ability to thermally revert back to the respective ground states of the molecule. Polymerization of the chromophores does show an increase in excited state lifetime,[148,155] however at high enough temperatures, constant UV irradiation may be necessary to maintain a high population of the excited state.

Both spiropyran and azobenzene can easily be transformed into monomers by reacting a pendant alcohol with an acid chloride to give methacrylate or acrylate derivatives of the monomer. While neither spiropyran- or azobenzene-based monomers are commer-

cially available, the synthesis of azobenzene monomers is significantly simpler as many azobenzenes are commercially available. In contrast, spiropyran must first be synthesized before being converted to monomer. Once synthesized, the photoresponsive monomer can be incorporated into a polymer via copolymerization with a thermoresponsive monomer to generate a polymer with light-triggered phase separation behavior. Ideally, the photoresponsive monomer should be a minority component, randomly distributed among the majority thermoresponsive monomer. This ensures that the polymer behaves mainly with LCST or UCST phase separation behavior. Polymers consisting of 4-phenylazophenyl methacrylate (AzoMA), an azobenzene monomer, are completely insoluble in ionic liquid, regardless of isomerization state. Thus having too much AzoMA will simply make the entire copolymer insoluble. For spiropyran, a higher density of the monomer increases the likelihood of photodegradation.[156] Keeping the photoresponsive monomer content low also reduces the synthetic complexity of polymer synthesis, as both azobenzene and spiropyran monomers must be synthesized.

In order to maintain the temperature-responsive properties that give the polymers a sharp UCST or LCST phase separation, it is important to make sure that the small amount of light-responsive monomer is distributed randomly along the polymer chain. This can be achieved through the use of monomers that have similar reactivities in the chosen polymerization technique. The relative reactivities of monomers can be quantified using reactivity ratios. The reactivity ratio for a propagating polymer chain with end A is given by the ratio of the rate constant for addition of another monomer A to the the rate constant for addition of the other monomer B. This is shown below in Equation 2.1, where k_{AA} is the rate constant for monomer A adding another monomer A, k_{AB} is the rate constant for monomer A adding monomer B, and r_A is the reactivity ratio for monomer A.[157]

$$r_A = \frac{k_{AA}}{k_{AB}} \tag{2.1}$$

The reactivity ratio can give insight into the distribution of monomer chains in the polymer backbone. If the reactivity ratios are ≈ 1 for both monomers, there is no preference for monomers A or B to add to chain ends A or B, so a random distribution of monomers will

be achieved. If both monomers have reactivity ratios $>> 1$, then both significantly prefer to add themselves and two homopolymers will be produced. If both monomers have reactivity ratios ≈ 0, then both prefer to add the opposite monomer, giving an alternating copolymer. These are ideal, limiting cases – most polymerizations do not lie at these extremes. If reactivity ratio A is $>> 1$ and B is ≈ 0, both monomers will prefer to add monomer A. In the limiting case, this leads to a block polymer where monomer A adds first at the fastest rate, and B is only incorporated once monomer A is consumed. In a more moderate case where both reactivity ratios are closer to 1, the polymerization will show composition drift, where at the beginning mostly monomer A is added and B begins to incorporate in a tapering gradient as more A is consumed. Figure 2.4 shows an example of a) composition drift, and b) a random incorporation.

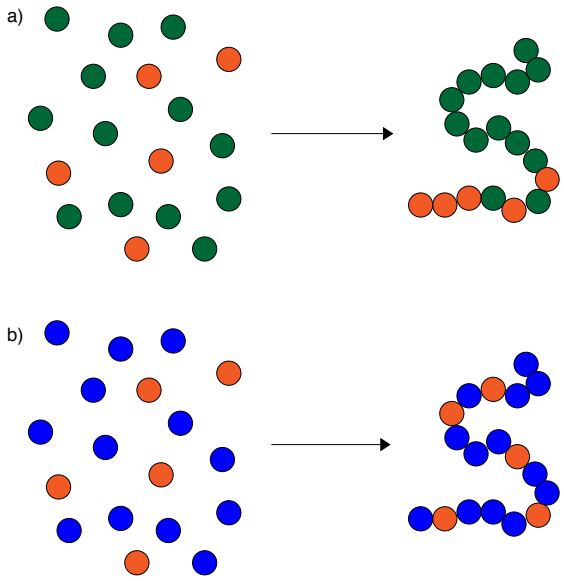

Figure 2.4: Cartoon illustration of copolymers produced with a) composition drift and b) random incorporation of monomers.

For the two temperature-responsive monomers mentioned, NIPAm and BzMA, the corresponding photoresponsive monomer would have a reactivity ratio close to 1 as an acrylamide or a methacrylate, respectively. Previous work has suggested that 4-phenylazophenyl acrylamide, the azobenzene monomer that would be most similar to NIPAm, was unable to be copolymerized with NIPAm.[85] The authors suggested that this was due to significant chain transfer ability of the azobenzene monomer. As a result, the studies copolymerizing

NIPAm with an azobenzene monomer have chosen to use AzoMA.[85,87,89,128] This unfortunately uses two monomers with dissimilar reactivities, giving reactivity ratios for AzoMA and NIPAm of 5.60 and 0.65, respectively, giving a distribution similar to Figure 2.4a.[85] This leads to a blocky distribution of monomers in the polymer chain, and can significantly slow down polymerization. This is reflected in the 68 hour reaction times used to generate these copolymers.[85] The pairing of AzoMA and BzMA is closer to an ideal case, as both monomers are methacrylates. Previous studies measured the reactivity ratios, reporting 1.7 for AzoMA and 0.8 for BzMA, giving a distribution of monomers similar to Figure 2.4b.[84] However, they based these reactivity ratios on compositions between 0.6 and 4 mol% AzoMA in the copolymer, where fitting for reactivity ratios would be more accurate with a range spanning both low and high AzoMA incorporations.

This work focuses on the synthesis of thermo- and photoresponsive copolymers, with the aim of achieving synthetic ease as well as a near–random distribution of the two monomers. While NIPAm/AzoMA copolymers have been previously reported,[85,126] and even carried forward to applications,[87–89,128] it was found that the synthesis of these polymers could not be achieved in a reasonable reaction time. As a result, the thermoresponsive monomer was changed to BzMA, which also has the benefit of a similar reactivity to AzoMA. The polymerization of AzoMA and BzMA homopolymers were successfully achieved by ATRP, as well as copolymers with varying compositions. The reactivity ratios were measured using compositions of AzoMA ranging from 10 to 90 mol%, to give the best possible fit over a range of compositions. The isomerization of azobenzene in the varying copolymers was studied using UV-vis spectroscopy, where the time to obtain a photostationary state under UV light was measured, as well as the thermal stability of the *cis* isomer. The polymerization of spiropyran acrylate (SPA) and NIPAm similarly was not successful, however a copolymer of SPA and BzMA was synthesized and visually tested for photoresponsive properties at room temperature.

2.2 Experimental

Materials

2-Cyano-2-propyl dodecyl trithiocarbonate, 4-phenylazophenol, methacryloyl chloride, acryloyl chloride, 2,3,3-trimethyl indole, 2-hydroxyl-5-nitrobenzaldehyde, 1-dodecanethiol, carbon disulfide, and *N*-isopropylacrylamide were used as purchased from Sigma Aldrich. 1-Ethyl-3-methyl imidazolium bromide and 1-butyl-3-methyl imidazolium chloride were used as purchased from Iolitec. Lithium bis(trifluoromethanesulfonyl)imide was used as purchased from 3M. Benzyl methacrylate was purchased from Sigma Aldrich and filtered through a neutral alumina column to remove inhibitor prior to polymerization. Azobisisobutyronitrile was purchased from Sigma Aldrich and purified by recrystallization from methanol.

Ionic liquid synthesis

The ionic liquids were prepared by an ion exchange reaction. The ethyl methyl imidazolium bromide salt (EMI Br, 0.5 mol) or butyl methyl imidazolium bromide salt (BMI Br, 0.5 mol) was mixed with lithium bis(trifluoromethanesulfonyl)imide (Li TFSI, 0.5 mol) in 250 mL of water, then stirred at 70 ºC for 48 h. Dichloromethane was added to the reaction, and the water was extracted. The organic layer was washed with deionized H_2O until there was no excess salt present in the water, as determined by a silver nitrate test. The dichloromethane/ionic liquid mixture was transferred to a round bottom flask and stirred with activated charcoal for 24 h to remove any residual color. After 24 h, the activated charcoal was removed by filtering over neutral alumina, and the dichloromethane was removed via rotary evaporation. The final ionic liquid was dried in a vacuum oven at 70 ºC for 72 h. The resulting pure ionic liquids were characterized by ^{1}H and ^{19}F NMR spectroscopy, as shown in the Appendix in Figures 6.3 and 6.4. For EMI TFSI, ^{1}H NMR (500 MHz, DMSO-d_6) δ ppm 1.42 (t, J=7.32 Hz, 3 H) 3.85 (s, 3 H) 4.19 (q, J=7.22 Hz, 2 H) 7.66 (t, J=1.83 Hz, 1 H) 7.74 (t, J=1.83 Hz, 1 H) 9.10 (s, 1 H). For BMI TFSI, ^{1}H NMR (500 MHz, DMSO-d_6) δ ppm 0.91 (t, J=7.48 Hz, 3 H) 1.27 (dq, J=15.03, 7.40 Hz, 2 H) 1.70 -

1.84 (m, 2 H) 3.85 (s, 3 H) 4.17 (t, J=7.32 Hz, 2 H) 7.69 (t, J=1.83 Hz, 1 H) 7.76 (t, J=1.83 Hz, 1 H) 9.11 (s, 1 H). ^{19}F NMR spectrum confirms successful anion exchange reaction by showing the presence of fluorine in the final ionic liquids.

AzoMA monomer synthesis

4-Phenylazophenyl methacrylate was synthesized via an acid chloride reaction to generate an ester, shown in Figure 2.5. 4-phenylazophenol (60 mmol) and triethylamine (120 mmol)

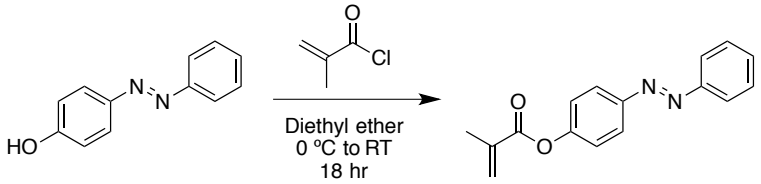

Figure 2.5: Synthesis of 4-phenylazophenyl methacrylate (AzoMA) through an acid chloride reaction.

were combined in a 500 mL roundbottom flask containing 120 mL of diethyl ether. The reaction flask was equipped with an addition funnel, to which an additional 24 mL of diethyl ether was added. The addition funnel was sealed with a septum, and the entire setup was purged with argon for 15 minutes. During the purge, the reaction was stirred over an ice/water bath to bring the temperature down to 0 ºC. After completion of the argon purge, methacryloyl chloride (72 mmol), was added to the addition funnel via syringe. The solution of methacryloyl chloride in the addition funnel was added dropwise to the stirring mixture of 4-phenylazophenol and triethylamine. The reaction was allowed to proceed overnight, while warming to room temperature.

The reaction was filtered through a fritted glass funnel to remove the light brown precipitate, triethylammonium chloride. The dark orange filtrate was added to a separatory funnel, and washed 4 times with deionized H_2O. The organic layer was dried over sodium sulfate, after which the diethyl ether was removed via rotory evaporation. The resulting orange solids were purified by recrystallization using the combined solvents of ethanol and water. The solids were stirred in 100 mL of ethanol heated to 75 ºC. Once the solids were fully dissolved, deionized H_2O was added in $\sim$1 mL portions until the solution became turbid. Ethanol was then added to the solution in $\sim$1 mL portions until clear again. The

solution was allowed to slowly cool to room temperature, forming a solid orange powder. The solids were removed by filtration, and recrystallized a further three times to produce pure 4-phenylazophenyl methacrylate, which was characterized by ^{1}H NMR spectroscopy, shown in Appendix Figure 6.5. ^{1}H NMR (500 MHz, DMSO-d$_6$) δ ppm 2.03 (s, 3 H) 5.92 - 5.98 (m, 1 H) 6.33 (s, 1 H) 7.38 - 7.48 (m, 2 H) 7.54 - 7.66 (m, 3 H) 7.85 - 7.94 (m, 2 H) 7.94 - 8.02 (m, 2 H).

Spiropyran acrylate synthesis

Spiropyran was synthesized in three steps as previously reported,[158] followed by reaction with acryloyl chloride to yield the spiropyran acrylate monomer. The reaction scheme is shown in Figure 2.6. In the first step of the spiropyran synthesis, 2,3,3-trimethyl indole

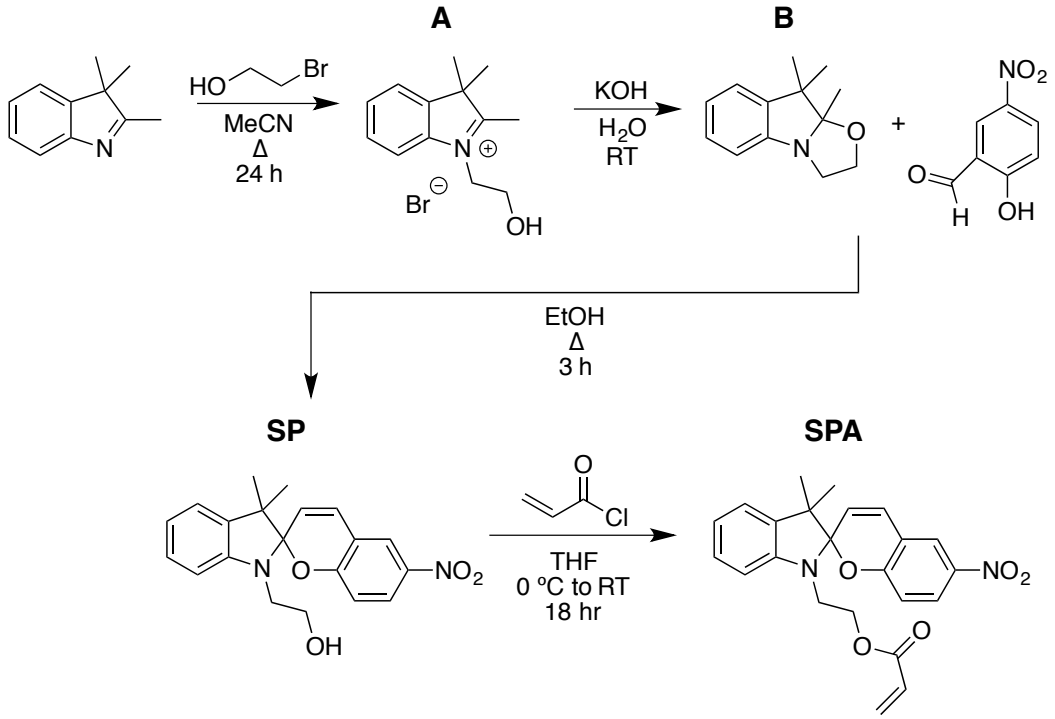

Figure 2.6: Four step synthesis of spiropyran acrylate from 2,3,3-trimethyl indole.

(16 mmol) and 2-bromoethanol (20 mmol) were combined in a 250 mL roundbottom flask with 20 mL of dry acetonitrile. The roundbottom was equipped with a reflux condenser, sealed with a septum, and purged with argon for 15 minutes. The reaction was heated to reflux for 24 hours. The acetonitrile was removed from the reaction via rotory evaporation,

leaving a dark pink oil. 25 mL of hexanes was added to the residue, and sonicated for 2 hours. After sonication, the hexanes were orange/red and a dark pink solid came out of solution. The dark pink solids were removed by filtration, then purified by recrystallization in 40 mL of chloroform. The resulting quaternized indole **A** was characterized by ^{1}H NMR spectroscopy, as shown in Appendix Figure 6.6. ^{1}H NMR (500 MHz, DMSO-d_6) δ ppm 1.55 (s, 6 H) 2.82 (s, 3 H) 3.88 (t, J=5.04 Hz, 2 H) 4.60 (t, J=5.19 Hz, 2 H) 7.54 - 7.67 (m, 2 H) 7.81 - 7.89 (m, 1 H) 7.96 (dd, J=5.65, 3.20 Hz, 1 H).

In the second step, **A** (9.3 mmol, 1 eq) was mixed with 21 mL of diH_2O in a 250 mL roundbottom flask. KOH (15 mmol, 1.6 eq) was dissolved in 25 mL of diH_2O, which was added by pipette to the stirring solution in the roundbottom. Upon addition of KOH, the pink solution immediately changed to yellow. The product was extracted from the water by extraction with 3 portions of 20 mL of diethyl ether. The organic layers were combined, and the diethyl ether was removed by rotory evaporation. The resulting yellow oil **B** was dried under vacuum. and characterized by ^{1}H NMR spectroscopy, shown in Appendix Figure 6.7. ^{1}H NMR (500 MHz, DMSO-d_6) δ ppm 1.01 - 1.15 (m, 3 H) 1.20 - 1.30 (m, 3 H) 1.32 (s, 3 H) 3.24 - 3.38 (m, 2 H) 3.38 - 3.53 (m, 1 H) 3.66 - 3.80 (m, 2 H) 6.74 - 6.87 (m, 2 H) 7.02 - 7.15 (m, 2 H).

The final step in the spiropyran synthesis combined **B** (11.6 mmol, 1 eq) with 2-hydroxy-5-nitrobenzaldehyde (17.4 mmol, 1.5 eq) in a 100 mL roundbottom flask with 29 mL of ethanol. A reflux condenser was added to the roundbottom flask and sealed with a septum. The reaction was purged with argon for 10 minutes, then heated to reflux for 20 hours. The reaction produced purple crystals, which were removed by gravity filtration. The crystals were rinsed with ethanol, then dried to give a sparkling purple solid, **SP**. The spiropyran was characterized by ^{1}H NMR spectroscopy, shown in Appendix Figure 6.8.. ^{1}H NMR (500 MHz, DMSO-d_6) δ ppm 1.05 (t, J=6.87 Hz, 2 H) 1.10 (s, 3 H) 1.20 (s, 3 H) 3.44 (dd, J=7.17, 5.04 Hz, 3 H) 4.34 (s, 1 H) 4.71 (s, 1 H) 6.01 (d, J=10.38 Hz, 1 H) 6.64 (d, J=7.93 Hz, 1 H) 6.78 (s, 1 H) 6.87 (d, J=8.85 Hz, 1 H) 7.05 - 7.16 (m, 2 H) 7.19 (d, J=10.38 Hz, 1 H) 8.00 (dd, J=8.85, 2.75 Hz, 1 H) 8.21 (d, J=2.75 Hz, 1 H).

To convert **SP** to a monomer, it was reacted with acryloyl chloride. Spiropyran (4.2 mmol, 1 eq) and triethylamine (12.5 mmol, 3 eq) were combined in a 200 mL roundbottom

flask with 29 mL of tetrahydrofuran. The reaction vessel was equipped with an addition funnel, to which an additional 10 mL of THF was added. The reaction was stirred over an ice/water bath while degassing with argon for 15 minutes. Acryloyl chloride (6.3 mmol, 1.5 eq) was added to the addition funnel. The acryloyl chloride solution was added dropwise to the reaction while stirring. The reaction was allowed to proceed overnight while warming to room temperature. The solids were filtered from the reaction using a fritted glass funnel, and the THF was removed by rotory evaporation. The resulting solid was purified by column chromatography in 1/6 ethyl acetate in hexanes. Thin layer chromatography easily identifies spiropyran without staining, as it turns purple under UV light irradiation. The position of the spots relative to the baseline is known as the retardation factor, rf. The first 6 fractions collected were cloudy and yellow in appearance, showing the high rf spiropyran spot, with low rf impurities. The following fractions 7-27 appeared clear, and showed no low rf impurities. Fractions 28-50 showed a faint spot corresponding to spiropyran, but has a stronger low rf spot which was not UV active. Collecting fractions 28-50 gave a relatively pure spiropyran acrylate by ^{1}H NMR. A second identical column was run, producing pure spiropyran acrylate, **SPA**, by ^{1}H NMR, shown in Appendix Figure 6.9.. ^{1}H NMR (500 MHz, DMSO-d_6) δ ppm 1.02 - 1.11 (m, 3 H) 1.17 - 1.23 (m, 3 H) 3.36 - 3.54 (m, 2 H) 4.20 (dt, J=11.14, 5.42 Hz, 1 H) 4.31 (ddd, J=11.75, 6.87, 5.19 Hz, 1 H) 5.91 (dd, J=10.38, 1.53 Hz, 1 H) 5.97 (d, J=10.38 Hz, 1 H) 6.10 (dd, J=17.24, 10.53 Hz, 1 H) 6.27 (dd, J=17.24, 1.37 Hz, 1 H) 6.73 (d, J=8.24 Hz, 1 H) 6.81 (t, J=7.32 Hz, 1 H) 6.87 (d, J=9.16 Hz, 1 H) 7.08 - 7.17 (m, 2 H) 7.21 (d, J=10.38 Hz, 1 H) 8.00 (dd, J=9.16, 2.75 Hz, 1 H) 8.22 (d, J=2.75 Hz, 1 H).

Chain transfer agent synthesis

2-(Dodecylthiocarbonothioylthio)-2-methylpropionic acid was synthesized as shown in Figure 2.7. 1-Dodecanethiol (0.17 mol, 1 eq) and acetone (83.2 g) were combined in a 1 L roundbottom flask equipped with an addition funnel. All solutions were added to the addition funnel through a syringe. The reaction was stirred over an ice water bath to cool to 0 ºC while purging with argon. A concentrated NaOH solution (0.18 mol, 1.05 eq NaOH,

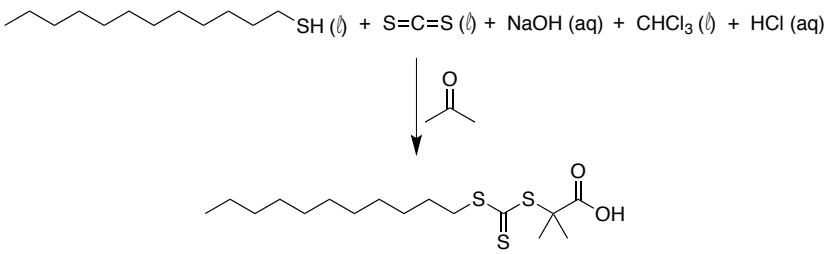

Figure 2.7: Synthesis of 2-(dodecylthiocarbonothioylthio)-2-methylpropionic acid.

in 7.25 g H_2O) was added to the addition funnel, then added dropwise to the reaction with vigorous stirring. This portion of the reaction was allowed to proceed for 1.5 hours. Carbon disulfide (0.18 mol, 1.05 eq) was added to the addition funnel with 17.2 g of acetone, then added dropwise to the reaction, which became a clear yellow liquid after the addition. Chloroform (30.6 g, 1.5 eq) was added to the addition funnel, and then entire reaction was purged again with argon. After a 10 minute purge, the whole portion of chloroform was added to the reaction. A second concentrated NaOH solution (0.86 mol, 5 eq, in 34.4 g H_2O) was added to the addition funnel, then dropwise into the reaction. The solution turned brown after the addition of NaOH. The reaction was allowed to warm to room temperature, having been kept at 0 ºC for all previous steps, and was left to proceed for 18 hours.

After this time, the addition funnel was removed and 260 mL of H_2O were added to the reaction. The reaction formed a significant heavy orange precipitate, and was stirred by hand with a spatula to ensure mixing. The spatula was removed, and 51.5 g of a 37.5 wt% solution of HCl in water was added. The reaction was stirred with the stirbar until the precipitate formed clumps. The remaining organic solvents were purged from the reaction using air. The solids were removed from the water by filtration through a Büchner funnel. These solids were dissolved in 420 mL of isopropanol by stirring for 1 hour to give a wine-red solution, which was filtered to remove any undissolved solids. The filtrate was rotovaped to remove the isopropanol, giving a sticky orange solid. The solids were recrystallized 4 times from hexanes to produce sparkling yellow sheet-like crystals, which were characterized by ^{1}H NMR spectroscopy, shown in Appendix Figure 6.10. ^{1}H NMR (300 MHz, Chloroform-d) δ ppm 0.83 - 0.92 (m, 3 H) 1.19 - 1.45 (m, 19 H) 1.59 - 1.76 (m, 8 H) 3.24 - 3.32 (m, 2 H).

Reversible addition-fragmentation chain transfer polymerization

Homopolymers were successfully synthesized using reversible addition-fragmentation chain transfer (RAFT) polymerization. Copolymers were attempted but did not result in any product. In a representative synthesis, *N*-isopropylacrylamide (8.4 mmol, 200 eq), 2-(dodecylthiocarbonothioylthio)-2-methylpropionic acid (0.042 mmol, 1 eq), azobisisobutyronitrile (AIBN) (0.0042 mmol, 0.1 eq), and toluene (4.2 mL) were combined in a Schlenk flask. The reaction was degassed by three freeze-pump-thaw cycles, then filled with argon to a pressure of 5 atm. The reaction was allowed to proceed for 20 h at 70 ºC, then quenched by placing the reaction in an ice-water bath. The resulting polymer was purified by precipitation in hexanes three times.

Atom transfer radical polymerization

Copolymers and homopolymers were both successfully synthesized using atom transfer radical polymerization (ATRP). In a representative homopolymer synthesis, benzyl methacrylate (10 mmol, 200 eq), HMTETA (0.1 mmol, 1 eq), and EBriB (0.1 mmol, 1 eq) were combined with anisole (90 mL) in a Schlenk flask. The mixture was degassed through three freeze-pump-thaw cycles, then placed under positive pressure of argon. A needle was placed in the septum to relieve pressure in the flask. The septum was removed from the reaction flask under a constant flow of argon, and copper (I) bromide (0.05 mmol, 0.5 eq) was added. After re-sealing the flask and increasing the argon pressure to 5 atm, the reaction was allowed to proceed at 90 ºC for 24 h. Reaction aliquots were taken at varying time points to determine the conversion of the reaction, which was determined via ^{1}H NMR spectroscopy. An example of the kinetics is shown in the NMR spectra collected in Figure 2.8. The reaction mixture was quenched by placing it an ice water bath and purified by precipitation in hexanes three times.

In a representative copolymer synthesis, benzyl methacrylate (170 mmol, 218 eq), AzoMA (9.0 mmol, 11.5 eq), HMTETA (0.78 mmol, 1 eq), and EBriB (0.78 mmol, 1 eq) were combined with anisole (90 mL) in a Schlenk flask. The mixture was degassed through three freeze-pump-thaw cycles, then placed under positive pressure of argon. A

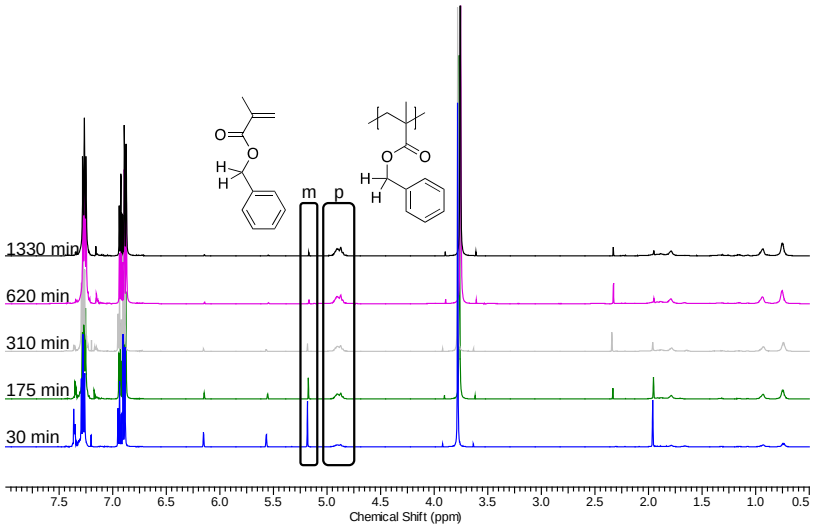

Figure 2.8: ^{1}H NMR spectra showing conversion of BzMA monomer (peaks labeled m) to polymer (peaks labeled p) from 30 to 1330 min, as monitored by the benzyl hydrogens in both monomer and polymer.

needle was placed in the septum to relieve pressure in the flask. The septum was removed from the reaction flask under a constant flow of argon, and copper (I) bromide (0.39 mmol, 0.5 eq) was added. After re-sealing the flask and increasing the argon pressure to 5 atm, the reaction was allowed to proceed at 75 ºC for 4 h. The reaction mixture was quenched by placing it an ice water bath and purified by precipitation in hexanes three times.

Free radical polymerization

Polymers were prepared by free radical polymerization for test polymerizations, reactivity ratio determination, and refractive index increment measurements. To make a preliminary test of the photoresponsive properties of spiropyran-based polymers, a copolymer of SPA and BzMA was synthesized by free radical polymerization. BzMA (6.1 mmol, 190 eq), SPA (0.12 mmol, 38 eq), and AIBN (0.032 mmol, 1 eq) were combined in a 100 mL Schlenk flask with 3 mL of toluene. The reaction was degassed with three freeze-pump-thaw cycles, filled with argon to 5 atm, and run for 20 hours at 90 ºC. The resulting polymer was purified by precipitation three times in hexanes, resulting in a light purple solid. The relative proportions of the two monomers in the final polymer were determined by ^{1}H NMR spectroscopy.

For reactivity ratio determination, BzMA (3.7 mol, 306 eq), AzoMA (0.41 mmol, 34 eq), and AIBN (0.012 mmol, 1 eq) were combined with 2 mL of anisole in a scintillation vial with a stirbar. The vial was sealed with a septum, purged with argon for 5 minutes, and then run at 75 ºC while taking reaction aliquots every 20 minutes. After 20 minutes, the reaction showed 10% conversion of BzMA monomer to polymer by ^{1}H NMR spectroscopy. Nine free radical polymerizations were set up under identical conditions with loading ratios of monomer ranging from 10 mol% to 90 mol% of AzoMA, increasing by 10 mol% increments. All reactions were quenched after 20 minutes, then precipitated 3 times in hexanes. The resulting polymers were characterized by ^{1}H NMR spectroscopy to determine the molar incorporation of the two monomers.

The refractive index increment of poly(4-phenylazophenyl methacrylate) (PAzoMA) was not available in the literature, and needed to be measured. The polymer was synthesized by free radical polymerization, combining AzoMA (3.7 mmol, 61 eq) and AIBN (0.061 mmol, 1 eq) in 3.7 mL of toluene. The reaction was degassed by three freeze-pump-thaw cycles, then filled with argon to 5 atm. The polymerization was allowed to proceed at 60 ºC for 20 hours, then precipitated twice in hot methanol. The resulting polymer showed no residual monomer present as detected by ^{1}H NMR spectroscopy.

Polymer characterization and molecular weight determination

Proton nuclear magnetic resonance (^{1}H NMR) spectra of the polymers were collected using a 500 MHz Bruker Avance II spectrometer, with deuterated chloroform as a solvent. The molecular weight distributions were analyzed using size exclusion chromatography (SEC) paired with refractive index and light scattering detectors, with tetrahydrofuran (THF) as the eluent.

Abbé Refractometry

The refractive index increment, dn/dc, of PAzoMA was measured by Abbé refractometry to enable measurement of the molecular weight distribution of AzoMA copolymers using a light scattering SEC detector. Five solutions of PAzoMA in THF were prepared with

concentrations of 10, 20, 30, 40, and 50 mg/mL of polymer. The refractive index of the five solutions and pure THF were measured using a red light source to mimic the wavelength of the HeNe laser in the light scattering SEC detector. Each refractive index measurement was taken three times to ensure the accuracy of the reading. The resulting data were plotted as a function of concentration, where the slope gives the dn/dc. The resulting data are shown in Figure 2.9. The dn/dc of a copolymer consisting of monomers A and B can be determined

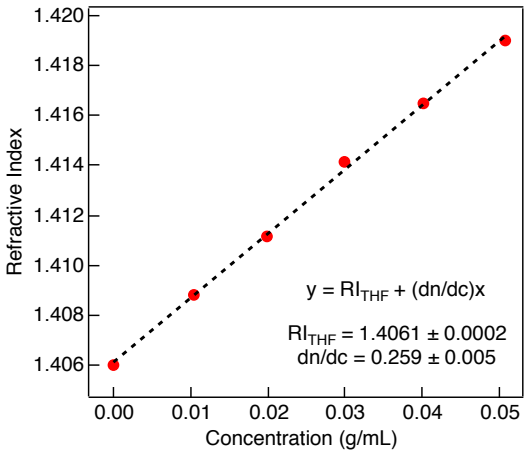

Figure 2.9: The refractive index of PAzoMA solutions in THF as a function of concentration, where the slope gives the dn/dc of PAzoMA in THF.

by the sum of the weight fraction of the monomer in the copolymer, w, multiplied by the dn/dc of the homopolymer.[159] This is described in Equation 2.2, and for the combination of AzoMA and BzMA, produces number average molecular weights that are similar to what is obtained through end group analysis in ^{1}H NMR spectroscopy.

$$\left(\frac{dn}{dc}\right)_{AB} = w_A\left(\frac{dn}{dc}\right)_A + w_B\left(\frac{dn}{dc}\right)_B \tag{2.2}$$

UV-vis spectroscopy

UV-vis spectra of the polymers were obtained using a Varian Cary 100 Bio UV-vis spectrophotometer with temperature control. Solutions of P(BzMA-*stat*-AzoMA) in EMI TFSI with concentrations between 0.02 and 0.1 wt% were used to ensure that the detector was not saturated. Measurements were taken using 700 µL quartz fluorescence cuvettes, with a path length of 2 mm. A reference solution of ionic liquid was used for background subtraction.

To determine the UV light irradiation time needed to achieve full *trans* to *cis* isomerization, solutions were irradiated with UV light for given time increments, and a UV-vis spectrum at room temperature was obtained after each time point. The thermal relaxation kinetics of the *cis* isomer were measured at 50, 60, 70, 80, and 90 ºC. The solutions were irradiated with UV light for at least twice the time needed to achieve full isomerization, then placed in the spectrophotometer at a given temperature. The absorbance at the peak absorbance in the UV region, 324 nm, was measured as a function of time for 30 minutes to an hour, showing a steady increase as the excited state *cis* isomer relaxed to the ground state *trans* isomer.

2.3 Results

NIPAm-based polymers

Despite following the exact reported literature procedure,[85] very little polymer was obtained after a 68 hour reaction time. The literature procedure calls for using 2-(dodecylthio carbonothioylthio)-2-methylpropionic acid, AIBN, NIPAm, and AzoMA at a concentration of 2M in toluene, and reacting for 68 hours at 65 ºC. The AzoMA loading was 10 mol% of the total monomer concentration. After precipitation, a very small amount of sticky orange solid was obtained. A large portion of the NIPAm monomer did not react, as it crystallized from the hexanes used as a poor solvent in the precipitation. As the two monomers are chosen have significantly different reactivities, the optimal chain transfer agent (CTA) for the two monomers differs. Figure 2.10 shows the structure of a) 2-(dodecylthiocarbonothioylthio)-2-methylpropionic acid and b) 4-cyano-4-[(dodecylsulfanylthiocarbonyl)s
acid. While a) is the most appropriate choice for acrylamides and acrylates, b) is more ef-

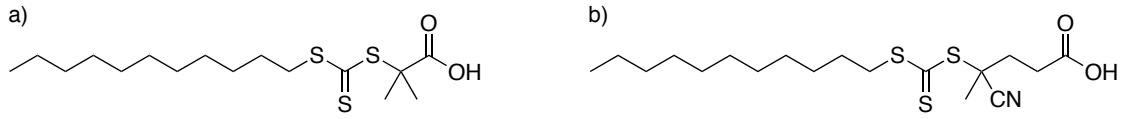

Figure 2.10: Chemical structure of a) 2-(dodecylthiocarbonothioylthio)-2-methylpropionic acid and b) 4-cyano-4-[(dodecylsulfanylthiocarbonyl)sulfanyl]pentanoic acid.

fective for methacrylamides and methacrylates. To determine if the chain transfer agent was the source of low polymer conversion, the polymerization was run again under identical conditions, instead using 4-cyano-4-[(dodecylsulfanylthiocarbonyl)sulfanyl]pentanoic acid as the chain transfer agent. Unfortunately the same results were obtained again, little conversion of monomer to polymer. Despite the low conversion in both cases, the polymer that was produced had a narrow molecular weight distribution, shown in Figure 2.11. These polymerizations yielded enough polymer for SEC and ^{1}H NMR spectroscopy, but

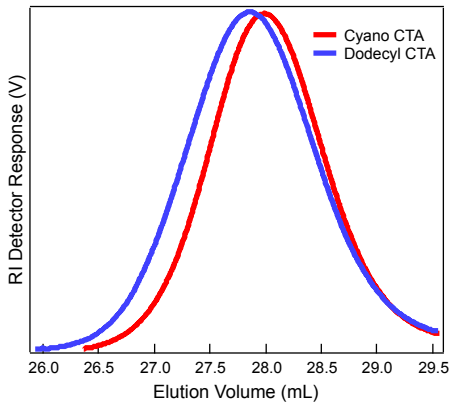

Figure 2.11: SEC traces of P(NIPAm-*stat*-AzoMA) copolymers synthesized using a cyano CTA (4-cyano-4-[(dodecylsulfanylthiocarbonyl)sulfanyl]pentanoic acid) (red trace) and a dodecyl CTA (2-(dodecylthiocarbonothioylthio)-2-methylpropionic acid) (blue trace).

not enough to perform significant testing. Given the low yield (*ca.* 10%) even after a 68 hour reaction time, rather than scaling up the reaction we chose to seek a method of increasing the yield while simultaneously decreasing the reaction time.

Many factors can contribute to an unsuccessful polymer synthesis. To determine the cause of the lack of conversion, four separate polymer syntheses were performed. Both monomers, NIPAm and AzoMA, were separately polymerized using both chain transfer agents. All reactions were run at 70 ºC for 20 hours, the NIPAm polymerizations were run at 1 M in toluene and the AzoMA polymerizations were run at 0.3 M due to low solubility of AzoMA in toluene. All other factors for the four polymerizations were kept the same. All four polymerizations successfully produced polymers, with the SEC traces of the resulting polymers shown in Figure 2.12. While the choice of chain transfer agent did not impact the molecular weight distribution of PNIPAm, it clearly had an effect on PAzoMA. The

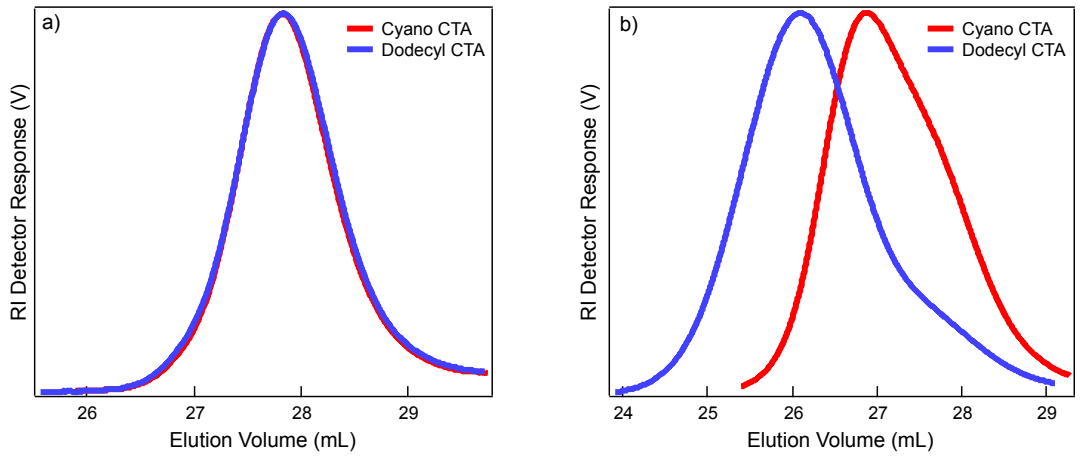

Figure 2.12: SEC traces of a) PNIPAm and b) PAzoMA polymerized by RAFT using a cyano CTA (4-cyano-4-[(dodecylsulfanylthiocarbonyl)sulfanyl]pentanoic acid) (red traces) and a dodecyl CTA (2-(dodecylthiocarbonothioylthio)-2-methylpropionic acid) (blue traces).

cyano CTA produced a significant shoulder, while the dodecyl CTA seems to give some tailing. Despite running the reaction for the same length of time, the molecular weights produced were also significantly different. Although the SEC traces were asymmetric, the polymerization still yielded a significant amount of polymer. This indicated that the AzoMA monomer may interfere with the RAFT polymerization, and the degree to which this interference impacts the copolymerization is more severe. The reactivity ratios also play an important role, with both monomers preferring to add AzoMA and a very small AzoMA loading, the polymerization would be expected to proceed slowly.[85] To separate the effect of the azo moiety on the RAFT polymerization and the impact of reactivity ratios, a polymerization was run replacing the AzoMA with the same molar quantity of AzoOH. Without the methacrylate, AzoOH cannot add to the polymer. With this addition, the yield of polymer was again very low, *ca.* 10%. This indicated that the azo moiety interfered with the RAFT polymerization of NIPAm, and modifying the monomer to an acrylamide or acrylate to yield a more similar reactivity ratio would not remedy the issue.

Other polymerization techniques were explored to successfully produce this copolymer. The anionic polymerization of NIPAm has been reported in the literature, however it involves polymerizing *N*-methoxymethyl-*N*-isopropylacrylamide and subsequent deprotection of the amide nitrogen after polymerization.[160] NIPAm has also successfully been poly-

merized with ATRP,[161,162] however there can be difficulties with amide monomers complexing the copper catalyst, preventing polymerization propagation.[163,164] The homopolymerization of AzoMA by ATRP was successful using two ligands, PMDETA (N,N,N',N",N"-pentamethyldiethylenetriamine) and HMTETA (1,1,4,7,10,10-hexamethyltriethylenetetr-amine) in anisole using CuBr (I) as the catalyst, at 90 ºC. The homopolymerization of NIPAm was unsuccessful. The reaction did not work with PMDETA or HMTETA in anisole, HMTETA in dichloromethane, with CuCl (I) instead of CuBr (I) with HMTETA in anisole, or with tris[2-(dimethylamino)ethyl]amine and CuCl (I) in anisole. Rather than continually attempting different combinations of reaction conditions to generate a homopolymer of PNIPAm, which may have not successfully extended to the copolymerization, it was decided to replace NIPAm with BzMA.

Benzyl methacrylate-based polymers

The ATRP of BzMA was run under identical conditions to the successful polymerization of AzoMA, using HMTETA as the ligand. The polymerization reached full conversion by ^{1}H NMR spectroscopy after 10 hours (Figure 2.8), quickly producing a polymer. The copolymerization of AzoMA and BzMA was carried out at 90 ºC, which also rapidly produced a copolymer. The reaction kinetics are shown in Figure 2.13a, with conversion measured

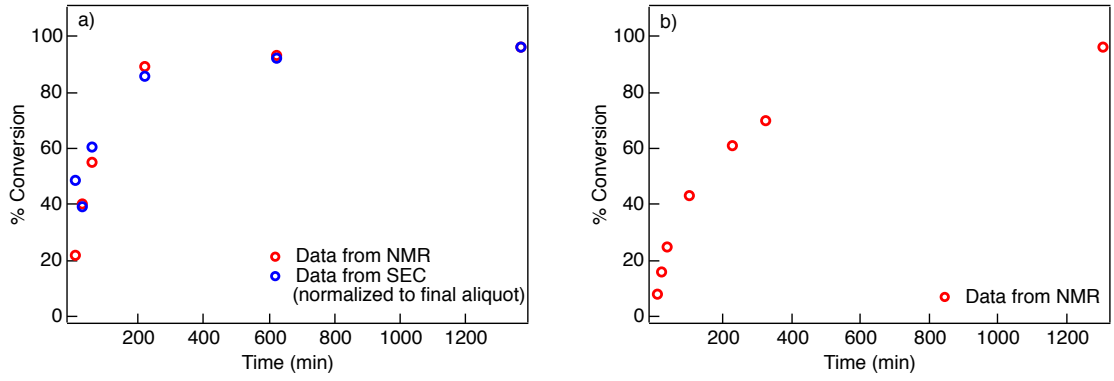

Figure 2.13: ATRP kinetics of BzMA and AzoMA at a) 90 ºC and b) 75 ºC. At 90 ºC, the conversion was measured both by molecular weight determination using SEC (blue symbols) and ^{1}H NMR spectroscopy. As the data were very similar for the two techniques, only ^{1}H NMR spectroscopy was used to measure conversion at 75 ºC.

both by SEC and ^{1}H NMR spectroscopy. The conversion by SEC was measured by obtain-

ing the molecular weight of the aliquots based on the dn/dc, and then normalizing all data by assuming that the conversion for the final aliquot by ^{1}H NMR spectroscopy was correct. The conversion by ^{1}H NMR spectroscopy was measured by comparing the benzylic proton conversion from monomer to polymer. As this temperature enabled the polymerization to reach $>$90% conversion in only 220 minutes, the temperature was brought down to 75 ºC, which considerably slowed the reaction (Figure 2.13b). For controlled radical polymerization, it is important to stop at 70% conversion or less to ensure that uncontrolled termination of the reaction does not occur. For the copolymerization, the point of $\sim$ 60% conversion occurs at 60 min for 90 ºC, and 230 min for 75 ºC. The longer reaction time gives more control over the molecular weight of the resulting polymer. If the reaction runs too quickly, then a difference in a few minutes can mean a dramatic difference in molecular weight. All future polymerizations were run at 75 ºC to maintain this control.

The rate of the polymerization was a drastic improvement over the NIPAm/AzoMA polymerization, and indicated that the reactivity ratios were potentially more similar between the two monomers. Given that both monomers are methacrylates, it would follow that they have very similar reactivities. To validate the numbers found by the Watanabe group from a range of 0.6 mol% to 4 mol% AzoMA incorporation,[84] we synthesized copolymers ranging from 10 mol% up to 90 mol%. When determining reactivity ratios, it is important to measure the copolymer composition with the lowest conversion possible. In practical terms, this is achieved by quenching the polymerization when the conversion is $\leq$10%, then measuring the relative proportion of the two monomers by ^{1}H NMR spectroscopy. This ensures that very few monomers have added to the polymer chain relative to those available in solution, reducing the effect of composition drift. If the polymerization was allowed to proceed to 100% conversion, the incorporation of the monomers would be the same as was fed into the polymerization. The polymerizations were prepared such that the molecular weight at *ca.* 10% conversion would be above 7 kDa, to allow for easy purification by precipitation. The reactions were run as free radical polymerizations, with the same solvent and concentration as the ATRP. A test polymerization was used to determine the time at which 10% conversion was reached, then the 9 polymerizations were run simultaneously. The resulting data are shown in Figure 2.14, where f_{AzoMA} is the molar ratio of

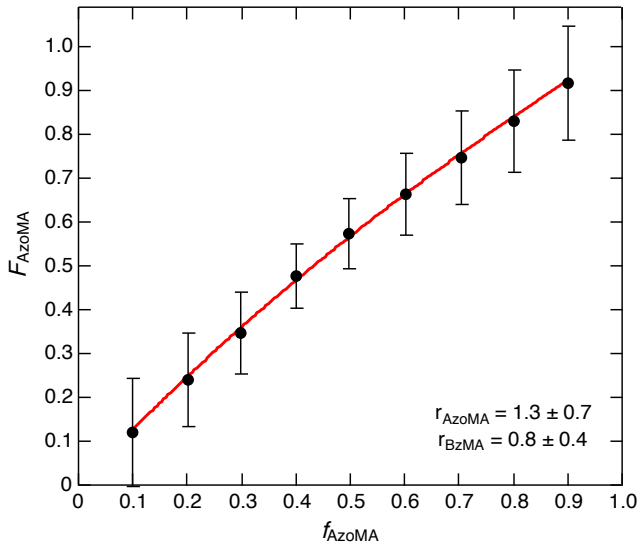

Figure 2.14: Composition of AzoMA copolymerized with BzMA in the feed, f_{AzoMA}, and in the polymer, F_{AzoMA}.

AzoMA in the feed and F_{AzoMA} is the molar ratio of AzoMA in the resulting polymer. The error in F_{AzoMA} arises from the error in integration of protons in ^{1}H NMR spectra. The data were fit with the Mayo-Lewis equation, Equation 2.3:

$$F_{AzoMA} = \left(\frac{r_{AzoMA} f_{AzoMA}^2 + f_{AzoMA} f_{BzMA}}{r_{AzoMA} f_{AzoMA}^2 + 2 f_{AzoMA} f_{BzMA} + r_{BzMA} f_{BzMA}^2} \right) \tag{2.3}$$

where r again represents the reactivity ratio of an individual monomer. The fit of the data gives r_{AzoMA} of 1.3±0.7 and r_{BzMA} of 0.8±0.4. These agree with the literature values within error, 1.7 and 0.8, respectively.[84] Within error, the relative reactivity ratios of the two monomers are very close to 1, with both monomers showing a slight preference for the addition of AzoMA. The distribution of monomers in the polymer chain is close to random, but as it is not perfectly random it will be referred to as a statistical copolymer.

A range of statistical copolymers were synthesized using ATRP, to span a variety of molecular weights at constant AzoMA content, as well as varied AzoMA content at a low molecular weight. To simplify the notation, P(BzMA-*stat*-AzoMA) polymers will be abbreviated at B*s*A, with the molecular weight and azobenzene incorporation listed in parenthesis after. A 35 kDa polymer with 6 mol% AzoMA would be named B*s*A (35-6). The SEC traces for the copolymers are shown in Figure 2.15. The molecular characteris-

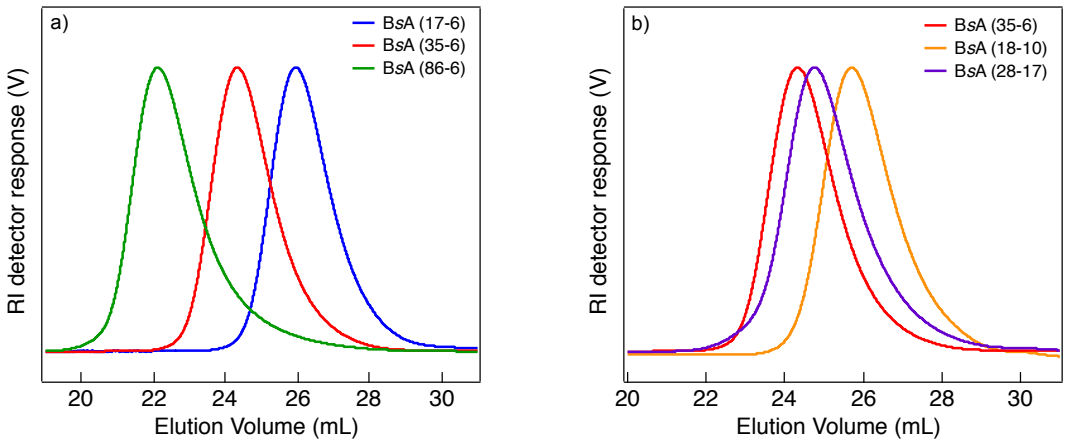

Figure 2.15: SEC traces of B*s*A copolymers with a) constant AzoMA content of 6 mol% and b) similar, low molecular weights with varying AzoMA content.

tics of these copolymers are gathered in Table 2.1. The end group analysis by ^{1}H NMR spectroscopy was unreliable because the peak from the initiator was difficult to resolve, so these numbers are not reported. The low dispersities of the polymers indicate that control

Copolymer	mol% incorporation of AzoMA [a]	M_n (kDa) [b]	$Đ$ [b]	Average AzoMA molecules per chain [a]
B*s*A (17-6)	6	17	1.05	~5
B*s*A (35-6)	6	35	1.06	~10
B*s*A (86-6)	6	86	1.09	~24
B*s*A (18-10)	10	18	1.06	~9
B*s*A (28-17)	17	28	1.10	~24

Table 2.1: Molecular characteristics of B*s*A copolymers. [a] Determined by ^{1}H NMR spectroscopy. [b] Determined by SEC based on the measured dn/dc of PAzoMA and the literature value of dn/dc = 0.144 for PBzMA.[165]

of the polymerization was successful. For AzoMA compositions of 6 mol%, the molecular weight approximately doubles with each increase, giving a wide range for testing of photoresponsive phase behavior, as will be discussed in Chapter 3. The AzoMA compositions are all higher than previously tested, which went no higher than 4 mol%.[84] This will provide information on how the copolymer composition impacts the photoresponsive behavior of the polymers.

UV light induced *trans* to *cis* isomerization of azobenzene

The UV-vis spectrum of B*s*A under visible light, in the *trans* ground state, shows a strong peak at 324 nm indicative of the π to π^* transition. A UV lamp with an output of 10 mW/cm^2 at a distance of 4 cm was used as the UV light source for these tests. As UV light is shone on the sample, this peak decreases in intensity, and a peak at 420 nm corresponding to the n to π^* transition of *cis* azobenzene grows in. Figure 2.16 shows the spectra for the three polymers with varying AzoMA content, B*s*A (17-6), (18-10), and (28-17). B*s*A (17-

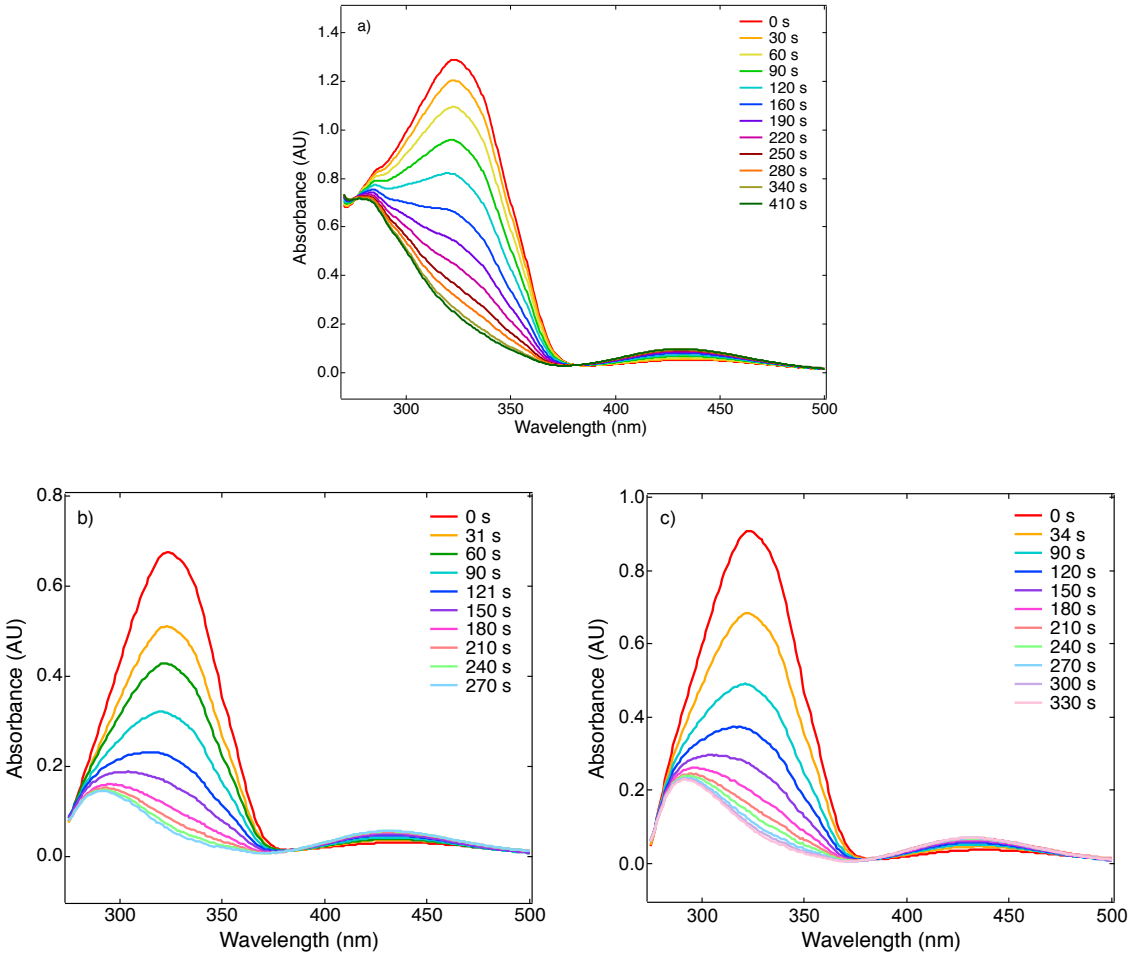

Figure 2.16: UV-vis absorption spectra of the isomerization of azobenzene in a) 0.1 wt% B*s*A (17-6) in EMI TFSI, b) 0.02 wt% B*s*A (18-10) in BMI TFSI, and c) 0.02 wt% B*s*A (28-17) in BMI TFSI under UV light with increasing irradiation time.

6) was tested in EMI TFSI, while B*s*A (18-10) and (28-17) were tested in BMI TFSI, due to insolubility at higher concentrations in EMI TFSI. The concentration for all samples was

kept low, as absorbances above 2 AU saturate the detector. The azobenzene moiety absorbs very strongly in the UV region, still showing a high absorbance at a low concentration and short path length of 2 mm. Only the samples with varying AzoMA content were tested using UV-vis spectroscopy. As the concentration of these samples is measured in wt%, the total amount of azobenzene in the polymer samples with 6 mol% AzoMA incorporation should be the same at a given concentration, and should have similar isomerization kinetics as a result. The samples all reach the photostationary *cis* state in under 10 minutes, ranging from ∼7 min for B*s*A (17-6) to ∼5 min for the higher AzoMA composition samples. This decrease in isomerization time for the solutions containing more AzoMA is likely because the concentration is lower, giving a lower absorbance. This allows the UV light to fully penetrate the sample. Between Figures 2.16 b and c, the time to reach the photostationary state increases from 270 s to 330 s with an increase in the AzoMA content of the polymer, where the concentration of polymer is held constant. In all cases, the isomerization occurs rapidly, and the difference between the time to reach the photostationary state of the three samples is relatively small.

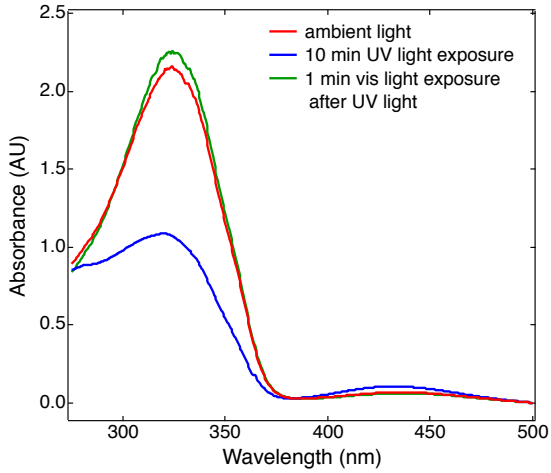

Figure 2.17: UV-vis spectra of azobenzene isomerization in 1 wt% B*s*A (17-6) in EMI TFSI showing the photostationary state after 10 min of UV irradiation, followed by reversion to the *trans* isomer after only 1 min of visible light irradiation.

The time required to re-isomerize the samples to *trans* using visible light was also tested. A visible light LED centered at 420 nm was used as the light source. For this sample, a UV LED was also tested, with a peak output at 320 nm. Although the UV LED

wavelength was closer to the main absorption band of *trans* AzoMA than the 365 nm broad spectrum mercury arc lamp previously used, it was unable to produce full isomerization. This is a result of the high absorptivity of azobenzene at this wavelength, and indicated that the broad spectrum lamp centered at 365 nm would be the best choice for future testing. The *trans* to *cis* isomerization under UV light and corresponding reversion to *trans* under visible light is shown in Figure 2.17. In contrast to the UV LED, the visible light LED was extremely efficient, returning the azobenzene to the ground *trans* state after only a minute of irradiation. Further, it shows that ambient UV light does impact the isomerization state, as the π to π^* peak has a stronger absorbance after the visible light LED irradiation than it did under the lighting in the lab. In order to obtain a sample with all *trans* isomers, the sample must be irradiated with the visible LED and then stored in the dark.

Kinetics of azobenzene thermal relaxation

The *cis* to *trans* isomerization can be triggered by visible light, or the excited *cis* state can be allowed to relax back to the *trans* state. The stability of the *cis* isomer is strongly dependent on the chemical environment, being tethered to a polymer chain increases the lifetime of the *cis* isomer.[148] The temperature plays a strong role in the thermal reversion to *trans*. At room temperature, the *cis* isomer is extremely stable. Figure 2.18 shows the thermal

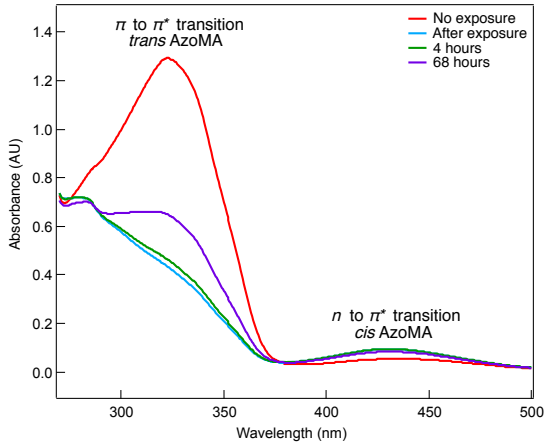

Figure 2.18: UV-vis spectra of 0.1 wt% B*s*A (17-6) in EMI TFSI under visible light (red curve), immediately after UV light exposure (blue curve), after storage in the dark for 4 hours at room temperature (green curve), and after storage in the dark for 68 hours at room temperature (purple curve).

reversion after 4 and 68 hours of storing the sample in the dark, at room temperature. After 4 hours, the sample is still predominantly *cis*, as shown by the minor change in the UV-vis spectrum. Even after 68 hours at room temperature, the sample has not fully returned to the *trans* isomer. While the *cis* isomer is very stable at room temperature, thermal reversion increases with increasing temperature. Figure 2.19 shows the thermal reversion of *cis* to *trans* in the three polymers with varying AzoMA content. This experiment monitors the

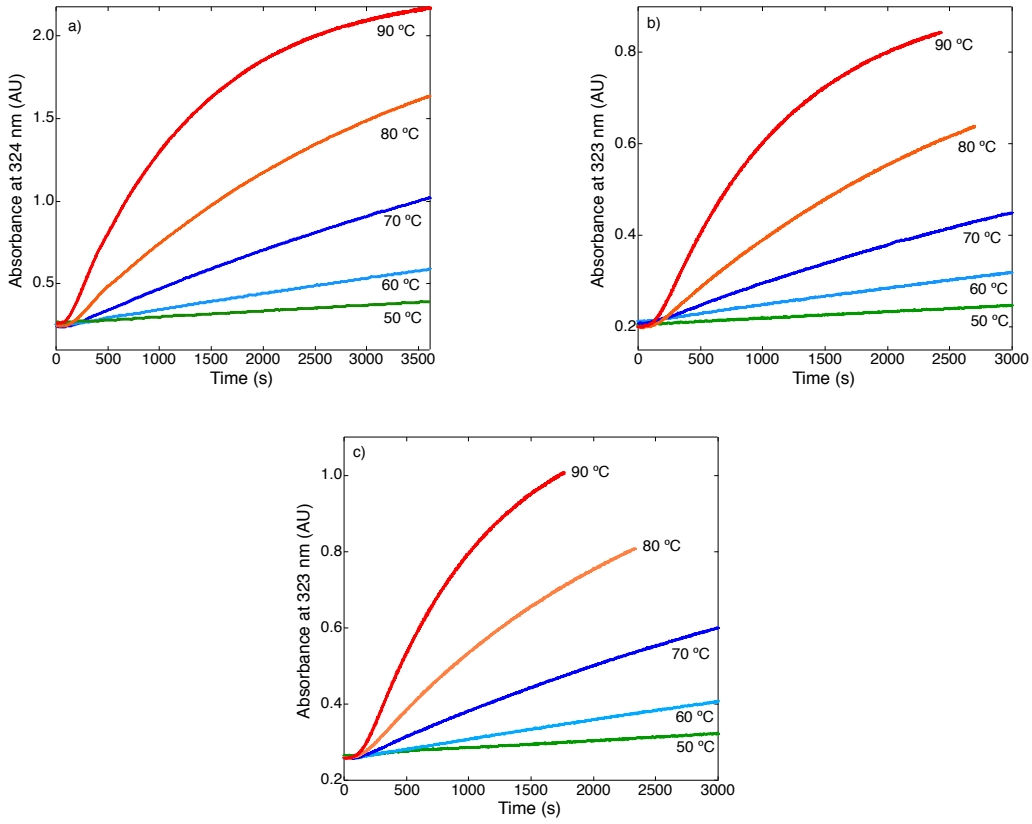

Figure 2.19: Absorbance of a solution of a) 0.1 wt% B*s*A (17-6) in EMI TFSI, b) 0.02 wt% B*s*A (18-10) in BMI TFSI, and c) 0.02 wt% B*s*A (28-17) in BMI TFSI at 324 nm over time with varying temperature.

absorbance at 324 nm, the peak wavelength for *trans* AzoMA. As this absorbance increases, the *trans* isomer concentration is increasing. From these data, it is clear that the *cis* isomer is relatively stable at slightly elevated temperatures, e.g., 50 ºC, however, increasing the temperature up to 90 ºC allows for a rapid thermal reversion back to the *trans* ground state.

Spiropyran as a photoresponsive monomer

Spiropyran acrylate in solution undergoes a dramatic color change upon isomerization to merocyanine. Figure 2.20 shows images of the monomer in an NMR tube. The first picture shows the color upon first dissolution in DMSO-d_6, a polar solvent that stabilizes the ring-opened merocyanine form. The sample is a dark purple, as expected from this spiropyran.[158] Irradiation with visible light (420 nm) yields the colorless spiropyran, which can be returned to merocyanine upon irradiation with UV light (365 nm). In contrast to azobenzene, where the polar excited *cis* state can only be accessed under UV light, the merocyanine form can be formed simply due to the chemical environment.[156] The interactions with solvent can compete with the light-driven isomerization, as will be discussed in Chapter 3.

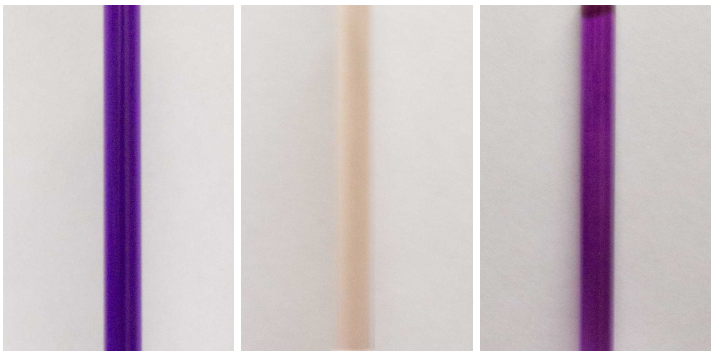

Figure 2.20: Isomerization of SPA dissolved in DMSO-d_6 under visible and UV light. The sample starts as the purple merocyanine isomer, is transformed to the colorless ring-closed spiropyran under visible light, and returned to merocyanine with UV light.

The copolymerization of spiropyran acrylate, SPA, with NIPAm was attempted via RAFT, using the same conditions that successfully produced a PNIPAm homopolymer. As with the copolymerization of NIPAm with AzoMA, little to no conversion to polymer occurred. Rather than continuing to troubleshoot the polymerization, the thermoresponsive monomer was switched to BzMA. To test the compatibility of BzMA and spiropyran, as well as the resulting photoresponsive properties of the polymer, the available SPA monomer was used rather than synthesizing spiropyran methacrylate. A faintly lilac copolymer was generated by free radical polymerization of BzMA and SPA, which was tested for photoresponsive phase separation behavior, discussed in Chapter 3. The UV-vis spectra of these

polymers were not obtained, as it was found that the azobenzene-based polymers had better performance.

2.4 Discussion

Thermal stability of *cis* azobenzene

The data in Figure 2.19 qualitatively show that azobenzene relaxes from *cis* to *trans* at elevated temperatures. This thermal relaxation can be quantified by considering this relaxation a first order kinetics process with respect to *cis* azobenzene concentration:[166]

$$-\frac{d[cis]}{dt} = \frac{d[trans]}{dt} = k[cis] \tag{2.4}$$

where $[cis]$ and $[trans]$ are the concentrations of the isomers, and k is the rate constant. As the absorbance for the *cis* isomer is considerably lower, it is easier to monitor the concentration of the *trans* isomer. At time $t = \infty$, all isomers will be fully relaxed to *trans*, thus the total isomer concentration can be represented at $[trans]_\infty$. At any given time t, the sum of the *cis* and *trans* concentrations at time $= t$ will be equal to the total isomer concentration, $[trans]_\infty$.

$$[trans]_\infty = [cis]_t + [trans]_t \tag{2.5}$$

The concentration of *cis* isomer can be replaced in the first order differential equation, and solved to give the rate law.

$$ln\Big([trans]_\infty - [trans]_t\Big) = -kt + ln\Big([trans]_\infty - [trans]_0\Big) \tag{2.6}$$

The $[trans]$ can be replaced by absorbance using Beer's law, where A_{324nm} is absorbance at 324 nm, ϵ is the absorptivity coefficient, and l is the path length.

$$A_{324nm} = \epsilon l[trans] \tag{2.7}$$

Substituting this in Equation 2.6 allows for the data in Figure 2.19 to be plotted as a function of $ln\Big([trans]_\infty - [trans]_t\Big)$ and time, and be fit to obtain a rate constant for thermal relaxation at each temperature. The resulting fits are shown in Figure 2.21.

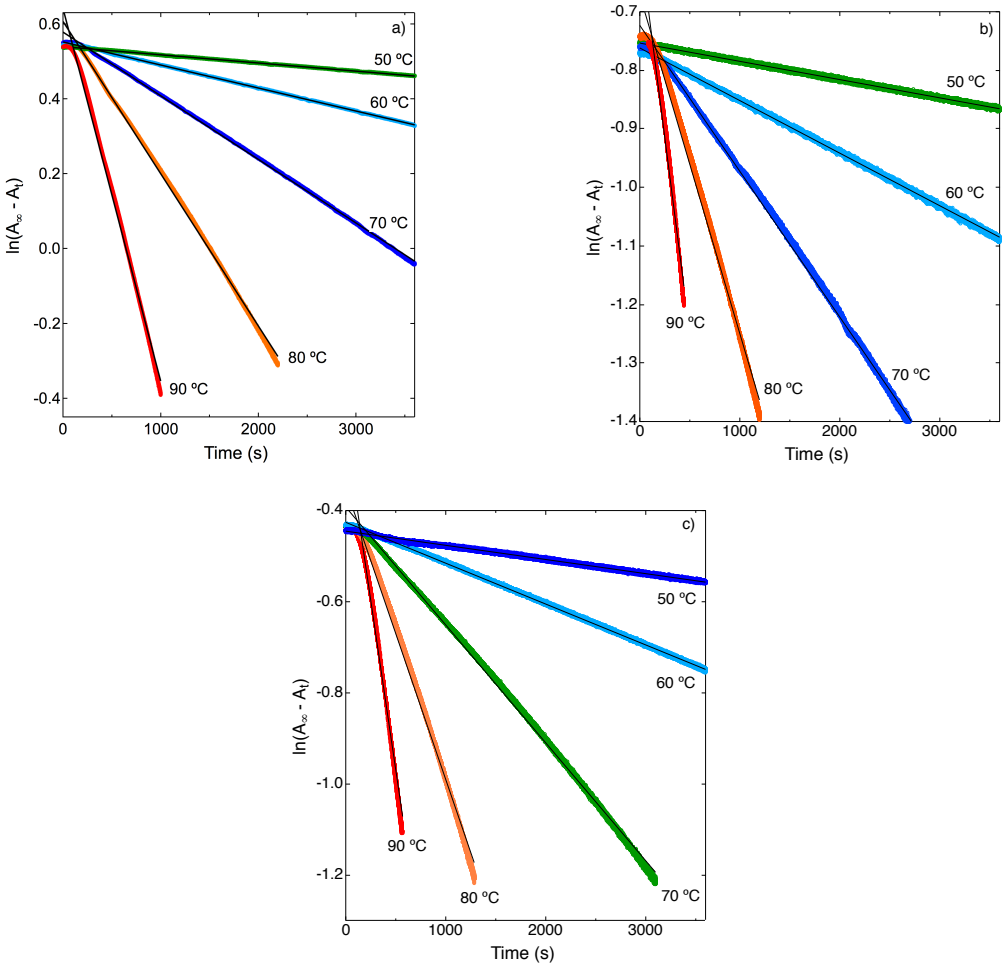

Figure 2.21: First order rate constant plots for a) 0.1 wt% B*s*A (17-6) in EMI TFSI, b) 0.02 wt%B*s*A (18-10) in BMI TFSI, and c) 0.02 wt%B*s*A (28-17) in BMI TFSI with fits to determine the rate constant of thermal relaxation.

The rate constants and corresponding half lives for each polymer at each temperature are collected in Table 2.2. In all cases, the rate constant for thermal relaxation increases with increasing temperature, as expected. The half-life of the *cis* isomer is lowest at the highest temperature, between 8-11 minutes. At 50 ºC, the half life dramatically increases to between 6-9 hours. While the thermal relaxation happens faster for the two polymers with higher AzoMA content than B*s*A (17-6), the kinetics between B*s*A (18-10) and B*s*A

BsA(17-6)			**BsA(18-10)**			**BsA(28-17)**		
Temp	k (s^{-1})	$t_{1/2}$ (s)	Temp	k (s^{-1})	$t_{1/2}$ (s)	Temp	k (s^{-1})	$t_{1/2}$ (s)
90 ºC	9.9 x 10^{-4}	700	90 ºC	1.3 x 10^{-3}	500	90 ºC	1.5 x 10^{-3}	500
80 ºC	4.0 x 10^{-4}	1700	80 ºC	5.7 x 10^{-4}	1200	80 ºC	6.3 x 10^{-4}	1100
70 ºC	1.7 x 10^{-4}	4100	70 ºC	2.5 x 10^{-4}	2800	70 ºC	2.6 x 10^{-4}	2700
60 ºC	6.2 x 10^{-5}	11300	60 ºC	9.0 x 10^{-5}	7700	60 ºC	9.0 x 10^{-5}	7700
50 ºC	2.2 x 10^{-5}	31900	50 ºC	3.1 x 10^{-5}	22100	50 ºC	3.1 x 10^{-5}	22500

Table 2.2: Kinetics of thermal relaxation of azobenzene in B*s*A solutions as determined by UV-vis spectroscopy.

(28-17) are very similar. The two higher AzoMA content polymers were tested at a lower concentration, which may allow faster relaxation. The ionic liquid has also changed from EMI TFSI to BMI TFSI, and the increase in the non-polar alkyl tail length of the solvent may decrease the stability of the polar *cis* isomer. Finally, it is also possible that the thermal relaxation kinetics increase with increasing azobenzene content, but reach a plateau after a certain amount of AzoMA. If the impact of concentration, AzoMA content, and solvent need to be deconvoluted, future experiments should be performed to hold both concentration and solvent identity constant.

The rate constants obtained from fitting the data can also be used to find an activation energy for thermal relaxation, using the Arrhenius equation:

$$k = Ae^{-E_a/RT} \tag{2.8}$$

where A is the pre-exponential factor, E_a is the activation energy, and R is gas constant. By plotting $ln(k)$ versus T^{-1}, the data can be fit with a linear expression to give the activation energy. This is shown in Figure 2.22 for the three polymer solutions. All values obtained for the activation energy of thermal *cis* to *trans* isomerization were very similar, 93$\pm$2 kJ/mol for B*s*A (17-6), 91$\pm$2 kJ/mol for B*s*A (18-10), and 95$\pm$1 kJ/mol for B*s*A (28-17). This suggests that the thermal relaxation has little to no dependence on the amount of azobenzene present in a single polymer chain. These numbers are also in agreement

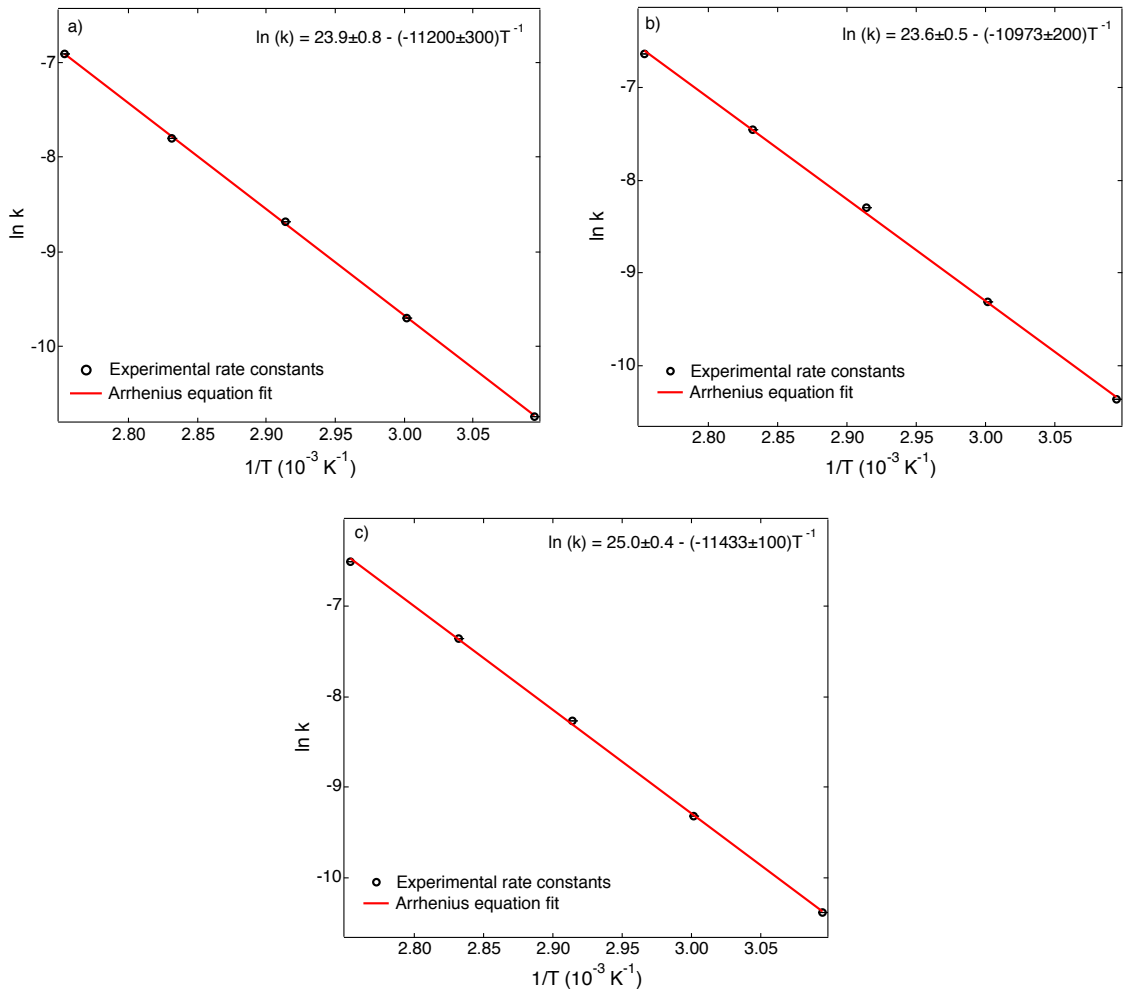

Figure 2.22: Arrhenius plots of a) 0.1 wt% B*s*A (17-6) in EMI TFSI, b) 0.02 wt%B*s*A (18-10) in BMI TFSI, and c) 0.02 wt%B*s*A (28-17) in BMI TFSI with fits to give the activation energy for thermal *cis* to *trans* isomerization.

with the activation energy for monomeric azobenzene in ionic liquid, 84 - 100 kJ/mol, suggesting that tethering the azobenzenes to a polymer chain does not affect the isomerization kinetics.[167]

2.5 Conclusions

The synthesis of copolymers can be complex, and fail for a multitude of reasons. The copolymerization of NIPAm with AzoMA and SPA was unsuccessful. In RAFT polymerization, it appeared that the azobenzene itself interfered with the polymerization of PNI-

PAm. Homopolymers of AzoMA and NIPAm were successfully synthesized under identical conditions by RAFT polymerization, but the addition of either AzoMA or the alcohol precursor to the monomer, AzoOH, halted the polymerization, giving little to no detectable yield even after long reaction times. For ATRP, PNIPAm was unable to be synthesized, likely because the amide in the NIPAm homopolymer interfered with the copper catalyst.

The copolymers of BzMA and AzoMA, and BzMA and SPA were both successfully synthesized to produce light-responsive polymers. The SPA/BzMA copolymers were able to change color under different wavelengths of light, although they were not extensively studied. The BzMA/AzoMA copolymers were synthesized with a range of molecular weights and copolymer compositions to investigate how these parameters impact the temperature- and light-responsiveness of the polymers. The temperature-responsive phase behavior will be discussed in detail in Chapter 3, while this work focused on the kinetics of the light-responsive azobenzene isomerization. Under 365 nm UV light produced by a mercury arc lamp, the polymers underwent *trans* to *cis* isomerization in under 10 minutes. Irradiation using a wavelength close to the peak absorbance of *trans* AzoMA, 320 nm, achieved significantly less isomerization than the 365 nm lamp. This is due to the significantly higher absorption of light at 320 nm, which blocks the light from fully transmitting through the sample. A 420 nm LED was able to achieve full isomerization back to the *trans* state in less than a minute. The thermal relaxation of the excited *cis* state was studied in B*s*A copolymers of varying compositions, but it was found that copolymer composition did not significantly impact the activation energy needed for thermal reversion.

2.6 Acknowledgments

This work was supported by the National Science Foundation through Award DMR-1707578. Thanks to Cecelia Rivera for her help in synthesis and characterization of the copolymers. Thanks to Prof. Valerie Pierre for the use of her lab's UV-vis spectrometer.

Chapter 3

LCST phase behavior of a thermo- and photoresponsive statistical copolymer in an ionic liquid[i] [ii]

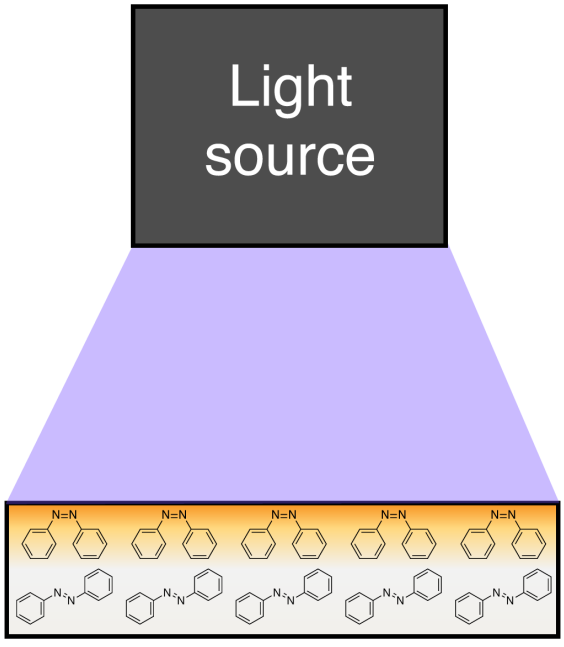

[i]Adapted with permission from Hall, C. C.; Rivera, C. A.; Lodge, T. P. The effect of light penetration depth on the LCST phase behavior of a thermo- and photoresponsive statistical copolymer in an ionic liquid. *Journal of Polymer Science Part A: Polymer Chemistry* **2018**. Copyright 2018 John Wiley and Sons.

[ii]This work was done in collaboration with Cecelia Rivera.

3.1 Preface

Polymers that are described as thermoresponsive change their solubility in a solvent with changes in temperature. This can reflect lower critical solution temperature (LCST) phase behavior, in which the polymer is soluble at low temperatures, and phase separates into polymer-rich and polymer-poor domains at higher temperatures. This transition is manifested in a change from a well-mixed, clear solution to a turbid one. Thus the LCST phase behavior of a polymer and solvent system can be investigated by measuring the cloud point of the solution. This measurement has a relatively simple experimental setup, passing a laser through the sample and measuring when the beam is no longer transmitted. When the temperature dependence of solubility is all that is needed, this experimental setup works well. However, in cases where additional factors, such as light, impact the solubility of the polymer in solvent, modifications are necessary. These compounds that are responsive to light typically have high molar absorptivities, which causes the light to be absorbed at the surface but unable to transmit through the full depth of a sample. In this case, it is important to be able to control the sample thickness, as well as vary it to understand how this absorbance of light impacts the light-responsive LCST phase behavior. A reflection cloud point technique allows for rapid screening of light-dependent phase separation temperatures of thermo- and photoresponsive polymer/ionic liquid solutions as a function of sample thickness, molecular weight, and copolymer composition.

We systematically investigated the LCST phase behavior of poly(benzyl methacrylate-*stat*-(4-phenylazophenyl methacrylate)) (P(BzMA-*stat*-AzoMA)). The LCST phase behavior of poly(benzyl methacrylate-*stat*-spiropyran acrylate) (P(BzMA-*stat*-SPA)) was also investigated at one molecular weight and concentration. Under UV light, the photoresponsive repeat units become more polar, increasing the solubility in the ionic liquids 1-ethyl-3-methyl imidazolium and 1-butyl-3-methyl imidazolium bis(trifluoromethanesulfonyl)imide. This light-dependent polarity change leads to two phase separation temperatures, depending on the illumination wavelength. The P(BzMA-*stat*-SPA) isomerization state was dominated by temperature, rather than light irradiation, so it could not be explored in depth for light-dependent LCST properties. However, the isomerization state of P(BzMA-*stat*-

AzoMA was dictated by light at all experimentally relevant temperatures, and was able to be studied at a variety of thicknesses, copolymer compositions, and molecular weights. For P(BzMA-*stat*-AzoMA) under visible light, the azobenzene moiety is in the *trans* ground state, and the LCST shows no sample thickness dependence. Under UV light, however, sample thickness plays a significant role. Samples around 1 mm thick show no apparent difference under UV and visible light, whereas thinner samples show an increasing difference between the phase separation temperatures with decreasing sample thickness. Neither phase separation temperature exhibits a significant dependence on molecular weight. Increasing the photoresponsive monomer content did not lead to an increase in the difference between the phase separation temperatures at fixed thickness, due to a concomitant increase in UV light absorbed at the sample surface.

3.2 Introduction

Appropriate combinations of polymers and ionic liquids yield materials with the desirable properties of the ionic liquid and the mechanical robustness of polymers.[168,169] The high thermal stability, wide electrochemical windows, high conductivity, and negligible vapor pressure make ionic liquids an attractive choice as solvents for a variety of applications.[46] Immobilizing the ionic liquid with polymers gives a wide range of possible applications including electrochemical mechanical actuators,[170] gate dielectrics in field effect transistors,[171] gas separation membranes,[172,173] and fuel cell membranes.[1] Using stimuli-responsive polymers adds another dimension to the control over the structure of the material, allowing for reversible gel formation or the controlled motion of an actuator.[174]

A simple choice for a stimulus is temperature. While the system is being physically altered, temperature does not permanently alter the system as do chemical changes, such as pH or ionic strength. This allows for reversible cycling, which is important for applications such as switches. Thermoresponsive polymers such as poly(N-isopropyl acrylamide) (PNIPAm)[61,62] and poly(benzyl methacrylate) (PBzMA)[57,59,145] have been well studied in ionic liquids. PNIPAm in ionic liquids undergoes phase separation on cooling, i.e., upper critical solution temperature (UCST) phase behavior. This is in contrast to the phase behav-

ior observed in water, where lower critical solution temperature (LCST) phase behavior is observed. PBzMA in ionic liquids phase separates on heating, following LCST phase behavior. This arises from the cation-π stacking between the ionic liquid and the phenyl ring on benzyl methacrylate, forming an ordered liquid clathrate-like structure that allows for mixing.[57] This gives a net negative entropy of mixing necessary for phase separation upon heating. Fundamental studies elucidating the phase separation behavior of these polymers enables their extension to applications. These fundamental studies explore how factors such as molecular weight, concentration, and solvent identity change the phase separation temperature. This enables tuning of the phase separation temperature to best suit the desired application. A well-explored application for thermoresponsive polymers in ionic liquids is as the endblock of an ABA triblock copolymer, with the B block being soluble in the ionic liquid.[175,176] This leads to a physically associated gel that can be thermoreversibly triggered to dissolve in ionic liquid, then return to the gel state.

Changing temperature to induce phase separation has been well-studied, but this trigger limits potential applications because the system is being physically altered. Controlling the phase separation in a manner that does not physically or chemically alter the system could open up a new range of applications for responsive ionic liquid/polymer systems, such as self-healing materials.[89,177,178] Using light as a stimulus could enable such contactless transitions. Two common light-responsive molecules are azobenzene and spiropyran, both of which increase in polarity under UV light. For azobenzene, the *trans* ground state under visible light is relatively non-polar, but upon irradiation with UV light, it undergoes *trans* to *cis* isomerization, inducing a significant dipole moment.[179] Spiropyran undergoes a similar transformation, where the ground state is relatively non-polar, and under UV light the polarity increases as a result of ring-opening to form the zwitterionic merocyanine species.[155] Both azobenzene and merocyanine can return to the less polar ground state via thermal reversion, or triggering with visible light. While spiropyrans have a higher change in polarity than azobenzenes,[140] they can undergo photodegradation, limiting their lifetime as photochromic compounds.[180] The effect is reduced when the spiropyran unit is tethered to a polymer chain, but the issue still persists.[134] Although the polarity change is smaller in azobenzene, it does not decompose with repeated cycling, which is favorable for applica-

tions requiring a long-lasting ability to respond to stimulus. The change in isomerization state also changes the color of spiropyrans, dependent upon the substituents on the ring and the polarity of the solvent.[154] In contrast, azobenzenes do not undergo a drastic color change with isomerization. Thus the identity of the isomer can be identified by sight with spiropyrans, but requires the use of UV–vis spectroscopy with azobenzenes.

Both azobenzene and spiropyran derivatives have been explored as monomers for copolymerization with thermoresponsive monomers. The change in polarity from the photoresponsive monomer under different wavelengths of light changes the solubility of the polymer in the solvent. This leads to two phase separation temperatures, dependent upon which photoresponsive isomer is present. An illustration of what this might look like for an LCST system is depicted in Figure 3.1. The best performing photoresponsive device would re-

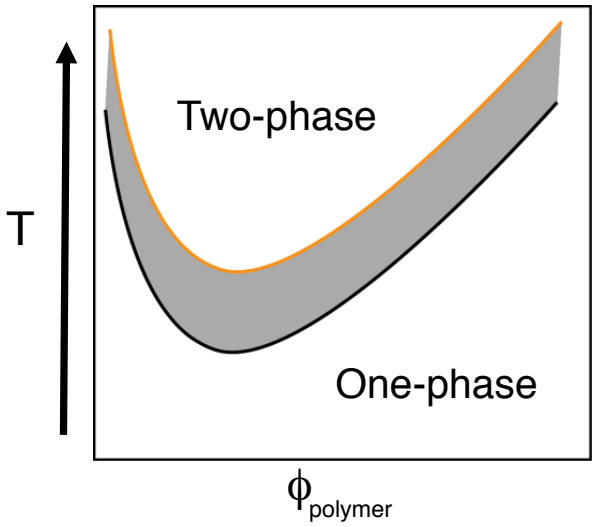

Figure 3.1: A cartoon of an LCST phase diagram with two boundaries. The lower black boundary represents the condition under which the polymer chain is less soluble, the upper orange where it is more soluble. The shaded grey region between the curves shows a bistable window where phase separation could be triggered using light as a stimulus.

quire a broad bistable window, shown as the shaded region in Figure 3.1. If the window is narrow, small temperature fluctuations could push the system out of the bistable region and into the one-phase or two-phase regime under either light source. The broader the window, the more resilient the system would be to minor changes in temperature. To make the window wider, the solubility difference under the two wavelengths of light needs to be increased. This can be achieved by increasing the content of photoresponsive monomer, but

this has some drawbacks as will be discussed below. Between azobenzene and spiropyran, spiropyran would be expected to have a wider window at the same monomer incorporation due to the larger change in polarity between the two isomers.

Photoresponsive phase separation has been well-studied in NIPAm and 4-phenylazophenyl methacrylate (AzoMA) copolymers in ionic liquids, over a range of both copolymer compositions as well as concentrations. For PNIPAm in ionic liquid, the phase separation temperature is affected by the molecular weight of the polymer; this effect is carried over to PNIPAm/AzoMA copolymers.[61] By incorporating 29 mol% AzoMA in the copolymer, differences in phase separation temperatures under UV and visible light of up to 43 ºC were observed.[85] In comparison, using 8 mol% AzoMA produced a window of only 8 ºC. This difference in phase separation temperatures gives a bistable temperature window, where phase separation can be triggered by light at any intermediate temperature. Although 29 mol% AzoMA gave a very wide bistable window, the phase transition broadened significantly. This gives a range of temperatures at which the system is undergoing phase separation, effectively removing those temperatures from viability for triggering. This broadening also indicates that there is a departure from the UCST phase separation observed from PNIPAm alone. This is due to the fact that the reactivity ratios of the two monomers are fairly dissimilar, $r_{AzoMA} = 5.60$ and $r_{BzMA} = 0.65$. Consequently, the AzoMA is not evenly distributed through the chain, as both monomers prefer adding AzoMA. As mentioned in Chapter 2, PAzoMA is completely insoluble in ionic liquids,[84] leading to large portions of the polymer chain which are poorly soluble. Depending on the distribution of monomers in the chain, portions with higher AzoMA content may begin to phase separate or associate at earlier temperatures, leading to the observed broadening. Limiting the AzoMA content to below 5 mol% reduces this broadness issue. These NIPAm/AzoMA copolymers have been studied in both AB diblock copolymers, showing light-induced micellization and de-micellization,[87] and ABA triblock copolymers for light-induced gelation and gel melting.[88,89] Interestingly, NIPAm/AzoMA copolymers in water seem to be limited to a bistable window of *ca.* $<$10 ºC, even when increasing the AzoMA incorporation.[124,181] As such, ionic liquids outperform as solvents as they are able to achieve significantly wider bistable windows.

The combination of spiropyran monomers with NIPAm has also been extensively explored for applications in aqueous media,[130,132,135,137,142,182–184] as well as ionic liquids.[21,23,139] Although there have been many studies of these materials in applications such as gels, fundamental studies of the LCST phase behavior in water or the UCST phase behavior in ionic liquid are lacking. A single study investigated a NIPAm/spiropyran methacrylate copolymer containing 2.5 mol% spiropyran methacrylate in water, and found that the LCST was 10 ºC lower under UV than visible light.[143] This is in contrast to the behavior expected in ionic liquid, where the increase in polarity under UV light should cause an increase in the solubility of the polymer. In the case of an LCST system, this would give a higher phase separation temperature. The authors do not offer an explanation for the fact that the LCST drops with an increase in polarity. This is in contrast to observations of NIPAm/AzoMA copolymers in water, where isomerization to the more polar *cis* form increases the LCST phase separation temperature.[124] The main focus of Ref. 143 was studying the photochemistry of the polymer by UV–vis spectroscopy, as opposed to details of the phase separation behavior. As such, there is a need for the synthesis and fundamental study of spiropyran-containing copolymers to better design these systems for applications.

There have also been some studies on BzMA/AzoMA copolymers, focusing on a small range of copolymer compositions, at or below 4 mol% AzoMA incorporation, and low concentrations,[84] or as gels.[86] Adding even a small amount of AzoMA depresses the phase separation temperature significantly – PAzoMA homopolymers are insoluble in common ionic liquids. For example, a 28 kDa PBzMA at 3 wt% in 1-ethyl-3-methyl imidazolium bis(trifluoromethanesulfonyl)imide (EMI TFSI) undergoes phase separation at 105 ºC.[59] For a 3 wt% solution of a BzMA/AzoMA copolymer with 4 mol% AzoMA incorporation reduced the phase separation temperature under visible light to 80 ºC.[84] The more polar *cis* isomer increases the solubility of the 4 mol% AzoMA polymer in the polar ionic liquid, bringing the phase separation temperature up to 102 ºC. This window is almost 3 times wider than the NIPAm/AzoMA polymer with double the AzoMA content. Ref. 84 reports that the maximum AzoMA content soluble in EMI TFSI is 4 mol%, but does not mention what other copolymer ratios were attempted, nor whether they tried any other ionic liquids.

To the author's knowledge, there have been no studies of BzMA/spiropyran copoly-

mers in ionic liquid. This work briefly discusses the case of spiropyran acrylate (SPA) copolymerized with BzMA at a single molecular weight, copolymer composition, and concentration. Spiropyran is strongly influenced by light, temperature, as well as the polarity of the solvent.[154] Due to the high LCST observed in BzMA and ionic liquid solutions, the temperature dominated the thermodynamics of isomerization over light irradiation.

For this work, BzMA/AzoMA (P(BzMA-*stat*-AzoMA) or B*s*A) copolymers are examined in more detail, exploring the phase separation temperature as a function of copolymer composition, molecular weight, and especially sample thickness. The LCST phase behavior is monitored using cloud point measurements, which gives the temperature at which the solution transitions from a homogeneous, clear mixture to a phase separated, turbid one. Although the cloud point does not correspond exactly to the coexistence curve (the binodal), it is closer than it is to the spinodal, and is a good measure of the LCST phase behavior at a given concentration.[52] The AzoMA and BzMA monomers are chemically similar, leading to reactivity ratios that are close to 1 (Figure 2.14). Thus, the monomers are distributed more evenly, making it less likely that the phase transition will broaden with increasing AzoMA content. This allows for investigation of a range of copolymer compositions, to examine whether the phase transition temperature window increases with increasing AzoMA content in this system. We found that increasing the AzoMA content decreases the solubility in EMI TFSI, however we were able to achieve dissolution of up to 6 mol% AzoMA, 2 mol% higher than previously studied.[84] To solubilize a copolymer with a higher AzoMA content, we used the ionic liquid 1-butyl-3-methyl imidazolium (BMI) TFSI. This increase in the alkyl chain length increases the solubility of the polymer in the ionic liquid, bringing the LCST above room temperature for polymers with AzoMA content up to 16 mol%. Changes in molecular weight may also impact the absolute temperature of the phase transition, as is the case with PNIPAm in ionic liquid.[62] We studied a range of copolymers from 17 kDa to 86 kDa to determine if molecular weight changes the phase separation properties under both visible and UV light.

Finally, sample thickness is a consideration for photoresponsive compounds. The strong absorbance of light drives the isomerization, but it can lead to inhomogeneity in light exposure.[185] If the sample is too thick, the light is only able to penetrate a short depth into

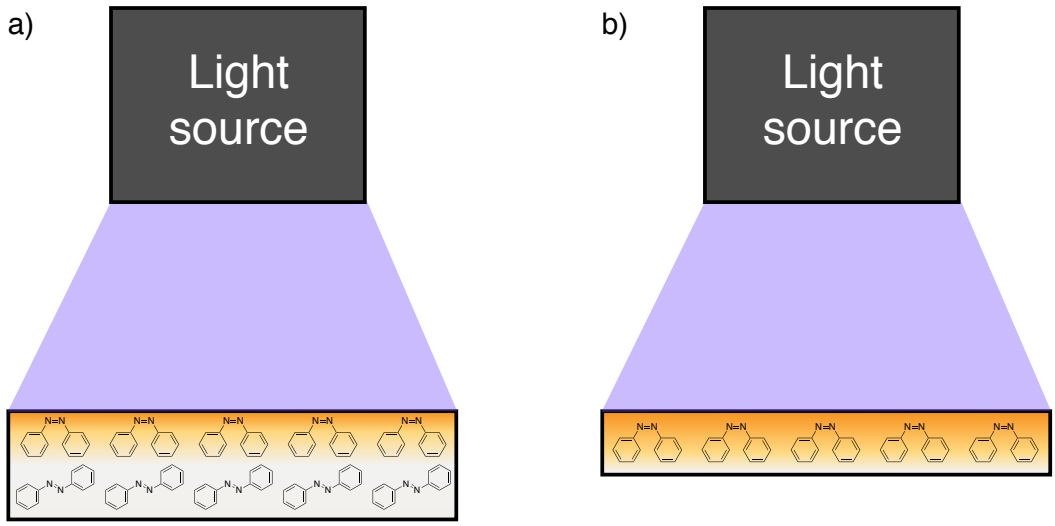

Figure 3.2: Illustration of how the absorbance of light by azobenzene in the polymer solution impacts the penetration depth of light through a) a thick sample and b) a thin sample. For thicker samples, only the surface of the solution is able to undergo *trans* to *cis* isomerization. The bulk still remains in the ground *trans* state.

the sample before it is entirely absorbed. This effect is illustrated by the cartoon in Figure 3.2, showing what isomers may be present in a thick sample versus a thin sample. Previous studies of both PNIPAm/AzoMA and BzMA/AzoMA copolymers focused on testing a single sample thickness of 200 μm. Understanding the sample thickness dependence on the phase separation behavior is crucial for extending these polymers to any potential applications. For each polymer examined here, a range of sample thicknesses was measured to investigate how significantly the absorption of the azobenzene chromophore impacts the measured phase transition temperature. We also estimated the penetration of UV light through the sample, and give a range for which samples would likely be thicker than the penetration depth.

3.3 Experimental

Materials

The P(BzMA-*stat*-AzoMA) and P(BzMA-*stat*-SPA) polymers were synthesized as described in Chapter 2. Ionic liquids were synthesized as described in Chapter 2. Stainless steel

washers were purchased from McMaster-Carr. Fischer Scientific microscope slides and coverslips were used. The polished aluminum plate used in the reflectance cloud point measurements was made in the machine shop using a 5 inch wide pipe of solid aluminum. A piece was cut the thickness of $\sim$3 inches, and two holes were drilled in the side to accommodate the cartridge heaters.

Sample preparation

All polymer/ionic liquid solutions were prepared using the cosolvent method. Polymer and ionic liquid were combined at the desired concentrations to achieve an overall mass of 5 g. THF was added to fully dissolve both polymer and ionic liquid, and the resulting solution was stirred overnight. The THF was removed by purging with nitrogen, and residual solvent was removed by drying in a vacuum oven at room temperature for 72 h. Room temperature was chosen to ensure that none of the samples would phase separate during the drying process.

Transmittance cloud point measurement

Transmittance cloud points were measured in two ways using home-built instruments. In an automated technique, a HeNe laser beam passes through the polymer solution contained in a round ampuole and onto a detector. The temperature of the sample is controlled by LabView software, both heating using cartridge heaters and monitoring the temperature of the heating block using a thermocouple. Thus the rate of temperature change can be precisely controlled and set as desired, typically 1 ºC/min. Cloud points are measured by a drop in transmittance of the laser beam, chosen as the point where 80% of the maximum value is reached. In the automated cloud point apparatus, the side of the sample perpendicular to the laser was covered by the heating block. To prevent blocking of the laser beam, the UV light was positioned at an angle to expose the side of the sample in the path of the laser.

Cloud points were also measured using a manually controlled setup, where the temperature of the sample was instead controlled using a hot plate equipped with an oil bath.

In this case, a HeNe laser was still employed, and the sample was contained in a quartz fluorescence cuvette. The fluorescence cuvette allows for the choice of path length of the cloud point measurement to be chosen as either 2 mm or 10 mm, and uses considerably less sample than ampules. The samples were concurrently irradiated with light during testing, using a lamp placed above the oil bath and aimed diagonally at the side of the cuvette. This setup is depicted in Figure 3.3

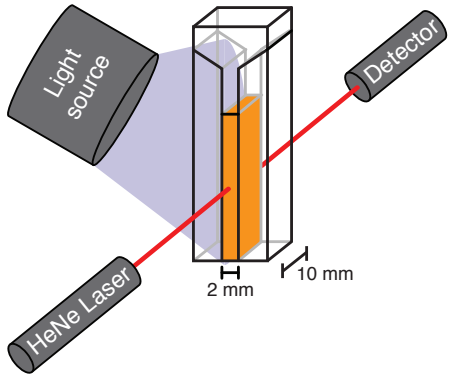

Figure 3.3: Transmittance cloud point setup, showing the sample contained in a cuvette, concurrent light irradiation at an angle, and path of the laser through the cuvette. Not depicted is the oil bath controlling the heat of the sample.

For visible light measurements, the samples were exposed for 10 min at room temperature, and the experiments were performed in the dark. For UV light measurements, the samples were exposed to the light for 1 h at room temperature, and the UV light remained on for the experiment. An hour ensures that the higher concentration samples are in the steady state – longer irradiation times did not have an effect on the cloud point. As the temperature was manually controlled using the hotplate, the rate of heating was less precise, but approximately 1 ºC/min.

Reflection cloud point measurement

Reflection cloud point measurements were performed in a similar manner to the transmittance measurements, both automated and manually. The samples were pipetted onto a microscope slide in the center of a stainless steel washer of a given thickness. A glass coverslip was placed over the sample, and the slides were sealed with epoxy. A HeNe laser was reflected down onto the sample using a mirror. When the sample is transparent, the

laser is transmitted through the sample and reflected from a polished aluminum plate up to another mirror, which directs the laser towards the detector. The desired illumination source was placed directly above the sample. This setup is depicted in Figure 3.4.

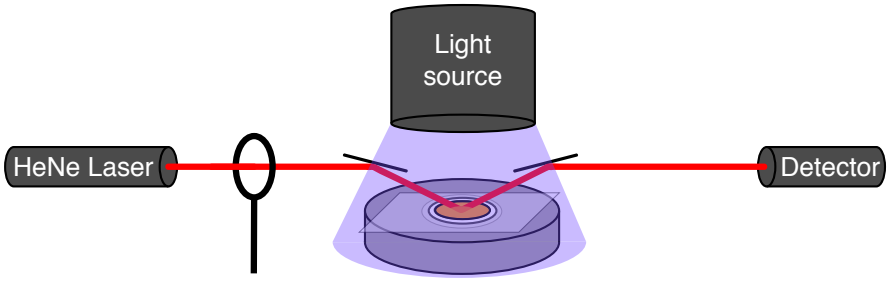

Figure 3.4: Reflection cloud point setup, with a HeNe laser passing through a shutter (shown as the open hoop), hitting a mirror and deflecting down through the sample. When the sample is clear, the laser transmits through to the polished aluminum plate, onto a second mirror, then to the detector. The light source is directly above the sample.

For visible light measurements, the samples were exposed for 10 min at room temperature, and the experiments were performed in the dark. For UV light measurements, the samples were exposed to the light for 1 h at room temperature, and the UV light remained on for the experiment. The samples were heated on the polished aluminum plate at a rate of 1 ºC/min. The temperature was recorded from a thermocouple secured to the top of the microscope slide, to ensure that the temperature reading is as close to sample temperature as possible. For the automated measurements, the temperature was controlled with the above mentioned LabView software and heating cartridges. For the manual measurements, the temperature was controlled with a hotplate. Due to the impact of the HeNe laser on the excited *cis* state of azobenzene, a shutter was implemented to reduce the total time the sample is exposed to the laser beam. In the automated setup, a motorized shutter controlled with an Arduino microcontroller reduces the exposure time of the laser on the sample, blocking the beam for 30 s then allowing for transmittance for 10 s. In the manual setup, a shutter was opened once every minute to obtain a reading on the detector, then shut. The cloud point was chosen as the point where transmittance is 80% of the maximum value achieved.

UV–vis spectroscopy

UV–vis spectroscopy was performed on a Shimadzu UV-1800 UV–vis spectrophotometer under ambient temperature conditions. The samples were measured in a quartz fluorescence cuvette, where the path length could be chosen as 10 mm or 2 mm. Due to the significant absorbance of azobenzene, the polymer solutions were all measured with a path length of 2 mm. EMI TFSI was used as a reference to obtain a solvent baseline.

3.4 Results

Transmittance cloud point

In both the manually controlled and automated transmittance cloud point experiments, the UV lamp was placed at an angle to the sample. UV power is a strong function of the distance of the lamp to the sample, and increasing the distance by a few centimeters can cause the power to drop by half. This creates difficulty with having the lamp expose the sample at an angle, as the lower portion of the sample will experience a lower UV power than the top of the sample. As an attempted proof-of-concept, the first tests were run on the automated setup. An example of a transmittance cloud point of 10 wt% B*s*A (17-6) in EMI TFSI taken under visible light and UV light is shown in Figure 3.5. For this sample,

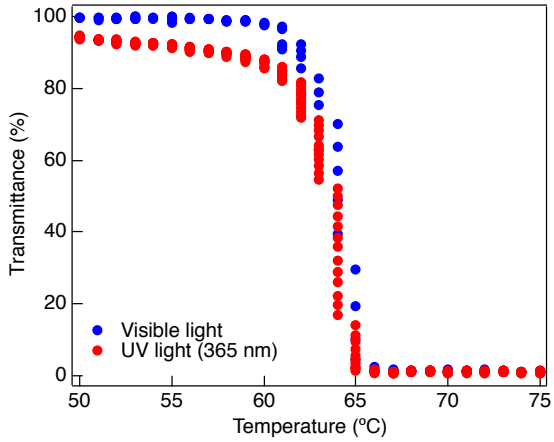

Figure 3.5: Transmittance cloud point of 10 wt% B*s*A (17-6) under visible (blue) and UV (red) light.

and all others tested, there was no discernible difference between the two cloud points. To determine if enough UV light was reaching the sample, a 0.1 wt% solution of B*s*A in EMI TFSI was placed in the setup and irradiated with UV light for a given amount of time. The sample was then tested via UV–vis spectroscopy to observe the isomerization state. As discussed in Chapter 2, the *cis* isomer is stable for hours at room temperature, so minimal thermal relaxation would be observed by removing the sample and transporting it to the spectrophotometer. The results are shown in Figure 3.6. In stark contrast to the results

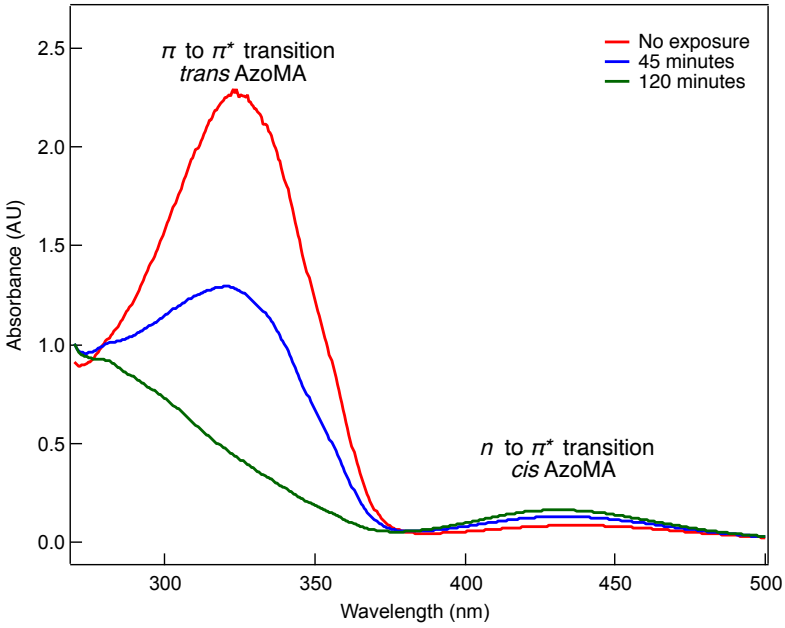

Figure 3.6: UV vis spectra of 0.1 wt% B*s*A (17-6) in EMI TFSI in the automated cloud point experimental setup with no UV light exposure (red), 45 minutes of exposure (blue), and 120 minutes of exposure (green).

found in Figure 2.16a where complete isomerization was achieved in $\sim$ 8 minutes for a sample of 0.2 wt% B*s*A (17-6), it takes 120 minutes to achieve full isomerization. This indicates that the sample was not getting enough UV power in the automated setup, and a new method of testing the light-dependent LCST phase behavior was needed.

In the automated setup, a majority of the sample was covered by the heating block. To better expose the full sample to UV light, the experimental setup was switched to manual temperature control using an oil bath. The 0.1 wt% solution was placed in the manually controlled setup, and the sample was exposed to UV light as depicted in Figure 3.3. With

this modification to the experimental setup, 60 minutes of exposure achieved full isomerization. This indicated that the problem of low UV power was resolved, so this setup was used to test the cloud point. A 1 wt% solution of B*s*A (17-6) showed a cloud point of 85

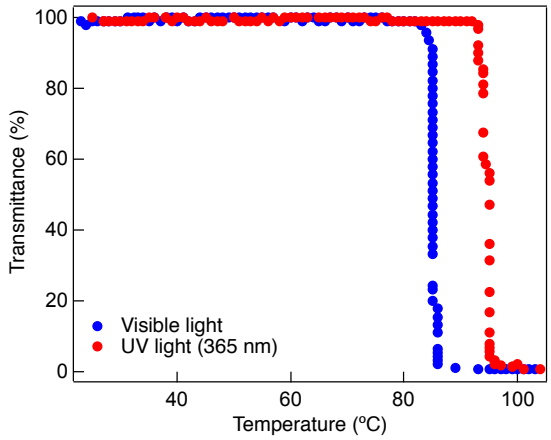

Figure 3.7: Manually controlled transmittance cloud point of 1 wt% B*s*A (17-6) in EMI TFSI under visible light (blue) and UV light (red).

ºC under visible light, and 94 ºC under UV light. These results are shown in Figure 3.7. These data suggested that the light-dependent cloud point of the B*s*A solutions could be measured using this experimental setup, so the concentration of the sample was increased to 10 wt%. With the increase in concentration, the visible light cloud point dropped to 65 ºC, in agreement with the temperature shown in Figure 3.5. Unfortunately, the cloud point under UV light was also measured at 65 ºC, giving the same results as the automated setup. With this result, it became clear that either the transmittance cloud point technique would not work, or that the polymer was not able to display light-dependent phase behavior at higher concentrations.

To test the hypothesis of the polymer not having a large enough change in solubility with light exposure, the P(BzMA-*stat*-SPA) with 2 mol% SPA incorporation described in Chapter 2 was tested for its photoresponsive properties. A 10 wt% solution of P(BzMA-*stat*-SPA) in EMI TFSI was exposed to UV light in the transmittance cloud point setup. The solution turned uniformly purple after 10 minutes, indicating the presence of the merocyanine isomer. There was no loss of color where the laser passed through the sample, indicating that the 633 nm HeNe laser was not impacting the isomerization state. The sam-

ple was irradiated for a further 30 minutes before beginning the cloud point experiment. Under UV light, the cloud point was measured as 85 ºC. The phase separated solution was no longer purple, instead was a dark yellow/orange. This did not necessarily indicate a change in the isomerization state of merocyanine back to spiropyran, as the color of merocyanine is strongly influenced by its chemical environment.[154] When the solution was tested under visible light, it phase separated at 85 ºC, and appeared the same color as the turbid sample under UV light. To determine if the lack of photoresponsive behavior was due to the sample itself, or a potential interaction with the HeNe laser at elevated temperatures, the sample was heated with UV light without the laser. The sample was visually observed using UV safety glasses, which gave the merocyanine isomer a faint orange glow and the ring-closed spiropyran showed no color. When the sample was heated to 50 ºC at a rate of 1 ºC/min, the color gradually faded from an orange to completely colorless despite the UV light . It remained colorless after 18 hours of continual UV irradiation at 50 ºC. When the sample was cooled back to room temperature while maintaining UV light exposure, the orange color returned. This indicates that the thermal isomerization from merocyanine to spiropyran dominates the light-driven spiropyran to merocyanine isomerization at elevated temperatures in the ionic liquid EMI TFSI. This precludes the use of spiropyran as a photoresponsive monomer with BzMA, unless an ionic liquid is chosen where the phase separation occurs at a temperature close to room temperature. Rather than investigating methods of decreasing the phase separation temperature for these copolymers, the azobenzene-based system was revisited.

Manually controlled reflection cloud point

Previous work investigating the light-dependent phase behavior of AzoMA copolymers with BzMA and NIPAm used a sample that was 200 μm thick.[84,85] This is one order of magnitude thinner than the 2 mm used in the transmittance experiments described above. Azobenzene is often used as a photoresponsive moiety in thin polymer films,[186,187] but only some publications suggest that this is necessary due to the high absorbance of azobenzene.[185,188] We found no report that systematically studied the effective penetration depth

of UV light through an azobenzene-containing sample.

To investigate if the absorbance of UV light by azobenzene was impacting the measured cloud point temperature, a reflectance cloud point experimental setup was designed. The manually controlled version, shown in Figure 3.4, was used to refine the experimental details. As the temperature control and data collection were both performed manually, the solution was under constant monitoring. This was immensely important in identifying issues with the setup that would have incorrectly indicated that the UV and visible light cloud points were the same. There were two cases requiring changes to the experiment, involving how sample thickness was defined and the interaction of the laser with the sample. Washers were purchased with a given height to define sample thickness. Originally, to reduce the heat lost between the aluminum plate and the sample, the washer was placed directly on the aluminum. The sample was pipetted in the center of the washer, and covered with a quartz disk. During the course of the cloud point measurement, spots of turbid solution would grow in, as shown in Figure 3.8. The spots grew as the temperature increased, and eventually the entire sample would become turbid. When the sample was held at a given

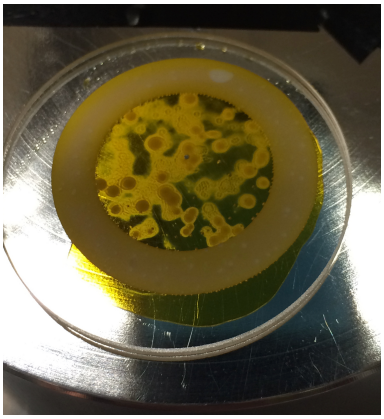

Figure 3.8: Spots appearing in the 10 wt% B*s*A (17-6) in EMI TFSI solution upon heating.

temperature for an extended period of time, the spots did not change at all, even after 24 hours. This indicated that the spot formation was not a nucleation of phase separation. The sample came into contact with two interfaces, aluminum and quartz. The wetting of these two interfaces could have a temperature dependence, so the sample preparation method was altered. The washer was placed on a microscope slide, the sample pipetted into the center, then covered with a glass coverslip and sealed with epoxy. With this method, the sample no

longer formed spots on heating. It is likely that the spot formation was due to some form of dewetting from one of the surfaces. The new sample preparation method also sealed the sample from air, preventing any moisture from interfering with the measurement.

The second issue noted with the reflectance cloud point measurement was related to the interaction of the HeNe laser with the sample. Under visible light and under UV light at temperatures below the visible light cloud point, the laser had no impact on the sample. With respect to Figure 3.1, this is the one phase region. However, samples under UV light at temperatures above the visible light cloud point would form a small spot where the laser hit the sample. In Figure 3.1, this is the shaded grey bistable window. The remaining sample would remain clear until the UV light cloud point was passed, reaching the two phase window for both wavelengths of light. Given that the spot only appeared in the bistable window, it appeared that the laser was causing *cis* to *trans* isomerization. The UV vis spectrum of these polymers were completely flat at 633 nm, so absorbance of the HeNe laser was unexpected. However, it has been documented that HeNe lasers can drive *cis* to *trans* isomerization in other azobenzenes tethered to a polymer chain.[189] To reduce the impact of the laser wavelength on the sample, a shutter was added. The shutter was only opened at a given temperature to record a measurement, then manually shut again. After this addition to the experimental setup, a visible spot no longer formed where the laser hit the sample.

Once these issues were resolved, this setup was used to confirm that the visible light cloud point and UV light cloud point were in fact different, and did have a dependence on sample thickness. However, due to poor control over the rate of change of temperature and the time-intensive nature of manually controlling the shutter and temperature as well as recording all of the data, the experiment was automated. This allowed for multiple polymers to be rapidly investigated at a variety of sample thicknesses.

Automated reflection cloud point measurements

To investigate the effect of molecular weight on the light-dependent phase behavior, a series of three B*s*A polymers were tested – 17 kDa, 35 kDa, and 86 kDa, all with 6 mol%

AzoMA incorporation. The UCST phase behavior of PNIPAm in ionic liquid shows a molecular weight dependence,[61] while the LCST of PNIPAm in water does not change significantly with molecular weight.[63] These polymers were tested at 10 wt% in EMI TFSI. Concentrations below the overlap concentration of the polymer, ca. 5 wt% for BsA (35-6), were too dilute to reliably detect a cloud point in the thin film geometry. Concentrations up to 20 wt% were soluble in EMI TFSI; higher concentrations produced turbid solutions at room temperature. 10 wt% was chosen as the respresentative concentration due to ease of sample preparation over the significantly more viscous 20 wt%.

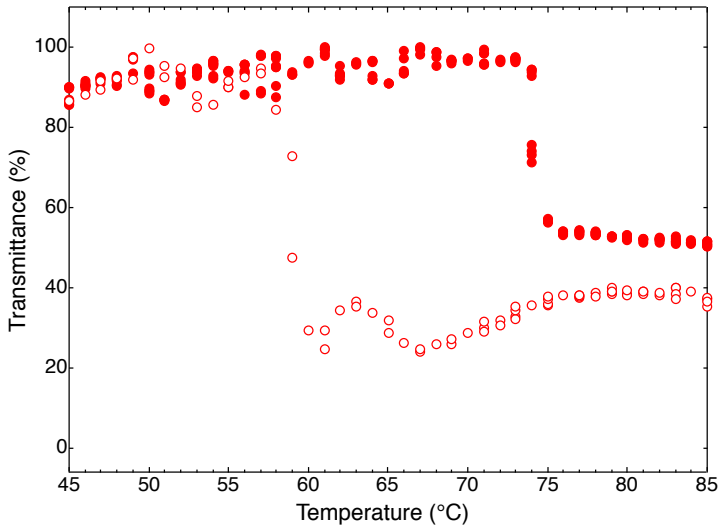

Figure 3.9: Representative cloud points of 10 wt% BsA (35-6) in EMI TFSI under UV (closed symbols) and visible light (open symbols) at a thickness of 100 µm.

The reflection geometry used for these cloud point measurements was designed to have the laser reflect from a polished aluminum plate when the sample is homogeneously mixed. However, there are also reflections that can occur at the various interfaces (glass-air, coverslip-sample) that can give rise to a measured laser power even when the sample is turbid. As a result, the samples typically never reached 0% transmittance after phase separation occurred. Similarly, each sample will have a different minimum in transmittance. A representative cloud point for BsA (35-6) at 100 µm thick is shown in Figure 3.9, where the clear drop in transmittance indicates the cloud point. The cloud point temperature is taken as 80% transmittance, scaled to the initial and final transmittance values. As previously demonstrated,[84] the more polar *cis* isomer increases the solubility of the polymer under

UV light, giving a cloud point approximately 15 ºC higher than under visible light.

Each polymer was measured across a range of sample thicknesses from 25 to 1500 µm. The results are shown in Figure 3.10. The cloud point under visible light, shown in open

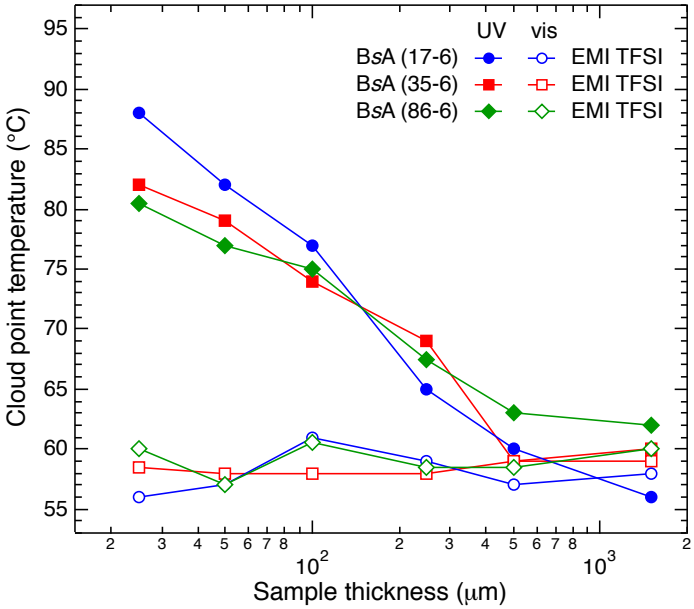

Figure 3.10: The cloud point temperature (ºC) of 10 wt% solutions in EMI TFSI of B*s*A (17-6), blue circles, (35-6), red squares, and (86-6), green diamonds, under UV light (closed symbols) and visible light (open symbols) as a function of sample thickness (µm).

symbols, is independent of sample thickness. Under these conditions the sample is in the *trans* ground state; the 420 nm LED serves to drive any *cis* isomers formed from ambient UV light back to the ground state. The UV light cloud points, in contrast, show a substantial dependence on sample thickness, as expected. For both 1500 µm and 500 µm, the UV cloud points occur at approximately the same temperature as under visible light. For these samples, the surface layer that is isomerized by the UV light before it is absorbed is small in comparison to the bulk. Once the visible light phase transition temperature is reached, the bulk will become turbid, giving the same cloud point as under visible light. As the samples become thinner, the visible and UV light phase separation temperatures diverge, as the sample thickness approaches the penetration depth of the UV light. Increasing the window between the two cloud points allows for more reliable light-triggered phase separation – minor temperature fluctuations, such as increased heat from turning on a UV lamp, will not change the temperature enough to move outside of the window.

The impact of changing copolymer composition was also investigated, by looking at a 10 wt% solution of B*s*A (28-17) in BMI TFSI. BMI TFSI was used as the polymer was insoluble in EMI TFSI at room temperature. To keep as many variables constant as possible, this was compared to B*s*A (35-6), which has the most similar molecular weight. B*s*A (35-6) was tested in BMI TFSI as well, but the cloud point setup does not give accurate measurements above ~100 ºC. The cloud points measured for all thicknesses of 10 wt% B*s*A (35-6) in BMI TFSI under both UV and visible light were between 100 and 105 ºC. Due to this, the comparison between 6 mol% and 16 mol% AzoMA incorporation was with B*s*A (35-6) in EMI TFSI, shown in Figure 3.11. The most important factor is the difference

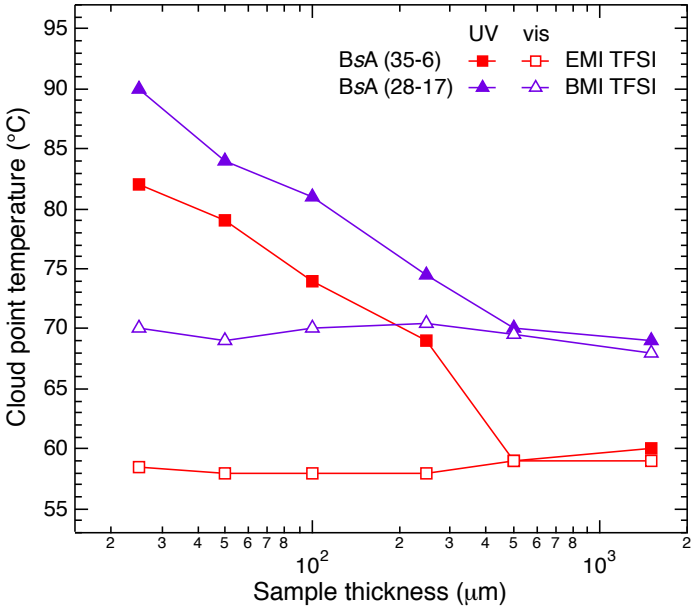

Figure 3.11: The cloud point temperature (ºC) of 10 wt% solutions in EMI TFSI of B*s*A (28-17), purple triangles, and (35-6), red squares, under UV light (closed symbols) and visible light (open symbols) as a function of sample thickness (μm).

between the UV and visible light cloud points for the individual polymers, which should not be impacted by the small change in ionic liquid. Previous studies have shown that the LCST phase behavior of poly(ethylene oxide) can be tuned by mixing the ionic liquids EMI BF_4 and BMI BF_4.[53] The measured LCST increases linearly with increasing BMI BF_4 content, indicating both that the change in cation alkyl chain length is not changing the fundamental interactions between the polymer and the solvent.

The effects of increasing the AzoMA content in the copolymer did not follow the ex-

pected trend. In a range of compositions of P(NIPAm-stat-AzoMA) copolymers in ionic liquid, it was previously found that increasing the AzoMA content increased the window between the phase separation temperatures under UV and visible light.[84] In contrast, Figure 3.11 shows that the window is virtually the same.

3.5 Discussion

Absorption of UV light by azobenzene

Based on both Figure 3.10 and 3.11, it is not surprising that the transmittance cloud point measurements did not yield a difference between UV and visible light. The 2 mm sample thickness in the transmittance measurements is larger than the thickest sample tested, which showed no difference for all tested polymers. The absorbance of UV light in the AzoMA monomer enables the *trans* to *cis* isomerization that changes the solubility of the polymer in ionic liquid, but it also means that the UV light has a finite penetration depth through the sample. Figure 3.12 shows the UV-vis spectrum for 0.02 wt% B*s*A (28-17) in BMI TFSI. The trans isomer has a strong absorbance in the UV region, even at a low concentration and a path length of 2 mm. Figure 3.12 has both the peak absorbance and the absorbance at 365 nm marked. While intuitively it would make sense to use a wavelength at the peak absorbance, the light will not be able to travel through as much of the sample. This effect was observed when using a 320 nm UV LED, which took significantly longer to achieve isomerization, and did not reach the same baseline as the mercury arc handheld UV lamp. By irradiating with a wavelength still in the UV absorbance peak, but as a point where the sample absorbance is significantly lower, the light has a greater impact on the sample. Regardless of the wavelength chosen, the strong absorbance is clear, which gave rise to the sample-thickness dependence of the cloud point under UV light.

Notably, the difference between the UV and visible light phase separation temperatures do not reach a plateau. This suggests that the penetration depth is still less than 25 μm for these samples. Due to signal limitations, this reflection setup was not able to measure below 25 μm. To determine whether $<$25 μm is reasonable, a penetration depth can be estimated

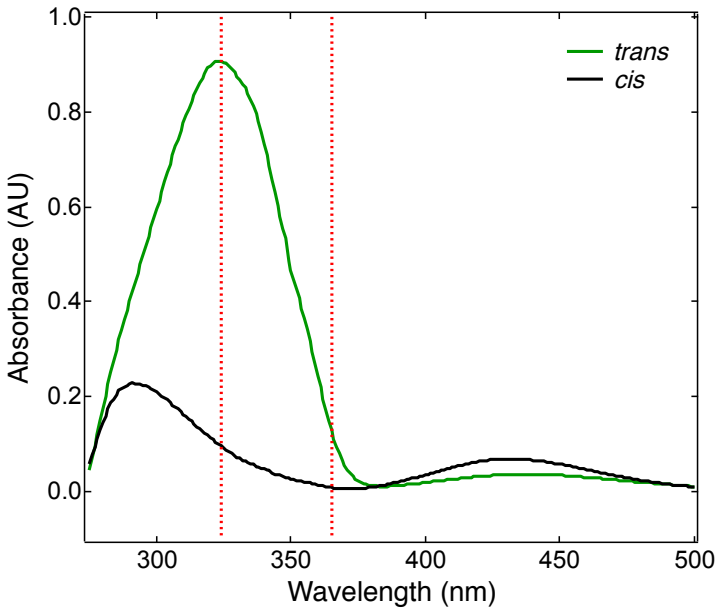

Figure 3.12: 0.02 wt% solution of B*s*A (28-17) in BMI TFSI in the steady state for *trans* (green) and *cis* (black). The red dotted lines correspond to the maximum absorbance of the *trans* isomer and the peak output of the UV lamp, 365 nm.

based on the molar extinction coefficient obtained from UV–vis spectrophotometry using Beer's law:

$$A = \epsilon c l \tag{3.1}$$

where A is the absorbance at a given wavelength, ϵ is the extinction coefficient, c is the concentration, and l is the path length. The absorbance is obtained from the UV–vis spectrum, the concentration is known, and the path length for all measurements was 2 mm. With this, ϵ can be calculated at a given wavelength. The molar extinction coefficient has units of $(\text{mm}\cdot\text{wt\%})^{-1}$, which can be used to estimate a penetration depth, δ_p for a given concentration:

$$\delta_p = \frac{1}{\epsilon c} \tag{3.2}$$

This can be done at 324 nm, the maximum of absorbance in the UV region, as well as at 365 nm, the peak output of the UV lamp utilized. The output of the UV lamp is centered at 365 nm, however the filter does not fully cut out shorter wavelength UV light, thus the true penetration depth likely falls between these two. For both wavelengths, the extinction coefficient depends on the isomerization state of the AzoMA, where the trans isomer has a

higher absorptivity than the cis. As the surface is exposed to UV light, the isomerization of the surface to cis will increase the penetration depth. Therefore, the estimated penetration depth is expressed as a range for each polymer.

For BsA (17-6), the penetration depth for a 10 wt% solution in EMI TFSI was estimated as 10–90 μm at 324 nm and 80–600 μm at 365 nm. Overall, this gives a range of 10–600 μm. As the azobenzene content is constant for all molecular weights, the penetration depths for all three polymers with 6 mol% AzoMA incorporation should be the same. Given these ranges, it is not unreasonable to assume that the samples are still thicker than the penetration depth of UV light, even at 25 μm. The penetration depth for a 10 wt% solution of BsA (28-17) in BMI TFSI was estimated as 4–40 μm at 324 nm and 30–450 μm at 365 nm. This gives an overall range of 4–450 μm, again making it reasonable that the samples were thicker than the penetration depth of light. This range is also significantly reduced from the penetration depths for the 6 mol% AzoMA incorporation polymers. As a result, the sample thicknesses accessible for the reflective cloud point measurements are further from reaching full penetration of UV light for BsA (28-17). If the samples were able to be tested at thicknesses equal to or less than the penetration depth of the UV light, BsA (28-17) would likely show the largest cloud point temperature window. In increasing the AzoMA content, it is expected that a larger polarity change will be induced in the polymer sample. This larger change in polarity should lead to a bigger difference between the visible and UV light phase separation temperatures. However, due to the decrease in penetration depth, a smaller portion of the 25 μm sample underwent *trans* to *cis* isomerization, giving a temperature window similar to the samples with a third less photoresponsive monomer.

Dependence of the cloud point on molecular weight and copolymer composition

There is no significant dependence on molecular weight for the cloud points under visible light. Under UV light, there is possibly a minor molecular weight dependence for the two thinnest samples, where the lowest molecular weight has the widest temperature window between UV and visible light phase separation. By plotting the cloud point temperatures

as a function of molecular weight, as shown in Figure 3.13, this is easily visualized. The

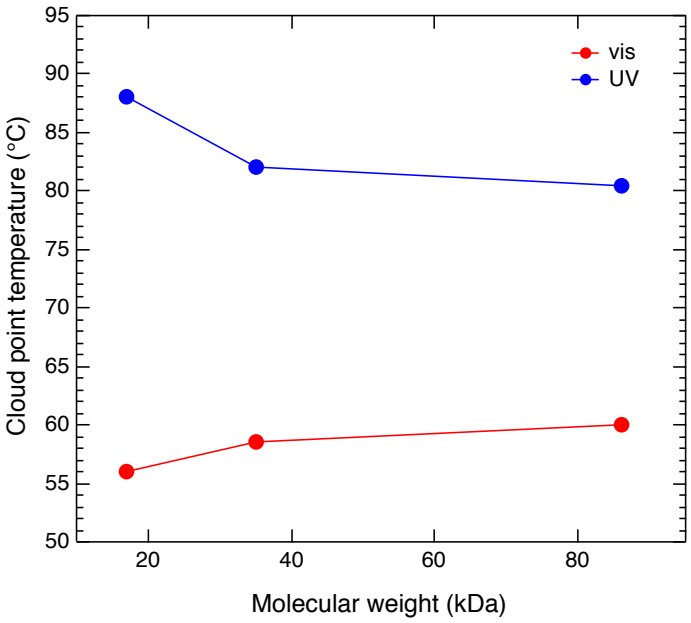

Figure 3.13: The cloud point temperature (ºC) as a function of molecular weight of 10 wt% solutions of polymer under UV (blue) and visible (red) light at a sample thickness of 25 µm.

lowest molecular weight showed a broadened bistable window, which may be a result of higher chain mobility for the shorter polymer chains. This would allow some of the isomerized AzoMA chains under UV light near the surface to move further in the sample, giving a higher phase separation temperature under UV light only. This effect seems to impact the sample only at 100 µm or less and the difference decreases at the thickness increases, which supports the theory of higher mobility. Diffusion of polymer chains would be more significant at smaller lengthscales, where in the thicker samples that small additional depth of *cis* isomers would have less of an impact. There is minimal difference for the other two molecular weights. Under visible light, the cloud point does not change significantly with increasing molecular weight. In general, therefore, the data are consistent with the conclusion that the cloud points are independent of molecular weight. This follows expectation for polymer/solvent systems that have LCST phase behavior such as PNIPAm in water, which has an LCST of ca. 32 ºC across a range of molecular weights.[63]

All four polymers show a similar trend with respect to sample thickness, and all can achieve a bistable window of 20 – 30 ºC, as shown in Figure 3.14. In general, BsA (28-17)

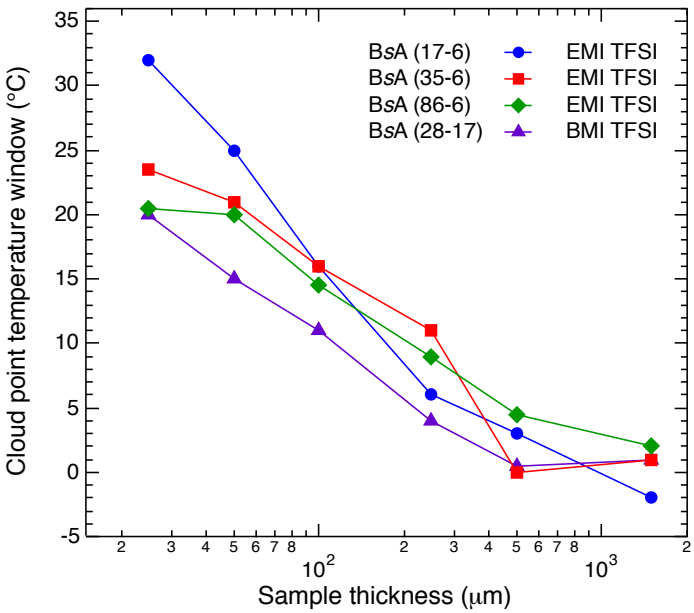

Figure 3.14

shows the narrowest window, with BsA (35-6) and BsA (86-6) being very similar to each other and having a slightly broader window. These two polymers can both be compared with BsA (28-17) in different ways – BsA (35-6) has a similar molecular weight, and BsA (86-6) has the same average number of AzoMA molecules per single polymer chain. As the samples have not reached the thickness equal to or less than the penetration depth of UV light, we cannot state definitively which of these variables matters more in allowing the two polymers with 6 mol% AzoMA incorporation to have a larger cloud point temperature window. Finally, the smallest molecular weight chain BsA (17-6) shows the broadest temperature window for the two thinnest samples tested, potentially as a result of diffusional mixing.

3.6 Conclusions

Light-responsive polymers change properties based on their absorption of light. This absorbance can lead to issues where only the sample surface shows a change in properties, and for sufficiently thick samples, this may lead to a lack of light-responsiveness entirely. There light-responsive molecules are also typically responsive to both light and tempera-

ture, which can lead to competing isomerization pathways. Attempted transmission cloud point measurements to detect the LCST phase behavior of a thermo- and photoresponsive solution of B*s*A in EMI TFSI showed that these samples were too thick to show different cloud points under UV or visible light. We also demonstrated that spiropyran undergoes thermal relaxation from the zwitterionic merocyanine species back to the spiropyran ground state, even with constant UV irradiation driving the spiropyran to merocyanine isomerization.

A new method for readily varying the sample thickness in cloud point measurements was developed. This setup allowed for the screening of the phase separation behavior of four thermo- and photoresponsive copolymers under a range of six sample thicknesses, from 25 μm to 1500 μm. Studying the effect of sample thickness gives an idea of how thin the samples need to be to approach full penetration of UV light through the sample. This was not achieved for any of the samples, even at 25 μm, as evidenced by a continuing increase in the window between the phase separation temperatures under UV and visible light. However, even without full penetration of the UV light, windows as large as 20–30 ºC were measured. This temperature difference is large enough to envision using poly(BzMA-*stat*-AzoMA) copolymers for further work in photoresponsive systems, such as light-induced micellization and gel network formation. The lack of molecular weight dependence in the phase separation temperature is also favorable for these applications. By knowing the phase separation temperature of a poly(BzMA-*stat*-AzoMA) copolymer at the concentration used, the bistable window for triggering micellization or gelation with light can be predicted. Target copolymer compositions can maintain low AzoMA content, and still have a broad temperature window for triggering as well. The less AzoMA that is necessary, the less "specialty" monomer needed. This also increases the likelihood that samples on the order of hundreds of nanometers thick will enable full penetration of UV light.

The previous work on the BzMA/AzoMA copolymers used only EMI TFSI, and as such was unable to get copolymers with compositions higher than 4 mol% AzoMA to dissolve in the ionic liquid. This study shows that significantly higher compositions are possible. Additionally, heating rate may play an effect on the cloud point temperature window. Ref.

84 used a heating rate of 0.1 ºC/min, an order of magnitude less than what was used for these tests. While the slower heating rate may allow for a more precise determination of the phase separation temperature, it also drastically increases the experiment time per sample. As mentioned in the introduction, the cloud point temperature is close to the binodal, so phase separation is expected to be minimally impacted by nucleation and growth. Thus heating rate should not have a significant impact on the measured cloud point, as long as it is reasonably slow.

3.7 Acknowledgments

This work was supported by the National Science Foundation through Award DMR-1707578. Thanks to Prof. Jennifer Laaser and Peter Schmidt for help putting together the home-built cloud point setups. Thanks to Prof. Marc Hillmyer for the use of his lab's UV–vis spectrometer.

Chapter 4

Controlling the morphology of a photoresponsive block polymer in an ionic liquid with light[i]

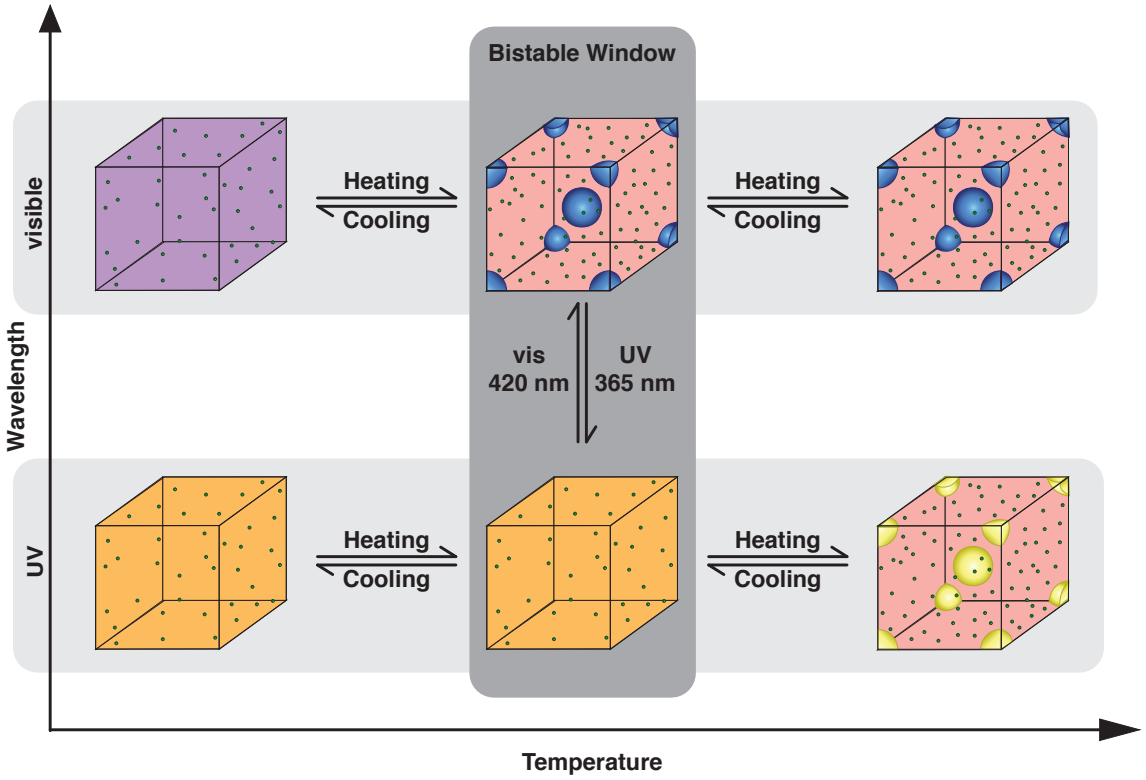

[i]This work was done in collaboration with Cecelia Rivera.

4.1 Introduction

Controlling the nanoscale ordering of block polymers has been extensively studied for many years, both in the bulk[26,28] and in solution.[42–44,65,70] The morphology of a bulk block polymer can be altered by changing the relative sizes of the blocks, changing the identity of the blocks themselves, or by changing temperature. The addition of solvent can allow for greater changes in the available morphologies for a block polymer of a given composition, and structure can also be tuned by choosing a neutral vs a selective solvent.[42–44,65,70] In all cases, to obtain an order-disorder or order-order phase transition, the system must be chemically or physically altered. The incorporation of a light-responsive moiety in the block polymer backbone may enable light-triggered phase transitions.

The use of azobenzene to control the ordering of liquid crystals has been extensively studied. Incorporation of azobenzene into liquid crystals, polymeric or otherwise, has been shown to enable photoinduced optical anisotropy.[18,190,191 192] The azobenzene can also be used to induce alignment of the liquid crystals.[193,194] This has been applied for use in optical switching, as well as image storage.[195–198] The reversibility of azobenzene isomerization makes it ideal for applications; the lack of a degradation pathway allows for reversible writing of images, as well as cycling for use in switches. The used of polarized light can also induce macroscopic flow of polymer films to generate surface relief gratings.[199] This work has recently extended to the use of azobenzene-containing liquid crystals in block polymers. The ability of the azobenzene moiety to drive alignment in the liquid crystal phase allows for macroscopic alignment of the block polymer as a whole.[90–93] In some cases, irradiation of these block polymers with UV light can induce a transition from an ordered phase, such as nematic, to a disordered phase.[96–98]

While there have been many studies of light-induced order-disorder transitions in azobenzene-containing liquid crystal block polymers, the exploration of azobenzene-containing amorphous "coil-coil" block polymers has not been as extensive. The use of azobenzene in the endblocks of an ABA triblock as a Langmuir-Blodgett layer has been able to produce an order-order phase transition.[94,95] However, this transition is not fully reversible, and requires a high amount of humidity. It is likely that water swells the film, and the

isomerization induces a change in the ordered morphology by either taking up water in the polar *cis* state, or excluding it in the non-polar *trans* state. Another study incorporated azobenzene in the poly(*n*-butyl methacrylate) block of a polystyrene-*block*-poly(*n*-butyl methacrylate) polymer.[183] They studied the phase behavior, including the lower critical ordering transition, LCOT. This is analogous to the LCST phase behavior observed in homopolymers, where phase separation occurs on heating. In the case of the LCOT, ordering occurs on heating. The author observed that they could bring the system close to the LCOT, however they did not achieve it. They also observed that the degree of ordering was light-dependent, as expected with the incorporation of azobenzene. Some work has also been done on blending polymers with additives to achieve ordering with light.[200]

To circumvent the reversibility issues seen in Refs. 94 and 95, the light-responsive block polymer could be combined with a solvent. This would allow the isomerization of azobenzene to control the selectivity of the solvent, and thus drive order-order or order-disorder phase transitions in solution. A related idea has been explored in dilute solution, through controlling the micellization and demicellization of a block polymer in ionic liquid using light.[87] This work has also been extended to an ABA system, where gelation can be controlled with light,[88] and the gel is capable of self-healing when irradiated with UV light.[89] These studies have not explored polymers at higher concentrations to access the traditional block polymer ordered morphologies.

This work uses a block polymer composed of poly(methyl methacrylate) (PMMA, M) and poly(benzyl methacrylate-*stat*-(4-phenylazophenyl methacrylate)) (P(BzMA-*stat*-AzoMA), B*s*A). The PMMA block is fully soluble in the ionic liquid EMI TFSI. As discussed in Chapter 3, B*s*A shows light-dependent lower critical solution temperature (LCST) phase behavior. Thus at low temperatures, EMI TFSI will act as a neutral solvent, dissolving both blocks. Increasing the temperature will induce an LCOT, driving the EMI TFSI out of the B*s*A blocks. We explored the phase behavior of this block polymer as a function of polymer architecture, azobenzene content, and concentration in ionic liquid. At higher concentrations, the block polymers form the traditional ordered phases such as lamellae and hexagonally packed cylinders. Low concentrations, below 40 wt%, show LCOTs with a transition from disorder to either weakly ordered spheres or a coexistence of hexagonally

packed spheres and face centered cubic spheres. These LCOTs were observed thermally using small angle X-ray scattering, and were able to be controlled using light as observed using rheology. The solutions were reversibly triggered between order and disorder, either by switching between UV and visible light, or UV light and allowing the azobenzene to thermally relax to the ground state. The ability to use light to control the morphology arises from this LCOT phase behavior. The ordering upon heating is due to a change in the solubility of the polymer in the solvent, which can be modified by changing the isomerization state of azobenzene. The *cis* state under UV light is more polar, increasing the solubility in polar EMI TFSI. Thus the ordered structure formed under visible light can be dissolved by UV light.

The ability to trigger an order-disorder phase transition with light could enable the use of these ionic liquid/block polymer solutions as adhesives. Homopolymers of azobenzene-based monomers have been shown to act as adhesives under visible light, and transition to a liquid-like state upon UV irradiation, allowing for easy removal of the adhesive.[201] The use of azobenzene in the hard block of a thermoplastic elastomer has been shown to enable control of the plasticity of the elastomer with light.[188] Combining these two concepts, the use of an azobenzene-containing block polymer as a thermoplastic elastomer could be used in adhesive applications.

4.2 Experimental

Materials

4-Cyano-4-[(dodecylsulfanylthiocarbonyl) sulfanyl] pentanoic acid, tris (2-carboxyethyl) phosphate hydrochloride, *n*-propylamine, methyl acrylate, and 4,4'-azobis (4-cyanovaleric acid) were used as purchased from Sigma Aldrich. Methyl methacrylate and benzyl methacrylate were purchased from Sigma Aldrich and the radical inhibitors were removed by running through a neutral alumina column. The ionic liquids EMI TFSI and BMI TFSI were synthesized as discussed in Chapter 2.

Block polymer synthesis

Block polymers were synthesized through sequential RAFT polymerization, followed by cleavage of the chain transfer agent to improve thermal stability. In a representative synthesis, the PMMA block was synthesized by combining methyl methacrylate (115.8 mmol, 333 eq), 4-cyano-4-[(dodecylsulfanylthiocarbonyl)sulfanyl]pentanoic acid (0.35 mmol, 1 eq), and 4,4'-azobis(4-cyanovaleric acid) (0.035 mmol, 0.1 eq) in a Schlenk flask with 46 mL of dioxane. The reaction was degassed through three freeze-pump-thaw cycles, and then placed in a 75 ºC oil bath with stirring and allowed to proceed for 12 hours. The reaction was quenched to 0 ºC in ice water to halt the polymerization. The resulting polymer was purified by precipitation three times, using dichloromethane as a good solvent and hexanes as a poor solvent. The resulting polymer was characterized using size exclusion chromatography (SEC) and ^{1}H NMR spectroscopy.

To ensure that the PMMA-CTA was fully functionalized with chain transfer agent, a small-scale test polymerization with BzMA and AzoMA was run. Once it was confirmed that polymerization of a second block did not show a significant population of dead chains based on size exclusion chromatography (SEC), the polymerization was scaled up. In a representative synthesis, PMMA-CTA (0.062 mmol, 1 eq), BzMA (10.6 mmol, 171 eq), AzoMA (1.18 mmol, 19 eq), and 4,4'-azobis(4-cyanovaleric acid) (0.0062 mmol, 0.1 eq) were combined in a Schlenk flask with 11 mL of dioxane. This mixture was degassed through three freeze-pump-thaw cycles, then placed in a 75 ºC oil bath with stirring and allowed to proceed for 18 hours. The reaction was quenched to 0 ºC, then purified by precipitation three times, using dichloromethane as a good solvent and hexanes as a poor solvent. The resulting polymer was characterized using size exclusion chromatography (SEC) and ^{1}H NMR spectroscopy.

The chain transfer agent was cleaved from the PMMA-*b*-P(BzMA-*stat*-AzoMA), M(B*s*A), via aminolysis and Michael addition of methyl acrylate. In a representative synthesis, M(B*s*A)-CTA (0.52 mmol, 1 eq) was dissolved in 200 mL of THF in a roundbottom flask. Tris (2-carboxyethyl) phosphate hydrochloride (0.79 mmol, 1.5 eq) was dissolved in 2 mL deionized H_2O, then added to the reaction vessel. The reaction was degassed with argon for

15 minutes, then *n*-propylamine (26.2 mmol, 50 eq) was added. The reaction was allowed to stir for 5 hours, then methyl acrylate (91.7 mmol, 175 eq) was added. The mixture was stirred for 12 hours at room temperature, after which the THF was removed by rotory evaporation. The polymer was purified by precipitation three times, using dichloromethane as a good solvent and hexanes as a poor solvent. The resulting polymer was characterized using size exclusion chromatography and ^{1}H NMR spectroscopy to ensure that the CTA was fully removed and the molecular weight distribution remained the same. CTA removal could not be quantified by UV-vis spectroscopy due to the overlap of AzoMA and CTA absorbances.

Polymer characterization

Proton nuclear magnetic resonance (^{1}H NMR) spectra of the polymers were collected using a 500 MHz Bruker Avance II spectrometer, with deuterated chloroform as a solvent. The molecular weight distributions were analyzed using size exclusion chromatography (SEC) paired with refractive index and light scattering detectors, with tetrahydrofuran (THF) as the eluent. The dn/dc for the copolymers was determined as discussed in Chapter 2, based on the measured dn/dc of PAzoMA, 0.259 mL/g, and the literature values for PBzMA, 0.144 mL/g,[165] and PMMA, 0.089 mL/g.[202] Thermogravimetric analysis was performed on a TA Instruments Q500 using a temperature ramp rate of 10 ºC/min, under an inert nitrogen atmosphere. Differential scanning calorimetry was performed using a TA Instruments Q1000 DSC. Samples ∼5-10 mg were loaded into DSC pans, and hermetically sealed. The samples were heated from –20 ºC to 220 ºC at a rate of 10 ºC/min, held for 5 minutes at 220 ºC, then cooled back to –20 ºC at the same rate. The heating cycle was repeated, and the glass transition temperature (T_g) was obtained from the second heating.

Sample preparation

Polymer in ionic liquid samples were prepared via the cosolvent method. The ionic liquids EMI TFSI and BMI TFSI were dried in a vacuum oven at 70 ºC for 24 hours prior to sample preparation. The polymer and ionic liquid were combined at the desired concentration, and

THF was added as a cosolvent to achieve full dissolution of all components. The solution was mixed for 24 hours to ensure homogeneity of the mixture, then filtered through a 45 μm syringe tip filter. The THF was removed by purging with N_2 gas while stirring. The polymer in ionic liquid solution was dried in a vacuum oven at 100 ºC for 48 hours to remove any residual THF.

Small amplitude oscillatory shear rheology

Small amplitude oscillatory shear measurements were performed on a TA Instruments Discovery HR3 rheometer, equipped with a 40 mm electrically heated upper plate, and a 20 mm quartz lower plate. The quartz lower plate is a component of a UV curing tool set, where light is exposed to the bottom face of the sample through a light guide originating in an OmniCure S1500 mercury arc lamp. The light is filtered to the desired wavelength range, either 365 or 400–500 nm, to produce UV or visible light, respectively. The power of the lamp can be controlled via TRIOS software by inputting a percentage of the lamp power, and measuring the UV light output. All measurements were performed with 10 or 50 mW/cm^2. During the measurements, the metal cover on the electrically heated upper plate was lowered to preserve the sample under a nitrogen atmosphere, block ambient light from impacting the measurement, and shield the operator from the UV light. The samples were measured with a gap of $\sim$200 μm.

Strain sweep measurements were performed on all samples to determine the linear viscoelastic regime, and to ensure that the strain was high enough to generate a signal. The loss modulus, G'', and storage modulus, G', were measured as a function of strain from 0.1 to 10 % strain, with a frequency of 1 rad/s. The linear viscoelastic regime is defined as the range of strains for which the modulus remains constant. For all samples discussed, a strain of 1% was used to remain in this regime. Frequency sweep measurements were performed at a constant temperature to give information about the morphology at that temperature. Samples were measured from 1 to 100 rad/s with 1% strain at a constant temperature. The scaling of G' and G'' with respect to frequency gives information about structure within the sample. Temperature sweeps measurements heated or cooled the sample from 30 ºC to 150

ºC (the limit of the UV cure accessory), at a rate of 3 ºC/min, with a strain of 1% and a frequency of 1 rad/s. Dramatic changes in modulus with respect to temperature, accompanied by a crossover of G' and G'', indicate an order-disorder phase transition. Temperature sweeps were performed both in the dark and with UV light exposure.

Time sweeps at a set temperature were performed to trigger order-disorder phase transitions using light. Samples were annealed for 30 minutes, then the UV light was switched on. Switching was performed either by turning the UV light off and monitoring the thermal relaxation, or by changing the filter from 365 nm to 400–500 nm. All time sweeps were performed with 1% strain and a frequency of 1 rad/s.

Small angle X-ray scattering

Small angle X-ray scattering was performed at the 5-ID-D beamline at Argonne National Labs. Samples with concentrations 40 wt% and below were loaded in quartz capillaries by loading small amounts of the highly viscous liquid in the top of the capillary, then centrifuging until the sample reached the bottom. This was repeated until the capillaries were approximately half full. Samples with concentrations above 40 wt% were prepared in DSC pans. The samples were dissolved in an equal volume of THF, then pipetted into the bottom of a DSC pan. The pans were placed on a hot plate to evaporate the THF. Additional THF was added to remove bubbles in samples, and this process was repeated until a uniform film was formed across the bottom of the DSC pan. All samples, capillaries and DSC pans, were placed in a vacuum oven at 100 ºC for 48–72 hours, then sealed. DSC pans were hermetically sealed with lids, and capillaries were sealed with epoxy.

Measurements were taken upon heating, with $\sim$5 minute anneals at each temperature increment, up to 150–200 ºC. The samples were cooled, measured after 5 minute anneals at each temperature. They were then subjected to cycling between room temperature and 150 or 200 ºC, to observe reversibility. The sample-to-detector distance was fixed at 7.5 m, the beam energy was 17.5 keV, and SAXS data were collected by a Rayonix detector. The 2D data were reduced by azimuthal integration to give intensity as a function of the scattering wave vector, q.

Grazing incidence small angle X-ray scattering

Grazing incidence small angle X-ray scattering was performed at the 8-ID-E beamline at Argonne National Labs. Samples were prepared on 2 cm x 2 cm pieces of silicon wafer by spin coating from a solution of methyl ethyl ketone. Film thicknesses were measured by ellipsometry, and samples were placed in a vacuum oven at 100 ºC for 48 hours to remove any residual solvent. Samples were stored under vacuum to reduce exposure to air and potential water uptake of the films.

Samples were measured using a temperature-controlled stage, open to the air, allowing for concurrent irradiation with UV or visible light. The beam energy was 11 keV, and GISAXS data were collected by a Pilatus 1M detector. Resulting 2D data were analyzed using GIXSGUI Matlab software provided and developed by the beamline scientists.

Optical anisotropy measurements

Samples displaying anisotropic phases by SAXS were probed for optical anisotropy, as an additional method of detected order-order or order-disorder phase transitions in the systems. Thin sample films on glass slides were prepared by dropcasting from a solution of THF. The solvent was evaporated by heating, and the glass slides were further dried in the vacuum oven at 100 ºC for 48 hours.

Birefringence measurements were performed by placing the glass slide between two crossed polarizers, and measuring the intensity of a HeNe laser passing through the polarizers and sample. Polarized optical microscopy was also employed, where light shone through a polarizer, onto the sample, through another polarizer, and onto a microscope camera. Images of the sample were recorded every 5 seconds while the sample was heated to 100 ºC.

4.3 Results

Characterization of block polymers

In Chapter 2, all copolymers were synthesized via ATRP. The synthesis of PMMA was successful by ATRP, however chain extension to grow a second block left a significant portion of dead chains, i.e. PMMA that did not grow a B*s*A block. This occurred despite running the polymerization of PMMA to low (<60%) conversions. Changes were made to the catalyst, ligand, solvent, and temperature. However, none of these changes worked. As a result, RAFT polymerizations were attempted. PMMA was successfully synthesized, and a kinetics reaction showed that chain extension was successful in generating a second block with no detectable dead PMMA chains. A total of five block polymers were synthesized, containing varying volume fractions of each block, and varying amounts of AzoMA. The molecular characteristics of each block polymer are listed in Table 4.1.

Sample [a]	M_n (M) [b]	M_n (B*s*A) [b]	mol% AzoMA incorporation [c]	f_M [d]	$Đ$ [e]
M(B*s*A) (28-14(4))	28	14	4	0.7	1.05
M(B*s*A) (22-24(5))	22	24	5	0.5	1.03
M(B*s*A) (13-46(5))	13	46	5	0.2	1.05
M(B*s*A) (24-20(10))	24	20	10	0.5	1.04
M(B*s*A) (18-31(11))	18	31	11	0.4	1.03

Table 4.1: Molecular characteristics of M(B*s*A) photoresponsive block polymers. [a] The numbers in parenthesis after the sample name represent the number average molecular weight of each block in kg/mol, the number in parenthesis after the molecular weight of the second block is the molar incorporation of AzoMA. [b] The number average degrees of polymerization were determined by ^{1}H NMR spectroscopy. [c] The molar incorporation of AzoMA was determined by the ratio of integrated protons in AzoMA and BzMA from ^{1}H NMR spectroscopy. [d] The volume fractions were calculated from the molecular weights of the block and the room temperature densities: ρ(PMMA) = 1.18 g/cm^3,[203] ρ(PBzMA) = 1.18 g/cm^3.[204] [e] The dispersity was measured using SEC with THF as the eluent, and light scattering and refractive index detectors.

During the synthesis, the molecular weight distribution and ^{1}H NMR spectrum were obtained for each step. Representative NMR spectra from M(B*s*A) (18-31(11)) are shown in Appendix Figures 6.11, 6.12, and 6.13. End group analysis was performed on the PMMA

homopolymer, which was in good agreement with the number average molecular weight found from SEC. The integration of the PMMA block was used to find the molecular weight of the second block by ^{1}H NMR spectroscopy, which was also in good agreement with the number average molecular weight from SEC. The molecular weight distribution was not affected by cleavage of the chain transfer agent, as shown in Figure 4.2.

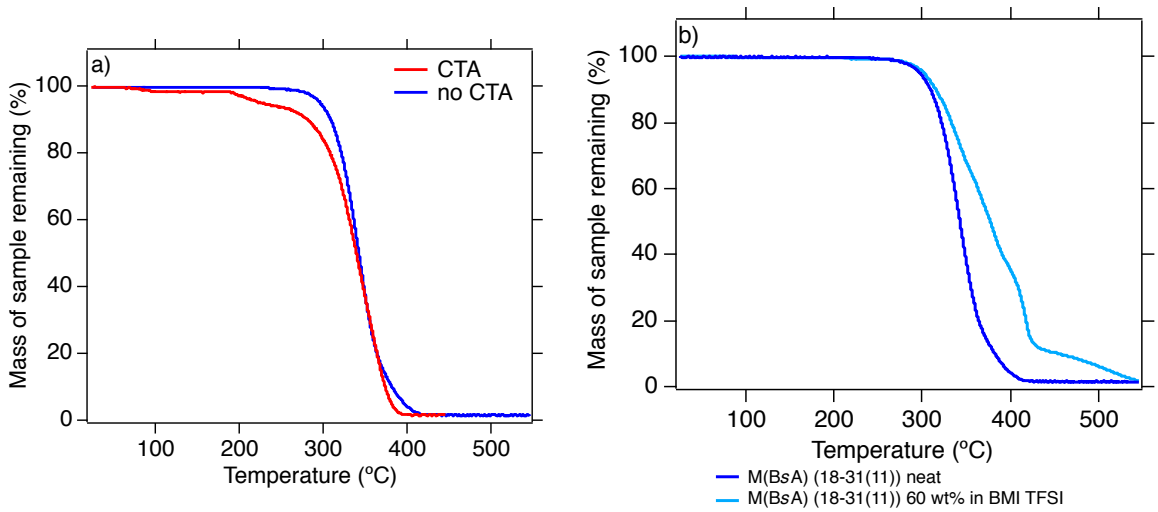

Figure 4.1: a) Thermogravimetric analysis of M(B*s*A) (18-31(11)) before (red) and after (blue) removal of the CTA. b)Thermogravimetric analysis of M(B*s*A) (18-31(11)) neat (blue) and as a 60 wt% solution in BMI TFSI (light blue).

In all cases where the chain transfer agent was removed, the SEC trace for the block polymer without the CTA lies directly over the trace with the CTA, indicating that the reaction did not cause any polymer degradation. The first polymer that was synthesized, M(B*s*A) (24-20(10)), did not have the CTA cleaved. This polymer was synthesized to determine whether any structure would be observed in the ionic liquid solutions, and was only used for a preliminary X-ray scattering experiment. However, the remaining block polymers had the chain transfer agent removed as it significantly reduces the thermal stability. The results of thermogravimetric analysis in Figure 4.1a show the degradation of M(B*s*A) (18-31(11)) before and after removal of the CTA. When the chain transfer agent is present, 2% mass loss occurs beginning at 75 ºC, then a further 5-10% is lost starting at 190 ºC. The onset of full degradation does not occur until 270 ºC. As this occurs despite rigorous drying of the polymer, these degradation events cannot be attributed to the loss of solvent. After removal of the CTA, the only degradation event occurs around 275 ºC. With this im-

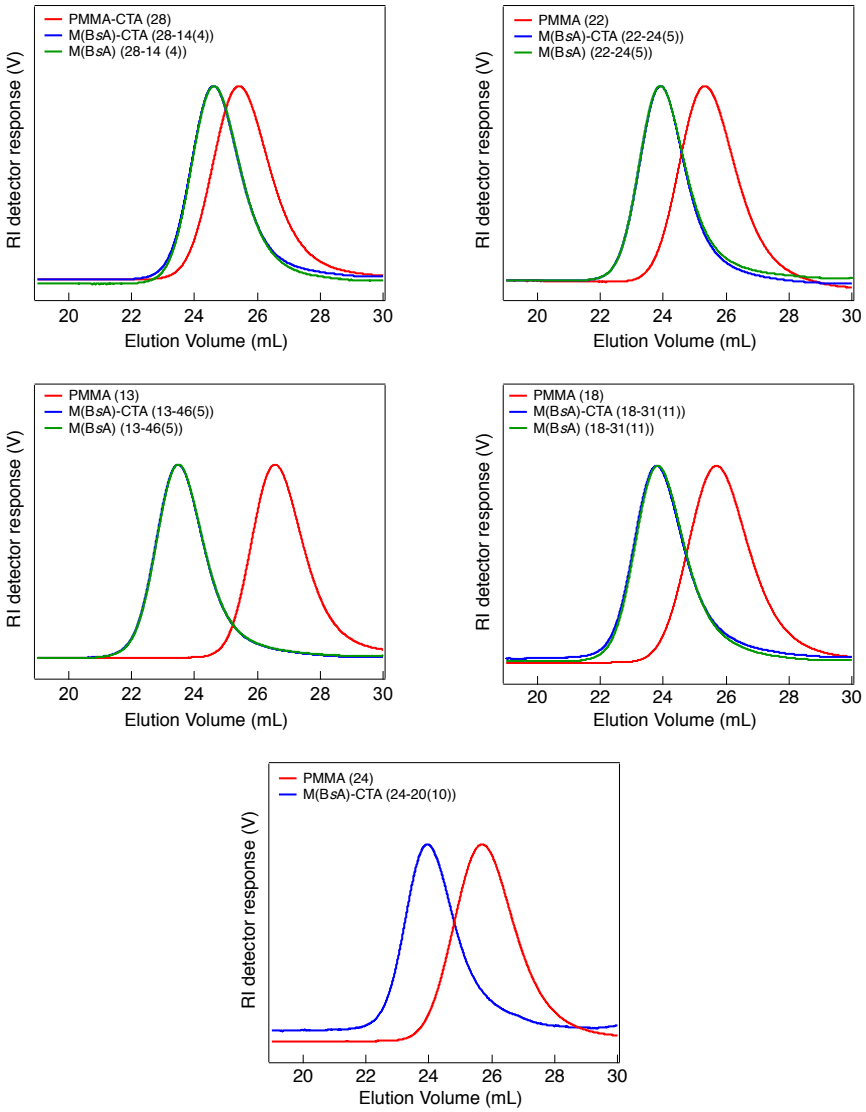

Figure 4.2: SEC traces of M(B*s*A) block polymers grown from PMMA-CTA macroinitiators. Red curves show the PMMA-CTA used for each polymer, blue curves show the M(B*s*A) polymers before removal of the CTA, and green curves show the M(B*s*A) polymers with the CTA removed.

provement in thermal stability of the polymer, the chain transfer agents were removed from all polymers used for further testing.

The addition of ionic liquids to the polymers did not decrease their thermal stability. Thermogravimetric analysis revealed that the addition of ionic liquid did not change the onset of degradation. Figure 4.1b shows a comparison of the degradation of neat M(B*s*A) (18-31(11)) and as a 60 wt% solution in BMI TFSI. As a solution in ionic liquid, the temperature range over which degradation occurs broadened, and an inflection point around 40% mass remaining is indicative of the onset of ionic liquid degradation. The polymers were also testing using differential scanning calorimetry, shown in Figure 4.3.

The two samples shown, M(B*s*A) (18-31(11)) neat and as a 60 wt% solution in BMI TFSI, display the same T_g at $\sim$ 68 ºC. The transition is less pronounced for the ionic liquid

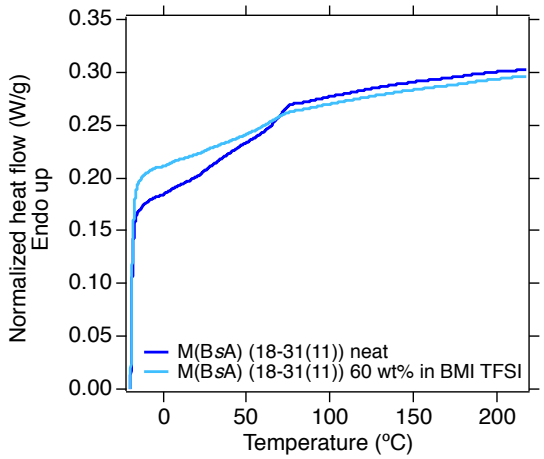

Figure 4.3: Differential scanning calorimetry of M(B*s*A) (18-31(11)) neat (blue) and as a 60 wt% solution in BMI TFSI (light blue).

solution, but it is still present. The literature values for T_g of PBzMA and PMMA are 54 and 110 ºC, respectively.[203,205] B*s*A was measured by DSC and found to have a T_g of 56 ºC, similar to the literature value of PBzMA. The intermediate glass transition temperature can be estimated using the Fox equation:[206]

$$\frac{1}{T_{g,copolymer}} = \frac{w_1}{T_{g,1}} + \frac{w_2}{T_{g,2}} \tag{4.1}$$

where w_1 is the weight fraction of one of the copolymer components, and $T_{g,1}$ is the glass transition temperature of the homopolymer of that component. Using this equation, the

T_g is estimated at 68 ºC, the same temperature as what is seen experimentally. While a single T_g can be indicative of a disordered block polymer melt, it can also occur in ordered systems; as will be discussed in the next section, it is expected that this solution is ordered as either hexagonally packed cylinders or lamellae. The glass transition completely disappears at lower concentrations, with solutions of 40 wt% and below showing no glass transition temperature.

Morphologies of block polymers by SAXS

The morphology of the block polymer solutions in ionic liquid were investigated by small angle X-ray scattering (SAXS). M(B*s*A) (24-20(10)) was the first polymer investigated, purely to determine if ordered morphologies could be formed or not. Three concentrations were tested, 25, 50, and 75 wt% in EMI TFSI. The resulting X-ray scattering data are shown in Figure 4.4, where the samples were measured every 10 ºC upon heating.

At the lowest concentration, spherical ordering is observed. At 150 ºC, the majority of peaks match well with body-centered cubic spheres, as indicated by the peak indices in Figure 4.4a. At lower temperatures, the principal scattering peak is split into three smaller peaks, and the indices match well with hexagonally packed spheres, shown in Figure 4.4d. Thus at this low concentration, spherical ordering dominates with a change in the dominant packing of the spheres upon heating. Notably, the solution also appears to form order upon heating from a solution of disordered spheres. Up to 60 ºC, the scattering shows broad peaks indicative of disordered spheres, which then form a higher order structure at 70 ºC and above. This ordering upon heating, also referred to as a lower critical ordering transition, LCOT, gives a phase transition that could be triggered with light. The higher concentration samples each show a single ordered morphology for all temperatures, hexagonally packed cylinders at 50 wt% and lamellae at 75 wt%. Between each of these concentrations, there may be an intermediate concentration where order-order phase transitions could be observed.

The polymers M(B*s*A) (28-14(4)) and (22-24(5)) were also studied using SAXS, in the ionic liquid BMI TFSI. It was hoped that by increasing the solubility of the B*s*A block in

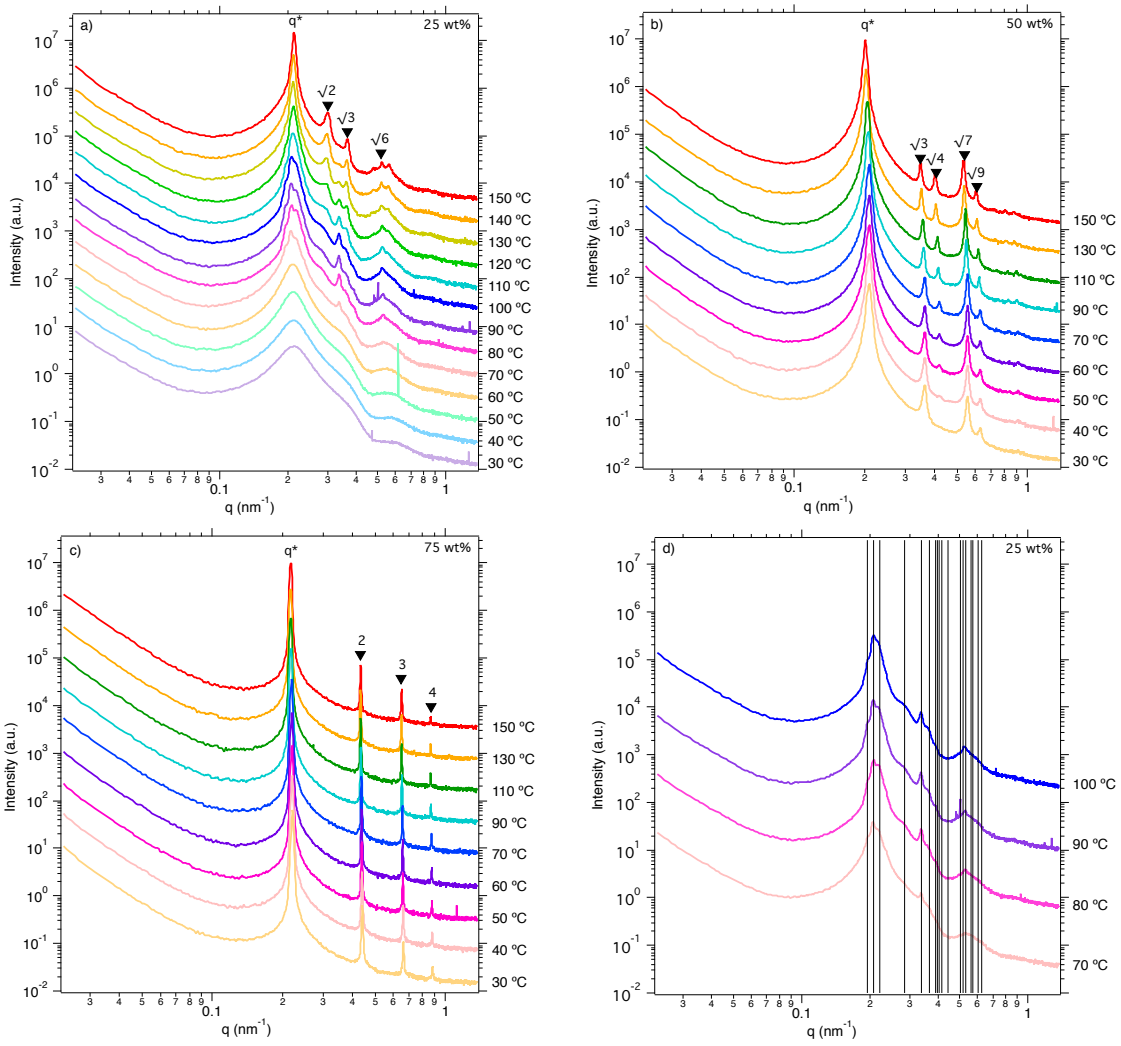

Figure 4.4: SAXS patterns of M(B*s*A) (24-20(10)) in EMI TFSI at a) 25, b) 50, and c) 75 wt%. The peak indices indicate BCC, HEX, and LAM morphologies, respectively. d) Peak indices for hexagonally close packed spheres for the 25 wt% solutions showing a principal scattering peak split into three small peaks.

the ionic liquid by switching from EMI to BMI, the higher concentration samples might also show an LCOT to a non-spherical ordered morphology. However these samples were prepared in capillaries using THF as a cosolvent to allow direct injection of the solutions to the bottom of the capillary. Despite prolonged heating in the vacuum oven, THF remained in many of the samples, as discovered when some capillaries burst after heating above 200 ºC. As a result, these data are not trusted, as it is unknown whether the samples did not burst also retained small amount of THF, which could impact the morphology of the solution. To circumvent this issue, THF was only used as a cosolvent to prepare higher concentration samples that would not flow. These samples were prepared in DSC pans rather than capillaries, to ensure that the THF would be able to evaporate. The samples that flow, *ca.* 40 wt% and below, were prepared in capillaries without the use of a cosolvent, as described in the experimental section.

The morphologies of M(B*s*A) (22-24(5)), (13-46(5)), and (18-31(11)) in EMI TFSI were investigated at a range of concentrations to locate LCOT phase behavior, as well as any possible OOTs. The resulting phase diagrams are shown in Figure 4.5. The features of interest are regions where phase transitions occur at a set polymer concentration. In this case, the lowest concentrations up to 40 wt% shown LCOT phase behavior. All other samples either show a single morphology at a given concentration, or coexistence between two morphologies. While these data can be used to search for a region with an ODT, they are not directly amenable to light triggering without further exploration. As a result, the focus will be on the samples ranging from 20 or 25 wt% up to 40 wt%.

Small amplitude oscillatory shear rheology of M(B*s*A) solutions

The polymers M(B*s*A) (22-24(5)), (13-46(5)), and (18-31(11)) in solution in EMI TFSI were all tested using small amplitude oscillatory shear to determine if the mechanical properties also show LCOT phase behavior. The temperature sweep measurements are shown in Figures 4.6, 4.7, and 4.8, with concentrations tested from 25 to 40 wt%. For all samples, at low temperatures G'' is greater than G', indicating liquid-like behavior. Frequency sweep measurements at room temperature for these samples show terminal flow behavior

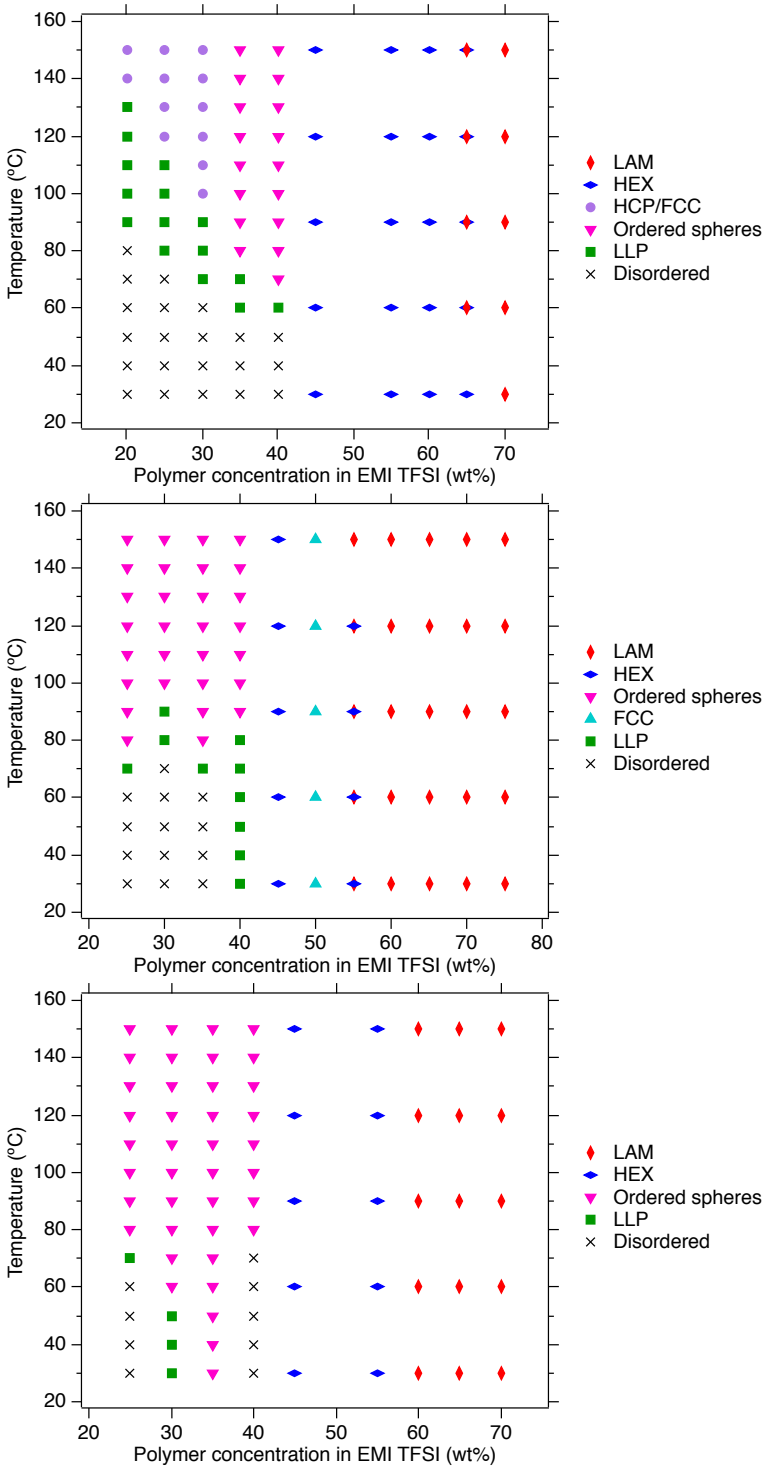

Figure 4.5: Phase diagrams of M(B*s*A) a) (22-24(5)), b) (13-46(5)), and c) (18-31(11)) in EMI TFSI.

consistent with a viscoelastic fluid, except for M(B*s*A) (18-31(11)) which is ordered at all temperatures under visible light. As the temperature is increased, G'' and G' cross over and reach a plateau at high temperatures where $G' > G''$. This transition is again in agreement with the structure formation observed in SAXS. The measurements under "visible" light were performed in the dark, after annealing at 100 ºC for an hour to ensure full thermal relaxation of any *cis* isomers present. When the UV light is turned on, the temperature at which G' and G'' increases, opening a bistable window with the potential for triggering LCOTs using light.

In general, as concentration increases, the temperature at which ordering occurs decreases. M(B*s*A) (18-31(11)) does not follow this trend; the LCOT temperature increases again at 40 wt%. This observation is in agreement with the SAXS data., although it is not clear why this occurs. It is possible that the sample would form different ordered structures with longer anneal times; that the equilibrium morphologies are driving different LCOTs. The higher concentration samples also show a greater difference between G' and G'' when the samples are ordered at elevated temperatures, as the greater concentration of polymer allows for the formation of a stronger network.

Once bistable windows were identified using temperature sweep measurements, time sweeps were performed at a set temperature to enable light-triggering of LCOTs. Samples were annealed at a temperature in the bistable window for 30 minutes. If the chosen temperature never displayed solid-like behavior, the temperature was increased. Once the UV light was turned on, if the sample never became liquid-like, the temperature was decreased. M(B*s*A) (22-24(5)) and (13-46(5)) were tested for light-dependent LCOTs at concentrations of 30 wt% and above. Although the samples showed ordering both by SAXS and (somewhat) by rheology at 25 wt%, and 20 wt% for M(B*s*A) (22-24(5)), the mechanical properties of the solution showed $G'' > G'$, even at temperatures shown to have an ordered morphology by SAXS. Due to sample limitations after repeated testing of conditions (varied gaps and UV powers), M(B*s*A) (18-31(11)) was unable to be tested for triggering with the optimal gap and UV power.

Triggering of M(B*s*A) (22-24(5)) was performed by switching filters between UV (365 nm) and visible light (400–500 nm). The data are plotted in Figures 4.9 and 4.10 as a

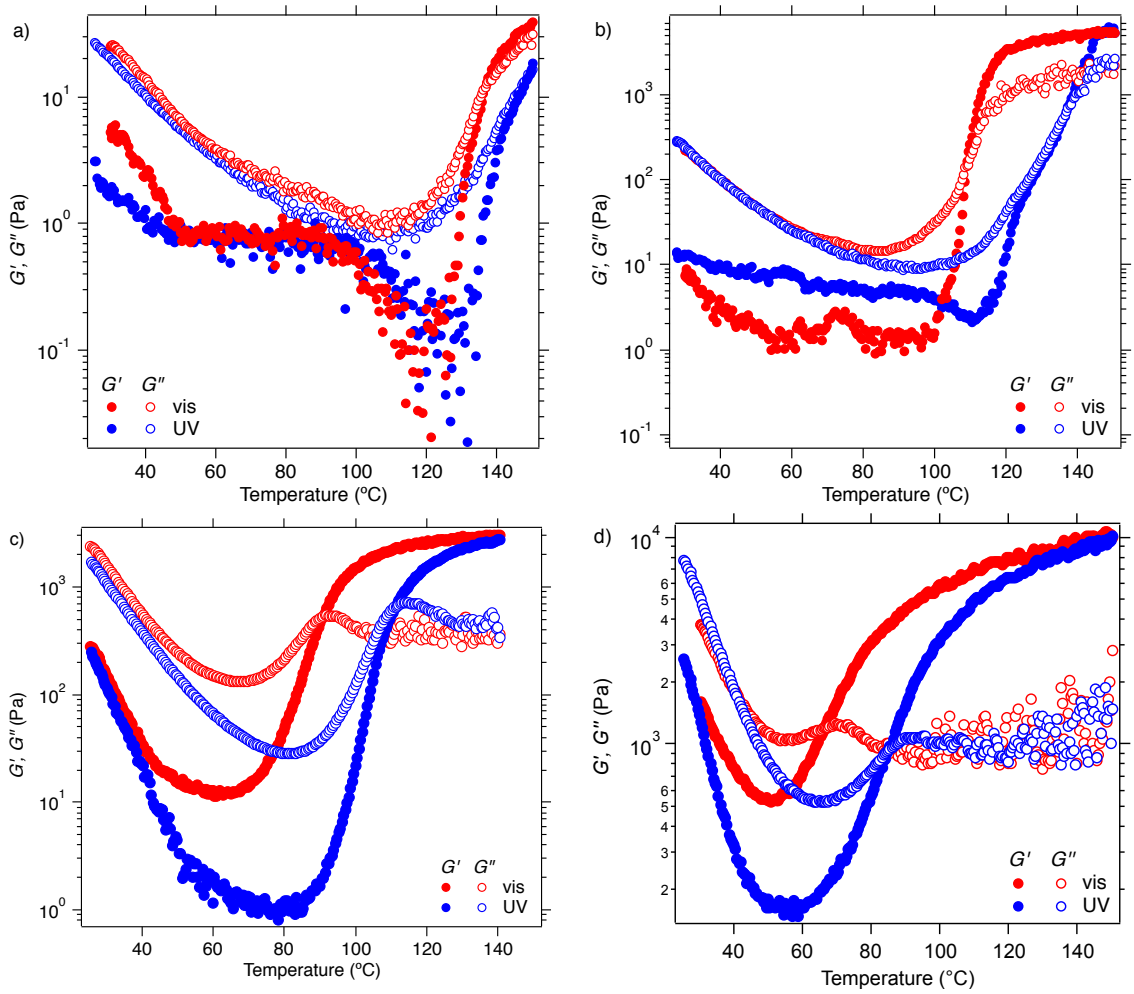

Figure 4.6: Temperature sweeps of M(B*s*A) (22-24(5)) at a) 25 wt%, b) 30 wt%, c) 35 wt%, and d) 40 wt% in EMI TFSI. Open circles indicate G'', closed circles indicate G'. Red data are taken in the dark, mimicking visible light conditions, and blue data were taken under UV light at a power of 50 mW/cm^2. Measurements were taken with gaps $\sim$200 µm, 1% strain, and a 1 rad/s frequency.

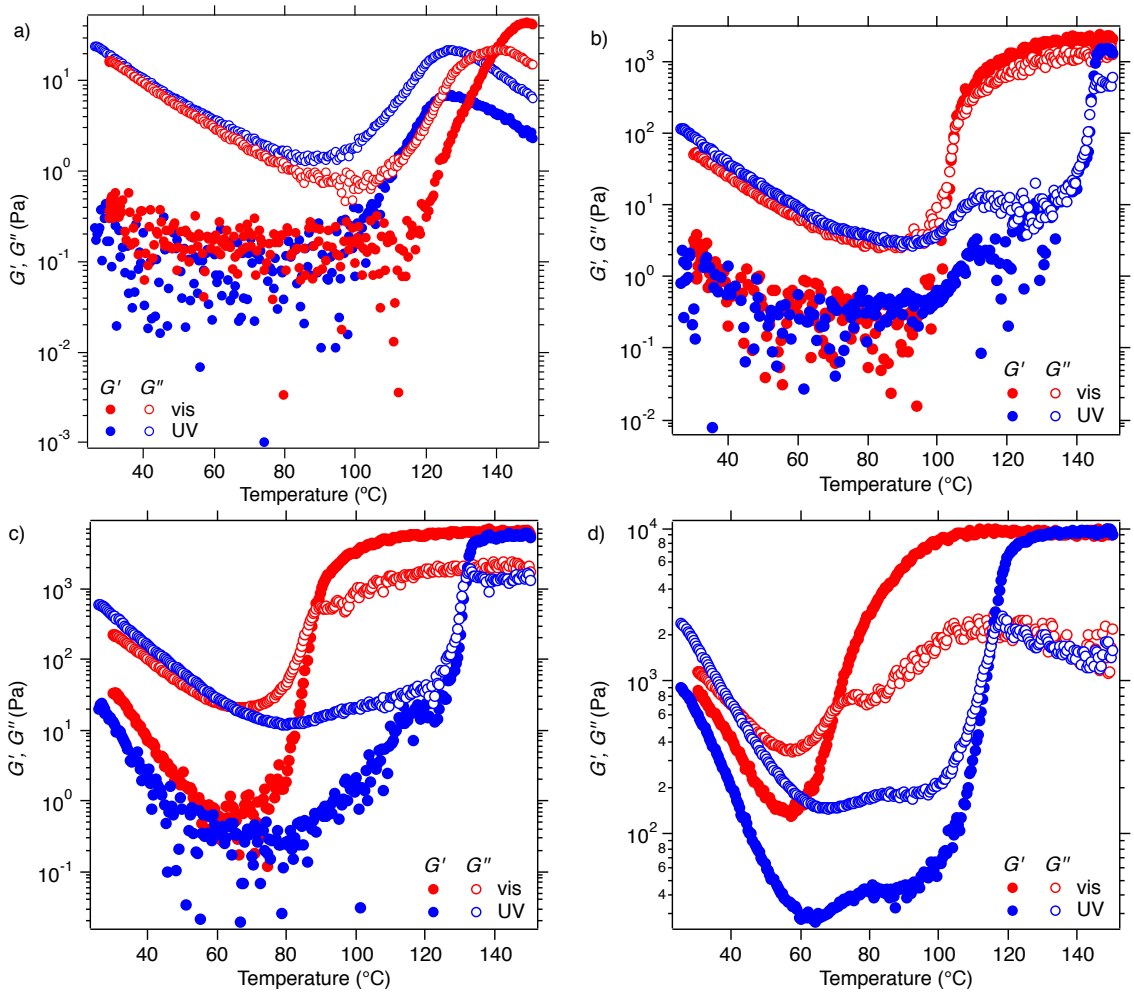

Figure 4.7: Temperature sweeps of M(B*s*A) (13-46(5)) at a) 25 wt%, b) 30 wt%, c) 35 wt%, and d) 40 wt% in EMI TFSI. Open circles indicate G'', closed circles indicate G'. Red data are taken in the dark, mimicking visible light conditions, and blue data were taken under UV light at a power of 50 mW/cm^2. Measurements were taken with gaps $\sim$200 µm, 1% strain, and a 1 rad/s frequency.

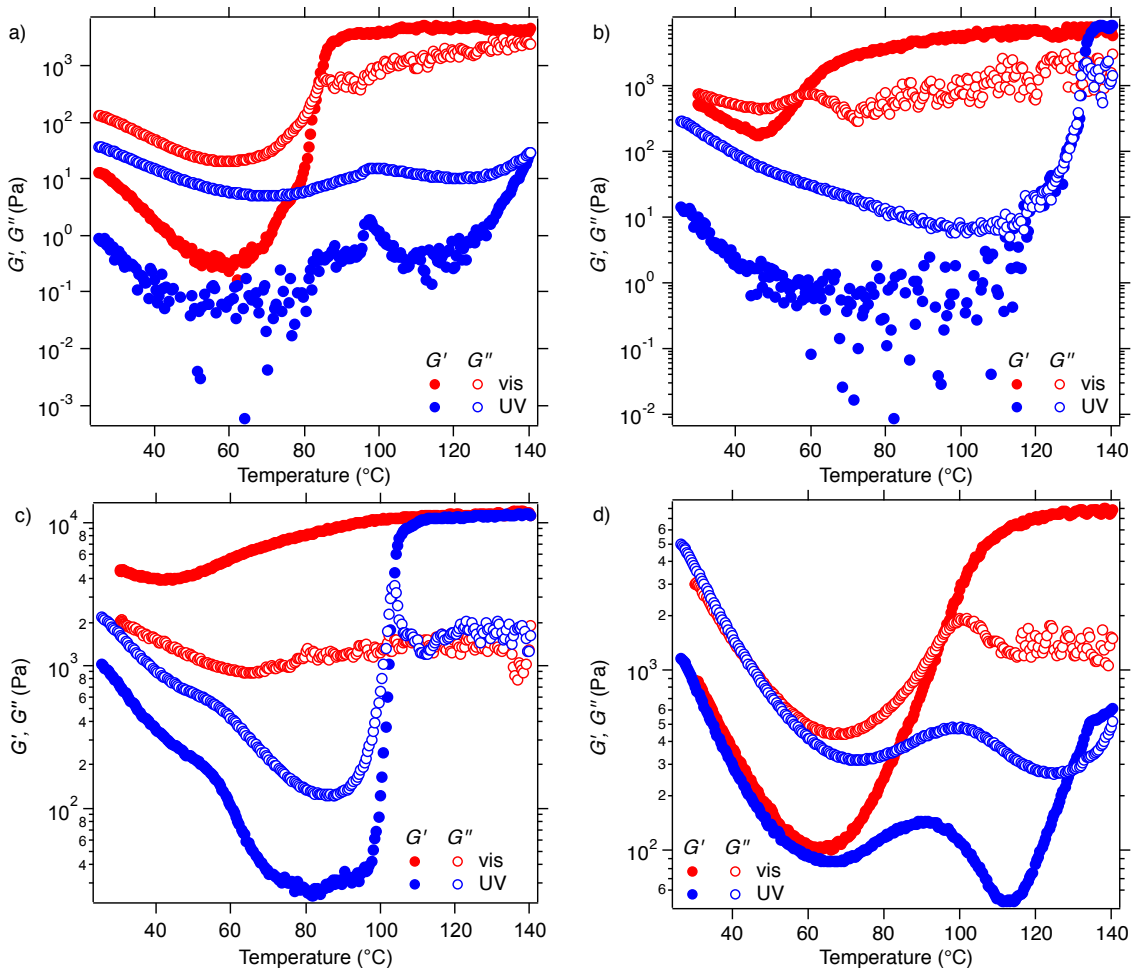

Figure 4.8: Temperature sweeps of M(B*s*A) (18-31(11)) at a) 25 wt%, b) 30 wt%, c) 35 wt%, and d) 40 wt% in EMI TFSI. Open circles indicate G'', closed circles indicate G'. Red data are taken in the dark, mimicking visible light conditions, and blue data were taken under UV light at a power of 10 mW/cm^2. Measurements were taken with gaps $\sim$350 µm, 1% strain, and a 1 rad/s frequency.

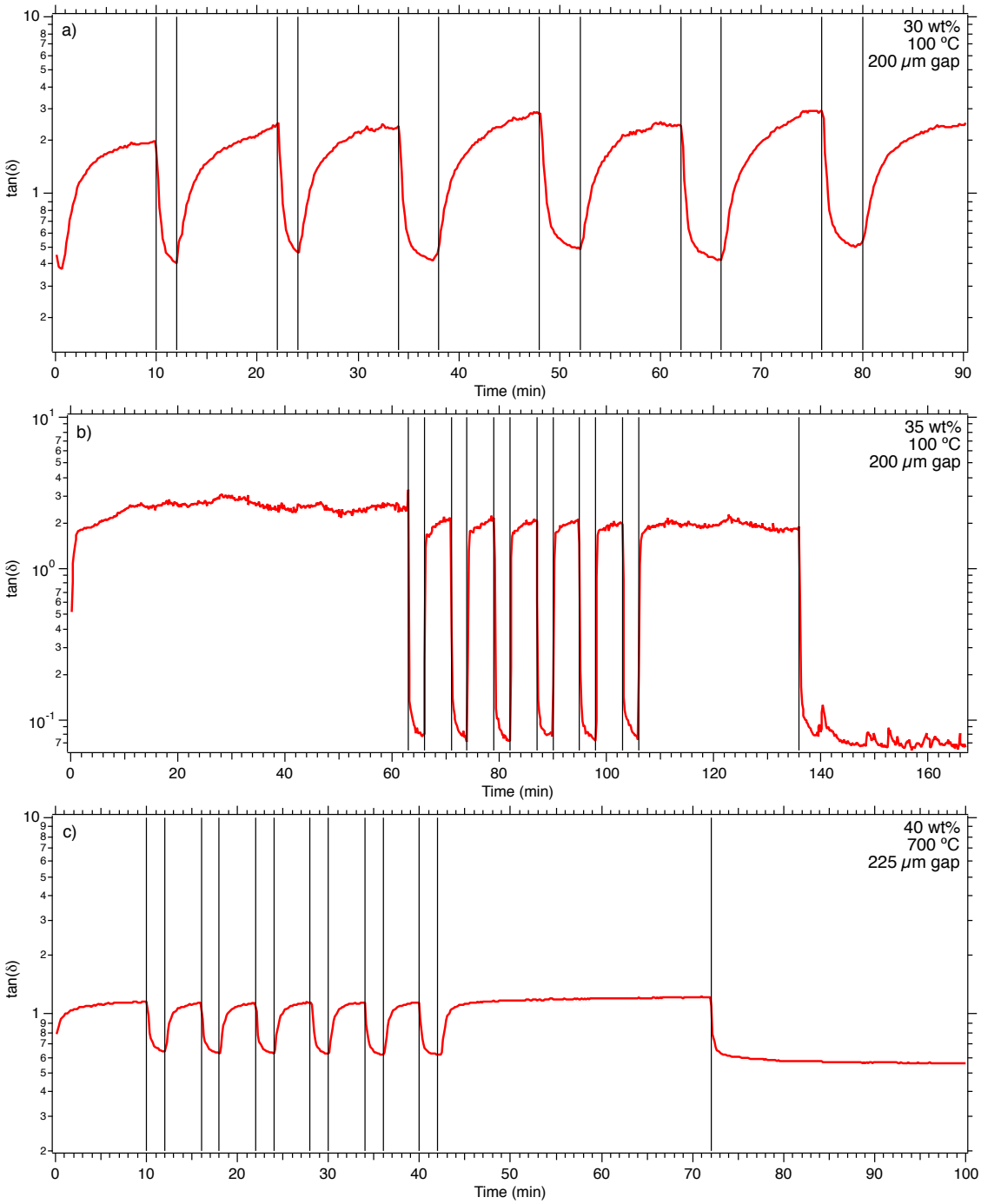

Figure 4.9: Light-triggered LCOT of M(B*s*A) (22-24(5)) a) 30 wt%, b) 35 wt%, and c) 40 wt% in EMI TFSI. Red trace is tan δ, black lines indicate when the filter was switched from UV to vis or vice versa. The inset indicates the exact gap used, as well at the temperature at which triggering was performed. All samples were measured with a UV power of 50 mW/cm^2, 1% strain, and 1 rad/s frequency.

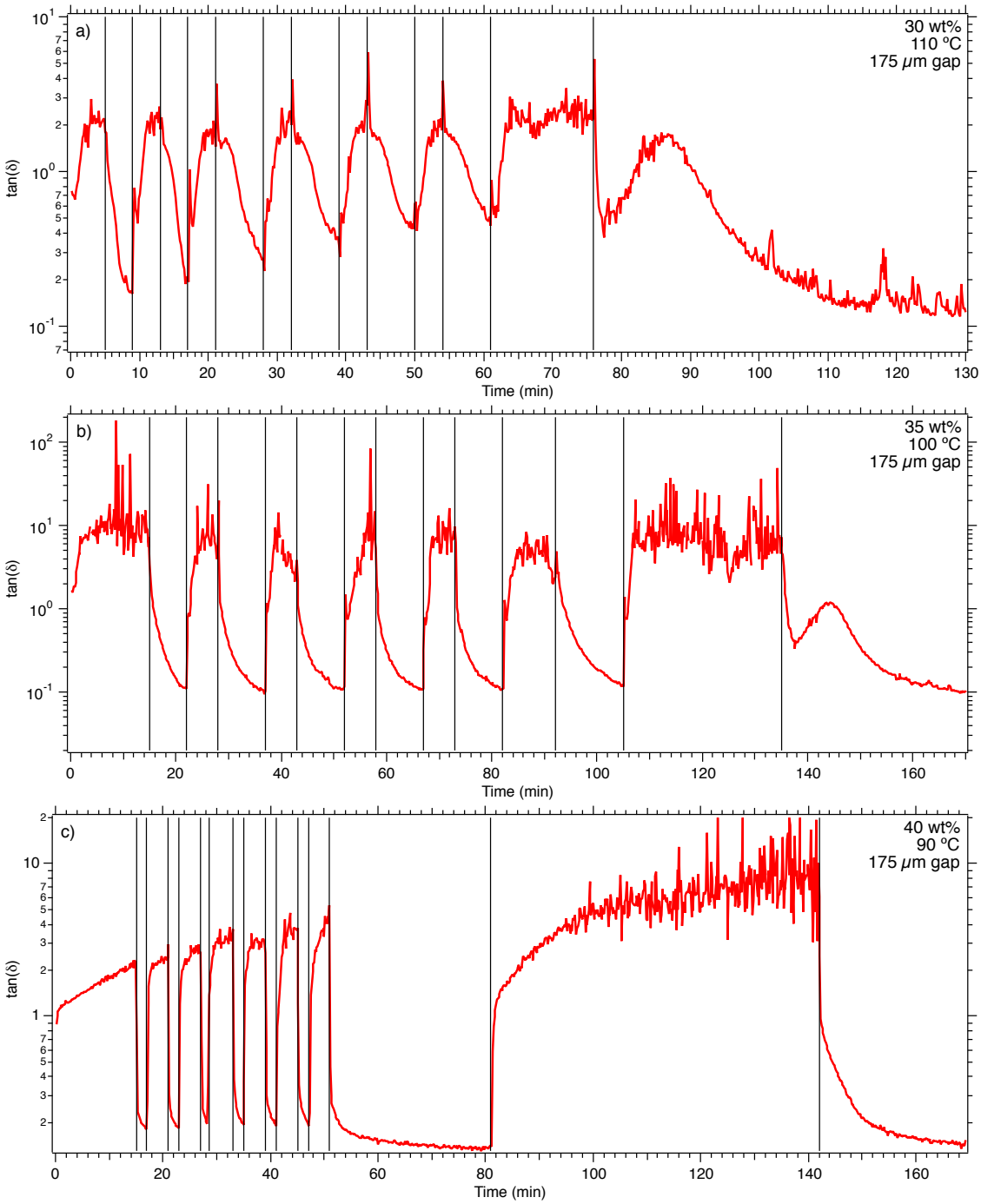

Figure 4.10: Light-triggered LCOT of M(B*s*A) (13-46(5)) a) 30 wt%, b) 35 wt%, and c) 40 wt% in EMI TFSI. Red trace is tan δ, black lines indicate when the filter was switched from UV to vis or vice versa. The inset indicates the exact gap used, as well at the temperature at which triggering was performed. All samples were measured with a UV power of 50 mW/cm^2, 1% strain, and 1 rad/s frequency.

function of tan δ rather than showing the storage and loss modulus individually, to simplify the plots; tan δ is the ratio of G'' to G', where δ is the phase angle between the applied sinusoidal stress and the measured displacement of the sine wave.

$$tan\delta = \frac{G''}{G'} \tag{4.2}$$

Thus when tan δ is greater than 1, $G'' > G'$ and the sample is liquid-like. When tan δ is less than 1, $G'' < G'$ and the sample is solid-like.

In general, the samples showed excellent reversibility. Even if the peak value of tan δ changed over multiple cycles, longer anneals under a certain wavelength of light returned the sample to a plateau value of tan δ. All M(B*s*A) (22-24(5)) samples showed similar tan δ values with each cycle, whereas 40 wt% M(B*s*A) (13-46(5)) showed a change in liquid-like tan δ with each cycle. This may be a result of the slower dynamics at the highest concentration, increasing the total amount of time required to reach the plateau value under UV light. Future tests allowing the sample to remain under UV light for longer before beginning the cycling, then longer times under UV light at each step, may prevent this gradual increase from occurring. Although achieving the steady state under UV light may be sluggish, it has been shown that it is not necessary to achieve full phase transitions for optical device applications, as long as some change in ordering has occurred.[207] Here, the change from liquid to solid and the reverse is rather rapid; the time to reach the plateau value vary between samples.

Finally notable is that after long anneals under UV light, then switching to visible light, 30 and 35 wt% M(B*s*A) (13-46(5)) showed an initial decrease in tan δ, followed by a brief return to a liquid-like state, before plateauing at a minimum value of tan δ. This may be due to instantaneous phase separation of the B*s*A block from the ionic liquid upon switching to visible light, followed by flow to form a more structured ordered morphology. Without in-situ scattering data, it is difficult to confirm what is occurring in this case.

The triggering of morphology changes can also be achieved simply by turning on and off the UV lamp, when the temperature is high enough that the thermal *cis* to *trans* isomerization of azobenzene occurs quickly. In figure 4.11, 35 wt% M(B*s*A) (22-24(5)) in EMI

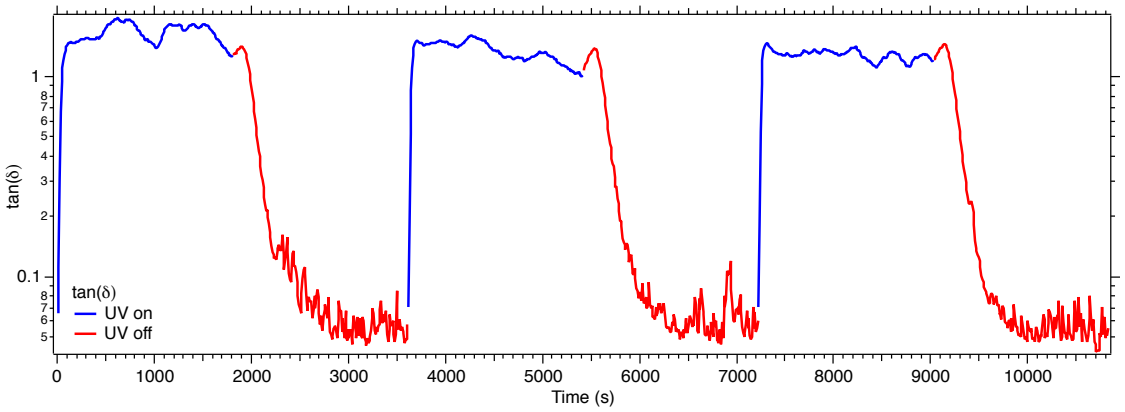

Figure 4.11: Triggering of LCOT phase behavior in 35 wt% M(B*s*A) (22-24(5)) in EMI TFSI using UV light, blue, and thermal reversion of azobenzene, red.

TFSI shows excellent reversibility over three cycles of LCOT phase behavior relying on this thermal relaxation and UV light.

Grazing incidence SAXS for detection of light-triggered LCOTs

The combination of SAXS and rheology show that samples form ordered morphologies upon heating, corresponding to a change from liquid-like to solid-like behavior. This change in mechanical properties can also be triggered with light at a single temperature. Grazing incidence small angle X-ray scattering (GI SAXS) was chosen to observe the change in morphology with light directly. This was not achieved in transmission SAXS measurements due to the difficulty of achieving in-situ light exposure with the current experimental setup. The path of the beam blocks two sides of the sample from light exposure, and the heating stage blocks the rest. However, in GI SAXS the sample is a thin film and light can be exposed to the top face. This is analogous to the change between transmittance and reflection cloud point measurements discussed in Chapter 3.

GI SAXS was attempted twice on thin film samples of M(B*s*A) (22-24(5)), (13-46(5)), and (18-31(11)). Unfortunately in both cases, no significant data were obtained. In general, the scattering that was observed was either very weak, only showing a principal scattering peak, or showed no ordering at all. There are many factors that could be contributing to the lack of signal. All of the samples of interest, at 40 wt% or less in concentration, are able to flow over long times. This could contributed to sample thinning with time, decreasing

the film thickness enough to prevent observable scattering. Recommended film thicknesses for GI SAXS are between tens and hundreds of nanometers. Samples were measured by ellipsometry before and after the scattering trip, and were found to have decreased as much as three times. However, all samples were still above the recommended lower limit of 50 nm. Another potential cause of weak scattering is the experimental setup. Due to the requirement of in-situ light exposure, the samples were not contained under vacuum. In GI SAXS, the scattering is significantly reduced over transmission SAXS as a result of only measuring the X-rays reflected from the substrate surface. By leaving the sample open to air, the scattering of the beam due to air becomes significant, reducing the signal even further. Paired with the broad scattering peaks observed for most of the samples showing light-induced ordering, it is possible that the flux simply was not high enough. Finally, the last contributor is the effect of confinement of a block polymer to a thin film. The ordering of a block polymer in the bulk is not always the same as what is observed in thin films, and the possibility for a divergence in bulk and thin film morphology is increased with thinner films.[208]

Optical anisotropy measurements for detection of OOTs

Two optical anisotropy measurements were attempted on lamellar and hexagonally packed cylinder-forming samples. To allow for concurrent testing with UV or visible light exposure, the samples were prepared as thin films on microscope slides. For static birefringence testing, placing the thin film between two crossed polarizers did not give any signal onto the detector. Anisotropic phases should depolarize the light, thus allowing some light to pass through the second polarizer and onto the detector. In this case, no depolarization occurred, indicating that the sample is isotropic. This is contrary to the observed ordered morphology in SAXS, as anisotropic samples were chosen specifically to test the viability of these measurements. Similarly, the measurements using polarized optical microscopy showed no birefringence for anisotropic samples. In this case, we did not expect the samples to have a specific alignment direction, and expected the films to consist of randomly oriented ordered grains. The depolarization of light by samples with randomly oriented anisotropic

grains are able to display birefringence at any angle, unlike single-grain samples where orientation of the polarization parallel or perpendicular to the grain is necessary.[209] For a sample with randomly oriented grains, the light is depolarized as it passes through domains that are in the correct orientation, resulting in birefringence.[66,68] In this case, the refractive index of both blocks are very similar, PMMA swollen with EMI TFSI approximated as 1.5082 for pure EMI TFSI and B*s*A approximated as 1.563 for PBzMA.[210,211] Although these numbers are not perfect for these case, it shows that they are likely very similar in this instance. Thus is it possible that no orientational birefringence will be observed in these samples, and optical anisotropy measurements may not be viable.

4.4 Discussion

Copolymer composition and concentration dependence of block polymer morphology

While M(B*s*A) (22-24(5)), (13-46(5)), and (18-31(11)) all show ordering upon heating for concentrations $\leq$40 wt%, the number and sharpness of higher order peaks varies. M(B*s*A) (22-24(5)) shows a coexistence of hexagonally packed spheres and face-centered cubic spheres for 30 wt% and below. Figure 4.12 shows 20 wt% M(B*s*A) (22-24(5)) showing the reflections expected for FCC and HCP. Increasing the concentration of this sample to 35 and 40 wt% decreases the ordering significantly, broadening the scattering peaks. An example of 35 wt% M(B*s*A) (22-24(5)) is shown in Figure 4.13.

While the SAXS pattern alone is slightly ambiguous, simply suggesting that the sample orders on heating, we can infer that spheres have formed based on neighboring concentrations as well as rheological data. At 30 wt%, the sample shows a highly ordered spherical morphology. Increasing the concentration to 45 wt%, the sample now shows hexagonally packed cylinders. The expected reflections for a simple cubic arrangement of spheres described the higher order peaks seen, whereas hexagonally packed cylinders does not. The identification of a spherical morphology can also be corroborated by frequency sweeps of the samples at temperatures where ordering is observed. Figure 4.14 shows the

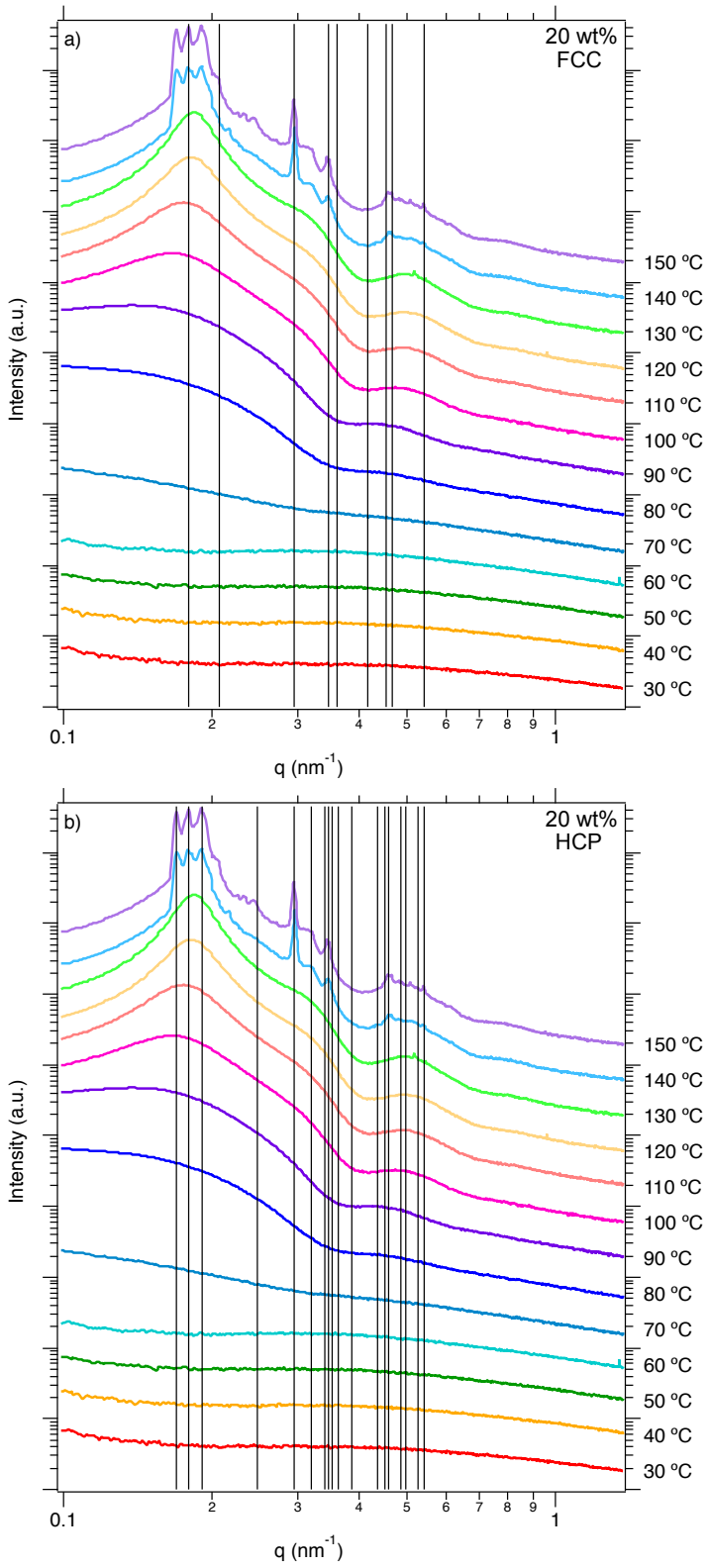

Figure 4.12: SAXS patterns for 20 wt% M(B*s*A) (22-24(5)) in EMI TFSI SAXS upon heating, with indices shown for a) FCC and b) HCP.

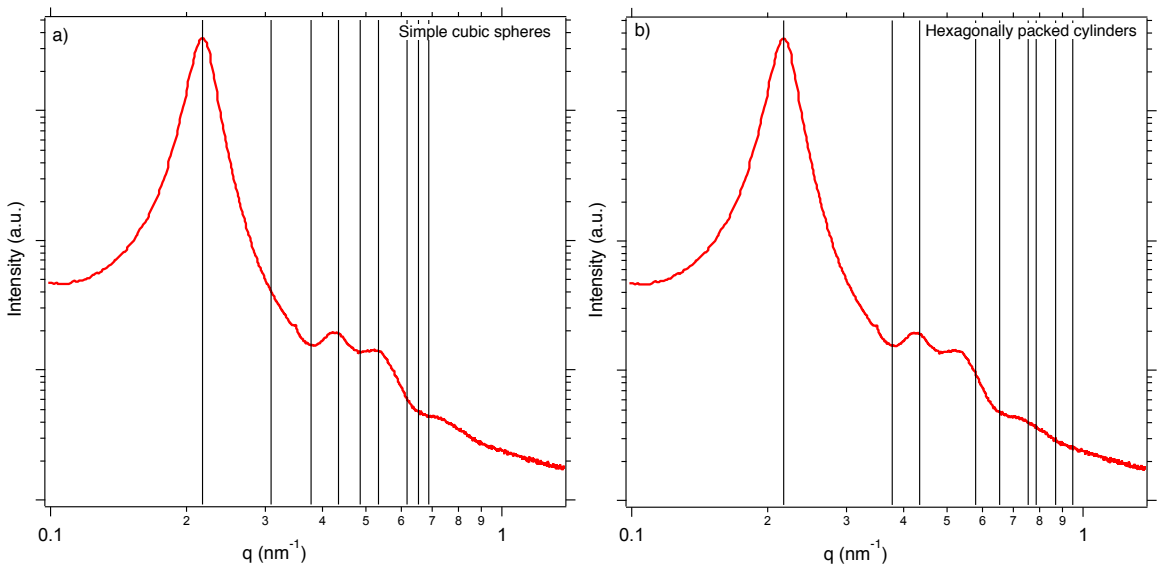

Figure 4.13: Scattering pattern of 35 wt% M(B*s*A) (22-24(5)) in EMI TFSI at 150 ºC, with indices shown for a) a simple cubic arrangement of spheres, and b) hexagonally packed cylinders.

frequency sweep data for 35 wt% M(B*s*A) (22-24(5)) at 150 ºC. The storage modulus is rel-

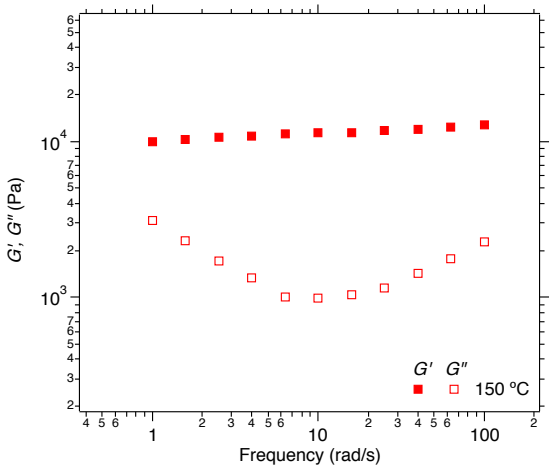

Figure 4.14: Frequency sweep of 35 wt% M(B*s*A) (22-24(5)) in EMI TFSI at 150 ºC, measured with 1% strain.

atively invariant with respect to frequency, suggesting a cubic phase is present. Thus given the neighboring morphologies with well-defined scattering patterns, and the match of the higher order reflections with cubic spheres, these samples with broad scattering peaks will be described as showing spherical ordering.

Given the low concentration of polymer in the sample, the PMMA block is significantly

swollen by the ionic liquid. The LCOT in this case is driven by the phase separation of B*s*A from the ionic liquid, in this case forming spherical micelle cores. Two samples, M(B*s*A) (22-24(5)) and (24-20(10)), show spheres with well-defined order at lower concentrations, whereas the remaining samples, M(B*s*A) (13-46(5)) and (18-31(11)) only have weaker spherical ordering. A notable difference between these samples is the molecular weight of the B*s*A block that forms the micelle core. EMI TFSI is a poor solvent for B*s*A above the LCOT, therefore the size of the polymer chain, R_g, will scale with $M_n^{1/3}$. Assuming that the radius of a micelle core is simply $2R_g$, the size of the core will approximately double from M(B*s*A) (22-24(5)) to (13-46(5)). The change is less drastic from (22-24(5)) to (18-31(11)), increasing only by a factor of 1.3. However in this case the composition of the copolymer also changes, and the increase in free volume required by the AzoMA monomer would likely cause an additional increase in the R_g. The block polymer architecture also impacts the type of micelle formed, and the preferred packing structure. Hairy micelles with long corona chains relative to the core size will typically pack on a BCC lattice, whereas crew-cut micelles with short corona chains will prefer an FCC lattice due to closer proximity between micelle cores.[43,212]

Finally, this weak ordering could be a result of dynamics rather than a fundamental structural difference between the polymers. Notably, the M(B*s*A) (22-24(5)) samples at 35 and 40 wt% also showed spherical ordering. The increase in concentration may have slowed the motion of the polymer chains to a great enough extent that these concentrations did not reach their equilibrium morphology with a 5 minute anneal at each temperature. It is possible that with longer anneals, all of the samples could reach a well-ordered spherical morphology. Figure 4.15 shows a comparison of the reversibility of morphology formation for the 25 wt% and 30 wt% samples. Both samples had been tested under identical conditions, heated at 10 ºC increments and annealed at each temperature for 5 minutes. The bottom scattering pattern shows the morphology at 150 ºC after this heating ramp, and the return of the samples to a disordered morphology upon cooling to 30 ºC. The difference arises when the samples are heated directly to 150 from 30 ºC . While the 25 wt% sample maintains all of the peaks observed with a slower heating rate, the scattering patten of the 30 wt% sample smooths out considerably. While it is still ordered, it would not longer

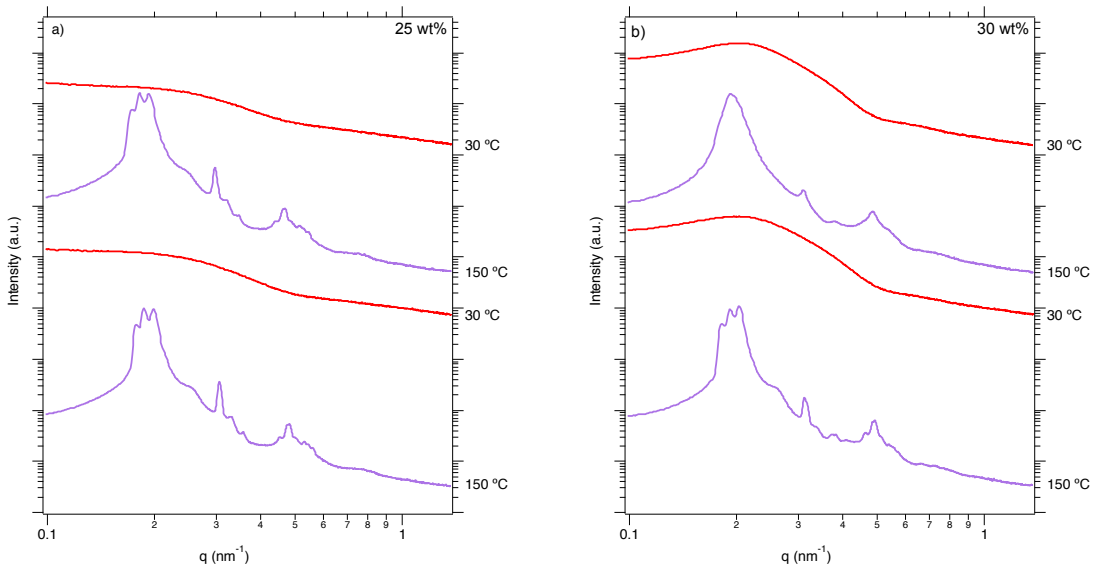

Figure 4.15: Scattering patterns of a) 25 and b) 30 wt% M(B*s*A) (22-24(5)) in repeated heating and cooling cycles. The bottom purple curves are the samples at 150 ºC after the first heating ramp, then the samples were cooled at 30 ºC increments down to the red 30 ºC curve directly above it. The samples were then heated directly to 150 ºC and annealed for 5 minutes, shown in the second purple curve. Finally they were cooled back to 30 ºC and annealed for 5 minutes, shown in the top red curve.

be discernible as hexagonally packed spheres. This suggests that the spherical morphologies observed in this sample at higher concentrations, as well as in M(B*s*A) (13-46(5)) and (18-31(11)), may be a result of slow ordering kinetics. Further work needs to be done to determine if these samples can form well-ordered spherical morphologies with longer annealing at elevated temperatures.

Gap and UV power dependence of LCOTs

The light-dependent rheological behavior of these samples is expected to follow a similar thickness-dependence as observed in Chapter 3 for cloud points. The absorption of UV light by azobenzene could lead to an uneven exposure of the sample during the measurement, potentially causing a domain of disorder close to the quartz plate, and an ordered sample where the UV light could not penetrate. At larger gaps, 300-400 µm and lower UV power, 10 mW/cm^2, 35 wt% M(B*s*A) (13-46(5)) showed this effect (Figure 4.16). While the sample under visible light has a smooth increase of modulus, under UV light the mod-

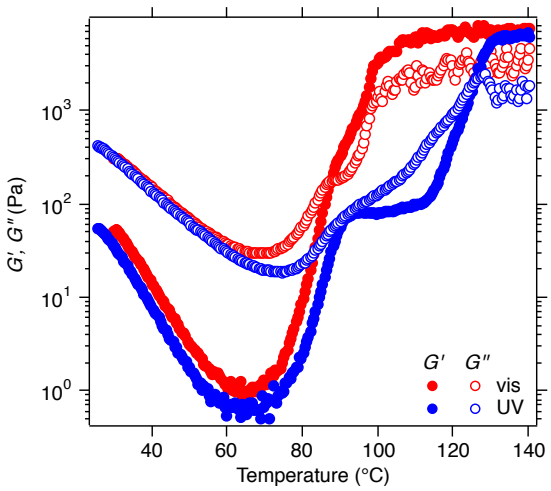

Figure 4.16: Temperature sweep of 35 wt% M(B*s*A) (13-46(5)) with a 400 µm gap, 10 mW/cm^2 UV power, 1% strain, and 1 rad/s frequency.

ulus increases with a step at the same temperature as under visible light, plateaus, and then increases to a fully solid-like state. This is indicative of the formation of two domains in the sample, one ordered and one still disordered. To separate the effects of UV power and gap, the sample gap was decreased to 200 µm and two UV light temperature sweeps were performed, one at each UV power. The data in Figure 4.7c shows the sample under 50 mW/cm^2, and the data at 10 mW/cm^2 overlays directly on top of those data. As with Chapter 3, the sample thickness has the largest impact on the ability of UV light to penetrate, and changing UV power does not significantly impact the temperature sweep measurements. The impact of sample thickness was observed in M(B*s*A) (13-46(5)) to a higher degree than (22-24(5)), which follows from the higher molecular weight of M(B*s*A). Although Chapter 3 demonstrated that molecular weight should not impact the LCST phase separation temperature at a set concentration, the concentration of the B*s*A blocks is not equal due to the change in block polymer composition between the two samples. At a given concentration of block polymer, M(B*s*A) (13-46(5)) will have a higher concentration of B*s*A, and thus will have a higher concentration of azobenzene, absorbing more light.

It was noted that having the lower UV power of 10 mW/cm^2 did cause a drift in the plateau value of tan δ for the triggering experiments. Although UV power will not impact the ultimate state reached by the sample, higher power will enable the sample to reach that state faster. The UV power of 10 mW/cm^2 was originally chosen to mimic the power

obtainable by the handheld UV lamp used in Chapter 3 and for the GI SAXS measurements. However, as 50 mW/cm^2 performed better for triggering, and did not significantly impact the temperature sweeps, this power was used for both measurements for the sake of consistency.

4.5 Conclusions

The combination of M(B*s*A) photoresponsive block polymer with the ionic liquid EMI TFSI produces a light responsive block polymer solution. At low concentrations, the samples undergo LCOTs upon heating, generating an ordered structure. The observation of LCOTs in block polymers is relatively rare in the bulk, generally arising due to differences in the thermal expansion coefficients of the two blocks.[213] Even aside from the ability to control these transitions with light, the use of a LCST-type polymer in a block polymer solution could generate more of these LCOT systems, enabling further study in this area.

The low concentrations samples were studied using temperature sweeps in rheology to determine the window in which light could be used to trigger LCOTs. Typically a temperature close to the center of the window allowed for the fastest triggering in the samples, and generated the largest difference between the ordered and disordered states. The triggering showed excellent reversibility, for most samples generating a very similar modulus with each cycle of ordering and disordering, for up to six cycles.

The morphologies of the ordered and disordered states under visible light were determined by SAXS. These data show that M(B*s*A) (22-24(5)) forms highly ordered spheres at 30 wt% and below. Reversibly triggering was achieved in the 30 wt% sample, however the two lower concentrations identified by SAXS did not have enough mechanical integrity to show a transition in rheology. The remaining samples where triggering was achieved showed a weakly ordered spherical morphology. This was corroborated by the confirmation of the existence of a cubic phase using frequency sweeps in rheology. To the author's knowledge, this is the first example of a fully reversible light-controlled LCOT in a block polymer that does not have a liquid crystalline block.

The higher order structure arises when the molecular weight of the B*s*A block is lower,

and the concentration is not too high. It appears that this is potentially a result of slow ordering kinetics at higher concentrations and molecular weights. To achieve this higher degree of ordering for more samples in a reasonable time frame, smaller molecular weights could be used to the B*s*A block. In order to ensure that decreasing the molecular weight does not increase the LCOT beyond what is accessible for measurement on the rheometer, 150 ºC, the azobenzene incorporation could be increased.

Another goal of this project was to potentially locate a concentration where an order-order phase transition (OOT) could be triggered by light. This would operate under the same mechanism of the light-triggered LCOT, where a change in solubility of the polymer block in the ionic liquid could be triggered using azobenzene isomerization. This would drive an OOT using light, rather than relying on a thermal transition. Although there were no OOTs observed at the concentrations studied, the construction of the phase diagrams shows the intermediate concentrations where OOTs are possible. Future work will be focused on locating these order-order phase transitions and studying whether or not it is possible to trigger them using light.

4.6 Acknowledgments

Thanks to Prof. Chris Ellison for the use of his lab's spin coater and ellipsometer. Thanks to Dr. Sung-Soo Kim for help in preparing GI SAXS samples.

Portions of this work were performed at the DuPont-Northwestern-Dow Collaborative Access Team (DND-CAT) located at Sector 5 of the Advanced Photon Source (APS). DND-CAT is supported by Northwestern University, E.I. DuPont de Nemours & Co., and The Dow Chemical Company. This research used resources of the Advanced Photon Source, a U.S. Department of Energy (DOE) Office of Science User Facility operated for the DOE Office of Science by Argonne National Laboratory under Contract No. DE-AC02-06CH11357. Portions of this work were performed at Sector 8 of the Advanced Photon source. This research used resources of the Advanced Photon Source, a U.S. Department of Energy (DOE) Office of Science User Facility operated for the DOE Office of Science by Argonne National Laboratory under Contract No. DE-AC02-06CH11357.

Chapter 5

Formation of multicompartment ion gels by stepwise self-assembly of a thermoresponsive ABC triblock terpolymer in an ionic liquid[i] [ii]

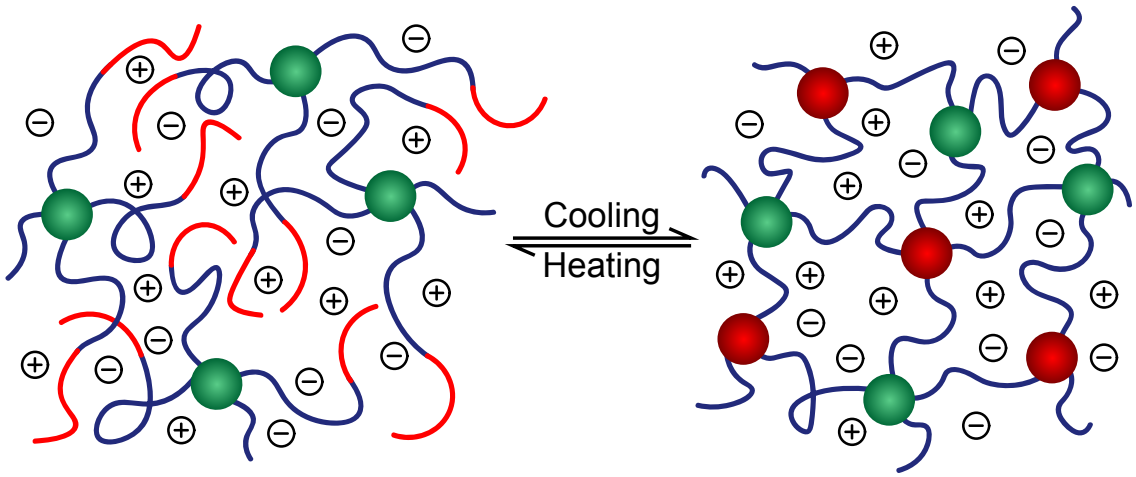

[i]Adapted with permission from Hall, C. C.; Zhou, C.; Danielsen, S. P. O.; Lodge, T. P. Formation of Multicompartment Ion Gels by Stepwise Self-Assembly of a Thermoresponsive ABC Triblock Terpolymer in an Ionic Liquid. *Macromolecules* **2016**. Copyright 2016 American Chemical Society.

[ii]This work was done in collaboration with Dr. Can Zhou and Scott Danielsen.

5.1 Preface

Ion gels are materials composed of an ionic liquid immobilized by a network-forming polymer, resulting in a soft solid with high ionic conductivity and tunable mechanical strength. Here, we demonstrate the thermoreversible gelation of a triblock terpolymer poly(ethylene-*alt*-propylene) -*block*- poly(ethylene oxide) -*block*- poly(*N*-isopropylacrylamide) (PON) in the ionic liquid 1-ethyl-3-methylimidazolium bis(trifluoromethylsulfonyl)imide (EMI TFSI). At high temperature, the polymers self-assemble into micelles with P cores and ON coronas. Below the upper critical solution temperature of PNIPAm in this ionic liquid, the N blocks aggregate, resulting in macroscopic gelation. The ion gels were characterized at concentrations of 1, 2, 5, and 10 wt%. Rheological measurements demonstrated that the PON ion gels had a greater percentage of elastically effective strands, leading to significantly higher mechanical strength, than was previously reported for the corresponding NON ion gels. This is consistent with the expectation that an ABC terpolymer architecture can suppress looping of the middle blocks. A combination of small-angle X-ray scattering, rheology, and dynamic light scattering demonstrated that PON ion gels exhibited a broader sol-gel transition, compared to previously studied PON hydrogels, a result which is attributed to the different thermoresponsive phase behavior of poly(*N*-isopropylacrylamide) in ionic liquids and water. Overall, this work demonstrates that the use of ABC triblock terpolymers allows for more efficient formation of strong ion gel networks at low polymer concentrations, which can be readily processed at moderate temperatures.

5.2 Introduction

Ionic liquids have been proposed for use in a wide variety of applications such as reusable, environmentally friendly solvents for catalysis,[46] electrolytes for electrochemical devices,[170,171,214–217] membranes for fuel cells and gas separations,[218,219] and as components in microfluidic devices.[22,220] However, neat ionic liquids cannot be utilized in many of these proposed applications because the liquid can easily flow or leak. A solution to this problem is to incorporate network-forming polymers to form ion gels. This strategy provides

mechanical strength, while maintaining or even exceeding the conductivity of neat ionic liquids.[168] Ionic liquids, in turn, have been shown to enhance the thermal stability and mechanical properties of network-forming polymers,[169] resulting in a synergistic relationship between polymer and ionic liquid.

Polymer networks are composed of polymer chains linked by covalent bonds[168,221,222] or physical association.[223,224] Physical association can be achieved through the use of ABA or ABC triblock polymer systems that are designed such that the A and C blocks exclude solvent, while the B block is well solvated. In an ideal network, every polymer chain will be elastically effective, with the solvated midblock connecting two spherical micelle cores formed by the endblocks. The properties of the gel can be tuned by changing the composition, architecture, molecular weight, and identity of the polymer. Incorporating stimuli-responsive endblocks allows reversible for sol-gel transitions that can be triggered on demand, enabling solvent-free processing of ion gels.[224] Poly(*N*-isopropylacrylamide) (PNIPAm) is a common thermoresponsive polymer that displays an upper critical solution temperature (UCST) in certain ionic liquids. Prior work demonstrated that the ABA triblock polymer PNIPAm-*block*-poly(ethylene oxide)-*block*-PNIPAm (NON) can form thermoreversible physical gel networks in ionic liquids at concentrations at and above 10 wt%.[175,176] NON imparted significant mechanical strength to the ionic liquid, while maintaining high conductivity.[175]

ABA systems, while effective, are not necessarily efficient, as they contain many elastically ineffective network defects where the polymer chains loop back into the same micelle core. To compensate for these network defects, larger amounts of polymer are necessary to achieve the same mechanical strength as an ideal network. An appealing alternative is the use of an ABC triblock terpolymer, where the two endblocks are mutually insoluble. A cartoon comparison between ABA and ABC ion gels is depicted in Figure 5.1. We previously studied the polymer poly(ethylene-*alt*-propylene)-*block*-PEO-*block*-PNIPAm (PON) in aqueous solutions.[225–227] This polymer forms a hydrogel via a stepwise micellization-gelation mechanism. Poly(ethylene-*alt*-propylene) (PEP) is insoluble in water at all temperatures, and forms micelle cores. In water, PNIPAm displays a lower critical solution temperature (LCST), giving rise to thermoreversible formation of micelle cores on heating.

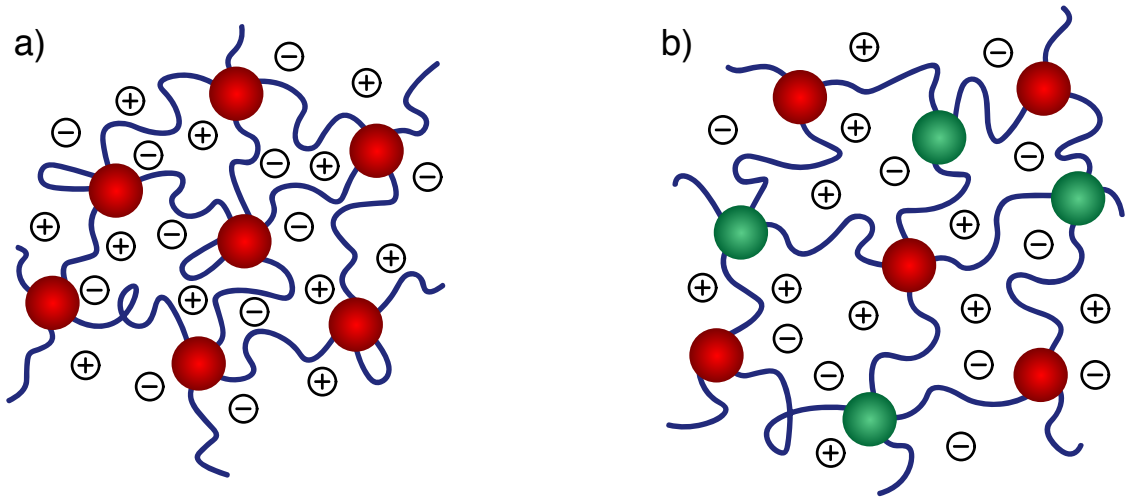

Figure 5.1: Physically associated ion gel formed by (a) ABA and (b) ABC triblock terpolymers.

The stepwise formation of the two cores removes the possibility for loops, resulting in a more efficient gel network relative to aqueous NON gels.[225] In particular, a detailed study by small-angle neutron scattering with contrast variation confirmed that the structure of PON hydrogels is consistent with the cartoon in Figure 5.1.[227]

In this work, we have extended the same PON terpolymer system to the ionic liquid 1-ethyl-3-methylimidazolium bis(trifluoromethylsulfonyl)imide (EMI TFSI) by forming a thermoresponsive ion gel that is presumably free from loops. In this case the PEP block is insoluble under all conditions, whereas the PNIPAm block is soluble at higher temperatures; consequently, gelation occurs on cooling. The strength and efficiency of the gels were analyzed at low concentrations of polymer. The results were compared to NON ion gels in terms of gel formation efficiency, and to PON hydrogels to elucidate whether the inverse phase behavior of PNIPAm has a significant effect on the properties of the gel.

5.3 Experimental

Materials

All reagents were used as received unless otherwise noted. 2,2'-Azobisisobutyronitrile (AIBN) and *N*-isopropylacrylamide (NIPAm) were purchased from Sigma Aldrich and

purified by recrystallization from methanol and benzene/*n*-hexane (65/35 v/v), respectively. 1,4-dioxane was purified by refluxing the solvent over Na (1 % w/v) and benzophenone (0.2% w/v) under an inert atmosphere until the blue color of the benzophenone ketyl radical anion persists, followed by distillation. 1-ethyl-3-methylimidazolium bis(trifluoromethylsulfonyl)imide (EMI TFSI) was synthesized by an amine quaternization and anion exchange process according to previously reported procedures.[225]

Block polymer synthesis

PON was synthesized by Dr. Can Zhou, as previously reported.[225–227] The poly(ethylene-*alt*-propylene) (PEP, P) and poly(ethylene oxide) (PEO, O) blocks were synthesized by anionic polymerization of isoprene, end capping with ethylene oxide, catalytic hydrogenation, and anionic polymerization of ethylene oxide, respectively.[228,229] The poly(N-isopropylacrylamide) block (PNIPAm, N) was then added via RAFT polymerization. The synthesis of NON, performed by Scott Danielsen, was achieved analogously by growing the PNIPAm blocks from an α,ω-dihydroxy-PEO macroinitiator via RAFT polymerization. In both cases the RAFT agent was removed after polymerization, as previously described. The resulting polymers were characterized with ^{1}H NMR spectroscopy and size exclusion chromatography (SEC), and their properties are summarized in Table 5.1.

Sample [a]	N_P [b]	N_O [b]	N_N [b]	f_P [c]	f_O [c]	f_N [c]	$Đ$ [d]
PON(3-25-11)	45	565	97	0.10	0.62	0.28	1.1
NON (10-20-10)	–	454	91	–	0.49	0.51	1.06

Table 5.1: Molecular characteristics of ABC and ABA triblock polymers. [a] The numbers in parenthesis after the sample name represent the number average molecular weight of each block in kg/mol. [b] The number average degrees of polymerization were determined by ^{1}H NMR spectroscopy. [c] The volume fractions were calculated from the molecular weights of the block and the room temperature densities: ρ(PEP) = 0.856 g/cm^3,[230] ρ(PEO) = 1.12 g/cm^3,[231] and ρ(PNIPAm) = 1.07 g/cm^3.[232] [d] The dispersity was measured using SEC with THF (PON) or THF/ *N,N,N',N'*-tetramethylethylenediamine (NON) as the eluting solvent.

PNIPAm synthesis

NIPAm (2.014 g, 0.0178 mol), AIBN (0.9 mg, 0.0054 mmol), and cumyl benzodithioate (16.45 mg, 0.0604 mmol) were dissolved in 10 mL of 1,4-dioxane. The reaction mixture was degassed through three freeze-pump-thaw cycles and reacted at 75 °C for 8.75 hours. The reaction was then quenched by cooling to 0 °C, and the product was precipitated in 500 mL of pentane three times. The resulting polymer was dried under vacuum at 50 °C overnight. The final PNIPAm polymer had a number average molecular weight of 13 kDa and a dispersity of 1.05 as determined by ^{1}H NMR spectroscopy and SEC, respectively.

Sample preparation

Ion gels were prepared by use of a co-solvent. Bulk polymer and ionic liquid were combined to achieve the desired concentration with an overall weight of 2–3 g. CH_2Cl_2 was added to achieve dissolution of the polymer. The solution was stirred for two hours, then passed through an 0.45 μm filter and purged overnight with N_2 to remove the co-solvent. The resulting ion gels were dried under vacuum to baseline pressure at 70 °C for 48 h.

Cloud point measurements

The cloud points of various concentrations of the PNIPAm homopolymer in EMI TFSI were determined by optical transmittance measurements. The samples were placed in a temperature-controlled oil bath and heated above the UCST. The sample was cooled at a rate of roughly 1 °C/min with continuous stirring. The temperature dependence of transmittance at 632.8 nm was monitored using a photomultiplier tube. The cloud point was defined as the temperature at which the transmission dropped to 80%.

Rheology

Rheological measurements were taken on an AR-G2 rheometer with parallel plate geometry, 40 mm diameter stainless steel plates with a 1 mm gap were used. The gap was adjusted at each temperature to compensate for the thermal expansion of the tool set. The Peltier-

controlled lower plate provided temperature control. A cover was placed over the fixture to prevent ambient moisture from affecting the measurements. Dynamic strain sweeps were performed at 1, 10, and 100 rad/s to determine the linear viscoelastic regime of the ion gels for each temperature range. The upper limit of the linear viscoelastic regime is defined as the critical strain, γ_c, below which the dynamic modulus remains invariant. The γ_c for the 10 wt% PON in ionic liquid at 70 °C was greater than 100%, whereas the ion gel at 0 °C had a critical value of 70%, shown in Figure 5.2. All further measurements were taken at or

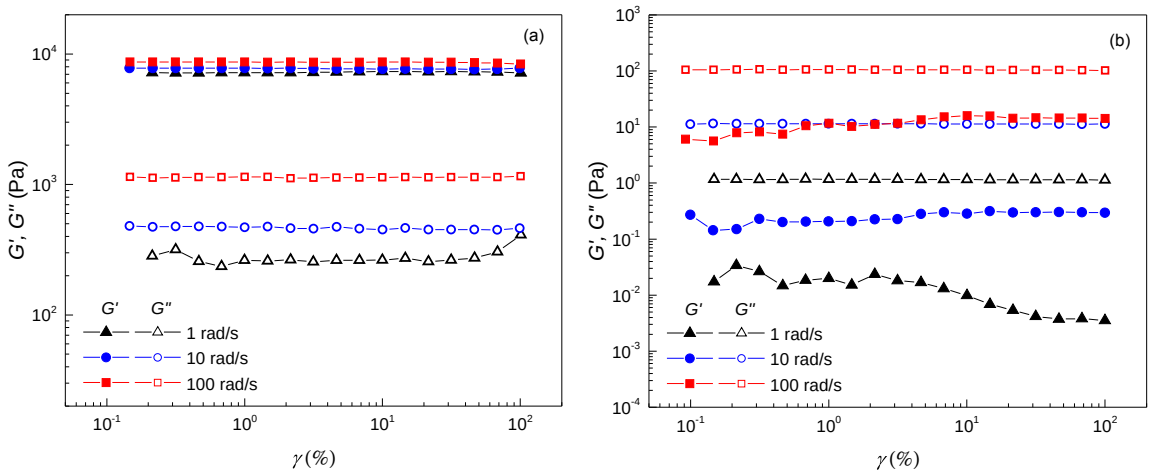

Figure 5.2: Dynamic strain sweeps of 10 wt% PON(3-25-11) at (a) 0 °C and (b) 70 °C. Measurements taken from 0.1 to 100% strain, at frequencies ω=1, 10, and 100 rad/s.

below 10% strain in order to remain within the linear viscoelastic regime. The response of the dynamic storage modulus (*G'*) and loss modulus (*G"*) were observed in a temperature sweep with ramp rates of 1, 0.5, and 0.2 °C/min, and a constant frequency of 10 rad/s. The intersection of the *G'* and *G"* curves was taken as the critical gelation temperature of the ion gel. Dynamic frequency measurements were also taken at various temperatures within the linear viscoelastic regime.

Dynamic light scattering

Dynamic light scattering measurements were performed on a 0.05 wt% solution of PON in EMI TFSI over a range of temperatures from 5 to 60 °C. The solutions were passed through 0.45 µm filters into glass tubes (ID = 0.25 in). The measurements were carried out on a Brookhaven BI-200SM DLS system equipped with a Mini L-30 HeNe laser operating

at 637 nm, a BI-NDO detector, and a TurboCorr correlator. The intensity autocorrelation functions were determined at three scattering angles between 60° and 120°. The hydrodynamic radius was calculated using the cumulant method, as described previously.[225]

Small angle X-ray scattering

Small angle X-ray scattering (SAXS) experiments were performed on the 5 wt% sample at the 12-ID-B beamline at the Advanced Photon Source, Argonne National Laboratory. The sample-to-detector distance was fixed at 2 m, and the detector used was a Pilatus 2M. The sample temperature was controlled at 67 °C by a Linkam capillary stage. The 2D data were reduced by azimuthal integration to give intensity as a function of the scattering wave vector, q.

5.4 Results

Cloud point of PNIPAm

The cloud points of two solutions of PNIPAm homopolymer in EMI TFSI, show in Figure 5.3, were used to approximate the UCST. The resulting liquid-liquid phase separation

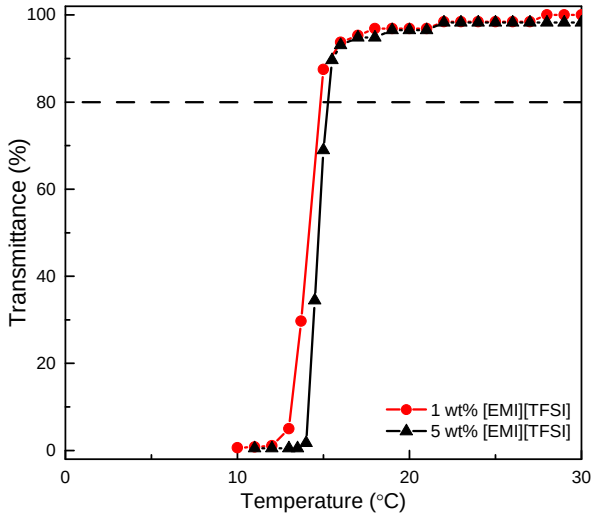

Figure 5.3: Cloud point of 1 and 5 wt% PNIPAm in EMI TFSI, measured at a cooling rate of approximately 1 °C/min. Dashed line indicates cloud point, the temperature at which the transmittance of the solution is 80%.

caused a drop in transmittance as the solution became more turbid. For a 1 wt% solution of 13 kg/mol PNIPAm, the cloud point was 14 °C, and for the 5 wt% solution the cloud point was 15 °C. Thus, over this modest range there is at most a slight concentration dependence in the UCST of PNIPAm, in agreement with previous reports.[61,62]

Gelation of PON triblocks in EMI TFSI

The thermoresponsive gelation of PON arises from the different solubilities of the three blocks, similar to what has been observed for the same polymer in water. In EMI TFSI, PEP is insoluble at all temperatures, PEO is soluble at all temperatures, and PNIPAm displays UCST phase behavior. Above the UCST, PON forms micelles with a PEP core and PEO-PNIPAm coronae.[225,226] This is illustrated as a cartoon in Figure 5.4, showing the green PEP-core micelles at all temperatures, and the reversible formation of red PNIPAm-core micelles upon heating. Dilute solutions of micelles (concentrations $\leq$10 wt%) do

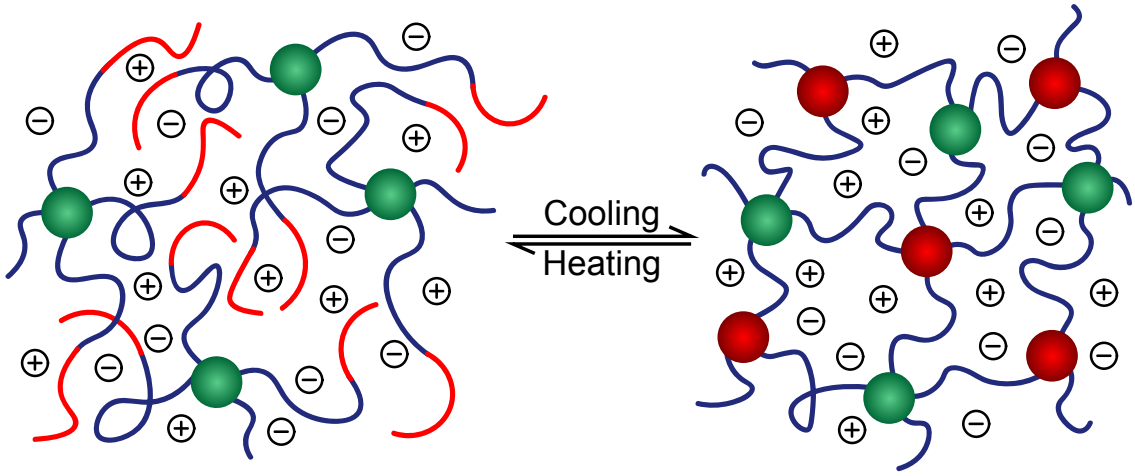

Figure 5.4: Cartoon illustrating the low temperature PEP-core micelle solution which, upon heating, forms a gel network by thermoreversible association of PNIPAm chains. Due to the insolubility of the two blocks, shown in red and green, each blue PEO chain will bridge two micelle cores, forming an elastic network.

not exhibit long-range order or form gels and thus behave as viscoelastic fluids.[233] As the solution is cooled below the UCST the PNIPAm coronae aggregate to form PNIPAm microdomains. These PNIPAm cores are bridged by PEO to the PEP cores, producing an elastic network.[226]

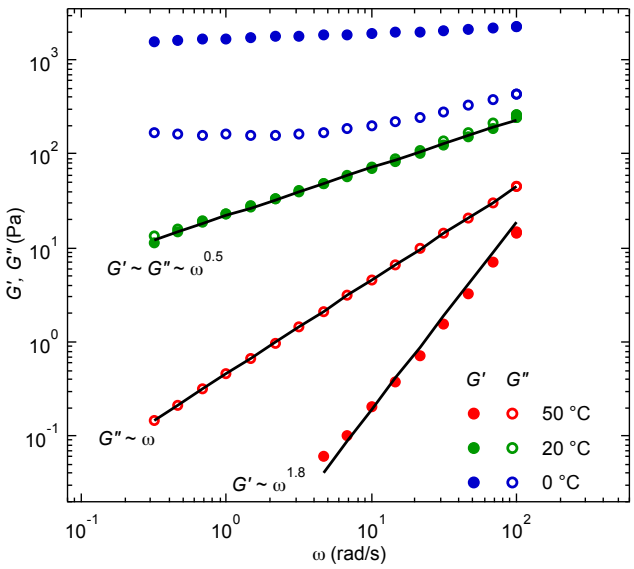

Figure 5.5: Dynamic frequency sweep of 5 wt% PON (3-25-11) in EMI TFSI. Three representative temperatures are shown, with the solid lines giving power law fits of the data.

We observed the gelation of PON(3-25-11) in EMI TFSI and then characterized the networks formed at low temperatures. Dynamic frequency sweeps were performed across a range of temperatures, with three representative temperatures of 0, 20, and 50 °C for the 5 wt% sample shown in Figure 5.5. At 0 °C, *G'* > *G"* and both moduli remain invariant with respect to frequency, indicative of solid-like behavior. At 20 °C, *G'* and *G"* overlap and follow the same power law dependence: $G' \approx G'' \sim \omega^{0.5}$. This dependence occurs at the transition between liquid-like and solid-like behavior, giving the sol-gel transition temperature (T_{gel}).[234] At 50 °C, *G"* > *G'*, consistent with liquid-like behavior. The power law fits display typical terminal rheological behavior for a viscoelastic fluid, G' $\sim \omega^{1.8}$ and G" $\sim \omega^{1}$. The slight deviation of G' from the predicted dependence (ω^2) is likely a result of uncertainties in the measurement for low values of the storage modulus.

Dynamic temperature sweeps of 1, 2, 5, and 10 wt% PON samples, shown in Figure 5.6, demonstrate the thermoreversible gelation of PON arising from the assembly of PNIPAm micelle cores. *G'* and *G"* were measured across a range of temperatures from 70 °C to 0 or –10 °C, with a temperature ramp of ±1 °C/min. All concentrations show a similar rheological response, suggesting that all samples have formed network structures. At high temperatures, the system behaves as a viscoelastic fluid. Upon cooling, *G'* and *G"* both

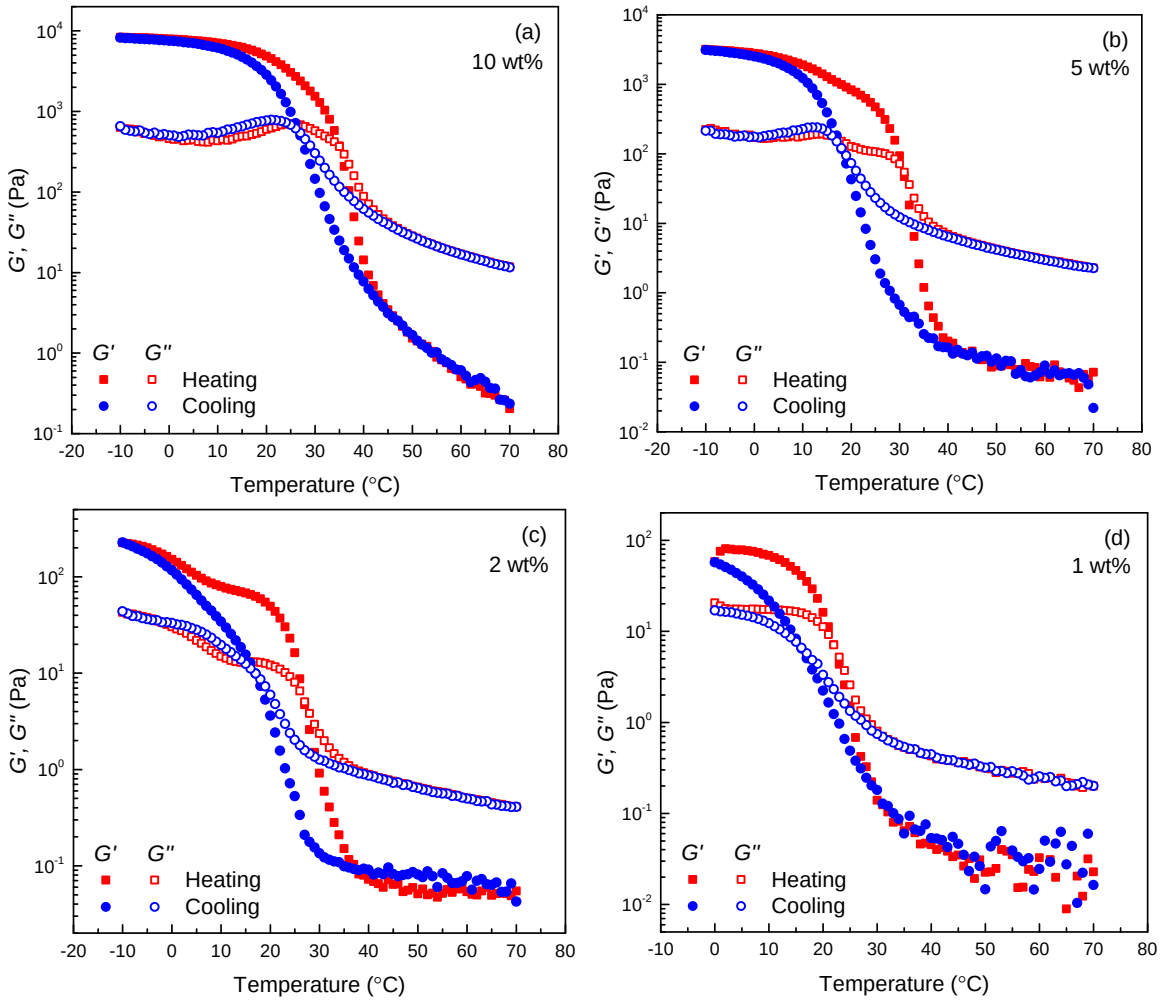

Figure 5.6: Dynamic temperature sweeps of (a) 10 wt%, (b) 5 wt%, (c) 2 wt%, and (d) 1 wt% PON in EMI TFSI. Measurements were taken at a cooling/heating rate of 1 °C/min and a frequency ω = 10 rad/s.

increase sharply, crossing to give solid-like behavior where *G'* is greater than *G"*. The temperature at which *G'* and *G"* intersect is taken as the sol-gel transition temperature. For 5 wt% PON, this intersection occurs at 18 °C, which agrees well with the T_{gel} determined by the dynamic frequency sweep measurements. Heating the sample produced a similar curve, with the gel-sol transition determined on heating occurring at a slightly higher temperature than that measured on cooling. This modest hysteresis (∼10 ºC) is in agreement with some previous studies of PNIPAm-containing block polymer micelles and gels in both water and ionic liquids.[176,235] Upon heating, the network structure melts via the disruption of the physical association of the PNIPAm blocks. The width of this hysteresis loop remained

invariant with respect to small changes in the heating or cooling rate (Figure 5.7).

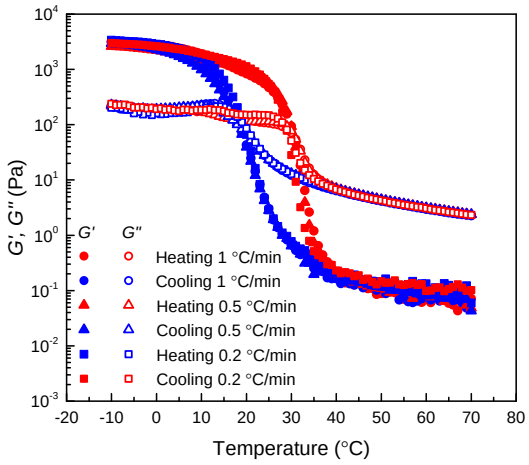

Figure 5.7: Dynamic temperature sweeps of 5 wt% PON(3-25-11) in EMI TFSI measured with heating rates of 1, 0.5, and 0.2 °C/min and a frequency ω =10 rad/s.

A notable feature in the dynamic temperature sweep is a small increase in the loss modulus between the lowest experimental temperature and the gelation point, most distinct upon heating. We hypothesize that this feature results from partial swelling of the PNIPAm micelle cores with ionic liquid. This swelling followed by PNIPAm dissociation upon heating would explain what appears to be a two-step process in the rheology. This small penetration of solvent into the cores is more apparent at lower concentrations, as the network on the whole is not as strong. This feature becomes less distinct with a slower heating rate, consistent with this hypothesis, as shown in Figure 5.8.

PEP-core micelles

Small angle X-ray scattering measurements were performed on a 5 wt% PON in EMI TFSI solution at elevated temperatures. Figure 5.9 shows the scattering pattern for this sample at 67 ºC, a temperature above the UCST of PNIPAm. At this elevated temperature, the PNIPAm blocks are fully solvated, as shown by the terminal flow observed in rheology. This ensures that the only spherical particles in solution would be PEP-core micelles. The scattering pattern was fit using a hard sphere interaction potential with the Percus-Yevick approximation as a closure.[236] The fit gives a micelle core radius of 5.1$\pm$6 nm and a volume

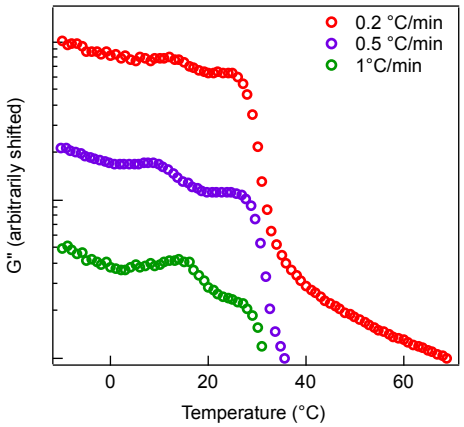

Figure 5.8: Dynamic temperature sweeps showing G" for 5 wt% PON(3-25-11) in [EMI][TFSI] measured with heating rates of 1, 0.5, and 0.2 °C/min and a frequency ω=10 rad/s. Data are arbitrarily shifted for clarity, to show the change in the two-step process of gel dissociation upon heating.

fraction of spheres of 0.0185. From these data, q^* was determined to be 0.189 nm^{-1}, corresponding to an average micellar spacing of 33 nm.

Dynamic light scattering (DLS) was also utilized to obtain the size of the PEP-core micelles, shown in Figure 5.10. These measurements were performed by Dr. Can Zhou. A dilute solution of 0.05 wt% PON(3-25-11) in EMI TFSI was measured at a range of temperatures to observe the particle size as a function of temperature. Interestingly, the DLS data showed no micelle aggregation when decreasing the temperature well below the UCST of PNIPAm in [EMI][TFSI], maintaining a single peak with relatively low dispersity. This suggests that the 0.05 wt% solution is too dilute for significant gel formation to occur. Rheological measurements showed that gelation could be observed up to 1 wt%, and no samples with lower concentrations were tested.

Gelation of NON triblocks in EMI TFSI

The thermoreversible gelation of NON(10-20-10) depends solely upon the UCST phase separation of PNIPAm from EMI TFSI. While this simplifies the synthesis of the polymer, it introduces the possibility to form defects in the elastic network where both endblocks are inserted in the same micelle core. This forms a loop, and does not contribute to the formation of a gel network, as shown in Figure 5.1a. We performed the same rheological

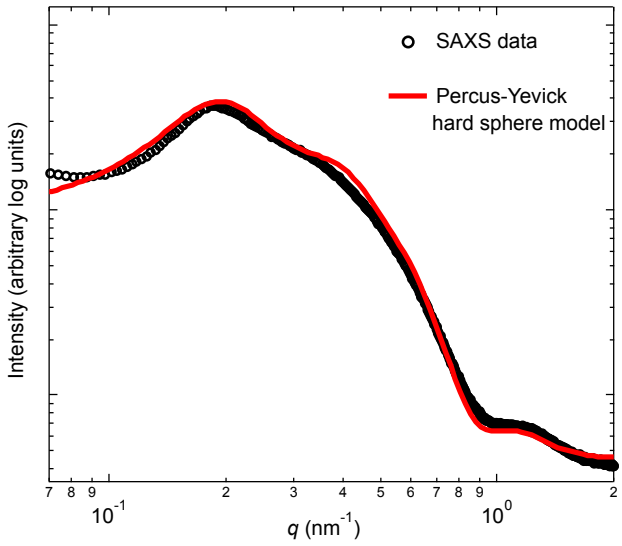

Figure 5.9: Small angle X-ray scattering of 5 wt% PON(3-25-11) in [EMI][TFSI] (black open circles) with fitting by the Percus-Yevick hard sphere model (solid red line).[236]

measurements for the NON(10-20-10) gels at concentrations of 10, 5, and 2 wt%. Figure 5.11a shows the dynamic frequency sweep data for 10 wt% NON(10-20-10) in EMI TFSI. The behavior is similar to what was observed for PON in Figure 5.5, where *G'* at 0 ºC is invariant with frequency, *G'* and *G''* overlap at 20 ºC and scale with $\omega^{0.5}$, indicating the gel point, and terminal flow of $G' \sim \omega^2$ and $G' \sim \omega$ at 50 ºC. Temperature sweeps were also performed on the NON(10-20-10) ion gels, showing gelation for 10 and 5 wt% (Figures 5.11b and c, respectively) upon cooling. The increase in loss modulus noted in Figure 5.8 was also observed here, which would be consistent with this feature resulting from the PNIPAm micelle cores. The gelation temperature appears to increase from 10 wt%, at 27 ºC, to 5 wt%, at 30 ºC. However, the observed gelation on cooling for the 10 wt% sample is relatively broad, leading to ambiguity in the exact gelation temperature. This broad overlap may be a result of both end blocks being PNIPAm. Finally, gelation is not observed in the 2 wt% sample, shown in Figure 5.11d. At both the highest and lowest temperatures measured, *G''* is greater than *G'*, indicating that the sample is a liquid both above and below the UCST of PNIPAm. Around the UCST of PNIPAm both *G'* and *G''* increase, and the modulus is overall higher at the lowest temperatures than at the highest temperatures. This indicates that the PNIPAm present in solution is still aggregating, but

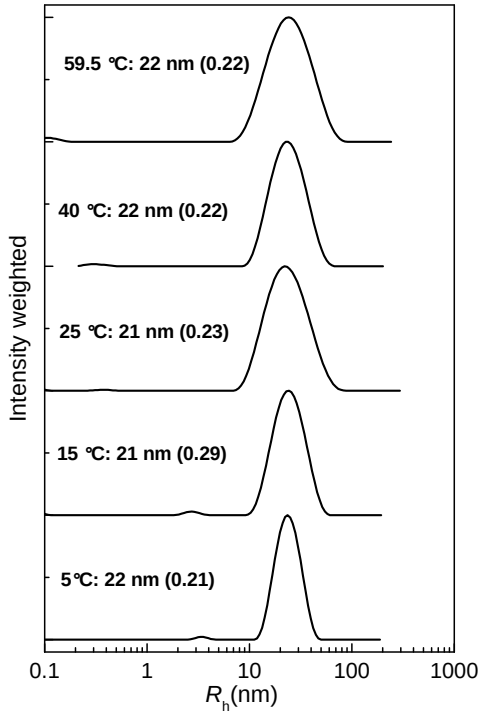

Figure 5.10: Distribution of hydrodynamic radii for a solution of 0.05 wt% PON(3-25-11) in EMI TFSI at and angle of 90°, with indicated mean hydrodynamic radii and dispersities calculated from the cumulant method.

it is not forming a sufficiently well-connected network to give a solid-like response at low temperatures.

5.5 Discussion

Efficiency of gel network formation

The dynamic temperature sweeps in Figure 5.6 exhibit a network plateau of *G'* at low temperatures for all concentrations examined. This plateau can be characterized by the modulus G_x, taken as the value of *G'* at the temperature for which the loss tangent (tan δ = *G" / G'*) displays a minimum. As shown in Figure 5.12, G_x increases with increasing PON concentration. A power law fit to the data gives a slope of 2.3 $\pm$ 0.2, in excellent agreement with the predicted value of 2.3 for both solutions of entangled polymers[235,237] and gels swollen with good solvents.[120]

The G_x for triblock polymer gels with unentangled midblocks can be modeled with

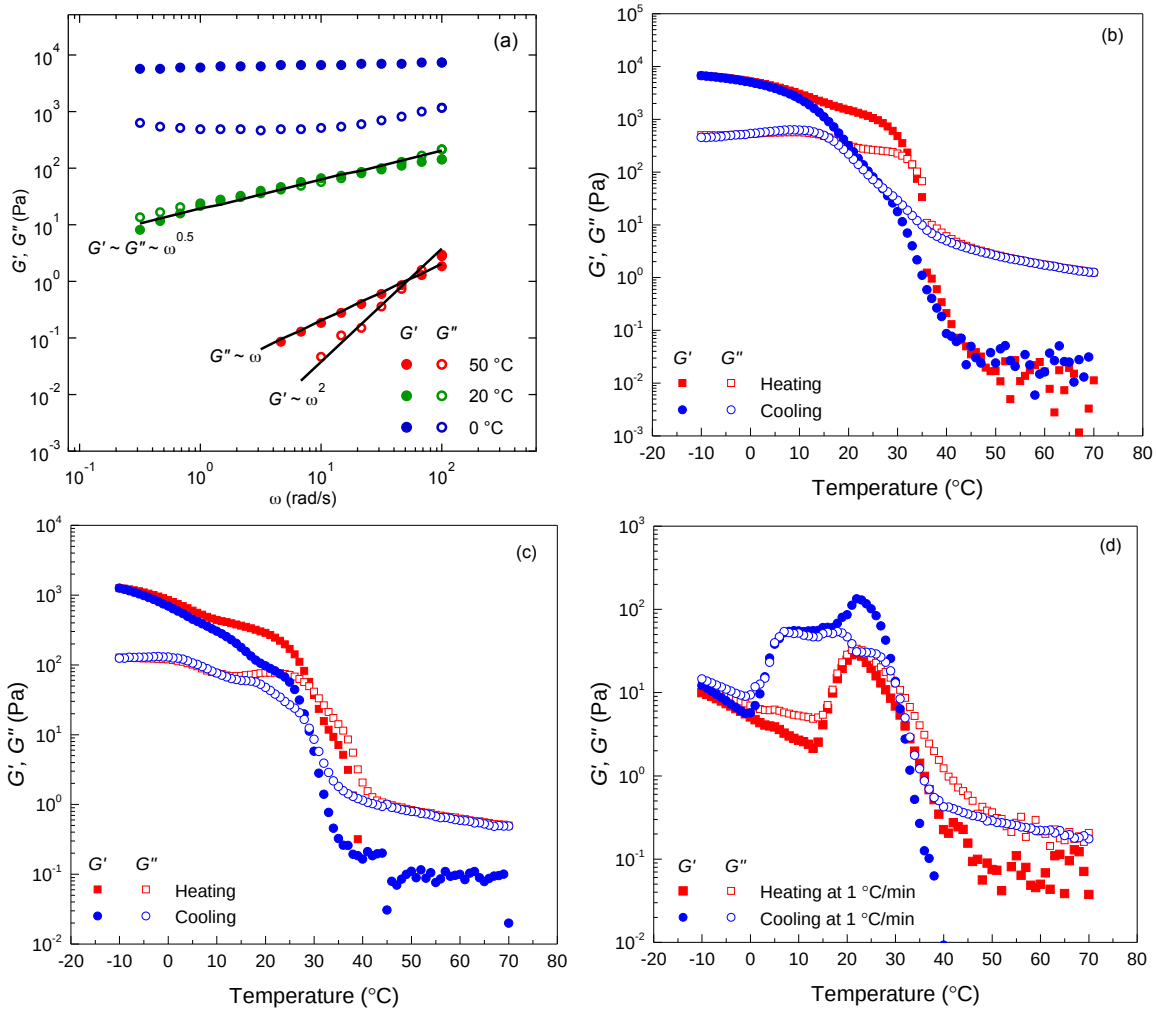

Figure 5.11: (a) Dynamic frequency sweeps of 10 wt% NON(10-20-10), with solid lines showing power law fits of the data. Dynamic temperature sweeps of (b) 10 wt%, (c) 5 wt%, and (d) 2 wt% NON(10-20-10) in EMI TFSI. Temperature sweep measurements were taken at a cooling/heating rate of 1 °C/min and a frequency ω = 10 rad/s.

classical rubber elasticity theory:

$$G = \nu kT = fnkT \tag{5.1}$$

where v is the number density of elastically effective chains, k is the Boltzmann constant, T is the absolute temperature, f is the fraction of elastically effective chains, and n is the chain number density. The number of entanglements per polymer chain in a good solvent,

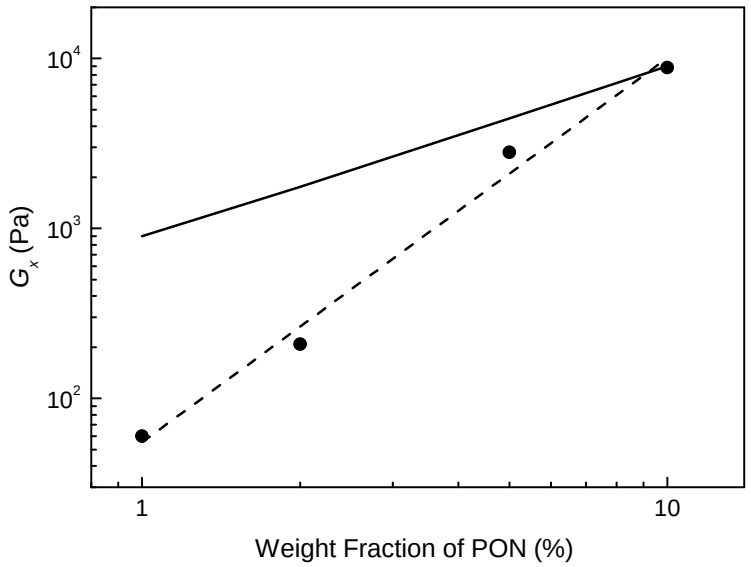

Figure 5.12: Concentration dependence of modulus (G_x) for PON(3-25-11) in EMI TFSI with 1–10 wt% polymer. The dashed line is a power law fit to the measured G_x, and the solid line represents the calculated G_x of an ideal network with unentangled midblocks.

n_e, can be estimated by the following equation:

$$n_e = N_e \phi_p^{5/4} = \frac{M}{M_e} \phi_p^{5/4} \tag{5.2}$$

where N_e is the number of entanglements per polymer chain in the melt, M is the polymer molecular weight, M_e is the polymer entanglement molecular weight in the melt, and ϕ_p is the polymer volume fraction.[238,239] For a 10 wt% solution of PON in EMI TFSI, M_{PEO} = 25 kg/mol, M_e, PEO = 1.6 kg/mol, and ϕ_{PEO}= 8.7%, giving an estimate of 0.7 entanglements per molecule. As this is less than 1 for the most concentrated sample examined, it is reasonable to assume that entanglements of the PEO midblock do not provide a significant contribution to the measured modulus. This allows us to assume that G_x arises solely from the physically associated network, enabling the use of classical rubber elasticity theory to estimate the number of elastically effective chains in the ion gels. Rearranging Equation 5.1 gives:

$$f = \frac{G_x}{nkT} \tag{5.3}$$

where nkT is the storage modulus of an ideal network in which the fraction of elastically effective chains is 1. The resulting data for G_x, f, and γ_c for the four tested concentra-

tions of PON in EMI TFSI are collected in Table 5.2. As the concentration of PON is

Conc. (wt%) [a]	G_x (Pa) [b]	f [c]	T_{gel} (ºC) [d]	γ_c (0 ºC) [e]	γ_c (70 ºC) [f]
PON(3-25-11)					
10	8850	98%	27	70%	>100%
5	2800	63%	18	55%	>100%
2	210	12%	17	35%	>100%
1	60 [g]	7%	16	0.4%	>100%
NON(10-20-10)					
10	6710	79%	28	35%	>100%
5	1260	30%	30	1.5%	>100%

Table 5.2: Characteristics of ion gels in EMI TFSI. [a] Concentration. [b] Modulus. [c] Percent of elastically effective PEO chains. [d] Critical gelation temperature determined as the point at which *G'=G"* in dynamic temperature sweep measurements. [e] Critical strain at 70 °C, determined from the dynamic strain sweep with a frequency ω = 10 rad/s. [f] Critical strain at 0 °C, determined from the dynamic strain sweep with a frequency ω = 10 rad/s. [g] The plateau modulus was chosen as the value of *G'* at the lowest measured temperature (0 °C) as no minimum loss tangent was obtained.

decreased from 10 wt% to 1 wt%, the percent of elastically effective chains drops from 98% to 7%. This matches Figure 5.12, where the lowest concentration of PON shows a large deviation of the experimental data from an ideal gel network. As the concentration increases, the two converge, suggesting that almost all of the polymer chains are elastically effective for the 10 wt% sample. From this, we infer that the ABC terpolymer strategy was successful in creating a network essentially free from looping defects. The deviation from ideal gel behavior in lower concentration samples occurs because the concentration of polymer is too low to produce a uniform network that spans the entire sample. The rheological measurement averages over regions that are not well connected in the network. Small amounts of interconnected micelle cores impart the solid-like behavior, but the low number of elastically effective chains means that the network is relatively short-range, giving large regions of ionic liquid without structure-forming polymer. Note that all the ion gel samples are optically transparent due to the similarity in refractive indices of the polymer and ionic liquid, and thus in this system optical clarity cannot be used as a diagnostic of

spatial heterogeneity.

The T_{gel} measured on cooling decreases as the polymer concentration decreases, from 27 to 16 °C over polymer concentrations from 10 to 1 wt%. This agrees with previous reports discussing the concentration dependence of the UCST of PNIPAm in EMI TFSI.[61,62] The critical strain of PON at 70 °C, when it behaves as a viscoelastic fluid, is large and does not have a concentration dependence. At 0 °C, the critical strain decreases from an exceptional 70% to 0.4% with decreasing PON concentration. This decreased gel toughness is correlated with the drop in the number of elastically effective chains for lower concentration samples, and the lack of homogeneity of the network across the macroscopic sample. The critical strain for the 10 wt% sample is quite high, presumably as a result of an effectively defect-free network.

Improved network efficiency of ABC over ABA triblocks

The PON(3-25-11) ion gels were also compared to the corresponding thermoreversible ABA triblock system, NON(10-20-10) in EMI TFSI. The NON ion gels were tested at concentrations of 10, 5, and 2 wt%, with a representative plot in Figure 5.13 showing the cooling portion of the dynamic temperature sweeps for the three concentrations compared to the corresponding PON ion gels. At the high concentrations of 5 and 10 wt%, the low temperature behavior is similar, in terms of the modulus; the breadth of the gelation is also similar. This was not the case in water, where the NON system had broad gelation, but the PON was very narrow.[226] This result was interpreted in terms of the presence of micelles with PNIPAm blocks at the edge of the coronas giving a structure that facilitated gelation; this argument clearly does not apply in the ionic liquid. However, while the PON triblock terpolymer created gels at all tested concentrations, NON only shows a clear sol-gel transition at 5 and 10 wt%, and poor or no gel formation at 2 wt%. In this respect, as in water, the presence of micelles improves the efficiency of gelation at low concentrations, and the ABC system outperforms the ABA equivalent (Figures 5.13b and c).

In more detail, G_x is lower at the two concentrations where NON does form a gel. At 10 and 5 wt% polymer the G_x is 6710 and 1260 Pa, corresponding to a fraction of bridging

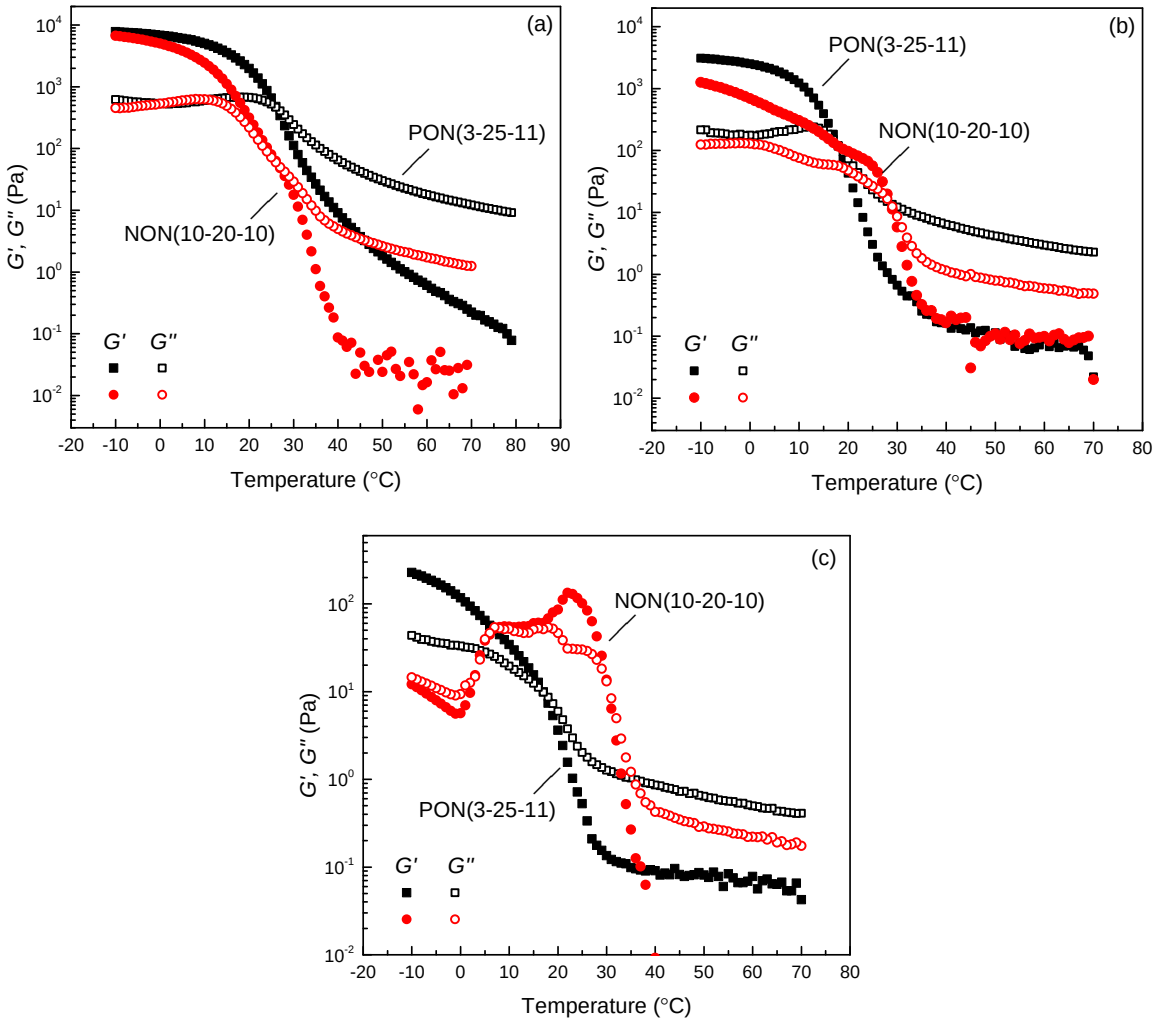

Figure 5.13: Temperature dependent shear moduli (*G'* and *G"*) of PON and NON at (a) 10 wt%, (b) 5 wt%, and (c) 2 wt%. Measured with a frequency ω = 10 rad/s and a cooling rate of 1 °C/min.

PEO chain of 79% and 30%, respectively (Table 5.2). The molecular weights of the two polymers are very similar (39 and 40 kg/mol for PON and NON, respectively), giving a very similar number of chains in solution at each wt%. The modulus G_x of 10 wt% NON is consistent with that found in previous work ($G_x \approx$ 5000 Pa for NON(3-23-3)).[175] The critical strains at 0 °C of the NON ion gel are also lower than those for PON. Overall, these data support the conclusion that PON forms a stronger network at a given concentration than NON. The reduction of looping network defects in PON gives an increased fraction of elastically effective chains for a given polymer concentration, enabling the gel to withstand

higher strains.

Mechanism of PNIPAm phase separation in EMI TFSI compared to water

A comparison of the gelation of PON in water versus EMI TFSI shows similar thermoreversible gelation behavior, but with a few key differences. The sol-gel transition in water was achieved with heating, as PNIPAm displays LCST phase behavior in water. A 5 wt% PON in water solution corresponds to a polymer volume fraction (ϕ_{PON}) of 4.6%. A 3.4 wt% solution of PON in EMI TFSI would achieve the same ϕ_{PON}, so we compare both the 2 and 5 wt% PON in EMI TFSI solutions to the 5 wt% hydrogel to give a more meaningful comparison between the two solvents. Plots overlaying the shear moduli of the two solvent systems are shown in Figures 5.14a and b, with the storage and loss moduli plotted in separate graphs for clarity. The storage modulus of the ion gel is twelve times higher than the hydrogel at 5 wt%, and about equal at 2 wt%. For equal ϕ_{PON}, or 3.4 wt% PON in EMI TFSI, these results suggest that the ion gel would have a slightly higher modulus.

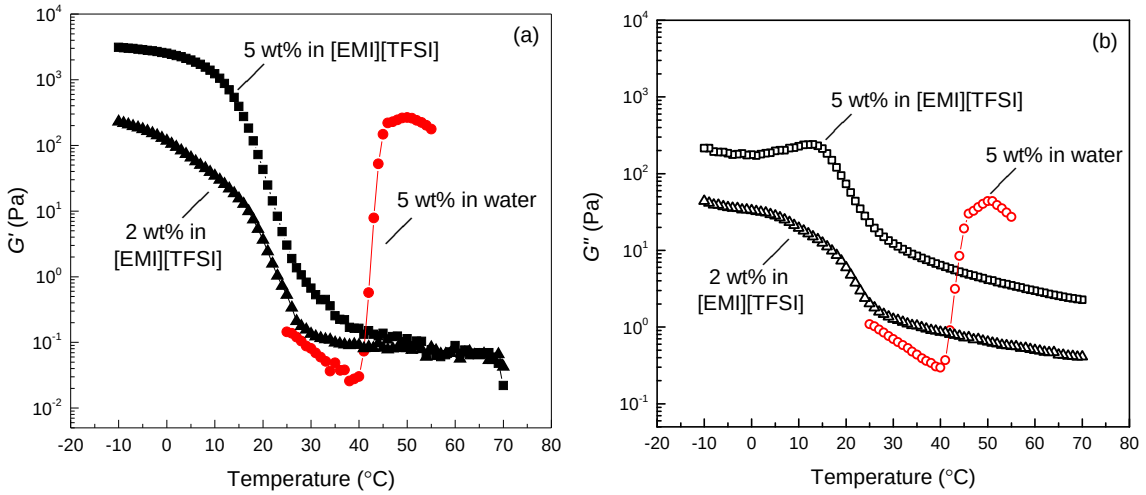

Figure 5.14: Temperature dependent shear moduli, (a) *G'* and (b) *G"* of PON(3-25-11) 5 wt% in [EMI][TFSI] vs water.[226] Measured with a frequency, ω, of 10 rad/s and a cooling (EMI TFSI) or heating (the same polymer in water) rate of 1 °C/min.

Another key difference between the two solvent systems is the breadth of the gelation transition. The hydrogel exhibits a much sharper sol-gel transition compared to the ion gel.

A broad gelation transition of PON in EMI TFSI is observed for all concentrations, (*ca.* 30 ºC) seen in Figure 5.6, whereas the previously reported data of the hydrogel[226] show a consistently (and remarkably) sharp gelation (*ca.* 2–4 ºC). There is a slight broadening of the gelation on decreasing concentration for both solvents, but the trend between water and ionic liquid remains the same. Previous investigations of the phase transitions of PNIPAm in water and ionic liquid show that the mechanisms causing the phase transition are fundamentally different.[64,240,241] These results suggest that the mechanism driving the UCST phase transition of PNIPAm in the ionic liquid is inherently more gradual than the LCST phase transition. The broader gelation in ionic liquid agrees with previous results found for PNIPAm homopolymer undergoing phase separation through a UCST.[61,235] In general, the LCST of aqueous solutions of PNIPAm is unique among non-ionic polymers for the sharpness of the transition, as well the invariance of transition temperature with changes in molecular weight and concentration.[144] Presumably this difference reflects the relative strength of the temperature dependence of the underlying free energy of mixing, *i.e.*, the enthalpic versus entropic contributions.

By considering the chain overlap concentration, micelle number density, and the intermicellar distance, we conclude that the breadth of the gelation is a function of a difference in the phase separation behavior rather than concentration. Considering the fluid state of the two systems, we analyzed the PEP-core micelles in ionic liquid and compared them to those formed in water. The PEP-core micelles formed at high temperatures in ionic liquid were characterized by SAXS (Figure 5.9) and fit with the Percus-Yevick hard sphere model, accounting for a diffuse sphere boundary and a distribution in the size of the micelle cores.[236] The model gave a core radius of 5.1 nm with a standard deviation in the core size of 0.6 nm.

This core radius was used to calculate the average number of polymer chains in each micelle core, or the aggregation number, N_{agg} :

$$N_{agg} = \rho_{PEP} \frac{N_A \left(\frac{4\pi}{3} R_c^3 \right)}{M_{PEP}} \tag{5.4}$$

where ρ_{PEP} is the bulk density of PEP, N_A is Avogadro's number, R_c is the micelle core

radius, and M_{PEP} is the molecular weight of the PEP block. This gave an aggregation number of 95 chains per micelle for PON (3-25-11) in EMI TFSI, assuming no solvent in the core. The aggregation number of the PEP-core micelles for 5 wt% PON (3-25-10) in water was previously reported to be 350, from cryogenic transmission electron microscopy images.[225] This difference suggests that the interfacial tension between PEP and water is much greater than between PEP and the ionic liquid, which is consistent with relative rankings of cohesive energy densities or solubility parameters. The size of the PEP-core micelles may also be dictated by the method of preparation. The PON hydrogel samples prepared by two different methods, thin film hydration and dialysis, showed a difference in PEP-core micelle size.[225] Therefore, it would not be unreasonable to assume that thin film hydration and the cosolvent method, for water and ionic liquid, respectively, may produce PEP-core micelles of different sizes simply due to differences in solution preparation.

The chain overlap concentrations for PON micelles in water and ionic liquid were determined using the aggregation numbers:

$$c^* = \frac{MN_{agg}}{N_A\left(\frac{4\pi}{3}R_c^3\right)} \tag{5.5}$$

where M is the molecular weight of the triblock, and R_h is the hydrodynamic radius calculated from DLS (Figure 5.10). The estimated c^* of the ionic liquid micelles is more than twice that of the aqueous micelles, 8.7 wt% and 4.0 wt% respectively. The relevant information about the PON micelles in both water and ionic liquid are collected in Table 5.3.

Overall, the PEP-core micelles formed in EMI TFSI are smaller than those in water. The core radius and aggregation number are both smaller, and the aggregation number is more than three times less. These smaller micelles require a higher concentration to begin to overlap, giving a c^* that is more than twice as large in EMI TFSI as water. The higher modulus of the ion gel network compared to the hydrogel is in good agreement with the six-fold larger micelle number density found for 5 wt% PON in EMI TFSI compared to the 5 wt% hydrogel (Table 5.3). The larger number density of micelles, arising from the smaller micelles, increases the number of crosslinks in the sample.

Solvent	R_c (nm) [a]	R_h (nm) [b]	N_{agg} [c]	c^* (wt%) [d]	Number density (micelles/mL) [e]	Inter-micellar distance (nm) [f]
EMI TFSI	5	21	95	8.7	$14x10^15$	33
Water	8	50	350	4.0	$2.3x10^15$	70

Table 5.3: Characteristics of PON(3-25-11) micelles in ionic liquid and PON (3-25-10) micelles in water. [a] Core radius of the micelles, calculated from cryo-TEM for PON (3-25-10) in water[225] and SAXS for PON (3-25-11) in EMI TFSI. [b] Hydrodynamic radius, calculated from DLS (data for PON in water from Ref. 225). [c] Aggregation number of micelles. [d] Chain-overlap concentration of micelles. [e] Number of micelles in a 1 gram sample of 5 wt% PON, calculated using the aggregation number and the density of water (ρ_{H_2O} = 1.0 g/cm^3) and EMI TFSI (ρ_{IL} = 1.4738 g/cm^3).[242] [f] The inter-micellar distance was calculated as $d = 2\pi/q^*$, where q^* was obtained from SAXS for the ionic liquid solution and from SANS for the aqueous solution.[227]

If the breadth of the gelation were a result of the distance between the micelles, any concentration above the chain-overlap concentration, c^*, should display a narrow transition. However, being above or below the c^* of 8.7 wt% for the ion gel does not appear to affect the breadth of the gelation; the 10 wt% PON in EMI TFSI sample does not have a significantly sharper gelation than the 5 wt% sample. The scattering experiments conducted on 5 wt% solutions of the PEP-core PON micelles also gave the distance between micelle cores (Table 5.3). The trend in inter-micellar distance does not appear to be correlated with the breadth of the gelation; the larger distance between the micelle cores in water might imply that it should be harder for the micelles to associate to form a gel.

5.6 Conclusions

In this study, we examined the thermoreversible gelation of the ABC triblock terpolymer PON in the ionic liquid EMI TFSI. The gels followed expected rheological behavior for gels at low temperatures, at the point of gelation, and as viscoelastic fluids at elevated temperatures. At a polymer loading of 10 wt%, the network exhibited an estimated 98% elastically effective strands. As a result, the gel was able to withstand high strains of $\sim$70% at 0 °C. This is in contrast to the corresponding ABA triblock, NON, which demonstrated only 79% elastically effective strands and withstood a lower strain of 35% at 0 °C. Simi-

larly, PON showed gel formation at concentrations as low as 1 and 2 wt%, whereas NON did not form a gel below 5 wt%. From these data, we conclude that the PON system forms a more efficient gel network, allowing for lower concentrations of polymer. This reduction in the amount of material needed, plus increased gel strength, makes PON or similar thermoreversible ABC triblock systems promising choices for ion gels for use in devices. The thermoresponsive nature of these systems offers the ability to easily process the material, both pre- and post-production. Additionally, the association of the PEP-core micelles was affected by solvent choice. The ionic liquid system demonstrated lower PEP aggregation numbers, which gave smaller micelles and a larger micelle number density for similar polymer loadings. The gelation in EMI TFSI occurred over a broad range of temperatures, independent of concentration.[226] The consistently sharp gelation of PON in water has previously been shown to be similarly independent of concentration. The consistency of the gelation across the range of concentrations suggests that the difference in PEP-core micelles did not affect the breadth of gelation. We interpret this breadth as arising from the relative steepness of the temperature dependence of the free energy of mixing that causes phase separation, either the UCST in ionic liquid or the LCST in water.

5.7 Acknowledgments

This work was supported by the National Science Foundation through Award DMR-1206-459 (TPL), and in part through the MRSEC Program (Awards DMR-1420013 and DMR-0819985). Dr. Yuanyan Gu for generously provided the EMI TFSI used in the studies. We thank Professor Marc Hillmyer for helpful discussions. Portions of this work were conducted at Sector 12 of the Advanced Photon Source (APS). Use of the APS, an Office of Science User Facility operated for the U.S. Department of Energy (DOE) Office of Science by Argonne National Laboratory, was supported by the U.S. DOE under Contract DE-AC02-06CH11357.

Chapter 6

Summary and future work

6.1 Introduction

The work presented in this thesis explored the combination of temperature and light responsive block polymers with ionic liquids. The work with light responsive polymers has primarily been exploratory, looking to understand the basics of how the polymer architecture influences the phase behavior or the structures formed. Chapter 2 focused on the synthesis and light-responsive properties of P(BzMA-*stat*-AzoMA) copolymers, with a significant effort towards finding a synthetic route that quickly and reliably produces these polymers with low dispersities. With this, the kinetics of the isomerization of azobenzene in these polymers were studied. These findings on thermal relaxation and time required for isomerization enabled informed experimental design for future chapters. Chapter 3 explored how light impacts the phase separation of these polymers from an ionic liquid as a function of copolymer composition and molecular weight. With the knowledge that molecular weight does not impact the phase separation behavior, the incorporation of these polymers into block polymers of varying architectures could be explored without significantly changing the behavior. The results on the impact of film thickness also informed choices of experimental parameters such as gap thickness in rheology. Chapter 4 used P(BzMA-*stat*-AzoMA) as a block in a block polymer, which when combined with EMI TFSI, produced solutions where light can be used to trigger transitions between order and disorder. Chapter 5 explored the use of an ABC triblock terpolymer in ionic liquid to form

thermoreversible gels, relying on the phase separation behavior of PNIPAm. With this basis of understanding, there are many directions where the current efforts can be continued, as well as extended to new areas. This chapter details future directions this work can be taken, both in extending a fundamental understanding of these thermo- and photoresponsive polymers, as well as looking towards applications of these materials.

6.2 Summary and future work

LCST phase diagram of P(BzMA-*stat*-AzoMA)

The work described in Chapter 3 focused on elucidating the phase behavior of P(BzMA-*stat*-AzoMA) in an ionic liquid as a function of molecular weight and copolymer composition. However, all tests were performed at the same concentration of 10 wt%. A cartoon of an LCST phase diagram of these materials, shown here again in Figure 6.1, illustrated what the phase behavior might be expected to follow, but it is based simply on the expectation for an LCST polymer system. This idealized cartoon does not necessarily represent

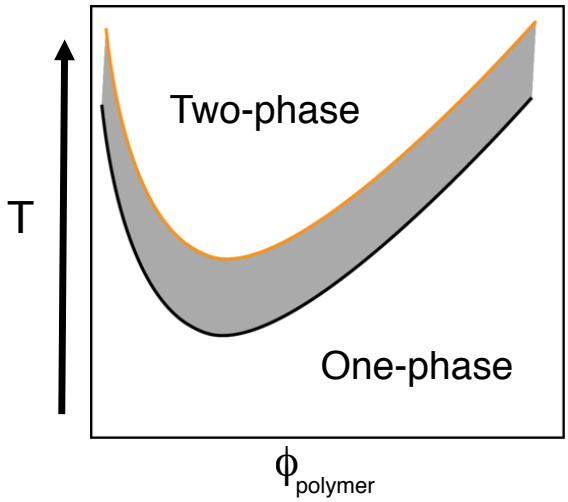

Figure 6.1: Cartoon illustration of an LCST phase diagram with two boundaries depending on light, where the upper orange bound is expected for *cis* azobenzene and the lower bound is expected for *trans*.

reality, however. Initial solubility tests show that B*s*A (17-6) is soluble in EMI TFSI up to 20 wt%, but is insoluble at higher concentrations up to 90 wt%. This indicates that

the prediction for an LCST phase diagram with a critical composition shifted towards low polymer compositions may not apply here. However, other factors may contribute. At high polymer concentrations, the sample would likely be relatively solid, especially given that the T_g is 56 ºC for B*s*A (17-6). It is possible that the sample preparation method of purging nitrogen while stirring caused bubble formation in the solution, which were then trapped as the solvent evaporated, giving the appearance of turbidity in the sample.

To get a better idea of the general shape of the phase diagram, BMI TFSI could be used rather than EMI TFSI. For polymers with low azobenzene incorporation, this would increase the LCST so that potentially all concentrations would be soluble. This may require refining of the reflection cloud point technique to be compatible with higher temperatures, where the current epoxy and electrical tape limit use to *ca.* 100 ºC. In addition to locating the critical composition, it is not necessarily clear whether or not the temperature gap between the two LCST phase boundaries will be consistent at all concentrations. The difference between the phase separation depends on a change of the solubility of the polymer in the solvent. When there is less solvent present in the system, it is possible that the change from *trans* to *cis* will have less of an effect. This would ultimately lead to the gap narrowing at higher polymer concentrations. In general, characterizing the phase diagram across the full range of concentration will lend to better understanding of the phase behavior observed in the block polymer system, as well as contribute fundamental understanding of the phase behavior of these light-responsive statistical copolymers.

Order-disorder phase transitions in non-spherical phases

In the three phase diagrams of block polymers constructed in Chapter 5, all of the observed LCOTs were achieved from disorder to ordered spherical phases. At low polymer concentrations, the PMMA block is highly swollen, generating a large effective volume fraction that gives rise to the spherical ordering. The LCOT occurs as a result of the LCST phase behavior of the B*s*A block, and at higher concentrations no LCOT is observed. This is consistent with the insolubility of B*s*A in EMI TFSI at high concentrations mentioned in the previous section. It is possible that if the phase boundary at high concentration did

increase in temperature significantly, as shown in Figure 6.1, that LCOTs would have been observed at higher polymer concentrations. However, this was not observed in this system, potentially giving further insight into the shape of the LCST phase boundary.

If the LCOT could be achieved at higher polymer concentrations, it is possible that it could enable a transition between disorder and non-spherical phases, such as lamellae or cylinders. This would be highly desirable for applications in thin films, where it could be employed in a technique similar to zone-annealing using temperature. Rather than sweeping a gradient of temperature across a film to generate aligned nanostructures, light could be used. In order to realize this, methods could be employed to increase the LCOT of the polymers. Switching the ionic liquid from EMI TFSI to BMI TFSI would easily generate an increase in the LCOT which may be sufficient to allow transitions from disorder to cylinders. The azobenzene content of the polymers could also be decreased, however decreasing it too much runs the risk of giving a narrow window of temperature where light-triggered LCOTs are possible. Changing the block polymer composition would likely not change the LCOT, as the work from Chapter 3 demonstrates that the molecular weight has only a minimal influence on the LCST behavior of B*s*A. However, the use of a highly asymmetric diblock with a majority of B*s*A may give rise to other morphologies than spheres at low concentrations, even with the swelling of PMMA.

Order-order phase transitions in light-responsive block polymer solutions

Recalling the phase diagrams shown in Chapter 4, we located LCOTs but were unable to identify any order-order phase transitions, OOTs. The phase diagram for M(B*s*A) (22-24(5)) is reproduced here in Figure 6.2 for easier reference. For concentrations where LCOTs are not observed, at 45 wt% and above, the samples display either a single phase or a coexistence of two morphologies. The coexistence of cylinders and lamellae has previously been discussed by Lodge and coworkers, occurring where a gyroid morphology could be expected.[43] They found that the coexistence was achieved both on heating and cooling, and persisted for a month, believing this to be the equilibrium state for the sample.

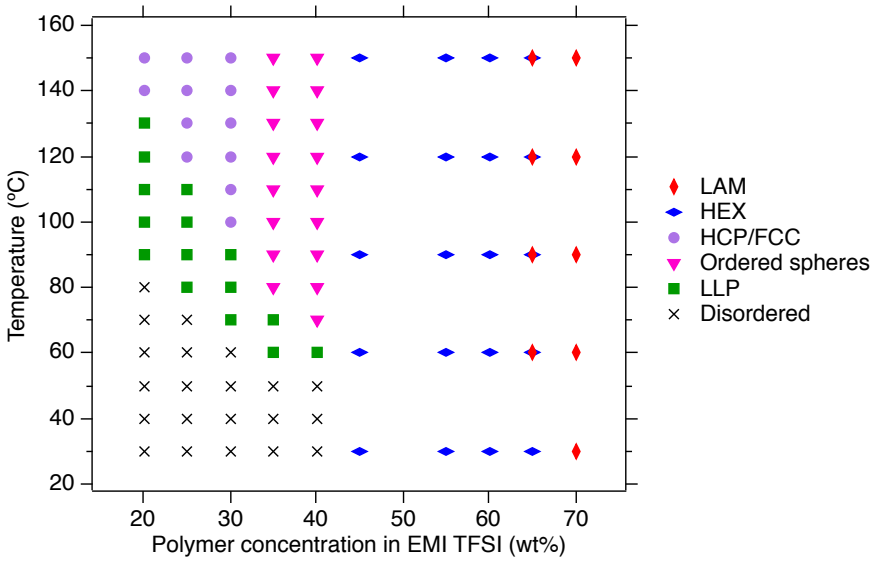

Figure 6.2: Phase diagram of M(B*s*A) (22-24(5)) as a function of concentration in EMI TFSI and temperature.

With the coexistence, because the growth of a second morphology is gradual, triggering may not produce a large, appreciable change. However, this is something that has not been explored using small temperature jumps or by small amplitude oscillatory shear measurements. As discussed in Chapter 4, transitions between order and disorder can be detected using rheology. Similarly, transitions between ordered phases with different mechanical properties can also be detected, showing either a rapid increase or decrease in modulus, with G' remaining dominant. The region from 60 to 70 wt% would be of particular interest to explore by rheology and SAXS to determine if a sharp order-order phase transition is accessible. Similarly, concentrations between 40 and 45 wt% might produce an OOT from spheres to cylinders.

The region 75 wt% and above was unexplored due to concerns over running out of material. Nor have the bulk morphologies of each of the polymers been probed. Attempts were made with the lab scale X-ray scattering instrument, however no scattering was obtained. This problem was also encountered using the exact samples that produced multiple higher order scattering peaks at Argonne, such as 60 wt% M(B*s*A) (22-24(5)). As such, the bulk measurements also need to be performed at Argonne National Lab. With the high concentrations, a significant amount of polymer is necessary for each sample. However, with the general shape of the phase diagram determined, it would be important to evaluate the

full phase diagram. It is possible that the higher concentrations lead to more morphologies, and more possibilities for OOTs. For M(B*s*A) (22-24(5)), the symmetrical diblock is likely lamellar in the bulk, so it is possible that no more morphologies will be observed at higher concentrations. M(B*s*A) (13-46(5)) has a PMMA volume fraction of 0.2, so the higher concentration samples may yield more. This is reflected in the phase diagram, where the lamellar morphology is observed as low as 60 wt%.

Modifying block polymer architecture and molecular weight to obtain LCOTs to well-ordered phases

Another technique could be employed to find LCOTs to well-ordered morphologies. This focus will be primarily on generating the hexagonal close packed spheres, HCP, as observed in M(B*s*A) (22-24(5)) at concentrations 30 wt% and below. As stated in Chapter 4, we believe that all of the ordered spherical morphologies formed are likely slowly transitioning to states with significantly sharper peaks by SAXS, such as HCP. Modifications to the block polymer architecture, such as changes in overall degree of polymerization or the volume fractions of the blocks, may enable well-ordered LCOTs for all samples.

The exact temperature at which the LCOT occurs likely has an impact on the ordered morphology observed. In M(B*s*A) (22-24(5)), samples at 30 wt% and below show HCP and between 35 and 40 wt% show broader scattering peaks. The LCOT decreases by 20 ºC from 30 wt% to 35 wt%, and this decrease in temperature causes a decrease in the mobility of the polymer chains. As a result, the transition from disorder to arrangement on a well-ordered lattice will take longer. While these samples might reach HCP, FCC, or BCC with time, for light-triggered LCOTs the samples should reach their equilibrium state as quickly as possible. To determine if this decrease in LCOT temperature is the cause of poorer ordering, the solvent could simply be switched from EMI TFSI to BMI TFSI.

Another notable difference between the samples that form well-ordered morphologies above the LCOT is the molecular weight of the B*s*A block. M(B*s*A) (24-20(10)) and (22-24(5)) both have lower molecular weights compared to 31 and 46 kDa. Decreasing the overall molecular weight of the block polymer may enable higher mobility, leading to the

ability to form the desired well-ordered structures. A variety of volume fractions could still be explored, and as mentioned a change in molecular weight should not significantly impact the LCST phase behavior of the B*s*A block. If anything, a slight increase in the LCST is observed at lower molecular weights, as discussed in Chapter 3. If this increase makes the LCOT too high in the block polymer system, it can always be decreased by increasing the incorporation of AzoMA in the B*s*A block.

Morphologies of high-concentration light-responsive ABA triblock copolymers

The possible application of these light-responsive block polymers in adhesives was discussed in Chapter 4. The maximum storage modulus achieved for these materials in their ordered state is *ca.* 10^4 Pa. The Dahlquist criterion, an empirical benchmark required for a pressure sensitive adhesive, is 0.3 MPa, or $3x10^5$ Pa.[243] The materials explored here have moduli that are too low to be effectively used in adhesives, although there are steps that could be taken to achieve a higher modulus. The previous section discussed decreasing the molecular weight to achieve better ordering, however in this case a well-defined ordered lattice is not necessary for adhesive function. As such, the molecular weight of the polymer could be increased in an attempt to increase the modulus.

Another technique would be to change the architecture entirely to produce a network morphology. ABA triblock copolymers have been explored as elastomers and PSAs, with work exploring incorporating azobenzene in both the A and B blocks of elastomers.[188] Work has also been done in ABA triblocks in ionic liquids where the A blocks are copolymers of NIPAm and AzoMA, generating a light-responsive gel that can dissolve and reform under different wavelengths of light.[88,89] Rather than exploring low concentrations to obtain gels, we would focus on higher concentrations to obtain high modulus materials for uses as adhesives. In this sense, the structure would be formed under visible light, then dissolved under UV light to allow for easy removal of the adhesive. As well as targeting the application in adhesives, it would be purely interesting to see if the ABA architecture allows for easier or poorer access to LCOTs and OOTs at a range of concentrations and

copolymer compositions. This could mirror the work performed in this thesis to construct phase diagrams for the AB diblock.

Light-responsive ABC terpolymer gels in ionic liquid

Chapter 5 explored the gelation of an ABC triblock terpolymer, relying on differences in the solubilities of the two end blocks to generate a gel network without looping defects. This gelation was thermoreversible, and used NIPAm as the temperature responsive block rather than BzMA. To connect this work to the exploration of light-responsive polymers, the end block of NIPAm could be replaced with B*s*A to give a light-responsive gel with suppression of looping defects. This would pair well with the exploration of the ABA phase behavior, as the dilute solutions of ABA triblock could act as a point of comparison to observe whether or not the ABC architecture improves the network formation.

In pursuing these goals, some modifications to the light responsive block may be necessary. At low concentrations, the LCOT may be inaccessibly high for rheological measurements, above 150 ºC. The 20 wt% sample of M(B*s*A) (22-24(5)) does not order until 140 ºC. The easiest technique to reduce the ordering temperature would be increasing the incorporation of AzoMA. However, the work presented in Chapter 5 probed concentrations as low as 1 wt%. It may be difficult at a concentration that low to incorporate enough AzoMA while maintaining a majority of BzMA to impart the LCST phase behavior. As such, the post-functionalization of polymers could be explored. This could allow the use of NIPAm, which displays UCST phase behavior in ionic liquids at much lower temperatures. Rather than directly copolymerizing NIPAm with an azobenzene-based monomer, it could be copolymerized with a compatible monomer with a functional group such as an alcohol. A simple reaction combining the polymer containing the pendant alcohols and an acid chloride-functionalized azobenzene would allow for functionalization. This would circumvent the issues observed in Chapter 2 while allowing for a phase transition at significantly lower temperatures. Comparison of these materials could then be made with the literature examples of P(NIPAm-*stat*-AzoMA)-*block*-PEO-*block*-P(NIPAm-*stat*-AzoMA). Synthesis of these materials could also enable exploration of pressure sensitive adhesives

that allow for light-triggered removal of the adhesive at temperatures closer to room temperature, which could be desirable in certain applications.

References

[1] Liu, S.; Zhou, L.; Wang, P.; Zhang, F.; Yu, S.; Shao, Z.; Yi, B. *ACS Appl. Mater. Interfaces* **2014**, *6*, 3195–3200.

[2] Park, M. J.; Choi, I.; Hong, J.; Kim, O. *J. Appl. Polym. Sci.* **2013**, *129*, 2363–2376.

[3] Ye, Y.-S.; Rick, J.; Hwang, B.-J. *J. Mater. Chem. A* **2013**, *1*, 2719–2743.

[4] Kelly, J. C.; Degrood, N. L.; Roberts, M. E. *Chem. Commun.* **2015**, *51*, 5448–5451.

[5] Thelen, J. L.; Wang, A. A.; Chen, X. C.; Jiang, X.; Schaible, E.; Balsara, N. P. *Macromolecules* **2018**, *51*, 1733–1740.

[6] Wakayama, H.; Yonekura, H.; Kawai, Y. *Chem. Mater.* **2016**, *28*, 4453–4459.

[7] Chen, L.; Phillip, W. A.; Cussler, E. L.; Hillmyer, M. A. *J. Am. Chem. Soc.* **2007**, *129*, 13786–13787.

[8] Jackson, E. A.; Lee, Y.; Hillmyer, M. A. *Macromolecules* **2013**, *46*, 1484–1491.

[9] Saba, S. A.; Mousavi, M. P. S.; Bühlmann, P.; Hillmyer, M. A. *J. Am. Chem. Soc.* **2015**, *137*, 8896–8899.

[10] Phillip, W. A.; Amendt, M.; O'Neill, B.; Chen, L.; Hillmyer, M. A.; Cussler, E. L. *ACS Appl. Mater. Interfaces* **2009**, *1*, 472–480.

[11] Qiu, X. P.; Winnik, F. M. *Macromol. Rapid Commun.* **2006**, *27*, 1648–1653.

[12] Liu, Y.; Servant, A.; Guy, O. J.; Al-Jamal, K. T.; Williams, P. R.; Hawkins, K. M.; Kostarelos, K. *Sens. Actuators B Chem.* **2012**, *175*, 100–105.

[13] Jeong, B.; Bae, Y. H.; Lee, D. S.; Kim, S. W. *Nature* **1997**, *388*, 860–862.

[14] Shantha, K. L.; Ravichandran, P.; Rao, K. P. *Biomaterials* **1995**, *16*, 1313–1318.

[15] Strozyk, M. S.; Carregal-Romero, S.; Henriksen-Lacey, M.; Brust, M.; Liz-Marzán, L. M. *Chem. Mater.* **2017**, *29*, 2303–2313.

[16] Parthenopoulos, D. A.; Rentzepis, P. M. *Science* **1989**, *245*, 843–845.

[17] Zhang, L.; Wang, L.; Yu, H.-J. *J. Zhejiang Univ. Sci. A Appl. Phys. Eng.* **2013**, *14*, 504–513.

[18] Xie, S.; Natansohn, A.; Rochoni, P. *Chem. Mater.* **1993**, *5*, 403–411.

[19] Paik, M. Y.; Krishnan, S.; You, F.; Li, X.; Hexemer, A.; Ando, Y.; Kang, S. H.; Fischer, D. a.; Kramer, E. J.; Ober, C. K. *Langmuir* **2007**, *23*, 5110–5119.

[20] Yu, N.; Wang, S.; Liu, Y.; Xue, P.; Ge, P.; Nan, J.; Ye, S.; Liu, W.; Zhang, J.; Yang, B. *Langmuir* **2017**, *33*, 494–502.

[21] Czugala, M.; O'Connell, C.; Blin, C.; Fischer, P.; Fraser, K. J.; Benito-Lopez, F.; Diamond, D. *Sens. Actuators B Chem.* **2014**, *194*, 105–113.

[22] Wu, C.-Y.; Liao, W.-H.; Tung, Y.-C. *Lab Chip* **2011**, *11*, 1740–1746.

[23] Byrne, R.; Ventura, C.; Benito Lopez, F.; Walther, A.; Heise, A.; Diamond, D. *Biosens. Bioelectron.* **2010**, *26*, 1392–8.

[24] Leibler, L. *Macromolecules* **1980**, *13*, 1602–1617.

[25] Lodge, T. P. *Macromol. Chem. Phys.* **2003**, *204*, 265–273.

[26] Bates, F. S.; Fredrickson, G. H. *Annu. Rev. Phys. Chem.* **1990**, *41*, 525–557.

[27] Bates, F. S.; Fredrickson, G. H. *Phys. Today* **1999**, *52*, 32–38.

[28] Bates, F. S.; Hillmyer, M. A.; Lodge, T. P.; Bates, C. M.; Delaney, K. T.; Fredrickson, G. H. *Science* **2012**, *336*, 434–440.

[29] Fredrickson, G. H.; Helfand, E. *J. Chem. Phys.* **1987**, *87*, 697–705.

[30] Bates, F. S. *Science* **1991**, *251*, 898–905.

[31] Hiemenz, P. C.; Lodge, T. P. *Polymer Chemistry*, 2nd ed.; CRC Press: Boca Raton, 2007.

[32] Hansen, C.; Durkee, J.; Kontogeorgis, G.; Panayiotou, C.; Willliams, L.; Poulsen, T.; Priebe, H.; Redelius, P. *Journal of Chemical Information and Modeling*, 2nd ed.; CRC Press: Boca Raton, 2007; Vol. 53.

[33] Chen, Q. P.; Chu, J. D.; DeJaco, R. F.; Lodge, T. P.; Siepmann, J. I. *Macromolecules* **2016**, *49*, 3975–3985.

[34] Matsen, M.; Schick, M. *Phys. Rev. Lett.* **1994**, *72*, 2660–2663.

[35] Khandpur, A. K.; Forster, S.; Bates, F. S.; Hamley, I. W.; Ryan, A. J.; Bras, W.; Almdal, K.; Mortensen, K. *Macromolecules* **1995**, *28*, 8796–8806.

[36] Bates, C. M.; Maher, M. J.; Janes, D. W.; Ellison, C. J.; Willson, C. G. *Macromolecules* **2014**, *47*, 2–12.

[37] Jin, C.; Olsen, B. C.; Luber, E. J.; Buriak, J. M. *Chem. Mater.* **2017**, *29*, 176–188.

[38] Yang, T.; Tian, S.; Zhu, Y.; Li, W. *Langmuir* **2016**, *32*, 13787–13794.

[39] Abate, A. A.; Vu, G. T.; Pezzutti, A. D.; García, N. A.; Davis, R. L.; Schmid, F.; Register, R. A.; Vega, D. A. *Macromolecules* **2016**, *49*, 7588–7596.

[40] Zhou, S. X.; Janes, D. W.; Kim, C. B.; Willson, C. G.; Ellison, C. J. *Macromolecules* **2016**, *49*, 8332–8340.

[41] Lodge, T. P.; Bang, J.; Hanley, K. J.; Krocak, J.; Dahlquist, S.; Sujan, B.; Ott, J. *Langmuir* **2003**, *19*, 2103–2109.

[42] Hanley, K. J.; Lodge, T. P. *J. Polym. Chem. B. Polym. Phys.* **1998**, *36*, 3101–3113.

[43] Lodge, T. P.; Pudil, B.; Hanley, K. J. *Macromolecules* **2002**, *35*, 4707–4717.

[44] Lodge, T. P.; Hamersky, M. W.; Hanley, K. J.; Huang, C.-I. *Macromolecules* **1997**, *30*, 6139–6149.

[45] Wasserscheid, P.; Welton, T. *Journal of Physical Chemistry B*; Wiley-VCH Verlag GmbH and Co. KGaA: Weinheim, 2002; Vol. 116.

[46] Welton, T. *Chem. Rev.* **1999**, *99*, 2071–2083.

[47] Castner, E. W.; Wishart, J. F.; Shirota, H. *Acc. Chem. Res.* **2007**, *40*, 1217–1227.

[48] Tokuda, H.; Hayamizu, K.; Ishii, K.; Susan, M. A. B. H.; Watanabe, M. *J. Phys. Chem. B* **2004**, *108*, 16593–16600.

[49] Susan, M. A. B. H.; Kaneko, T.; Noda, A.; Watanabe, M. *J. Am. Chem. Soc.* **2005**, *127*, 4976–4983.

[50] Flory, P. J.; Krigbaum, W. R. *Annu. Rev. Phys. Chem.* **1941**, *9*, 660–661.

[51] Flory, P. J. *J. Chem. Phys.* **1942**, *10*, 51–61.

[52] Hoarfrost, M. L.; He, Y.; Lodge, T. P. *Macromolecules* **2013**, *46*, 9464–9472.

[53] Lee, H.-N.; Lodge, T. P. *J. Phys. Chem. Lett.* **2010**, *1*, 1962–1966.

[54] Lee, H.-N.; Newell, N.; Bai, Z.; Lodge, T. P. *Macromolecules* **2012**, *45*, 3627–3633.

[55] Rodríguez, H.; Francisco, M.; Rahman, M.; Sun, N.; Rogers, R. D. *Phys. Chem. Chem. Phys.* **2009**, *11*, 10916–10922.

[56] Lee, H. N.; Lodge, T. P. *J. Phys. Chem. B* **2011**, *115*, 1971–1977.

[57] Fujii, K.; Ueki, T.; Niitsuma, K.; Matsunaga, T.; Watanabe, M.; Shibayama, M. *Polymer* **2011**, *52*, 1589–1595.

[58] Fujii, K.; Ueki, T.; Hashimoto, K.; Kobayashi, Y.; Kitazawa, Y.; Hirosawa, K.; Matsugami, M.; Ohara, K.; Watanabe, M.; Shibayama, M. *Macromolecules* **2017**, *50*, 4780–4786.

[59] Ueki, T.; Watanabe, M. *Langmuir* **2007**, *23*, 988–990.

[60] Ueki, T.; Karino, T.; Kobayashi, Y.; Shibayama, M.; Watanabe, M. *J. Phys. Chem. B* **2007**, *111*, 4750–4754.

[61] Ueki, T.; Watanabe, M. *Chem. Lett.* **2006**, *35*, 964–965.

[62] Asai, H.; Fujii, K.; Ueki, T.; Sawamura, S.; Nakamura, Y.; Kitazawa, Y.; Watanabe, M.; Han, Y.-S.; Kim, T.-H.; Shibayama, M. *Macromolecules* **2013**, *46*, 1101–1106.

[63] Heskins, M.; Guillet, J. E. *J. Macromol. Sci. A Chem.* **1968**, *2*, 1441–1455.

[64] Ueki, T. *Polym. J.* **2014**, 1–10.

[65] Hanley, K. J.; Lodge, T. P.; Huang, C. I. *Macromolecules* **2000**, *33*, 5918–5931.

[66] Balsara, N. P.; Perahia, D.; Safinya, C. R.; Tirrell, M.; Lodge, T. P. *Macromolecules* **1992**, *25*, 3896–3901.

[67] Lodge, T. P.; Fredrickson, G. H. *Macromolecules* **1992**, *25*, 5643–5650.

[68] Garetz, B. A.; Newstein, M. C.; Dai, H. J.; Jonnalagadda, S. V.; Balsara, N. P. *Macromolecules* **1993**, *26*, 3151–3155.

[69] Zhao, J.; Majumdar, B.; Schulz, M. F.; Bates, F. S.; Almdal, K.; Mortensen, K.; Hajduk, D. A.; Gruner, S. M. *Macromolecules* **1996**, *29*, 1204–1215.

[70] Lodge, T. P.; Hanley, K. J.; Pudil, B.; Alahapperuma, V. *Macromolecules* **2003**, *36*, 816–822.

[71] Wanka, G.; Hoffmann, H.; Ulbricht, W. *Macromolecules* **1994**, *27*, 4145–4159.

[72] Alexandridis, P.; Olsson, U.; Lindman, B. *Macromolecules* **1995**, *28*, 7700–7710.

[73] Alexandridis, P.; Zhou, D.; Khan, A. *Langmuir* **1996**, *12*, 2690–2700.

[74] Alexandridis, P. *Curr. Opin. Colloid Interface Sci.* **1997**, *2*, 478–489.

[75] Alexandridis, P. *Macromolecules* **1998**, *31*, 6935–6942.

[76] Svensson, B.; Alexandridis, P.; Olsson, U. *J. Phys. Chem. B* **1998**, *102*, 7541–7548.

[77] Svensson, M.; Alexandridis, P.; Linse, P. *Macromolecules* **1999**, *32*, 637–645.

[78] Ivanova, R.; Lindman, B.; Alexandridis, P. *Langmuir* **2000**, *16*, 9058–9069.

[79] Ivanova, R.; Lindman, B.; Alexandridis, P. *Langmuir* **2000**, *16*, 3660–3675.

[80] Ivanova, R. *Langmuir* **2000**, *16*, 3676–3689.

[81] Holmqvist, P.; Alexandridis, P.; Lindman, B. *Macromolecules* **1997**, *30*, 6788–6797.

[82] Holmqvist, P.; Alexandridis, P.; Lindman, B. *J. Phys. Chem. B* **1998**, *102*, 1149–1158.

[83] Zipfel, J.; Berghausen, J.; Schmidt, G.; Lindner, P.; Alexandridis, P.; Richtering, W. *Macromolecules* **2002**, *35*, 4064–4074.

[84] Ueki, T.; Yamaguchi, A.; Ito, N.; Kodama, K.; Sakamoto, J.; Ueno, K.; Kokubo, H.; Watanabe, M. *Langmuir* **2009**, *25*, 8845–8848.

[85] Ueki, T.; Nakamura, Y.; Yamaguchi, A.; Niitsuma, K.; Lodge, T. P.; Watanabe, M. *Macromolecules* **2011**, *44*, 6908–6914.

[86] Ueki, T.; Yamaguchi, A.; Watanabe, M. *Chem. Commun.* **2012**, *48*, 5133.

[87] Ueki, T.; Nakamura, Y.; Lodge, T. P.; Watanabe, M. *Macromolecules* **2012**, *45*, 7566–7573.

[88] Ueki, T.; Nakamura, Y.; Usui, R.; Kitazawa, Y.; So, S.; Lodge, T. P.; Watanabe, M. *Angew. Chem. Int. Ed.* **2015**, *54*, 3018–3022.

[89] Ueki, T.; Usui, R.; Kitazawa, Y.; Lodge, T. P.; Watanabe, M. *Macromolecules* **2015**, *48*, 5928–5933.

[90] Tian, Y.; Watanabe, K.; Kong, X.; Abe, J.; Iyoda, T. *Macromolecules* **2002**, *35*, 3739–3747.

[91] Ding, L.; Mao, H.; Xu, J.; He, J.; Ding, X.; Russell, T. P. *Macromolecules* **2008**, *41*, 1897–1900.

[92] Morikawa, Y.; Kondo, T.; Nagano, S.; Seki, T. *Chem. Mater.* **2007**, *19*, 1540–1542.

[93] Seki, T.; Nagano, S. *Chem. Lett.* **2008**, *37*, 484–489.

[94] Kadota, S.; Aoki, K.; Nagano, S.; Seki, T. *J. Am. Chem. Soc.* **2005**, *127*, 8266–8267.

[95] Kadota, S.; Aoki, K.; Nagano, S.; Seki, T. *Colloids Surf. A Physicochem. Eng. Asp.* **2006**, *284-285*, 535–541.

[96] Tsutsumi, O.; Shiono, T.; Ikeda, T.; Galli, G. *J. Phys. Chem. B* **1997**, *101*, 1332–1337.

[97] Okano, K.; Mikami, Y.; Hidaka, M.; Yamashita, T. *Macromolecules* **2011**, *44*, 5605–5611.

[98] Aoki, K.; Iwata, T.; Nagano, S.; Seki, T. *Macromol. Chem. Phys.* **2010**, *211*, 2484–2489.

[99] Liu, F.; Urban, M. W. *Prog. Polym. Sci.* **2010**, *35*, 3–23.

[100] Kocak, G.; Tuncer, C.; Bütün, V. *Polym. Chem.* **2017**, *8*, 144–176.

[101] Eichenbaum, G. M.; Kiser, P. F.; Simon, S. A.; Needham, D. *Macromolecules* **1998**, *31*, 5084–5093.

[102] Eichenbaum, G. M.; Kiser, P. F.; Dobrynin, A. V.; Simon, S. A.; Needham, D. *Macromolecules* **1999**, *32*, 4867–4878.

[103] Chen, G.; Hoffman, A. S. *Nature* **1995**, *373*, 49–52.

[104] Kiser, P. F.; Wilson, G.; Needham, D.; Glynn, T.; Group, W.; Gilman, N. W.; Boulevard, E. *Nature* **1998**, *394*, 459–462.

[105] Torres-Lugo, M.; Peppas, N. A. *Macromolecules* **1999**, *32*, 6646–6651.

[106] Philippova, O. E.; Hourdet, D.; Audebert, R.; Khokhlov, A. R. *Macromolecules* **1997**, *30*, 8278–8285.

[107] Horkay, F.; Tasaki, I.; Basser, P. J. *Biomacromolecules* **2001**, *2*, 195–199.

[108] Sprouse, D.; Jiang, Y.; Laaser, J. E.; Lodge, T. P.; Reineke, T. M. *Biomacromolecules* **2016**, *17*, 2849–2859.

[109] Jeon, C. H.; Makhaeva, E. E.; Khokhlov, A. R. *Macromol. Chem. Phys.* **1998**, *199*, 2665–2670.

[110] Majewski, P. W.; Gopinadhan, M.; Osuji, C. O. *J. Polym. Chem. B. Polym. Phys.* **2012**, *50*, 2–8.

[111] Du, L.; Xu, Z.-Y.; Fan, C.-J.; Xiang, G.; Yang, K.-K.; Wang, Y.-Z. *Macromolecules* **2018**, *51*, 705–715.

[112] Stopin, A.; Rossignon, A.; Keshavarz, M.; Ishida, Y.; Christianen, P. C. M.; Bonifazi, D. *Chem. Mater.* **2016**, *28*, 6985–6994.

[113] Filipcsei, G.; Csetneki, I.; Szilágyi, A.; Zrínyi, M. *Oligomers - Polymer Composites - Molecular Imprinting*; Springer Berlin Heidelberg: Berlin, Heidelberg, 2007; pp 137–189.

[114] Keplinger, C.; Kaltenbrunner, M.; Arnold, N.; Bauer, S. *Proc. Natl. Acad. Sci. USA* **2010**, *107*, 4505–4510.

[115] Richter, A.; Paschew, G. *Adv. Mater.* **2009**, *21*, 979–983.

[116] Park, I.-S.; Jung, K.; Kim, D.; Kim, S.-M.; Kim, K. J. *MRS Bull.* **2008**, *33*, 190–195.

[117] Lovinger, A. J. *Science* **1983**, *220*, 1115 – 1121.

[118] Kodama, K.; Nanashima, H.; Ueki, T.; Kokubo, H.; Watanabe, M. *Langmuir* **2009**, *25*, 3820–3824.

[119] Seuring, J. *ACS Macro Lett.* **2013**, *2*, 597–600.

[120] Kobayashi, K.; Huang, C.-I.; Lodge, T. P. *Macromolecules* **1999**, *32*, 7070–7077.

[121] Kröger, R.; Menzel, H.; Hallensleben, M. L. *Macromol. Chem. Phys.* **1994**, *195*, 2291–2298.

[122] Howley, C.; Marangoni, D. G.; Kwak, J. C. T. *Colloid Polym. Sci.* **1997**, *275*, 760–768.

[123] Yuan, W.; Jiang, G.; Wang, J.; Wang, G.; Song, Y.; Jiang, L. *Macromolecules* **2006**, *39*, 1300–1303.

[124] Kungwatchakun, D.; Irie, M. *Makromol. Chem. Rapid Commun.* **1988**, *9*, 243–246.

[125] Moniruzzaman, M.; Fernando, G. F.; Talbot, J. D. R. *J. Polym. Chem. A Polym. Chem.* **2004**, *42*, 2886–2896.

[126] Akiyama, H.; Tamaoki, N. *Macromolecules* **2007**, *40*, 5129–5132.

[127] Deshmukh, S.; Bromberg, L.; Smith, K. A.; Hatton, T. A. *Langmuir* **2009**, *25*, 3459–3466.

[128] Ma, X.; Usui, R.; Kitazawa, Y.; Tamate, R.; Kokubo, H.; Watanabe, M. *Macromolecules* **2017**, *50*, 6788–6795.

[129] Yang, F.; Cao, Z.; Wang, G. *Polym. Chem.* **2015**, *6*, 7995–8002.

[130] Ziółkowski, B.; Florea, L.; Theobald, J.; Benito-Lopez, F.; Diamond, D. *J. Mater. Sci.* **2015**,

[131] Wang, B.; Chen, K.; Yang, R.; Yang, F.; Liu, J. *Carbohyd. Polym.* **2014**, *103*, 510–519.

[132] Lone, S.; Ahn, J. I.; Kim, M. R.; Lee, H. M.; Kim, S. H.; Lodge, T. P.; Cheong, I. W. *Langmuir* **2014**, *30*, 9577–9583.

[133] Dong, J.; Wang, Y.; Zhang, J.; Zhan, X.; Zhu, S.; Yang, H.; Wang, G. *Soft Matter* **2013**, *9*, 370–373.

[134] Florea, L.; Diamond, D.; Benito-Lopez, F. *Macromol. Mater. Eng.* **2012**, *297*, 1148–1159.

[135] Guragain, S.; Bastakoti, B. P.; Ito, M.; Yusa, S.-I.; Nakashima, K. *Soft Matter* **2012**, *8*, 9628–9634.

[136] Mo, C.; Lin, L.; Xiaoqiang, L. *Adv. Mater. Lett.* **2011**, *2*, 415–418.

[137] Shiraishi, Y.; Sumiya, S.; Manabe, K.; Hirai, T. *ACS Appl. Mater. Interfaces* **2011**, *3*, 4649–4656.

[138] Huang, C. Q.; Wang, Y.; Hong, C. Y.; Pan, C. Y. *Macromol. Rapid Commun.* **2011**, *32*, 1174–1179.

[139] Benito-Lopez, F.; Byrne, R.; Răduţă, A. M.; Vrana, N. E.; McGuinness, G.; Diamond, D. *Lab Chip* **2010**, *10*, 195–201.

[140] Lee, H. I.; Wu, W.; Oh, J. K.; Mueller, L.; Sherwood, G.; Peteanu, L.; Kowalewski, T.; Matyjaszewski, K. *Angew. Chem. Int. Ed.* **2007**, *46*, 2453–2457.

[141] Jiang, J.; Tong, X.; Morris, D.; Zhao, Y. *Macromolecules* **2006**, *39*, 4633–4640.

[142] Sumaru, K.; Ohi, K.; Takagi, T.; Kanamori, T.; Shinbo, T. *Langmuir* **2006**, *22*, 4353–4356.

[143] Ivanov, A. E.; Eremeev, N. L.; Wahlund, P. O.; Galaev, I. Y.; Mattiasson, B. *Polymer* **2002**, *43*, 3819–3823.

[144] Schild, H. G. *Prog. Polym. Sci.* **1992**, *17*, 163–249.

[145] Matsugami, M.; Fujii, K.; Ueki, T.; Kitazawa, Y.; Umebayashi, Y.; Watanabe, M.; Shibayama, M. *Anal. Sci.* **2013**, *29*, 311–314.

[146] Hartley, G. *J. Chem. Soc.* **1938**, *0*, 633–642.

[147] Rabek, J. F. *Experimental methods in photochemistry and photophysics. 2*; A Wiley-Interscience Publication; Wiley & Sons, 1982.

[148] Griffiths, J. *Chem. Soc. Rev.* **1972**, *1*, 481.

[149] Badger, G. M.; Drewer, R. J.; Lewis, G. E. *Austral. J. Chem.* **1966**, *19*, 643–666.

[150] Shen, Q.; Cao, Y.; Liu, S.; Steigerwald, M. L.; Guo, X. *J. Phys. Chem. C* **2009**, *113*, 10807–10812.

[151] Levitus, M.; Glasser, G.; Neher, D.; Aramendía, P. F. *Chem. Phys. Lett.* **1997**, *277*, 118–124.

[152] Bletz, M.; Pfeifer-Fukumura, U.; Kolb, U.; Baumann, W. *J. Phys. Chem. A* **2002**, *106*, 2232–2236.

[153] Lenoble, C.; Becker, R. S. *J. Phys. Chem.* **1986**, *90*, 62–65.

[154] Wu, Y.; Sasaki, T.; Kazushi, K.; Seo, T.; Sakurai, K. *J. Phys. Chem. B* **2008**, *112*, 7530–7536.

[155] Zhang, S.; Zhang, Q.; Ye, B.; Li, X.; Zhang, X.; Deng, Y. *J. Phys. Chem. B* **2009**, *113*, 6012–6019.

[156] Klajn, R. *Chem. Soc. Rev.* **2014**, *43*, 148–184.

[157] Mayo, F. R.; Lewis, F. M. *J. Am. Chem. Soc.* **1944**, *66*, 1594–1601.

[158] Raymo, F. M.; Giordani, S. *J. Am. Chem. Soc.* **2001**, *123*, 4651–4652.

[159] Tuzar, Z.; Kratochvil, P. *Polym. Lett.* **1969**, *7*, 825–828.

[160] Ishizone, T.; Ito, M. *J. Polym. Sci. A Polym. Chem.* **2002**, *40*, 4328–4332.

[161] Shinde, V. S.; Girme, M. R.; Pawar, V. U. *Indian J. Chem.* **2011**, *50*, 781–787.

[162] Lu, X.; Zhang, L.; Meng, L.; Liu, Y. *Polym. Bull.* **2007**, *59*, 195–206.

[163] Teodorescu, M.; Matyjaszewski, K. *Macromolecules* **1999**, *32*, 4826–4831.

[164] Teodorescu, M.; Matyjaszewski, K. *Macromol. Rapid Commun.* **2000**, *21*, 190–194.

[165] Podzimek, S. *Light Scattering, Size Exclusion Chromatography and Asymmetric Flow Field Flow Fractionation*; Wiley Online Books; John Wiley & Sons, Inc.: Hoboken, NJ, USA, 2011; pp 37–98.

[166] Hair, S. R.; Taylor, G. A.; Schultz, L. W. *J. Chem. Ed.* **1990**, *67*, 709.

[167] Baba, K.; Ono, H.; Itoh, E.; Itoh, S.; Noda, K.; Usui, T.; Ishihara, K.; Inamo, M.; Takagi, H. D.; Asano, T. *Chem. Eur. J.* **2006**, *12*, 5328–5333.

[168] Bin, A.; Susan, H.; Kaneko, T.; Noda, A.; Watanabe, M. *J. Am. Chem. Soc.* **2005**, *127*, 4976–4983.

[169] Scott, M. P.; Brazel, C. S.; Benton, M. G.; Mays, J. W.; Holbrey, D.; Rogers, R. D. *Chem. Commun.* **2002**, 1370–1371.

[170] Lu, W.; Fadeev, A. G.; Qi, B.; Smela, E.; Mattes, B. R.; Ding, J.; Spinks, G. M.; Mazurkiewicz, J.; Zhou, D.; Wallace, G. G.; MacFarlane, D. R.; Forsyth, S. A.; Forsyth, M. *Science* **2002**, *297*, 983–987.

[171] Yuan, H.; Shimotani, H.; Tsukazaki, A.; Ohtomo, A.; Kawasaki, M.; Iwasa, Y. *Adv. Funct. Mater.* **2009**, *19*, 1046–1053.

[172] Gan, Q.; Rooney, D.; Xue, M.; Thompson, G.; Zou, Y. *J. Memb. Sci.* **2006**, *280*, 948–956.

[173] Jiang, Y.-Y.; Zhou, Z.; Jiao, Z.; Li, L.; Wu, Y.-T.; Zhang, Z.-B. *J. Phys. Chem. B* **2007**, *111*, 5058–5061.

[174] So, S.; Hayward, R. C. *ACS Appl. Mater. Interfaces* **2017**, *9*, 15785–15790.

[175] He, Y.; Lodge, T. P. *Chem. Commun.* **2007**, 2732–2734.

[176] He, Y.; Lodge, T. P. *Macromolecules* **2008**, *41*, 167–174.

[177] Bergman, S. D.; Wudl, F. *J. Mater. Chem.* **2008**, *18*, 41–62.

[178] Syrett, J. A.; Becer, C. R.; Haddleton, D. M. *Polym. Chem.* **2010**, *1*, 978–987.

[179] Hartley, G. S. *Nature* **1937**, *140*, 281.

[180] Radu, A.; Byrne, R.; Alhashimy, N.; Fusaro, M.; Scarmagnani, S.; Diamond, D. *J. Photochem. Photobiol. A Chem.* **2009**, *206*, 109–115.

[181] He, J.; Tremblay, L.; Lacelle, S.; Zhao, Y. *Polym. Chem.* **2014**, *5*, 5403–5411.

[182] Li, C.; Zhang, Y.; Hu, J.; Cheng, J.; Liu, S. *Angew. Chem. Int. Ed.* **2010**, *49*, 5120–5124.

[183] Chen, W.; Wei, X.; Balazs, A. C.; Matyjaszewski, K.; Russell, T. P. *Macromolecules* **2011**, *44*, 1125–1131.

[184] Szilágyi, A.; Sumaru, K.; Sugiura, S.; Takagi, T.; Shinbo, T.; Zrínyi, M.; Kanamori, T. *Chem. Mater.* **2007**, *19*, 2730–2732.

[185] Fukuda, T.; Matsuda, H.; Shiraga, T.; Kimura, T.; Kato, M.; Viswanathan, N. K.; Kumar, J.; Tripathy, S. K. *Macromolecules* **2000**, *33*, 4220–4225.

[186] Nagano, S.; Koizuka, Y.; Murase, T.; Sano, M.; Shinohara, Y.; Amemiya, Y.; Seki, T. *Angew. Chem. Int. Ed.* **2012**, *51*, 5884–5888.

[187] Sano, M.; Shan, F.; Hara, M.; Nagano, S.; Shinohara, Y. *Soft Matter* **2015**, *11*, 5918–5925.

[188] Zhao, Y.; He, J. *Soft Matter* **2009**, *5*, 2686.

[189] Ramanujam, P. S.; Hvilsted, S.; Zebger, I.; Siesler, H. W. *Macromol. Rapid Commun.* **1995**, *16*, 455–461.

[190] Fischer, T.; Läsker, L.; Stumpe, J.; Kostromin, S. *J. Photochem. Photobiol. A Chem.* **1994**, *80*, 453–459.

[191] Ichimura, K.; Momose, M.; Kudo, K.; Akiyama, H.; Ishizuki, N. *Langmuir* **1995**, *11*, 2341–2343.

[192] Kurihara, S.; Sakamoto, A.; Yoneyama, D.; Nonaka, T. *Macromolecules* **1999**, *32*, 6493–6498.

[193] Wu, Y.; Zhang, Q.; Kanazawa, A.; Shiono, T.; Ikeda, T.; Nagase, Y. *Macromolecules* **1999**, *32*, 3951–3956.

[194] Ichimura, K.; Akiyama, H.; Ishizuki, N.; Kawanishi, Y. *Makromol. Chem. Rapid Commun.* **1993**, *14*, 813–817.

[195] Ikeda, T.; Tsutsumi, O. *Science* **1995**, *268*, 1873–1875.

[196] Natansohn, A.; Rochon, P.; Gosselin, J.; Xie, S. *Macromolecules* **1992**, *25*, 2268–2273.

[197] Ho, M. S.; Natansohn, A.; Rochon, P. *Macromolecules* **1995**, *28*, 6124–6127.

[198] De Sio, L.; Serak, S.; Tabiryan, N.; Umeton, C. *J. Mater. Chem.* **2011**, *21*, 6811.

[199] Kim, C. B.; Wistrom, J. C.; Ha, H.; Zhou, S. X.; Katsumata, R.; Jones, A. R.; Janes, D. W.; Miller, K. M.; Ellison, C. J. *Macromolecules* **2016**, *49*, 7069–7078.

[200] Daga, V. K.; Schwartz, E. L.; Chandler, C. M.; Lee, J. K.; Lin, Y.; Ober, C. K.; Watkins, J. J. *Nano Lett.* **2011**, *11*, 1153–1160.

[201] Ito, S.; Yamashita, A.; Akiyama, H.; Kihara, H.; Yoshida, M. *Macromolecules* **2018**, *51*, 3243–3253.

[202] Jackson, C.; Chen, Y. J.; Mays, J. W. *J. Appl. Polymer Sci.* **1996**, *61*, 865–874.

[203] Sperling, L. *Introduction To Physical Polymer Science*, 4th ed.; John Wiley & Sons, Inc.: Hoboken, NJ, USA, 2006.

[204] Yokota, K.; Kani, M.; Ishii, Y. *J. Polym. Sci. A* **1968**, *6*, 1325–1339.

[205] Bertinetto, C.; Duce, C.; Micheli, A.; Solaro, R.; Starita, A.; Tiné, M. R. *Polymer* **2007**, *48*, 7121–7129.

[206] Fox, T. G. *Bull. Am. Phys. Soc.* **1956**, *1*, 123.

[207] Kurihara, S.; Sakamoto, A.; Nonaka, T. *Macromolecules* **1998**, *31*, 4648–4650.

[208] Li, W.; Liu, M.; Qiu, F. *J. Phys. Chem. B* **2013**, *117*, 5280–5288.

[209] Folkes, M. J.; Keller, A. *Polymer* **1971**, *12*, 222–236.

[210] Froeba, A. P.; Kremer, H.; Leipertz, A. *J. Phys. Chem. B* **2008**, *112*, 12420–12430.

[211] François, A.; Riesen, N.; Gardner, K.; Monro, T. M.; Meldrum, A. *Opt. Express* **2016**, *24*, 12466.

[212] Bang, J.; Lodge, T. P.; Wang, X.; Brinker, K. L.; Burghardt, W. R. *Phys. Rev. Lett.* **2002**, *89*, 215505.

[213] Mulhearn, W. D.; Register, R. A. *ACS Macro Lett.* **2017**, *6*, 808–812.

[214] Zakeeruddin, S. M.; Grätzel, M. *Adv. Funct. Mater.* **2009**, *19*, 2187–2202.

[215] Lewandowski, A.; Świderska-Mocek, A. *J. Power Sources* **2009**, *194*, 601–609.

[216] Imaizumi, S.; Kokubo, H.; Watanabe, M. *Macromolecules* **2012**, *45*, 401–409.

[217] Katakabe, T.; Kaneko, T.; Watanabe, M.; Fukushima, T.; Aida, T. *J. Electrochem. Soc.* **2005**, *152*, A1913–A1916.

[218] Tang, J.; Tang, H.; Sun, W.; Plancher, H.; Radosz, M.; Shen, Y. *Chem. Commun.* **2005**, 3325–3327.

[219] Bara, J. E.; Lessmann, S.; Gabriel, C. J.; Hatakeyama, E. S.; Noble, R. D.; Gin, D. L. *Ind. Eng. Chem. Res.* **2007**, *46*, 5397–5404.

[220] Wang, W. H.; Zhang, Z. L.; Xie, Y. N.; Wang, L.; Yi, S.; Liu, K.; Liu, J.; Pang, D. W.; Zhao, X. Z. *Langmuir* **2007**, *23*, 11924–11931.

[221] Klingshirn, M. A.; Spear, S. K.; Subramanian, R.; Holbrey, J. D.; Huddleston, J. G.; Rogers, R. D. *Chem. Mater.* **2004**, *16*, 3091–3097.

[222] Matsumoto, K.; Endo, T. *Macromolecules* **2009**, *42*, 4580–4584.

[223] Lodge, T. P. *Science* **2008**, *321*, 50–51.

[224] An, Y.; Solis, F. J.; Jiang, H. *J. Mech. Phys. Solids* **2010**, *58*, 2083–2099.

[225] Zhou, C.; Hillmyer, M. A.; Lodge, T. P. *Macromolecules* **2011**, *44*, 1635–1641.

[226] Zhou, C.; Hillmyer, M. A.; Lodge, T. P. *J. Am. Chem. Soc.* **2012**, *134*, 10365–10368.

[227] Zhou, C.; Toombes, G. E. S.; Wasbrough, M. J.; Hillmyer, M. A.; Lodge, T. P. *Macromolecules* **2015**, *48*, 5934–5943.

[228] Hillmyer, M. A.; Bates, F. S. *Macromolecules* **1996**, *9297*, 6994–7002.

[229] Allgaier, J.; Poppe, A.; Willner, L.; Richter, D. *Macromolecules* **1997**, *30*, 1582–1586.

[230] Fetters, L. J.; Lohse, D.; Richter, D.; Witten, T.; Zirkel, A. *Macromolecules* **1994**, *27*, 4639–4647.

[231] Smith, G.; Yoon, D.; Jaffe, R. *Macromolecules* **1996**, *29*, 3462–3469.

[232] Shields, D.; Coover, H. *J. Polym. Sci.* **1959**, *39*, 532–533.

[233] Zhang, S.; Lee, K. H.; Sun, J.; Frisbie, C. D.; Lodge, T. P. *Macromolecules* **2011**, *44*, 8981–8989.

[234] Winter, H. H.; Chambon, F. *J. Rheol.* **1986**, *30*, 367–382.

[235] Mok, M. M.; Liu, X.; Bai, Z.; Lei, Y.; Lodge, T. P. *Macromolecules* **2011**, *44*, 1016–1025.

[236] Kinning, D. J.; Thomas, E. L. *Macromolecules* **1984**, *17*, 1712–1718.

[237] Colby, R. H. *Rheol. Acta* **2010**, *49*, 425–442.

[238] Milner, S. T. *Macromolecules* **2005**, *38*, 4929–4939.

[239] Seitz, M. E.; Burghardt, W. R.; Faber, K. T.; Shull, K. R. *Macromolecules* **2007**, *40*, 1218–1226.

[240] Yamauchi, H.; Maeda, Y. *J. Phys. Chem. B* **2007**, *111*, 12964–12968.

[241] Koyama, M.; Hirano, T.; Ohno, K.; Katsumoto, Y. *J. Phys. Chem. B* **2008**, *112*, 10854–10860.

[242] Jacquemin, J.; Husson, P.; Padua, A. A. H.; Majer, V. *Green Chem.* **2006**, *8*, 172.

[243] Benedek, I. *Pressure-Sensitive Adhesives and Applications*, 2nd ed.; Marcel Dekker: New York, NY, 2004.

Appendix

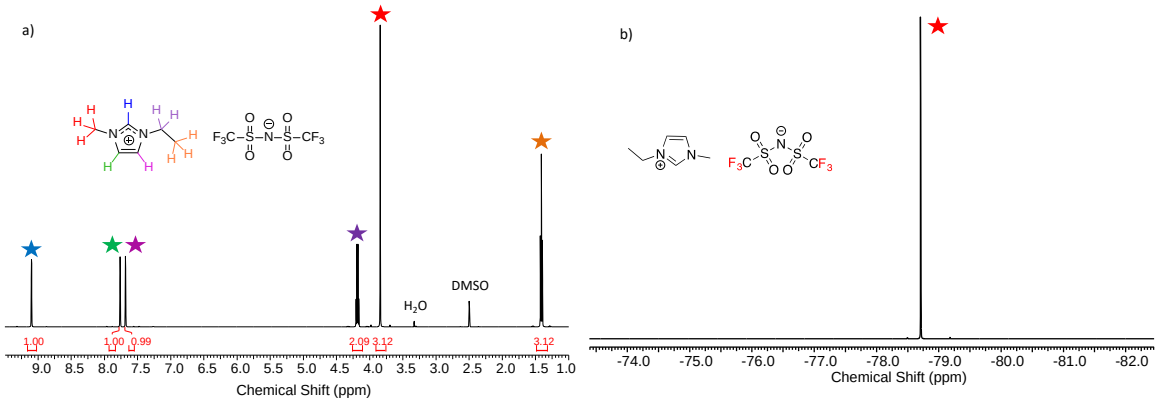

Figure 6.3: a) ^{1}H and b) ^{19}F NMR spectra of EMI TFSI.

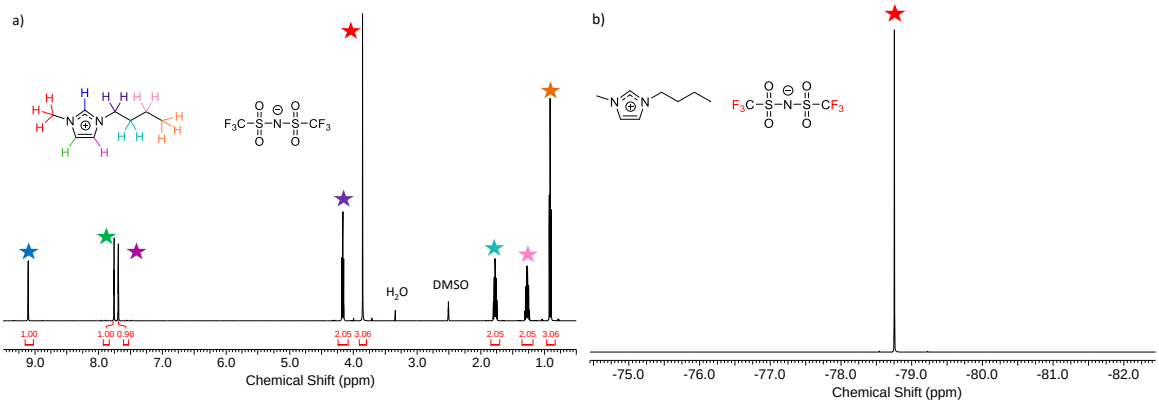

Figure 6.4: a) ^{1}H and b) ^{19}F NMR spectra of BMI TFSI

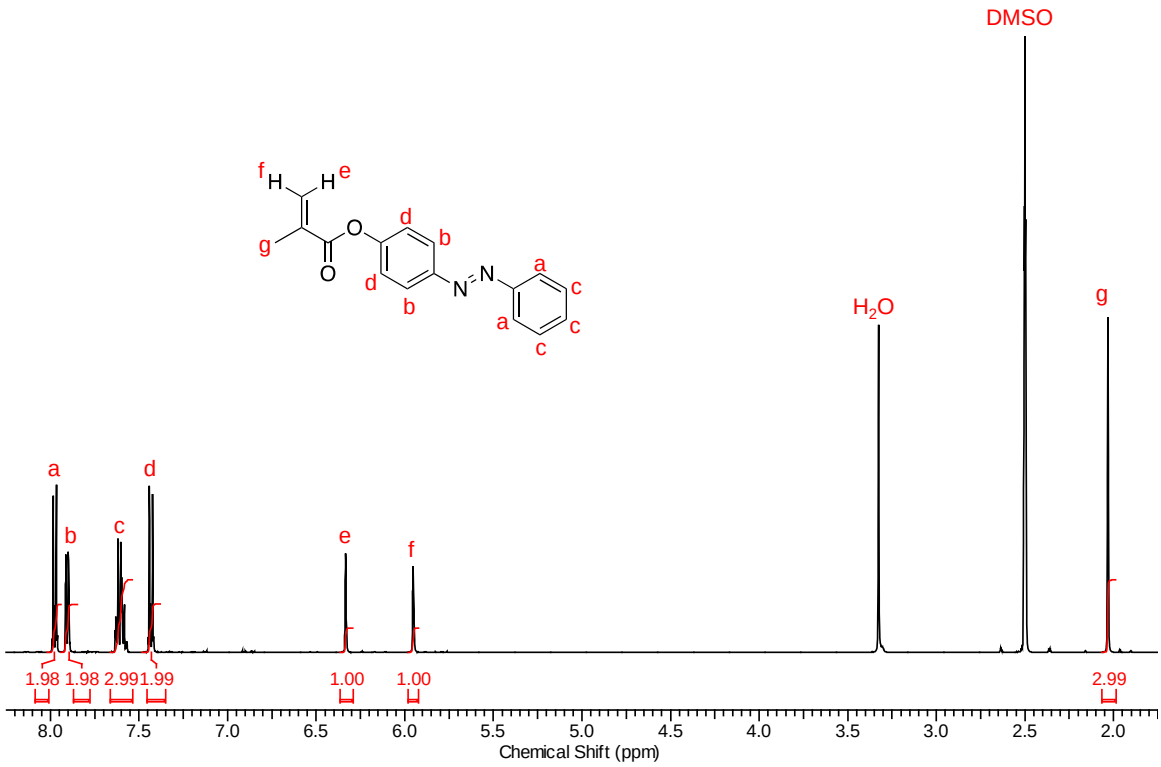

Figure 6.5: ^{1}H NMR spectrum of AzoMA

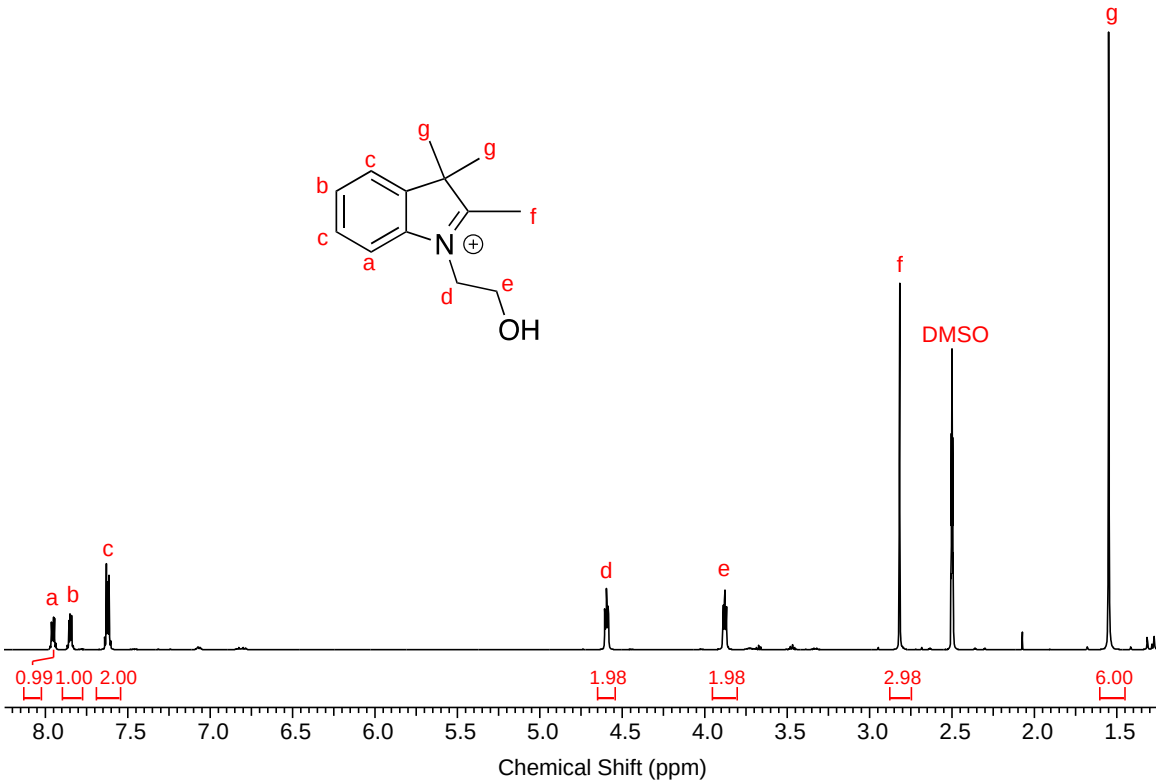

Figure 6.6: ^{1}H NMR spectrum of **A**.

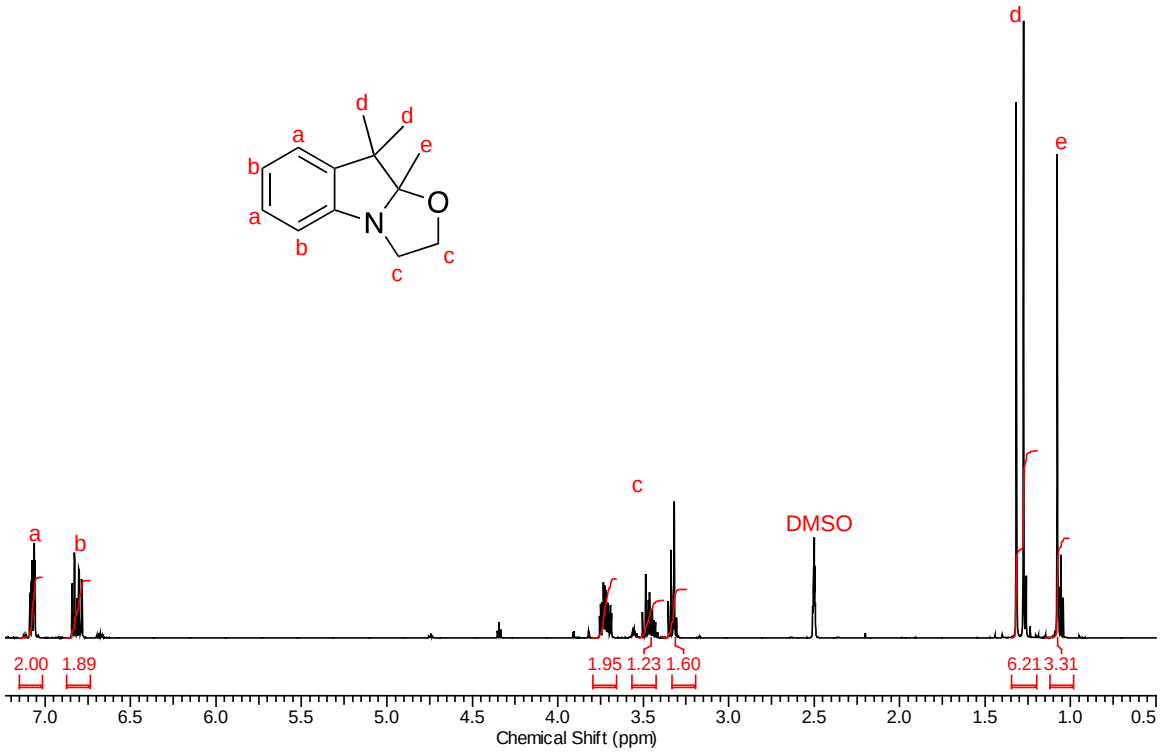

Figure 6.7: ^{1}H NMR spectrum of **B**.

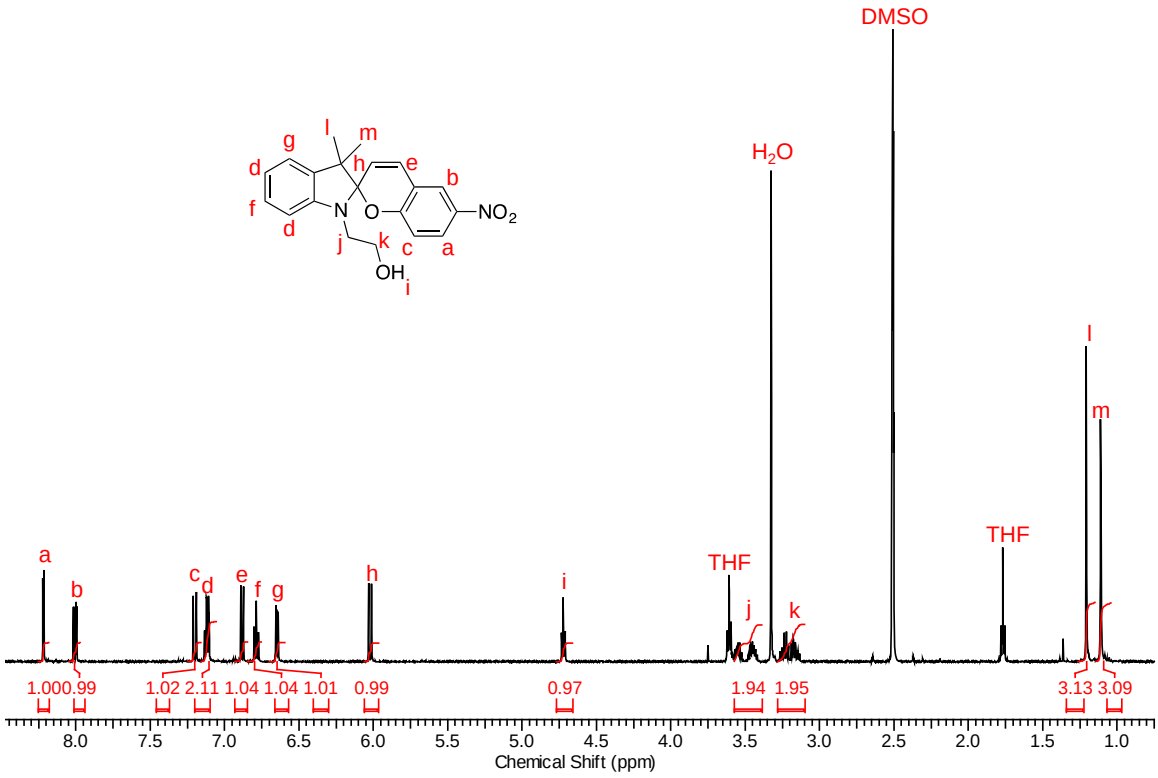

Figure 6.8: ^{1}H NMR spectrum of **SP**.

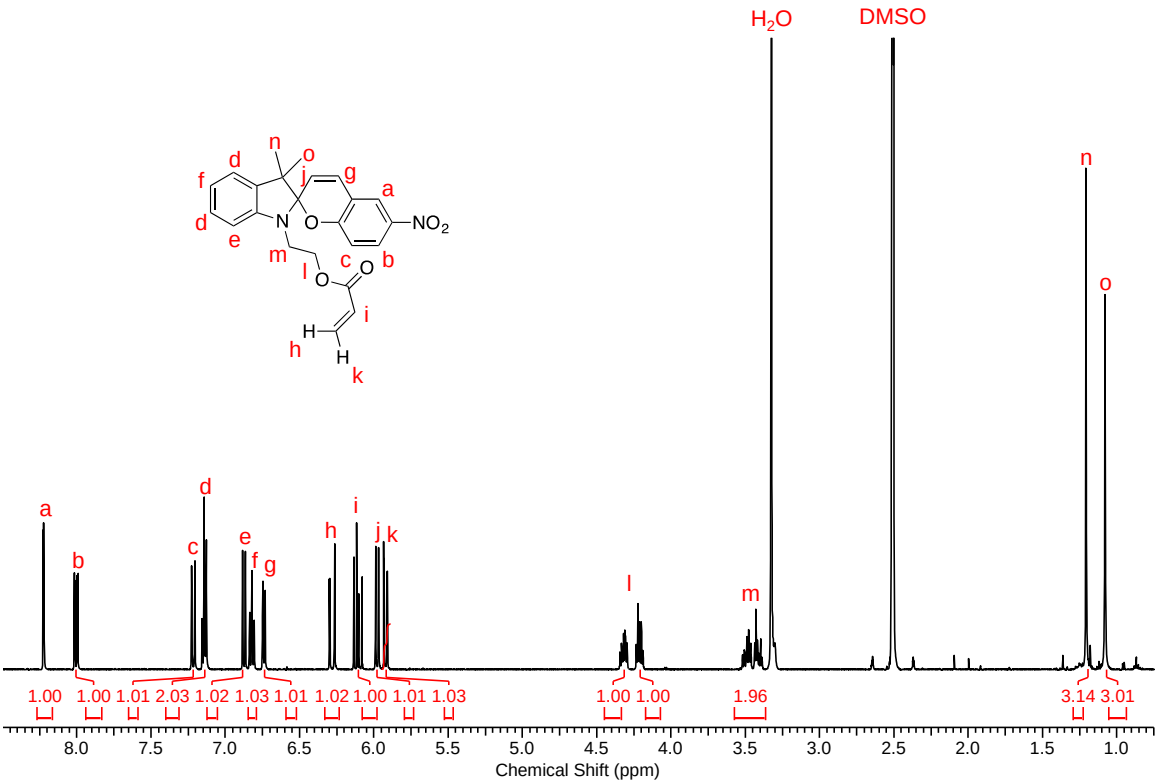

Figure 6.9: ^{1}H NMR spectrum of **SPA**.

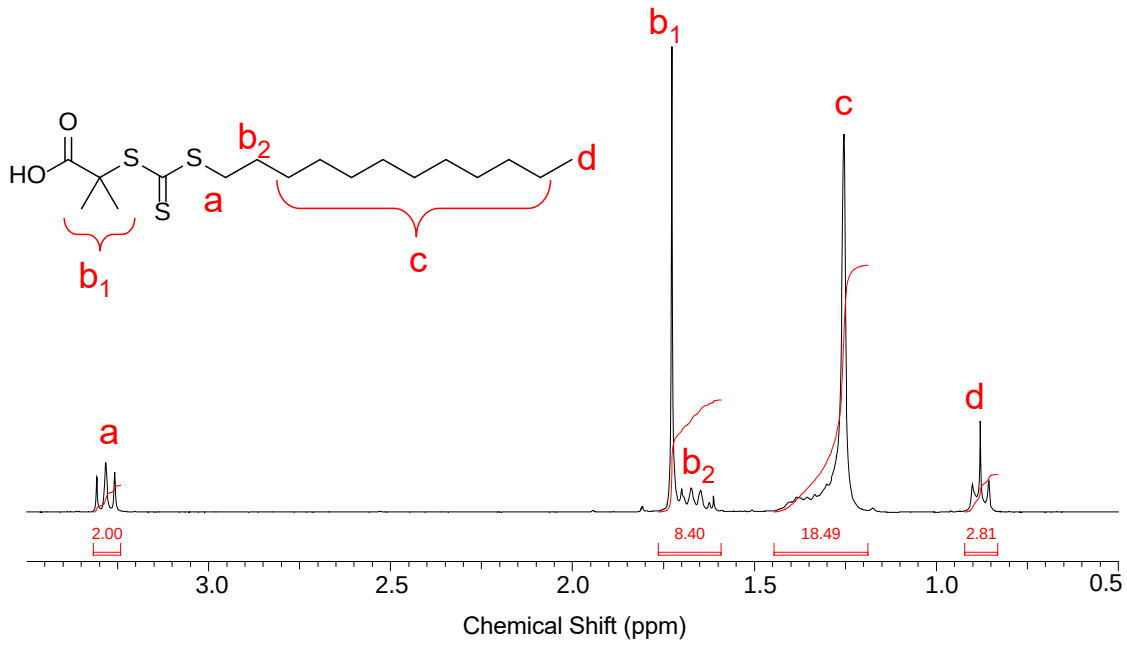

Figure 6.10: ^{1}H NMR spectrum of 2-(dodecylthiocarbonothioylthio)-2-methylpropionic acid.

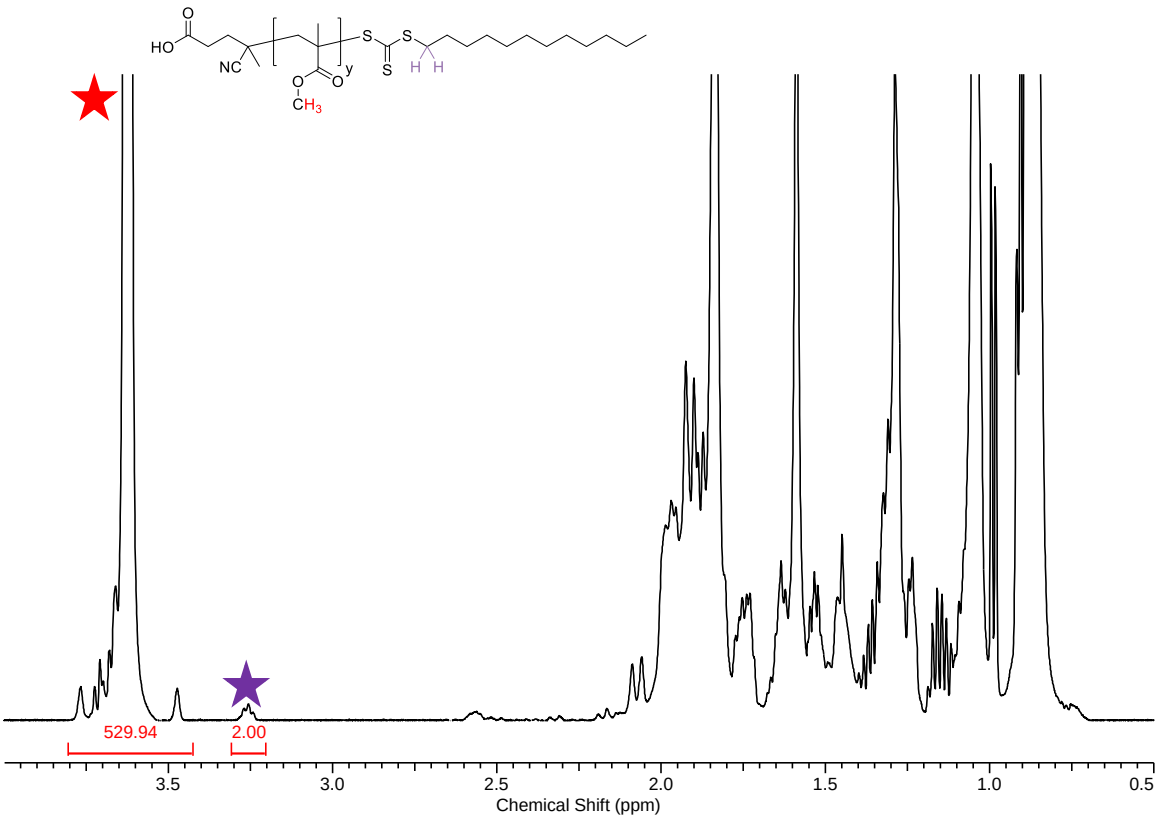

Figure 6.11: ^{1}H NMR spectrum of PMMA-CTA, the macro-CTA used for polymerization of M(B*s*A) (18-31(11)).

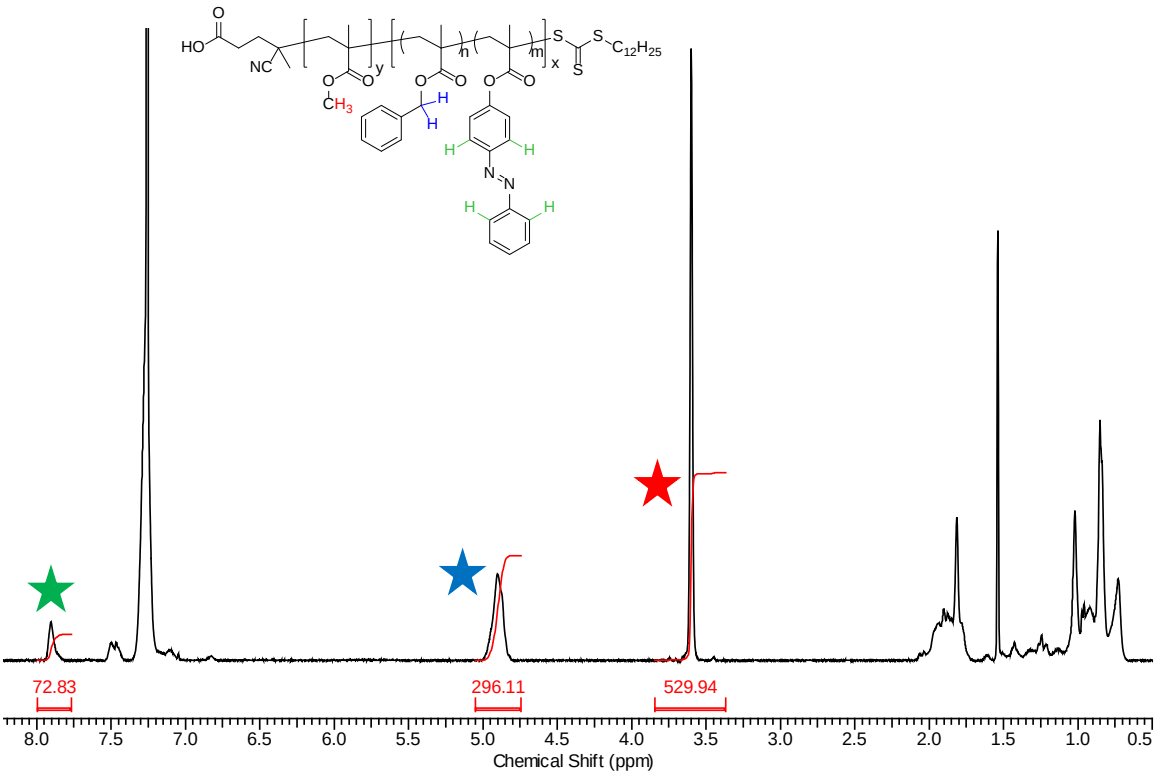

Figure 6.12: ^{1}H NMR spectrum of M(B*s*A)-CTA (18-31(11)), showing chain transfer agent peaks between 1.0 and 1.5 ppm.

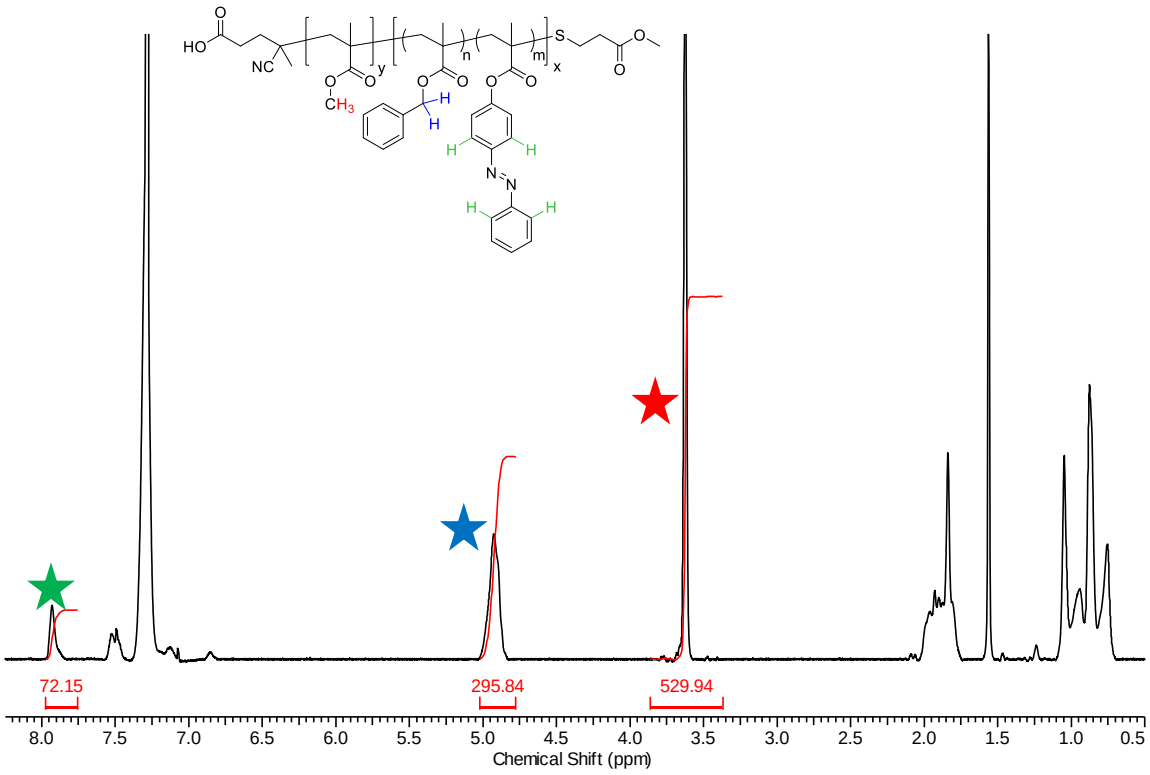

Figure 6.13: ^{1}H NMR spectrum of M(B*s*A) (18-31(11)), showing the disappearance of chain transfer agent peaks between 1.0 and 1.5 ppm.